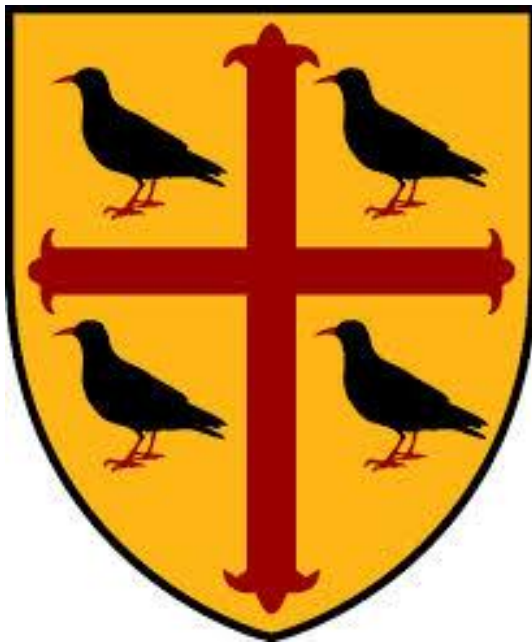


Effect of pH on Hydrogen Pick-up and Corrosion of Zircaloy-4



James Sayers
St Edmund Hall

*Thesis for submission of DPhil in Materials Science at the
University of Oxford*

Trinity 2017

Abstract

This thesis was part of the MUZIC-2 collaboration and describes the effect of the water chemistry on the corrosion and hydrogen pick-up in Zircaloy-4. Samples of Zircaloy-4 were oxidised in an autoclave containing pure water at 360°C ($\text{pH}_{360} = 6.15$) and at 350°C in an elevated pH ($\text{pH}_{350} = 8.82$, with 50% deuterated water) compared to commercial reactors. They were examined by scanning transmission electron microscopy (STEM), Thermal Desorption Spectroscopy (TDS) and Secondary Ion Mass Spectroscopy (SIMS).

The corrosion of Zircaloy-4 was not affected by the pH range tested during the pre-transition period of oxidation.

The oxide-metal (OM) interface was characterised along with second phase particles (SPPs) present in the metal and the oxide. It was found that the region of oxygen-saturated zirconium (OSZ) and ZrO follow a cyclical growth pattern which has the same periodicity as the advance of the OM interface. The OSZ gradually thickens as the oxidation rate decreases in the late pre-transition period, before disappearing after transition and then growing again in the second cycle of oxidation.

The oxidation of Fe and Cr and the Fe/Cr ratio in SPPs were examined. The SPPs were oxidised after the surrounding Zr oxidised. The Fe/Cr content in the middle of the SPPs decreased quickly as the Fe was found to migrate towards cracks formed at the edge of SPPs. Cr migrated much more slowly towards the cracks than Fe and oxidised before Fe.

The hydrogen/deuterium content of the samples was measured with TDS. Two characteristic desorption peaks for hydrogen have been found at ~350°C and ~650°C. The latter occurs when the difference in free energy between hydrogen in the metal and in the gas phase becomes positive. There is a delay to the desorption when an oxide layer is present, until the temperature reaches the point at which it is dissolved into the metal, allowing the hydrogen to desorb.

The hydrogen pick-up during the first 1.5 μm of oxide growth was similar for both environments. For thicker oxides the samples exposed to pure water showed four times the amount of hydrogen pick-up compared to the high pH samples.

The modelling of hydrogen desorption from Zr was carried out using the Tritium Migration and Analysis Program (TMAP). It was possible to replicate the low temperature peak with the literature values for the binding energy of hydrogen with Zr and the hydrogen diffusion activation energy (E_D), but for the high temperature peak the required E_D was higher than the literature value. An attempt at modelling both peaks simultaneously is shown.

Acknowledgements

I would first like to thank my supervisors, Professor Sergio Lozano-Perez and Dr Susan Ortner. Sergio has been the best supervisor I could ask for, he has always made time to help me with my experiments, and with my analysis of the results. Thanks to Sue for always taking the time to go through my writing and improving it over the years. The meetings I had with both Sue and Sergio were always positive and generated lots of different ideas.

Thanks goes to everyone in the MUZIC-2 collaboration for the illuminating discussions at the various meetings I was fortunate enough to attend and present at.

I want to thank all the support staff in the David Cockayne Centre for Electron Microscopy for keeping all the equipment in working order, and always willing to give me a helping hand.

A big thanks to Dr Thomas Aarholt, who was a massive help with my electron microscopy and with using Hyperspy. His enthusiasm for his work always gave me a big boost.

I couldn't have completed my NanoSIMS work without Dr Kexue Li, who collected all the fantastic data I have used in this thesis. I also wanted to thank him for taking the time to show me how to use his Matlab application for data analysis, and for generating the 3D profiles shown in Chapter 5.

Without the patience and expertise of Andree De Backer I would not have achieved anything with my TMAP simulations.

Thanks also to Charlie Ayres, Kalle Heinola, Aleksandra Baron-Wiechec, Anna Widdowson, and Ionut Jecu at CCFE for facilitating my visits to Culham and making sure the TDS was always at its best when I visited.

Thanks to my family, who have been immensely supportive of me throughout my life and with my decision to take on a DPhil. Finally thanks to all my friends, from all the corners of the Earth, I couldn't have done it without your help and support, and I might not have even have thought of doing a DPhil without the constant prodding from some certain people.

Contents

1 - Preface

1.1 – MUZIC-2 Collaboration	1
1.2 – The Current Work	1

2 – Literature Review

2.1 – Introduction	3
2.2 – Zirconium and Zirconium Alloys	4
2.3 - Corrosion of Zirconium Alloys	6
2.3.1 – Oxidation Rate	7
2.3.2 – Oxide Microstructure	10
2.4 – Hydrogen in Zirconium	11
2.4.1 – Hydrogen Pick-up	11
2.4.2 – Hydrogen Diffusion	16
2.5 – Water Chemistry of Nuclear Reactors	18
2.5.1 – Effects of pH	19
2.5.2 – Lithium Hydroxide and Boric Acid	20
2.6 – Hydrogen Desorption in Zirconium	25
2.7 – MUZIC-2	31
2.8 – References	32

3 – Experimental Techniques

3.1 – Transmission Electron Microscopy	41
3.1.1 – Sample Preparation For TEM	43
3.2 – Electron Energy Loss Spectroscopy	48
3.2.1 – Principal Component Analysis	50
3.2.2 – Multiple Linear Least Squares Fitting	54
3.3 – Thermal Desorption Spectroscopy	55
3.3.1 – Hydrogen Hot-Gas Extraction	59
3.4 – Secondary Ion Mass Spectroscopy	59
3.5 – Digital Scanning Calorimetry	60
3.6 – Samples Investigated	60
3.7 – References	62

4 – Oxidation vs. pH

4.1 – Oxide Growth	65
4.2 – EELS Analysis	67
4.2.1 – Low-Loss EELS	67
4.2.2 – OSZ and ZrO in High pH Samples	71
4.2.3 – OSZ and pH	88
4.2.4 – SPP Oxidation	96
4.3 – Discussion	124
4.4 – Summary	130
4.5 – References	131

5 – Hydrogen Measurements

5.1 – Digital Scanning Calorimetry	134
5.2 – Thermal Desorption Spectroscopy	138
5.2.1 – Initial Findings	138
5.2.2 – Calibration Tests	140
5.2.3 – Cold Rolled Samples	143
5.2.4 – Hydrogen Charged Samples	144
5.2.5 – Impact of Oxide on Hydrogen Desorption	146
5.2.6 – Effect of pH on Hydrogen Content	149
5.2.7 – Hydrogen Content of Samples Oxidised at High pH	150
5.3 – Hydrogen Content Measurements by Westinghouse and PSI	153
5.4 – NanoSIMS Results	157
5.4.1 – Diffusion Profiles	157
5.4.2 – 3D Profiles	161
5.5 – Discussion	164
5.6 – Summary	166
5.7 – References	167

6 – Simulation of Thermal Desorption Experiments

6.1 – Introduction to TMAP	170
6.2 – Input File For TMAP	171
6.3 – Interaction of Hydrogen With Metals	173
6.4 – TMAP Tests	174

6.4.1 – Binding Energy	176
6.4.2 – Diffusion Coefficient/Energy	177
6.4.3 – Solubility	179
6.4.4 – Fraction of Traps Filled	179
6.4.5 – Trap Concentration	180
6.4.6 – Two Trap Test	181
6.5 – Discussion	182
6.6 – Summary	185
6.7 – References	185

7 – Summary and Future Work

7.1 – Oxide Growth	187
7.2 – SPP Oxidation	187
7.3 – Hydrogen Pick-up Results	189
7.4 – Modelling	190
7.5 – Future Work	190

Appendix A

A.1 – Example Input File	192
A.2 – Example Input File For 2 Traps	194

1 – Preface

Contents

1.1 – MUZIC-2 Collaboration	1
1.2 – The Current Work	1

1.1 – MUZIC-2 Collaboration

MUZIC-2 was the second phase of a large international collaboration between industry and academic institutions seeking to understand the fundamental mechanisms behind aqueous corrosion and hydrogen pick-up of the zirconium alloys used for fuel cladding in Light Water Reactors. The collaboration was led by Westinghouse, and the industrial partners were: the US Electric Power Research Institute (EPRI), Électricité de France, Rolls-Royce, AMEC Foster Wheeler, Sandvik, Studsvik, Vattenfall, the Paul Scherrer Institute, and the UK National Nuclear Laboratory. The academic institutions were: University of Oxford, Imperial College London, Chalmers Institute of Technology, University of Manchester, and Pennsylvania State University.

1.2 – The Current Work

This thesis fits into the MUZIC-2 collaboration by testing samples of Zircaloy-4 oxidised in pure water at 360°C ($\text{pH}_{360}=6.15$) and in 50% heavy water with 2 ppm Li, 95 ppm K and 1050 ppm B at 350°C ($\text{pH}_{350}=8.82$) to answer if there is an effect of proton availability on aqueous corrosion and hydrogen pick-up. If the oxidation rate is not affected by the proton availability, then this means that the rate of electron transport through the oxide is much higher than the proton transport rate. This would mean that during the same period of oxidation the hydrogen pick-up would be similar.

Weight gain measurements were used to follow the oxidation kinetics. STEM was used to examine the OM interface and the SPPs present in the metal and the oxide, and to observe if there is any noticeable difference in the growth and morphology of the OM interface due to the pH. TDS and SIMS were used to observe the hydrogen/deuterium content of the samples and how this differed as a function of oxidation time and pH, along with SIMS for samples spiked with deuterium.

A literature review is presented in Chapter 2 to provide background information and cover the most recent research in zirconium oxidation. Chapter 3 describes the different techniques and equipment used in this work. Chapter 4 presents the STEM investigations on the OM interface, including

characterization of the different phases present, and the oxidation of SPPs. Chapter 5 reports the hydrogen measurements with TDS and the SIMS depth profiles. Chapter 6 shows my attempts at modelling the hydrogen desorption using the tritium migration and analysis program. Chapter 7 is the summary of the thesis, and contains some suggestions for further work.

All the work in this thesis is my own, and where other people's work is included it is acknowledged.

No part of this thesis has been submitted for any other degree at this or any other university.

2 – Literature Review

Contents

2.1 – Introduction	3
2.2 – Zirconium and Zirconium Alloys.....	4
2.3 - Corrosion of Zirconium Alloys.....	6
2.3.1 – Oxidation Rate	7
2.3.2 – Oxide Microstructure	10
2.4 – Hydrogen in Zirconium.....	11
2.4.1 – Hydrogen Pick-up	11
2.4.2 – Hydrogen Diffusion.....	16
2.5 – Water Chemistry of Nuclear Reactors.....	18
2.5.1 – Effects of pH	19
2.5.2 – Lithium Hydroxide and Boric Acid.....	20
2.6 – Hydrogen Desorption in Zirconium	25
2.7 – MUZIC-2.....	31
2.8 – References	32

2.1 – Introduction

My project investigated how the water chemistry changes the corrosion behaviour of Zircaloy-4 and its ability to pick up hydrogen. This literature review will therefore cover:

- The use of different zirconium alloys in nuclear reactors (including why oxidation and hydrogen pick-up are problems, and some developments in alloy design necessitated by the desire to minimize corrosion and hydrogen pick-up).
- A short review of the oxidation process including a distinction between initial oxidation, transition and breakaway, and a discussion of the source of hydrogen. My project looked at samples oxidised in an autoclave at pH = 8.82 at 350°C, in water containing 1050ppm (parts-per-million) boron and 2ppm lithium, so I will cover studies that have looked at effects of pH, Li and B on the oxidation process.
- A review of the factors known to affect the hydrogen pick-up, and why pH and water chemistry might be relevant.

- Within the project, the hydrogen absorbed by the zirconium alloy samples will be analysed using the thermal desorption technique, so the review will also cover some aspects of the desorption of hydrogen from zirconium alloys.

My project was part of the MUZIC-2 collaboration, and I will summarise the findings of this collaboration at the end of this chapter.

2.2 – Zirconium and Zirconium Alloys

Zirconium has an atomic number of 40 and a relative atomic mass number of 91.22. It is in the same group of the periodic table as Titanium and Hafnium, with which it shares some of its physical and mechanical properties. It has two crystallographic phases: α -zirconium, which has the HCP structure up to 863°C; and β -zirconium with the BCC structure above this temperature. Its melting point is 1845°C¹.

Many of the properties required for fuel cladding, such as good mechanical properties at elevated temperature, resistance to corrosion and a low neutron absorption cross section, are all met by zirconium¹, with a neutron absorption cross section of 0.18 barns. In addition it is much more abundant than any other suitable material.

In the nuclear industry there are several different reactors in use. The most common are water cooled reactors, such as pressurised-water reactors (PWRs), or boiling-water reactors (BWRs). Water-cooled reactors (both light water cooled and heavy water cooled) use zirconium alloys as structural materials in their fuel assemblies. There are substantial differences in the water chemistry used in the two reactor types: hydrogenated in PWRs and oxygenated in BWRs. Figure 2.1 shows the different reactor types and the zirconium alloys used in their fuel assemblies. The compositions of the zirconium alloys named in Figure 2.1 are summarised in Table 2.1

Although the Zircalloys have good corrosion resistance, they oxidise in the coolant water, producing hydrogen as a by-product. Zircaloy-2 (Zry-2) and Zircaloy-4 (Zry-4) both have adequate corrosion properties in BWRs so both alloys are still used in this reactor type. In PWRs however, the nickel content of Zry-2 led to large amount of hydrogen being absorbed^{2,3} by the cladding, causing hydrogen

embrittlement and a loss of mechanical strength. Zry-4 has essentially the same composition as Zry-2, except for the removal of nickel, and was developed as its replacement for PWR applications.

Alternatives to Zry-4 have since been developed, such as the Zr-Nb alloys (e.g. M5, E110 and ZIRLO) which have been shown to oxidise more slowly than Zry-4⁴⁻¹². Alloy X2, currently being researched¹³, has the same composition as E110.

Parameter	Western type <i>PWR</i>	<i>VVER</i> (440/1000) MW	CANDU ¹	<i>BWR</i>	<i>RBMK</i> ²
1. Coolant	Pressurized H ₂ O	Pressurized H ₂ O	Pressurized D ₂ O	Boiling H ₂ O	Boiling H ₂ O
2. Fuel Materials (Pressure tube materials)	Zry-4, <i>ZIRLO</i> , DUPLEX, M5, Inconel, SS ³	Zr-alloy E110	Zry-4 (Zr2.5Nb)	Zry-2, Zry-4, Inconel, SS	Zr-alloy E110, (Zr2.5Nb)
3. Average power rating, (kWt)	80-125	83/108	9-19	40-57	5
4. Fast Neutron Flux, Average, n/cm ² .s	6-9E13	5E13/7E13	1.5-2E12	4-7E13	1-2E13
5. Temperatures, °C					
Average Coolant inlet	279-294	267/290	249-257	272-278	270
Average Coolant outlet	313-329	298/320	293-305	280-300	284
Max Cladding OD	320-350	335/352	310	285-305	290
Steam mass content, %				7-14	14
6. System pressure, bar	155-158	125/165	96	70	67
7. Coolant Flow, m/s	3-6*	3.5/6	3-5	2-5*	3.7
8. Coolant Chemistry**					
Oxygen, ppb	<0.05	<0.1		200-400	<20
Hydrogen (D ₂), ppm	2-4		(3-10)	.05-.30	-
cc/kg	25-50	30-60			
Boron (as Boric acid), ppm	0-2200	0-1400	-	-	-
Li (as LiOH), ppm	0.5-3.5	0.05-0.6	1	-	-
K (as KOH), ppm	-	5-20		-	-
NH ₃ , ppm		6-30			
NaOH, ppm		0.03-0.35			

¹Canadian Deuterium Uranium (CANDU), ²Reaktor Bolshoi Mozhnosti Kanalov (RBMK), ³Stainless Steel (SS),

⁴Voda Voda Energo Reactor (VVER), ⁵Zirconium Low Oxidation (*ZIRLO*)

Figure 2.1 – Properties of different water cooled reactors¹⁴. Image reprinted with permission from ANT International.

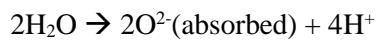
Alloy	Composition (wt. %)					
	Sn	Nb	Fe	Cr	Ni	O
Zircaloy-2	1.2-1.7	-	0.07-0.2	0.05-0.15	0.03-0.08	0.1-0.14
Zircaloy-4	1.2-1.7	-	0.18-0.24	0.07-0.13	-	0.1-0.14
M5	-	0.8-1.2	0.015-0.06	-	-	0.09-0.12
E110	-	0.9-1.1	0.014	<0.003	0.0035	0.05-0.07
ZIRLO	1	1	0.1	-	-	0.12

Table 2.1 – Composition of zirconium alloys¹⁵.

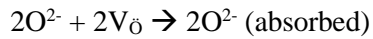
2.3 - Corrosion of Zirconium Alloys

Zirconium readily undergoes oxidation with dissociated oxygen from the water in the reactor. Hydrogen gas is also released. The reaction process is summarized in Figure 2.2¹⁶. The 5 labelled reactions are¹⁷:

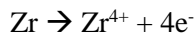
1. Adsorption of oxygen anion at the water-oxide interface after dissociation of water:



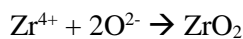
2. Absorption of oxygen anion by anionic vacancies:



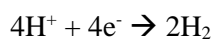
3. After diffusing through the oxide (which is the mechanism by which new zirconia forms^{1,18}), the oxygen anions react with zirconium atoms, generating zirconium cations and liberating 4 electrons:



4. Formation of zirconia:



5. In the remainder of the reaction, either the electrons generated flow to the oxide surface, to recombine there with the protons produced or the protons can flow in the opposite direction:



Note that the diffusion of Zr is considered to be negligible.

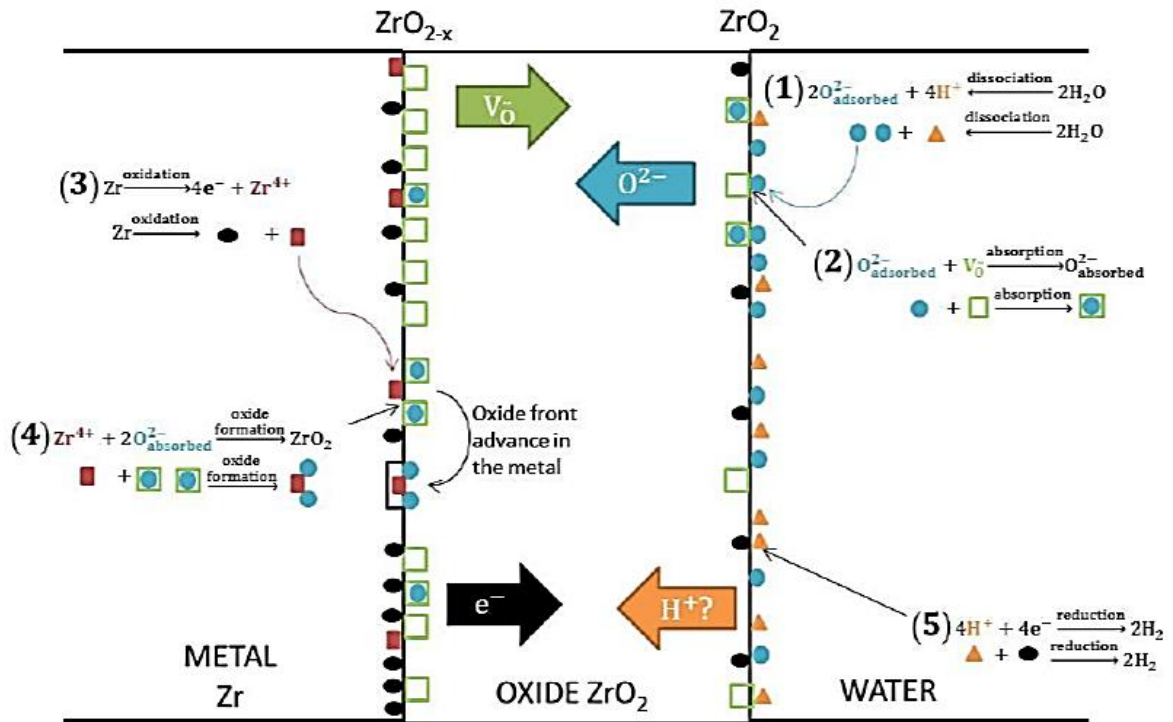


Figure 2.2 – Schematic of the corrosion of zirconium as shown by Couet¹⁶. The labelled reactions occur in series, and the rate-limiting steps (transport of oxidizing species) are shown with the large arrows in the oxide layer.

2.3.1 – Oxidation Rate

The oxidation process of zirconium in a reactor can be separated into two parts, pre-transition and post-transition. In the pre-transition stage, the oxide forms a protective layer which hinders further corrosion. The oxide growth as a function of time can be displayed by the following rate equation:

$$W = k * t^n \quad (1)$$

In this equation W is the weight gain (mg/dm^2), t is the time in days, and k & n are constants. In high temperature gaseous environments, the oxide growth rate initially has $n = 0.5$ (referred to in the literature as parabolic). However in the aqueous environment of a nuclear reactor core, the initial oxide growth rate tends towards cubic^{18,19} (i.e. $n = 1/3$). Studies on the activation energy for oxidation have shown a wide range of values, from 55 – 177 kJ/mol ^{20–24}.

After the oxide has grown to a few microns²⁵, there is an acceleration in the oxidation, which is called the transition point. There then follows another cycle of parabolic/cubic growth. This can occur several times (see Figure 2.3), before the cyclic behaviour develops into a high and linear growth rate, which is known as the ‘breakaway’. Various studies have shown that the time to transition is the main

factor dominating corrosion performance^{11,12,26-29}. Bouineau et al.³⁰ showed how the autoclave temperature modified the corrosion rate (shown in Figure 2.4). During the first cycle (Figure 2.4b), there is a difference in the time to transition for the different temperatures, although the 350/360°C experiments show a similar oxide thickness at transition.

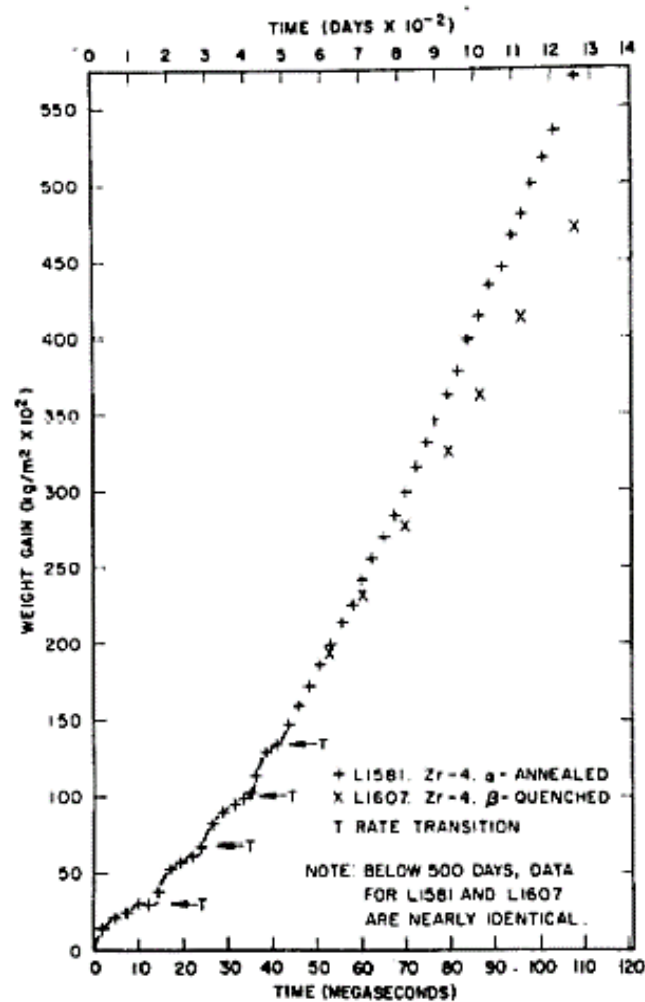


Figure 2.3 – Weight gain of Zircaloy-4 shown by Bryner²⁷. Reprinted from Journal of Nuclear Materials, vol. 82, Bryner J., The cyclic nature of corrosion of Zircaloy-4 in 633 K water, pages 81-101, copyright 1979, with permission from Elsevier.

The rate-determining step for pre-transition oxidation is not generally agreed, and may not be the same under all conditions. Cox considers electron and oxygen transport to be the rate-determining process during the pre-transition period³¹. Beie et al.³² suggested that the oxygen diffusion through a barrier layer at the metal/oxide interface is the rate determining process in a later period of oxidation.

In my experiments I will be comparing samples exposed to pure water and at a higher pH. This means that there will be a difference in the proton availability. As shown in Figure 2.2 protons are used for charge balance with the electrons liberated during corrosion, either by the electrons flowing through

the oxide to form hydrogen gas, or by the inward migration of protons to form hydrides. If the oxidation rate does not change due to changing the number of available protons, the rate of electron transport must be much higher than the proton transport through the oxide. This would also mean that hydrogen pick-up would be similar.

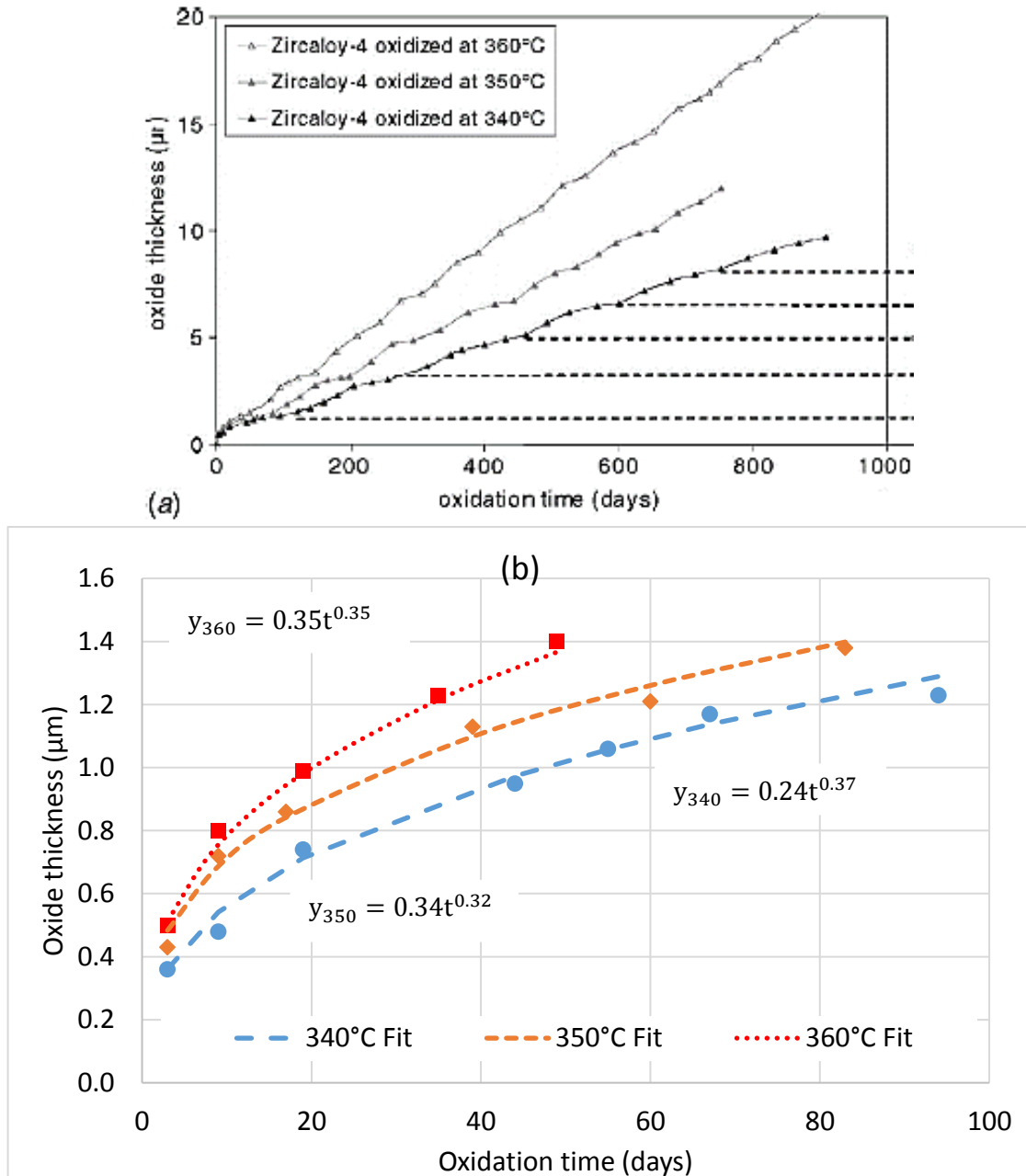


Figure 2.4 – Change in oxidation rate vs. temperature found by Bouineau et al.³⁰ The upper image shows the effect over several transition cycles (the black dashed lines show the approximate transition thickness for the 340°C experiment). The lower image is a close up of the first cycle, showing a longer time to transition for the 350°C experiment compared to the 360°C, although the thickness of the oxide at transition was similar. The equations for oxide growth were computed by myself on Matlab. Reproduced with permission from Bouineau V, Ambard A, Bénier G, et al. “A new model to predict the oxidation kinetics of zirconium alloys in a pressurized water reactor” *Zirconium in the Nuclear Industry: 15th International Symposium, ASTM STP 1505*, Kammenzind B, Limbäck M, Eds, copyright ASTM International, 100 Barr Harbour Drive, West Conshohocken, PA 19428.

2.3.2 – Oxide Microstructure

When monoclinic zirconia is formed it occupies more space than the zirconium metal by a factor of 1.56:1³³ (known as the Pilling-Bedworth ratio³⁴) Since the oxide forms by the inward diffusion of oxygen, and remains attached to the metal substrate, this excess volume produces an in-plane compressive stress in the oxide and a matching tensile stress in the metal. The stress mismatch at the metal-oxide interface causes the interface to deviate from planar, i.e. the interface undulates such that there are regions where the oxide is thicker. This redistributes the near-interface stresses, leading to out-of-plane tensile stresses in the thinner regions of the oxide, close to the oxidation front, and out-of-plane compression in the thicker regions³⁵. As the local tensile stresses develop, they induce in-plane cracks at delays in the oxidation front. These cannot extend while their tips lie in the compressive region. As the oxidation front moves inwards, the near-interface stress fields move away from the small in-plane cracks. These can then open and extend under the macroscopic compressive stresses in the oxide. The growth of the in-plane cracks partly relieves the overall compressive stresses in the oxide. Plastic deformation of the metal substrate also relieves the stresses caused by oxidation^{36–40}.

The stable phase of ZrO_2 is monoclinic, but the tetragonal phase is stabilised by compressive hydrostatic stress^{41,42}. The presence of metastable tetragonal zirconia at the metal/oxide interface is considered to relate in part to the high biaxial compressive stresses at that location^{12,43–45}. It may also be stabilised by the small size of newly nucleated ZrO_2 grains^{46,47}, which are predicted to be easier to form than monoclinic grains. As the oxide grows, and the various stress-relieving mechanisms operate, the compressive stress on the tetragonal grains decreases, causing them to undergo martensitic transformation to the monoclinic phase, accompanied with a volume expansion.

It is thought by some that porosity in the oxide correlates with a higher corrosion rate^{32,48}, but this is contradicted by other studies^{11,49}. The contradiction may occur because the authors did not distinguish between forms of porosity which provide a short circuit path for the environment through the oxide (such as through-thickness cracks or linked fine-scale porosity) and forms which do not (such as in-plane cracks).

2.4 – Hydrogen in Zirconium

The hydrogen generated during oxidation can form hydrogen gas and diffuse into the coolant, where it is released, or it can migrate through the oxide and enter the metal.

When hydrogen reaches the metal it forms bonds with either Zr vacancies in the lattice, or octahedral/tetrahedral interstitial sites. There have been several theoretical studies of the binding energy of hydrogen in zirconium. Iwasawa et al.⁵⁰ found that the binding energy of hydrogen to a Zr vacancy was 0.2 eV, and in the absence of a vacancy the migration energy of H between different interstitial sites ranged from 0.37 – 0.66 eV. This is a similar range to that shown by Chandra et al.⁵¹ for the diffusion activation energy, which was 0.36 – 0.49 eV. To convert from kJ/mol to eV/atom multiply by the Boltzmann constant (in eV/K), then divide by the molar gas constant ($8.617 \times 10^{-5} / 8.134 = 1.036 \times 10^{-5}$ eV/J/mol)

Christenson et al.⁵² found that the binding energy of hydrogen to octahedral and tetrahedral sites was 0.28 eV and 0.23 eV respectively, and Griessen⁵³ found the binding energy of H at vacancies to be ~0.25 eV.

2.4.1 – Hydrogen Pick-up

The ratio of hydrogen absorbed to the hydrogen generated during corrosion is known as the hydrogen pick-up fraction, $f_H = \frac{H_{\text{absorbed}}}{H_{\text{generated}}}$. When hydrogen is absorbed, it forms various zirconium hydrides, which can cause cladding embrittlement⁵⁴. Several different factors can influence f_H , such as the hydrogen and oxygen content of the corrosion media, the composition of the alloy, the temperature, pressure and pH⁵⁵.

As summarised by Garzarolli & Cox⁵⁵, there are several mechanisms by which the hydrogen can pass through the oxide:

- Diffusion through the oxide lattice (as protons, H^+ ; or hydroxyl ions, OH^-).
- Migration of hydrogen via pores in the oxide.
- Transport of H through oxidised second phase particles (SPPs).

- Transport of H through non-oxidised SPPs.

As stated by the authors however, ‘The mechanism governing the H ingress process is not really known’.

Several alloying elements affect f_H in binary Zr-based alloys, with Sn, Fe, Cr and Sb reducing f_H and Ni increasing f_H (see Figure 2.5³). Couet et al.⁵⁶ also found that niobium decreases f_H (see Figure 2.6). Some of these effects are maintained in more complex alloys. Kass⁵⁷ for example showed Fe also reduced f_H in Zr-0.5Sn, but Berry et al.³ found the effect of Sb to be weaker in Zry-2 than in Zr. The deleterious effects of Ni were retained in Zry-2 (see Figure 2.7). Couet et al.⁵⁶ found that Cu increased f_H in Zr-Nb (see Figure 2.6). Harada et al.⁵⁸ found that for Zry-2 and Zry-4, Fe and Sn had little effect on f_H , while Cr had no effect on f_H in Zry-2. They also showed that Ni increased f_H in Zry-2. Takahashi et al.⁵⁹ calculated that H^+ diffuses more slowly through oxides containing Fe or Cr than for pure zirconia.

Hatano et al.⁶⁰, along with Couet et al.⁵⁶ found that smaller Zr (Fe,Cr)₂ precipitates lead to a lower f_H than for larger precipitates. SPPs are incorporated into the oxide in an un-oxidised state^{59–63}, and Hatano et al. concluded that the larger SPPs remain un-oxidised in the oxide and act as shortcuts for hydrogen through the oxide. However Tejland et al.⁶⁴ showed the distribution of SPPs was quite broad, so even if the SPPs do allow for faster migration of hydrogen, the oxide will still have a greater impact on the hydrogen migration.

Couet et al.⁶⁵ proposed that the mechanism by which alloying elements affected f_H is controlled by the space charges in the oxide, which seeks to balance the ingress of hydrogen with the oxide electronic conductivity. They suggested that niobium in solution would dope the oxide layer and act as a donor to the hydrogen and cause f_H to be reduced, but have not determined the reason for copper increasing f_H .

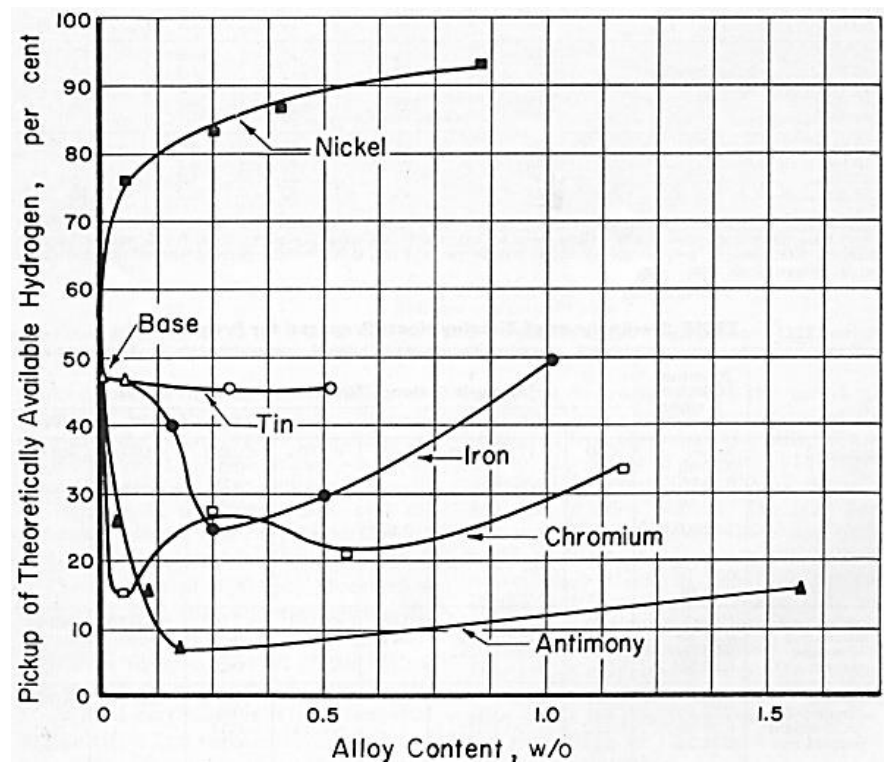


Figure 2.5 – Hydrogen pick-up vs alloying metal concentration³. Reproduced with permission from NACE International, Houston, TX. All rights reserved. Berry W., Vaughn D., White E., Hydrogen pickup during aqueous corrosion of zirconium alloys, Corrosion, Vol. 17, Issue 3, 1961. © NACE International 1945.

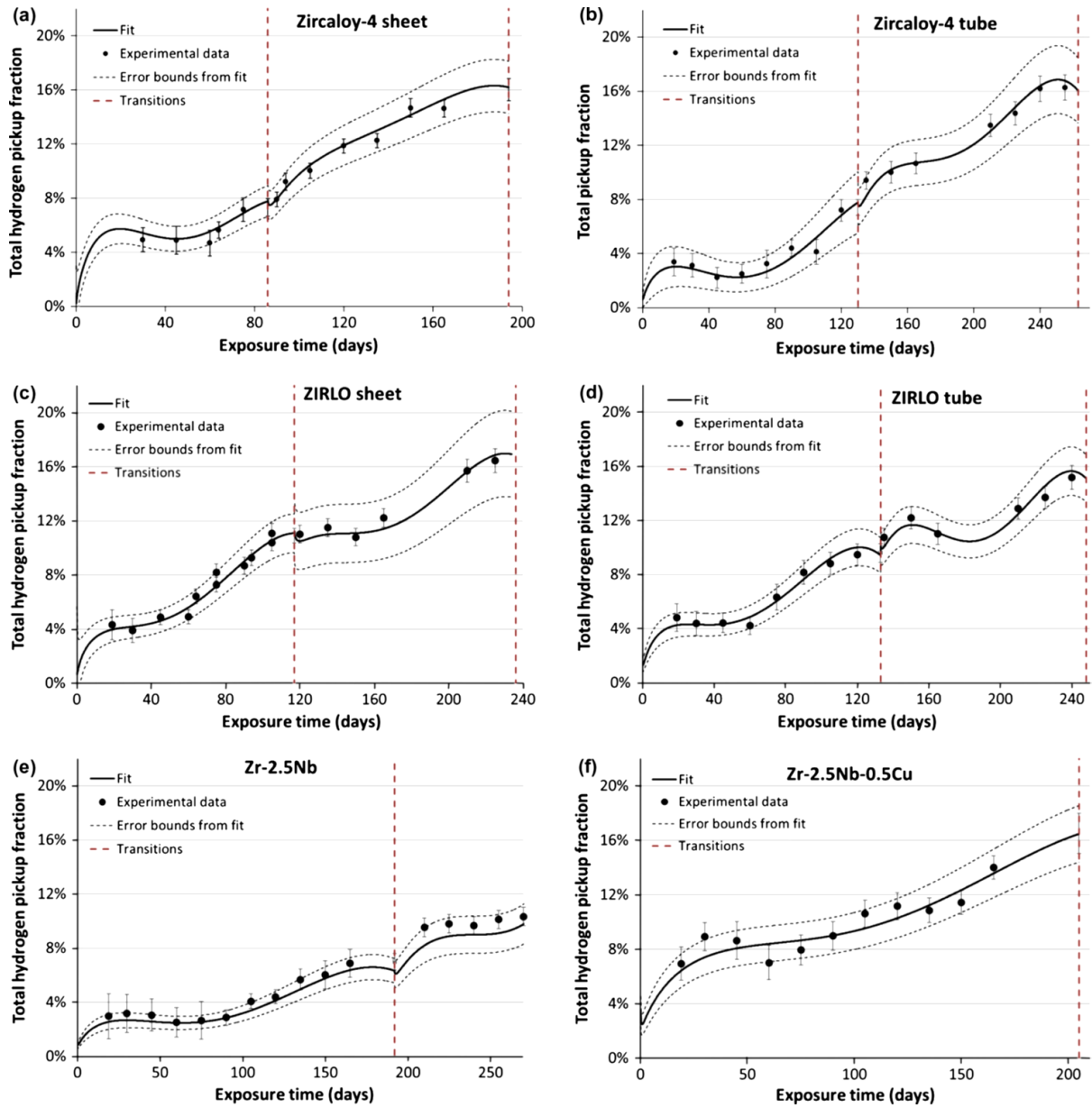
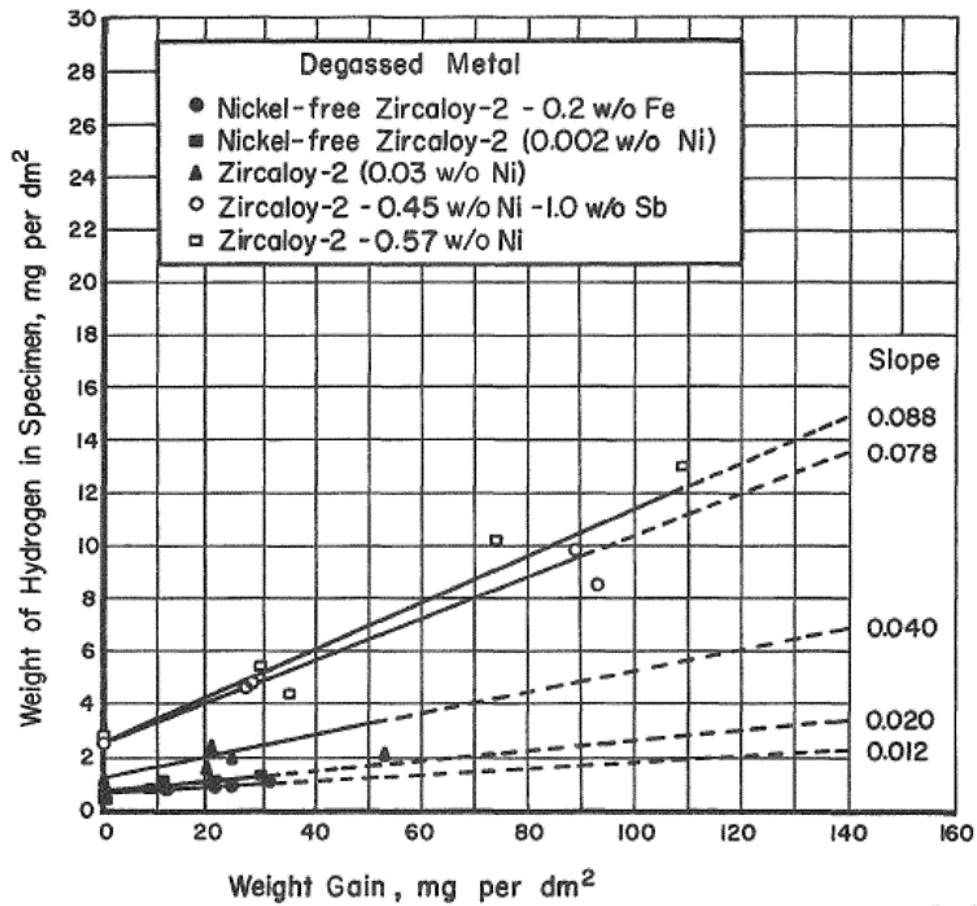


Figure 2.6 – Total hydrogen pick-up fraction as function of exposure time for various zirconium alloys⁵⁶. Reprinted from Journal of Nuclear Materials, vol. 451 (1-3), Couet A., Motta A.T., Comstock R.J., Hydrogen pickup measurements in zirconium alloys: Relation to oxidation kinetics, pages 1-13, copyright 2014, with permission from Elsevier.



A-32258

Figure 2.7 – Effect of Ni and Sb on hydrogen pick-up in Zry-2³. Reproduced with permission from NACE International, Houston, TX. All rights reserved. Berry W., Vaughn D., White E., Hydrogen pickup during aqueous corrosion of zirconium alloys, Corrosion, Vol. 17, Issue 3, 1961. © NACE International 1945.

Harada & Wakamatsu⁶⁶ carried out hydrogen pick-up measurements on Zry-2 and Zry-4, and found that the instantaneous f_H varied with the corrosion rate (as shown in Figure 2.8). During the pre-transition oxide growth the oxidation rate gradually decreases, but the instantaneous f_H increased during this time period. After transition, when the corrosion rate increased the instantaneous f_H decreased. This observation was repeated at the subsequent transitions. These results were also seen by Couet et al.⁵⁶, as shown in Figure 2.6.

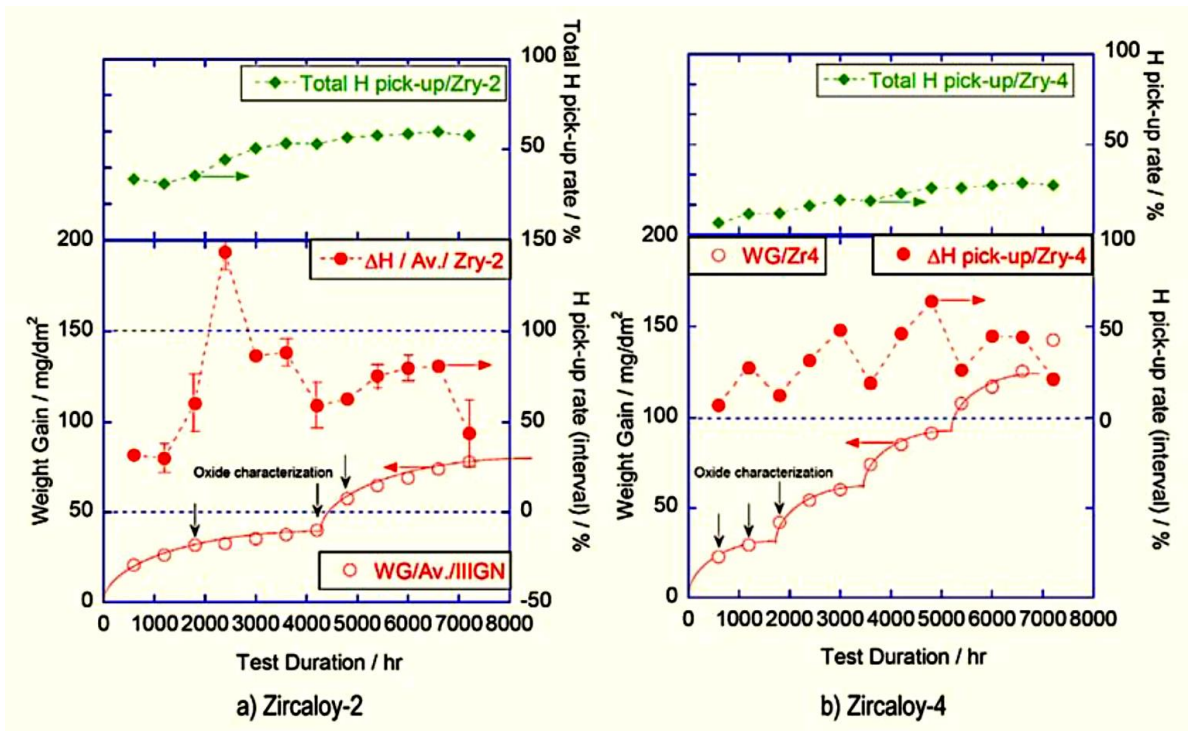


Figure 2.8 – Weight change of Zry-2 and Zry-4 in 360°C pure water⁵⁵. These graphs show the cyclic nature of f_H and oxide growth, and that the instantaneous f_H (middle graph) increases as the oxidation rate decreases, then decreases as the oxidation rate increases at transition. The black arrows indicate samples the authors chose for oxide characterisation. Image reprinted with permission from ANT International.

2.4.2 – Hydrogen Diffusion

Tupin et al.⁶⁷ examined deuterium (hydrogen) diffusion through zirconia and also the desorption of deuterium from zirconia. The SIMS tests they carried out showed in the pre-transition samples there are two parts to the oxide (shown in Figure 2.9); an external oxide a few hundred nanometres thick and an internal oxide approximately 1 μm thick. The external oxide was more permeable to deuterium than the internal oxide, where the transport was more limited by diffusion. In the post-transition samples, an intermediate layer with a constant deuterium concentration was found between the internal and external oxide, shown in Figure 2.10. These results backed up what was found previously by Harada and Wakamatsu⁶⁶.

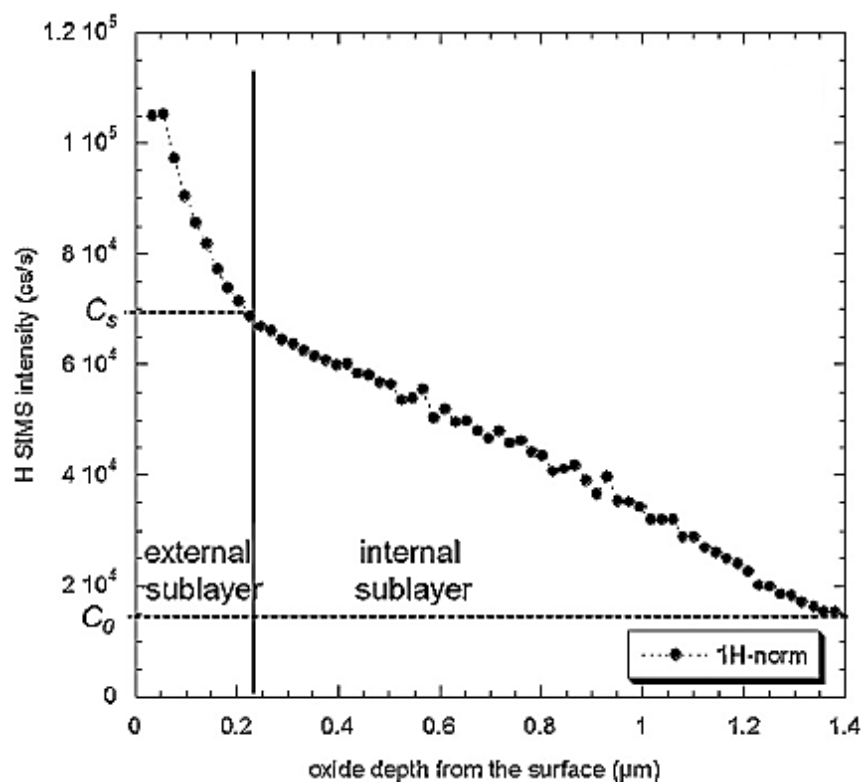


Figure 2.9 – Hydrogen depth profile produced by Tupin et al.⁶⁷, with the vertical bar separating the external and internal oxide. Reprinted from Corrosion Science, vol. 116, Tupin M., Martin F., Bisor C., et al., Hydrogen diffusion process in the oxides formed on zirconium alloys during corrosion in pressurized water reactor conditions, pages 1-13, copyright 2017, with permission from Elsevier.

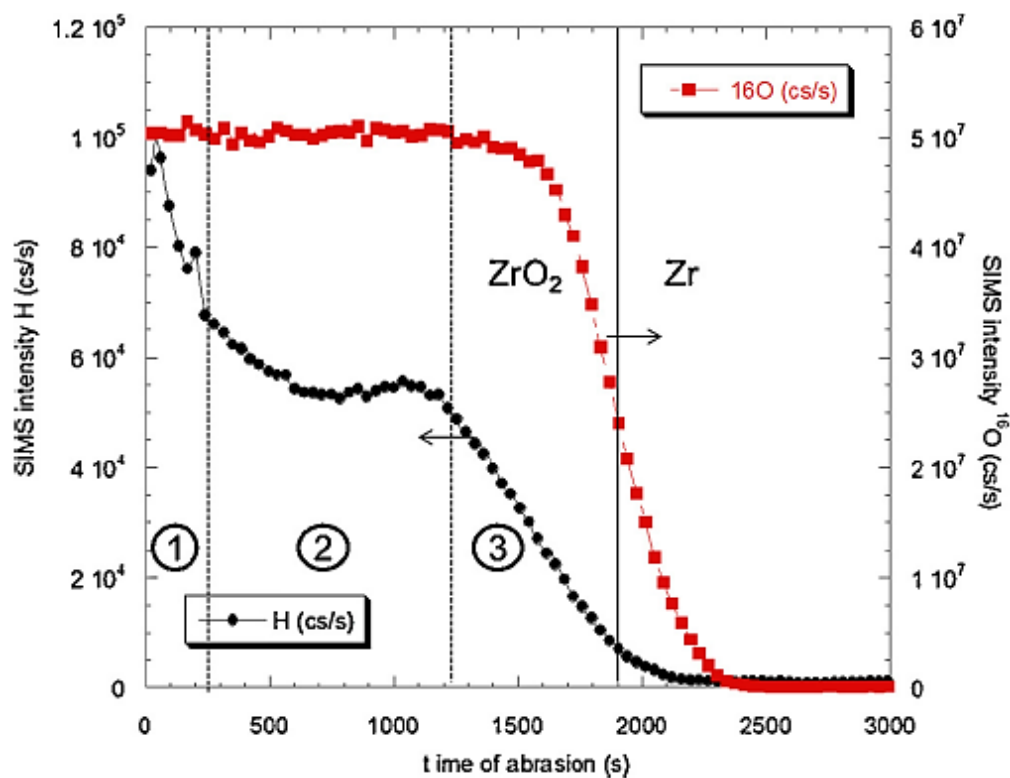


Figure 2.10 – Hydrogen (black circles) and oxygen (red squares) depth profiles in a post-transition oxide, as found by Tupin et al.⁶⁷. The numbered regions are: 1) external oxide, 2) intermediate oxide, 3) internal oxide. Reprinted from Corrosion Science, vol. 116, Tupin M., Martin F., Bisor C., et al., Hydrogen diffusion process in the oxides formed on zirconium alloys during corrosion in pressurized water reactor conditions, pages 1-13, copyright 2017, with permission from Elsevier.

2.5 – Water Chemistry of Nuclear Reactors

This section covers the importance of water chemistry (or pH) on the corrosion of the nuclear cladding.

The water chemistry of nuclear power plants has gradually evolved over the last few decades, to the point where the water chemistry is regarded as the problem solver rather than the problem causer for materials, as summarised by Wood⁶⁸. In his paper he notes some of the significant landmarks in the improvement of water chemistry, which are:

- Introduction of amines in the 1990s to improve pH control.
- The use of elevated lithium and pH in the primary systems of PWRs.
- Depleted zinc injection and use of enriched boric acid in PWRs in Germany.

It can be difficult to distinguish between the intrinsic effect of pH and the effects of the chemical additions used to influence the pH, chiefly LiOH and boric acid (H_3BO_3). Some papers therefore refer to pH when talking about the water chemistry, while others refer to the molar concentration of the solution used, or the concentrations in parts-per-million (ppm). For LiOH, 1 ppm equates to a concentration of 4.2×10^{-4} M, and for Boric acid (H_3BO_3) 1 ppm is approximately 1.6×10^{-4} M. Relating the concentrations to the pH is more complex as boric acid is a buffer. Figure 2.11 shows the pH of aqueous solutions with different concentrations of LiOH at room temperature and in the absence of boric acid. The pH of water decreases as temperature increases (which is important to consider when a plant is powered on and off), so the values below would be reduced for the elevated temperatures used in most experiments. Staudt & Marchl⁶⁹ showed that increasing the concentration of boric acid leads to a lower pH at 300°C, and that a decrease in the Li concentration decreases pH at 300°C. This chapter includes sections reviewing work in which pH, Li and B variations have been the main subject of study.

g/L LiOH	Molarity LiOH	pH Measured at RT	pH Theoretical at RT
0.013	0.0005	10.1	10.1
0.1	0.004	10.8	11.6
1.0	0.042	11.9	12.6
2.5	0.104	12.1	13.0
5.0	0.209	12.3	13.3
10.0	0.418	12.3	13.6
23.9	1.00	12.5	14.0

Figure 2.11 – pH of various LiOH solutions⁷⁰. Reproduced with permission from NACE International, Houston, TX. All rights reserved. Manolescu A.V., Mayer P., Simpson C.J., Effect of lithium hydroxide on corrosion rate of zirconium—2.5 wt% niobium in 340°C water, Corrosion, Vol. 38, Issue 1, 1962. © NACE International 1945.

2.5.1 – Effects of pH

In general zirconium alloys oxidise independently of pH, as long as the pH is not extremely low or extremely high (below 1 or above 13)³¹ or results from the addition of an aggressive species like LiOH.

EPRI carried out an investigation⁷¹ into how the primary coolant pH affected Westinghouse PWR plant radiation fields, more specifically operator dose rates. Radioactive corrosion products are the main contributor to operator dose rates, and the pH of the coolant is known to be important in determining which corrosion products form.

The purpose of the EPRI investigation was to determine the benefit to dose rates of operating modified and elevated lithium regimes compared to operating at a pH = 6.9 at 300°C regime (pH₃₀₀ = 6.9). The modified lithium regime had 2.2ppm Li and pH₃₀₀ 7.4, and was found to produce a reduction of approximately 20% to the dose rates compared to pH₃₀₀ 6.9 regime in Inconel grids (Inconel is a nickel-chromium superalloy). The elevated lithium regime (3.35ppm Li, pH₃₀₀ = 7.4) provided an extra 10% benefit to dose rates. Comparing Inconel and Zircaloy grids in the pH₃₀₀ = 6.9 regime found that the Zircaloy grids had between 23-26% lower dose rates than the Inconel grids, which was in good agreement with the Westinghouse estimates.

This shows that the pH of the environment in the reactor can be of a benefit to the dose rates in the reactor, but it is not obvious from this study if there is a benefit to corrosion or hydrogen pick-up.

2.5.2 – Lithium Hydroxide and Boric Acid

An example of the effect of LiOH at extreme pH was found by Manolescu et al.⁷⁰ They found that LiOH causes a large decrease in the oxidation resistance and a large increase in f_H at pH = 12 for Zry-2 and Zr-2.5Nb. For these alloys and pH levels they found that the corrosion is linearly dependent on time and LiOH concentration (see Figure 2.12).

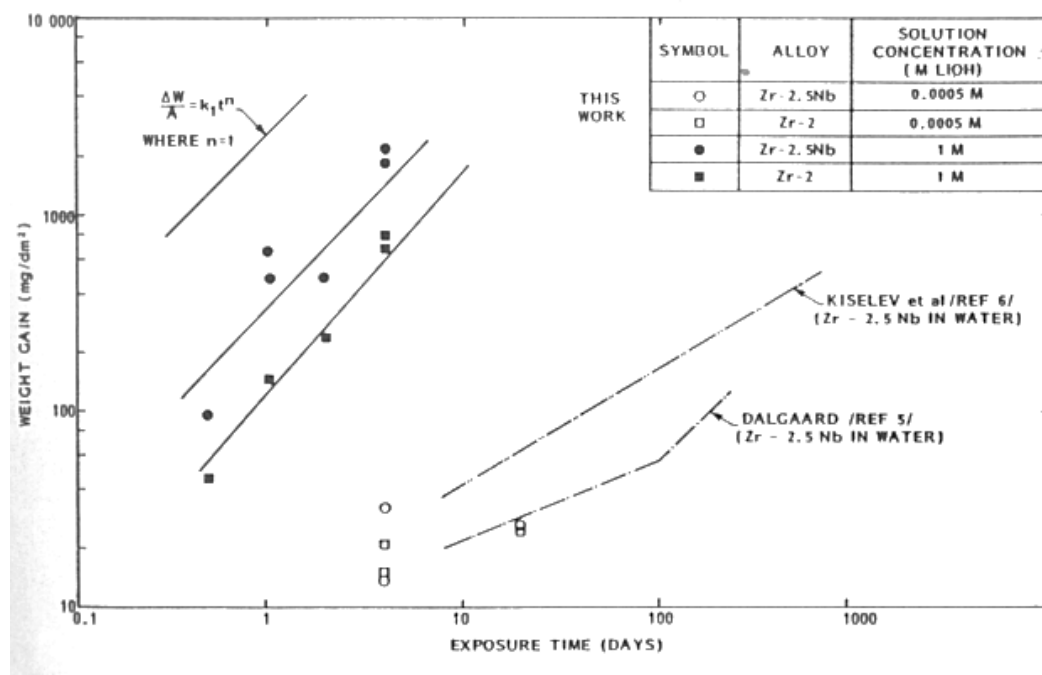


Figure 2.12 – Corrosion curves found by Manolescu et al.⁷⁰ Reproduced with permission from NACE International, Houston, TX. All rights reserved. Manolescu A.V., Mayer P., Simpson C.J., Effect of lithium hydroxide on corrosion rate of zirconium—2.5 wt% niobium in 340°C water, Corrosion, Vol. 38, Issue 1, 1962. © NACE International 1945.

In general it is found that corrosion of zirconium alloys is enhanced in lithiated water^{72–75}, causing more equiaxed grains to form in the oxide. TEM analysis shows if there are equiaxed grains and misoriented columnar grains in the oxide the underlying metal will oxidise more rapidly than if there are well oriented columnar grains^{73,75,76}.

Pêcheur et al.⁷³ carried out STEM analysis and SIMS on autoclaved samples of Zry-4 exposed to different Li concentrations (1.5 ppm Li, 650 ppm B; 70 ppm Li; out of pile-loop test with 10 ppm Li and 650 ppm B). Figure 2.13 shows the initial oxidation rates in 650ppm B and either 1.5ppm Li or 10ppm Li are similar, but the increase of [Li] leads to an enhanced oxidation rate after about 100

days. Before this enhanced oxidation they found that a thin inner barrier layer impedes the lithium access to the metal-oxide interface, with the lithium content in the oxide depending on the water chemistry conditions. Their TEM analysis found that the new grains at the metal-oxide interface were equiaxed and smaller than the columnar grains.

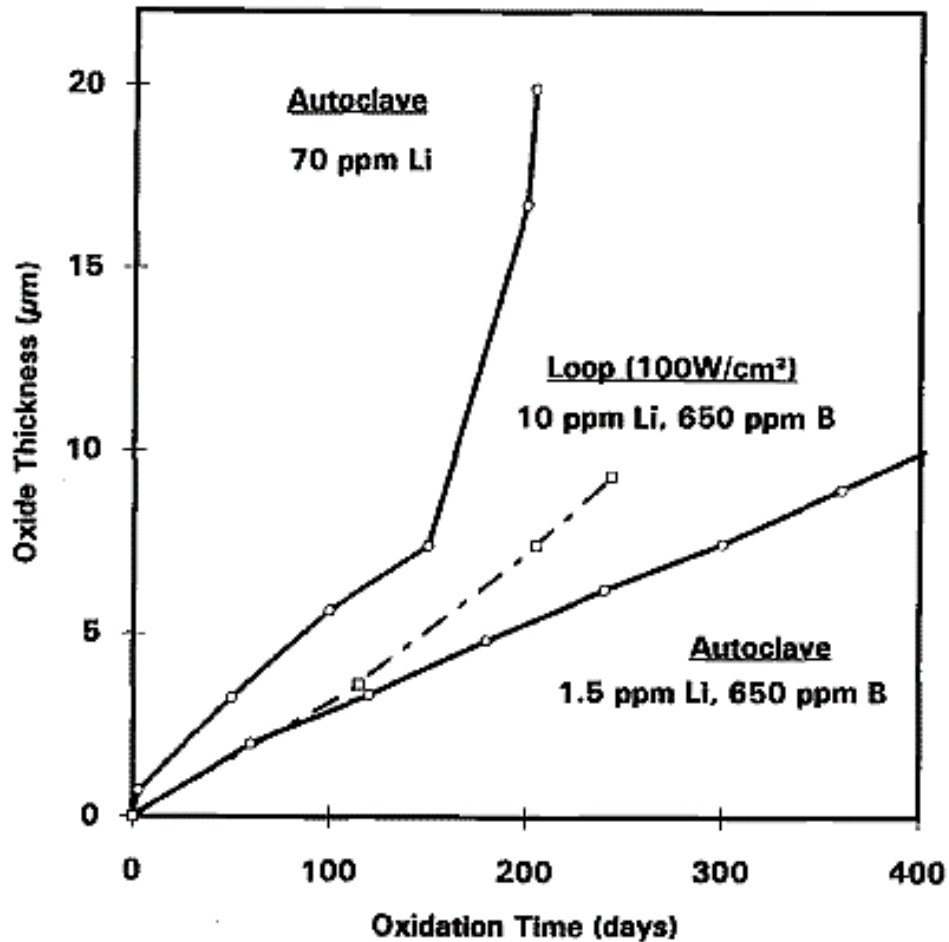


Figure 2.13 – Oxidation of Zircaloy-4 samples in various LiOH environments⁷³. Reproduced, with permission from Pêcheur, D., Godlewski, J., Billot, P., and Thomazet, J., "Microstructure of oxide films formed during the waterside corrosion of the Zircaloy-4 cladding in lithiated environment," *Zirconium in the Nuclear Industry: Eleventh International Symposium, ASTM STP 1295*, E. R. Bradley and G. P. Sabol, Eds., American Society for Testing and Materials, 1996, pp. 94-113 copyright ASTM International, 100 Barr Harbor Drive, West Conshohocken, PA 19428.

Pêcheur et al.⁷³ used SIMS to obtain the lithium profile in the oxide (shown in Figure 2.14). The graph shows that the inner oxide layer acts as a barrier to lithium ingress to the metal oxide interface. Just before the accelerated corrosion however, this barrier layer starts to decrease and allows more lithium to reach the metal/oxide interface and allow oxidation to increase.

Oskarrson et al.⁷⁶ compared samples of Zry-2 and Zry-4 in water and 70 ppm LiOH. They found that the pre-transition oxidation rate wasn't affected, but the transition occurs earlier and the post-transition oxidation rate is increased (see Figure 2.15).

It has been suggested that porosity which develops when zirconium alloys are exposed to LiOH could be the mechanism by which lithium is incorporated into the oxide.^{77,78}

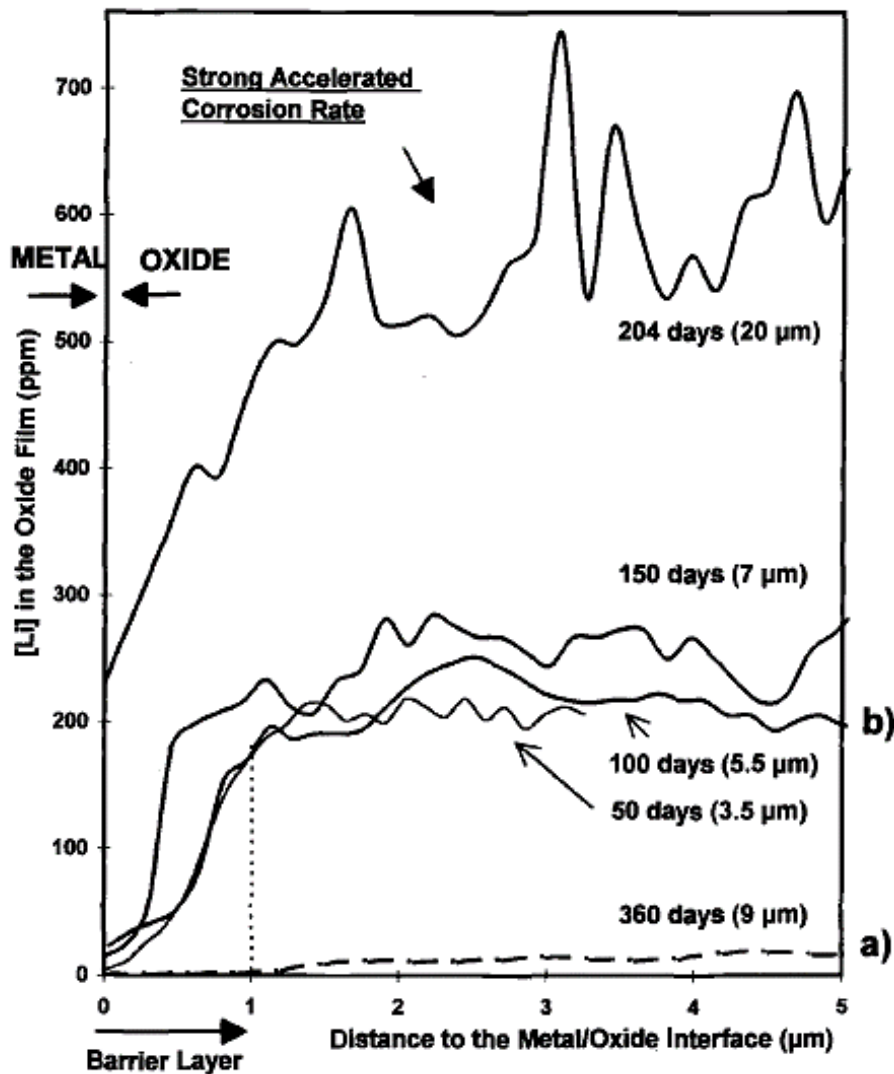


Figure 2.14 – Lithium profiles in oxide films formed on autoclaved Zry-4, with a) 1.5 ppm Li & 650 ppm B, and b) 70 ppm Li & 0 B⁷³. Reproduced, with permission from Pêcheur, D., Godlewski, J., Billot, P., and Thomazet, J., "Microstructure of oxide films formed during the waterside corrosion of the Zircaloy-4 cladding in lithiated environment," *Zirconium in the Nuclear Industry: Eleventh International Symposium, ASTM STP 1295*, E. R. Bradley and G. P. Sabol, Eds., American Society for Testing and Materials, 1996, pp. 94-113 copyright ASTM International, 100 Barr Harbor Drive, West Conshohocken, PA 19428.

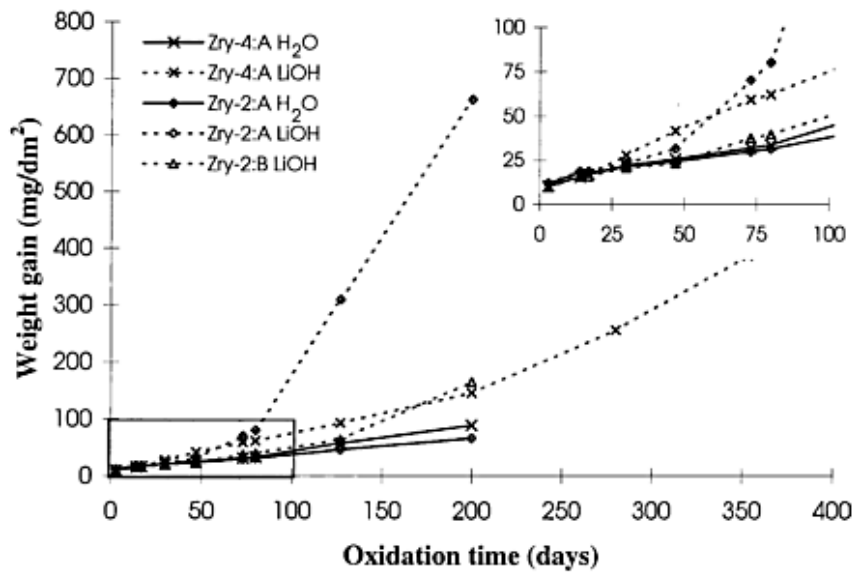


Figure 2.15 – Corrosion curves obtained by Oskarsson et al.⁷⁶ Reprinted from Journal of Nuclear Materials, Vol. 295, Oskarsson M., Ahlberg E., Pettersson K., Oxidation of Zircaloy-2 and Zircaloy-4 in water and lithiated water at 360 °C, pages 97-108, copyright 2001, with permission from Elsevier.

Cox reported tests to determine how adding boric acid to LiOH solutions affected the corrosion. In low LiOH solutions boric acid was found to have little effect on the corrosion^{78,79}, but in 1.0 M LiOH the presence of boric acid inhibited the generation of deep pores. It was suggested that this is due to the precipitation of a complex $\text{Li}_x\text{Zr}_y\text{B}_z$ salt, which plugs deep pores as they form and prevents a deep pore network forming.

Kido et al.⁸⁰ showed that adding lithium and boric acid to oxygen free water at 360°C could reduce f_H (see Figures 2.16 & 2.17).

My samples will be exposed 2 ppm Li and 1050 ppm B (which are the amounts used in reactor primary water) at 350°C, which means that compared to samples exposed to pure water there should be less f_H .

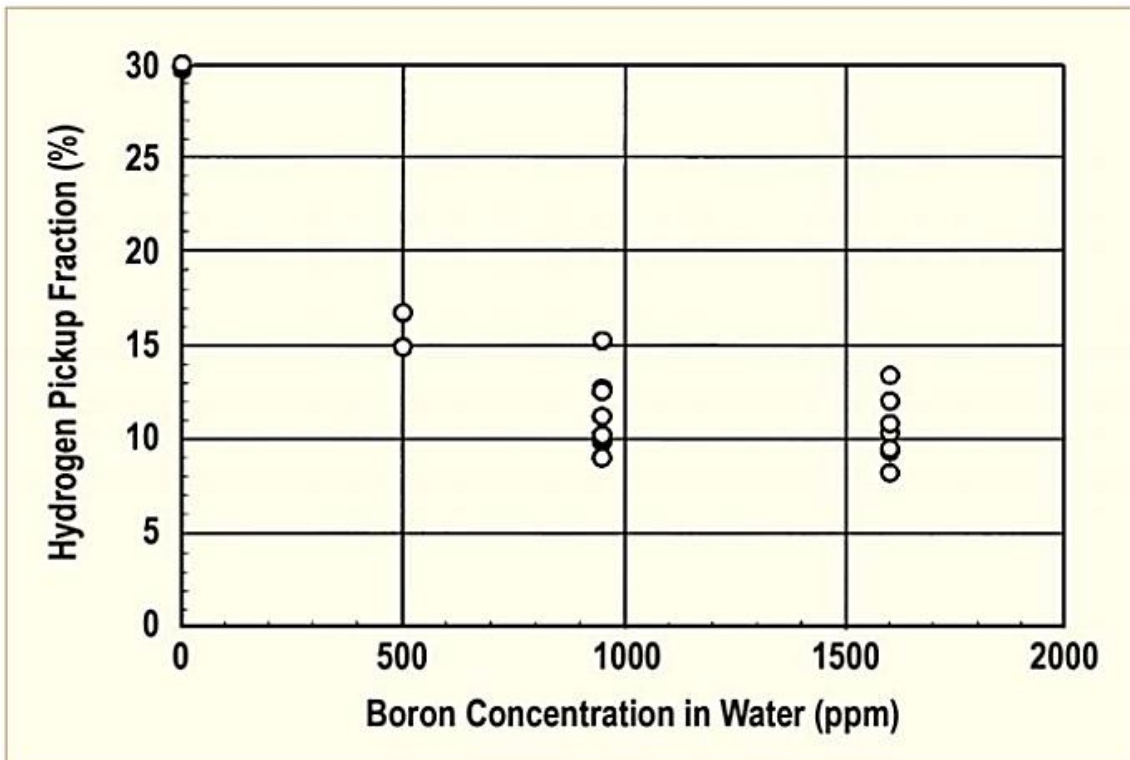


Figure 2.16 – Effect of boric acid on f_H in oxygen free water at 360°C⁵⁵. Image reprinted with permission from ANT International.

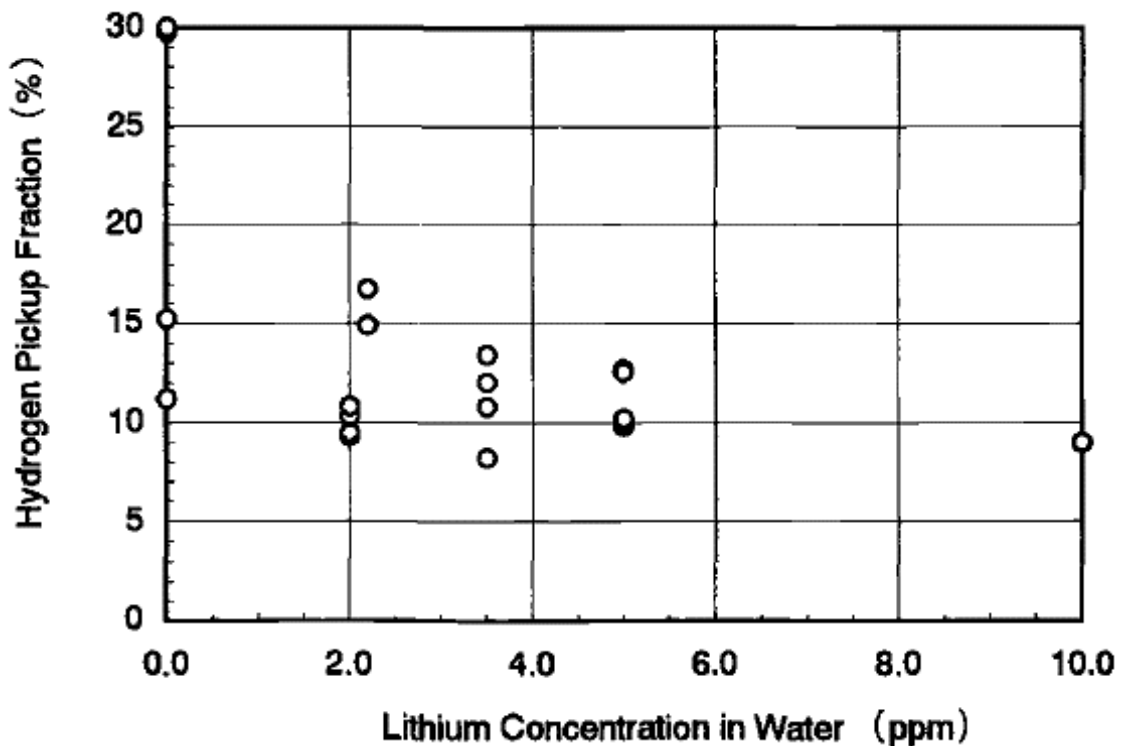


Figure 2.17 – Effect of lithium concentration on f_H in oxygen free water at 360°C⁸⁰. Reproduced, with permission from Kido, T., Wada, S., Takahashi, T., Uchida, H., Komine, I., and Inoue, Y., Behavior of lithium and boron in irradiated and unirradiated oxides formed on Zircaloy-4 claddings," *Zirconium in the Nuclear Industry Twelfth International Symposium, ASTM STP 1354*, G. P. Sabol and G. D. Moan, Eds., copyright ASTM International, 100 Barr Harbor Drive, West Conshohocken, PA 19428.

2.6 – Hydrogen Desorption in Zirconium

The concentration of dissolved hydrogen in equilibrium with a given external pressure decreases with increasing temperature, which is shown by Gulbransen & Andrew⁸¹ as:

$$p(H_2) = \left(\frac{N_{H(\alpha)}}{N_s - N_{H(\alpha)}}\right)^2 * \exp\left(\frac{2F_\alpha - F_{H_2(gas)}}{RT}\right) \quad (2)$$

In equation (2), $p(H_2)$ is the hydrogen pressure, $N_{H(\alpha)}$ is the number of hydrogen atoms in the alpha-phase, N_s is the number of sites, F_α is the free energy of hydrogen in the alpha phase, $F_{H_2(gas)}$ is the free energy of hydrogen in the gas phase, R is the molar gas constant and T is the temperature. When zirconium is heated in a vacuum, therefore, hydrogen is released. This can be observed by thermal desorption spectroscopy (TDS)/thermally programmed desorption (TPD). Figures 2.18 & 2.19 show typical spectra for hydrogen desorbing from zirconium in an oxygen containing atmosphere, where the peak from Figure 2.19 corresponds to the peak at 727°C (1000 K) in Figure 2.18. The slight shift in the peak is most likely to be due to a difference in the heating rates used in the two measurements, as heating a sample more slowly shifts desorption peaks to lower temperatures (Peterson et al.⁸² heated the sample at 35 °C/s, but Chen et al.⁸³ didn't state their heating rate). The larger peak in Figure 2.18 is attributed by the authors to the change in crystal structure during the $\alpha - \beta$ phase change (which occurs at the minimum around 1100K). However hydrogen has a higher solubility limit in β -Zr than α -Zr^{84,85}, which means the authors were incorrect in their analysis. Chen et al. proposed that the hydride dissolution is restricted by the presence of oxygen in the atmosphere.

Gulbransen and Andrew⁸¹ measured the decomposition pressures for hydrogen in zirconium at different temperatures and found that the difference in free energy between hydrogen in α -Zr and hydrogen in the gas phase (as H_2) changes from a negative to a positive value between 600°-700°C. This means that in this temperature range, it is more energetically favourable for hydrogen to be in the gas phase than in the metal. They also found that to keep a particular ppm of hydrogen in zirconium required a higher pressure of hydrogen for higher temperatures.

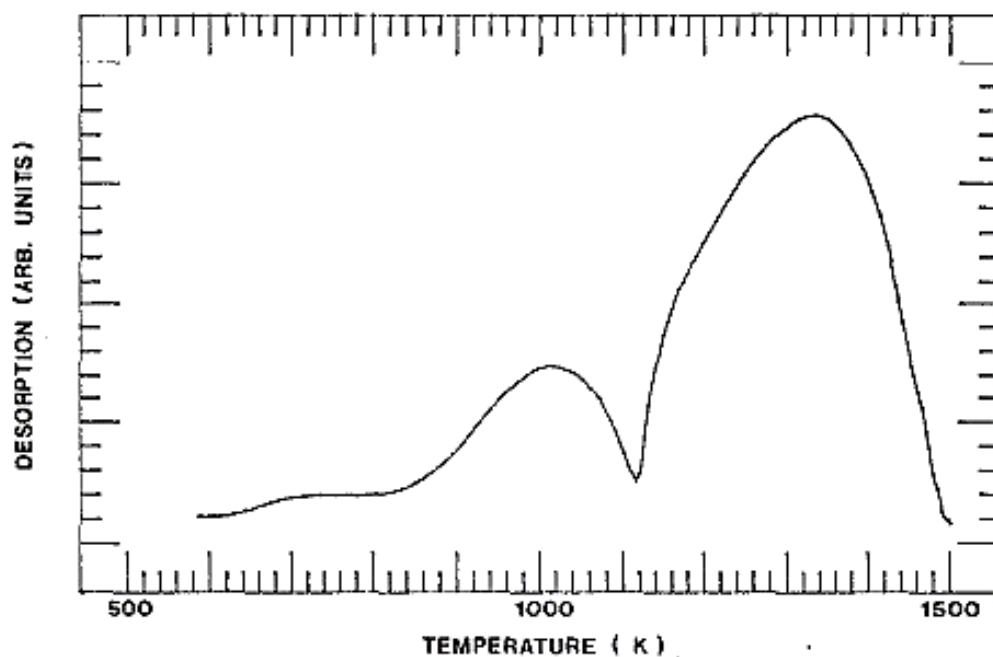


Figure 2.18 – Typical TDS spectrum of hydrogen desorbing from zirconium⁸². Reprinted from Applied Surface Science, Vol. 24, Peterson W.J., Gilbert R.E., Hoflund G.B., The interaction of hydrogen with polycrystalline zirconium Part II. The effect of preadsorbed oxygen, pages 121-124, copyright 1985, with permission from Elsevier.

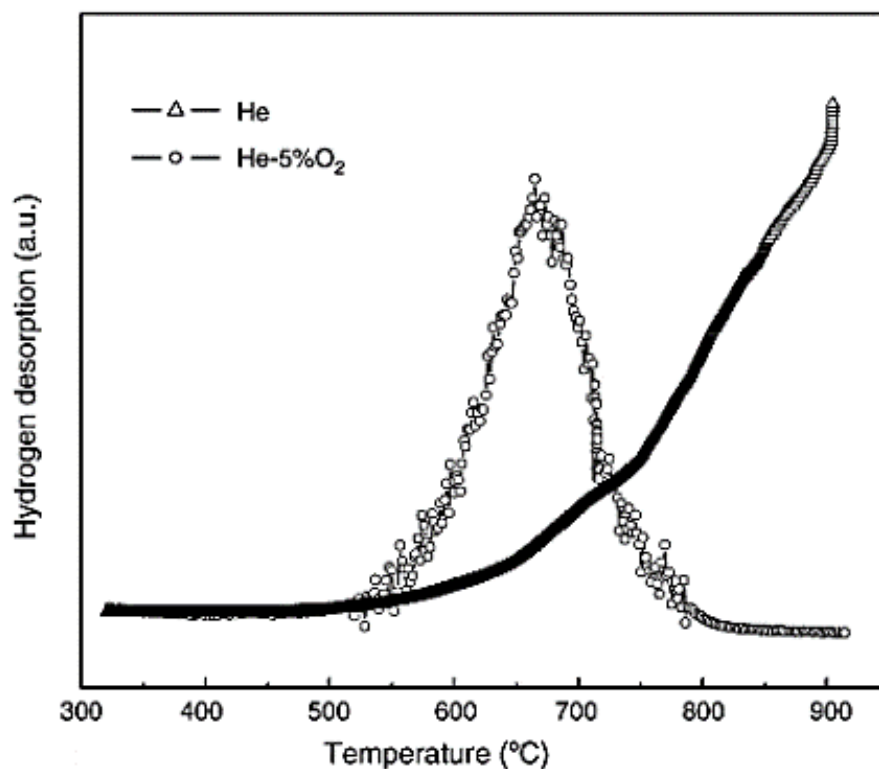


Figure 2.19 – Hydrogen desorption shown by Chen et al.⁸³ In their experiments they heated a sample of zirconium hydride in a helium atmosphere and a helium-5% oxygen atmosphere. The presence of oxygen causes an oxide layer to form on the zirconium, which draws the hydrogen from the metal and allows it to be desorbed. Reprinted from Journal of Alloys & Compounds, Vol. 469 (1-2), Chen W, Wang L, Lu S. Influence of oxide layer on hydrogen desorption from zirconium hydride, pages 142-145, copyright 2009, with permission from Elsevier.

Asbury et al.⁸⁶ found that hydrogen adsorbs dissociatively at the metal surface. They found this by charging a sample of zirconium with deuterium gas at 427°C, cooling to room temperature and exposing the sample to oxygen. Figure 2.20 shows the TDS that followed, with the sharp upward curve being the same high temperature curve in Figure 2.18. The HD curve shows that when the deuterium gas was absorbed it did so monotonically. The atoms then recombined before being desorbed, which is why there is a HD peak. They also found that the presence of oxygen at the surface draws hydrogen from the bulk rather than from the atmosphere. They proved this by first charging a sample of zirconium with oxygen, then with deuterium gas and Figure 2.21 shows the TDS results, which clearly show that none of the deuterium gas was absorbed from the air.

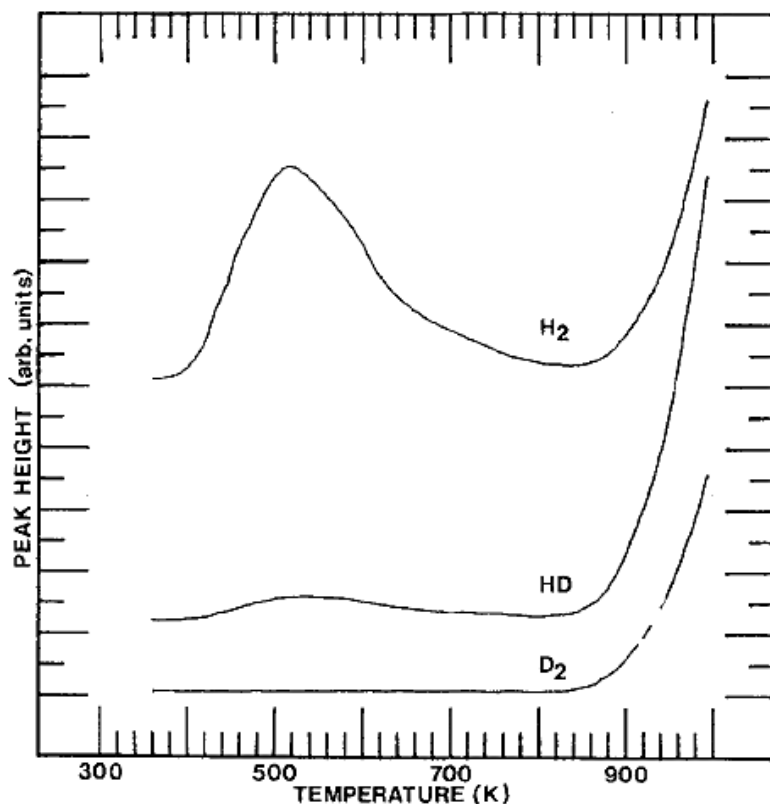


Figure 2.20 – TDS for a sample charged with deuterium at 427°C, followed by an oxygen dose at room temperature⁸⁶. Reprinted from Surface Science, vol. 185, Asbury D.A., Hoflund G.B., Peterson W.J., Gilbert R.E., TPD and ESD studies of the interaction of hydrogen and oxygen on polycrystalline zirconium, pages 213-226, copyright 1987, with permission from Elsevier.

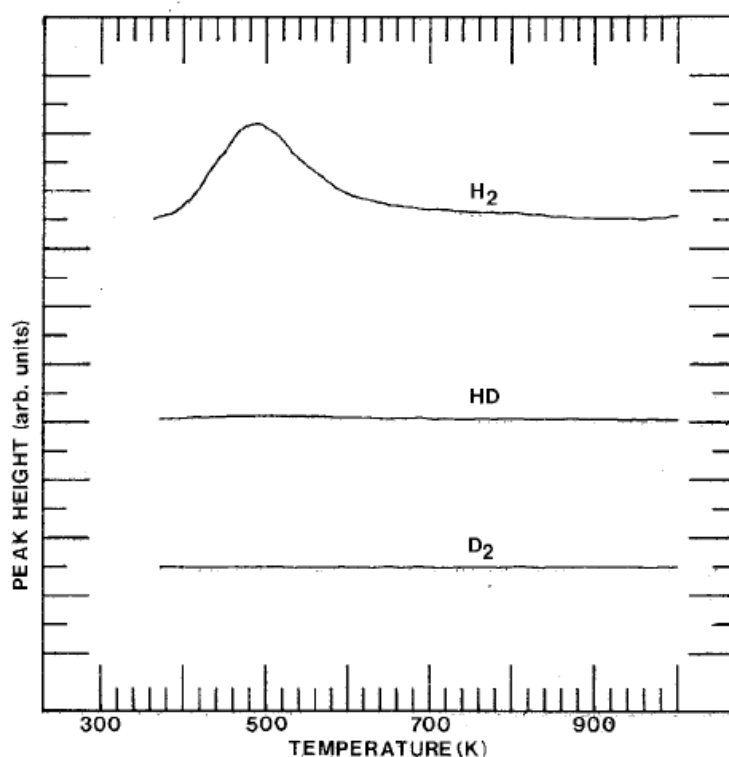


Figure 2.21 – TDS after oxygen dose at 27°C followed by deuterium dose at 27°C⁸⁶. Reprinted from Surface Science, vol. 185, Asbury D.A., Hoflund G.B., Peterson W.J., Gilbert R.E., TPD and ESD studies of the interaction of hydrogen and oxygen on polycrystalline zirconium, pages 213-226, copyright 1987, with permission from Elsevier.

Tupin et al.⁶⁷ tested samples with TDS which were oxidised for up to 50 days (maximum oxide thickness = 1.6 μm) and found two peaks (shown in Figure 2.22), the first at 467°C and the second at 567°C, labelled by the authors as site 1 and site 2 respectively. By carrying out short charging with deuterium Site 1 was found to be located near the surface of the oxide, and the second deeper in the oxide (possibly close to the OM interface). They then tested a sample oxidised for 171 days (oxide thickness = 3.6 μm) and found there was only a single peak at 527°C (shown in Figure 2.23), thought to be from site 1. The authors gave two reasons for the shift to a higher temperature: 1 – the time taken for the deuterium to diffuse through the thicker oxide would make it appear to desorb at a higher temperature. 2 – The existence of a third interaction site located in the intermediate oxide.

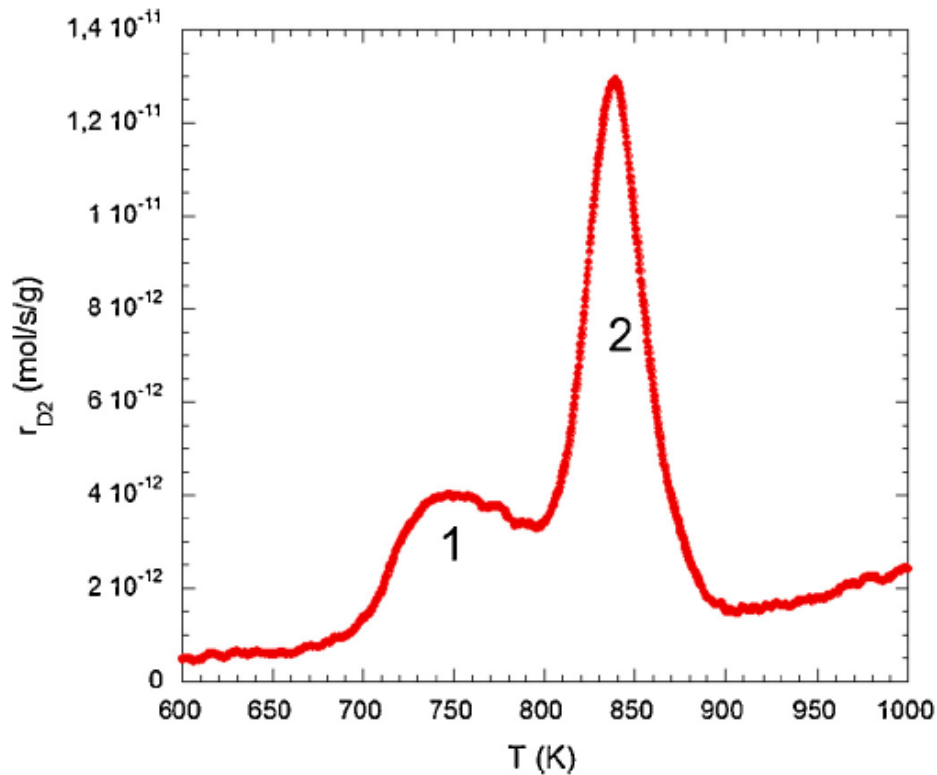


Figure 2.22 – Hydrogen desorption shown by Tupin et al.⁶⁷ from ZrO_2 . The two peaks are thought to be due to the external and internal oxides respectively. Reprinted from Corrosion Science, vol. 116, Tupin M., Martin F., Bisor C., et al., Hydrogen diffusion process in the oxides formed on zirconium alloys during corrosion in pressurized water reactor conditions, pages 1-13, copyright 2017, with permission from Elsevier.

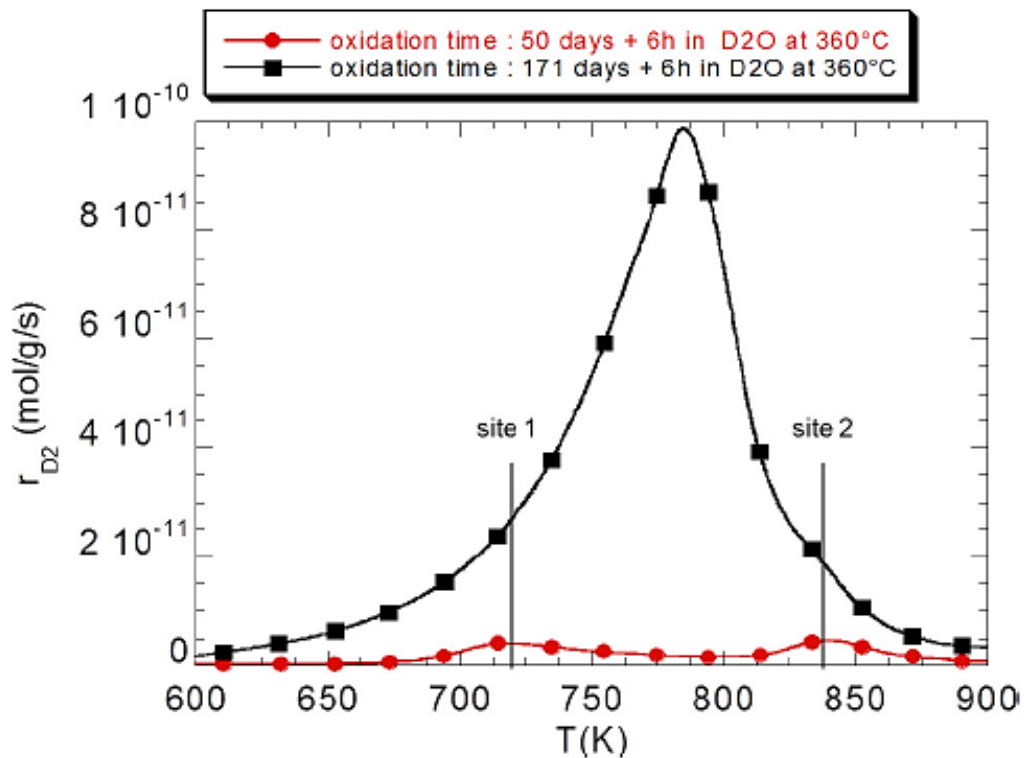


Figure 2.23 – Hydrogen desorption from 171 day oxide (black line) compared with 50 day oxide (red line), as shown by Tupin et al.⁶⁷ Reprinted from Corrosion Science, vol. 116, Tupin M., Martin F., Bisor C., et al., Hydrogen diffusion process in the oxides formed on zirconium alloys during corrosion in pressurized water reactor conditions, pages 1-13, copyright 2017, with permission from Elsevier.

It has been found that zirconium oxide acts as a barrier to hydrogen absorption and desorption⁸⁷⁻⁸⁹ (which is a possible reason for the delayed peak found by Tupin et al. in Figure 2.23). X-ray photoelectron spectroscopy (XPS) studies have shown that O-H bonds form in the oxide, which indicates why this happens^{83,90}. A similar suggestion is made by Peterson et al.⁸² that at the surface, the hydrogen exists as hydroxyl groups. They found that when charging a zirconium sample with just hydrogen, and then heating it, that a negligible amount of hydrogen was desorbed. However when charged with oxygen beforehand, the samples then desorbed hydrogen. This happened even if no hydrogen charging took place, as can be seen in Figure 2.24.

Foord et al.⁹¹ found that at high temperature, oxygen and other impurities (such as CO, NO and N₂) diffuse from the surface of zirconium into the bulk at high temperatures, and the removal of this barrier could be a reason hydrogen is released at high temperatures. This was later confirmed by Hoflund et al.⁹², and also by Roustilia et al.⁹³, where they used XPS to analyse the role of hydrogen charging and temperature on hydrogen and oxygen dissolution at the surface of zirconium. Heating the sample caused oxygen to migrate from the surface and increases its reactivity with hydrogen. Exposing the surface to hydrogen at 20°C produced zirconium hydride on the surface which decomposes with increasing temperature.

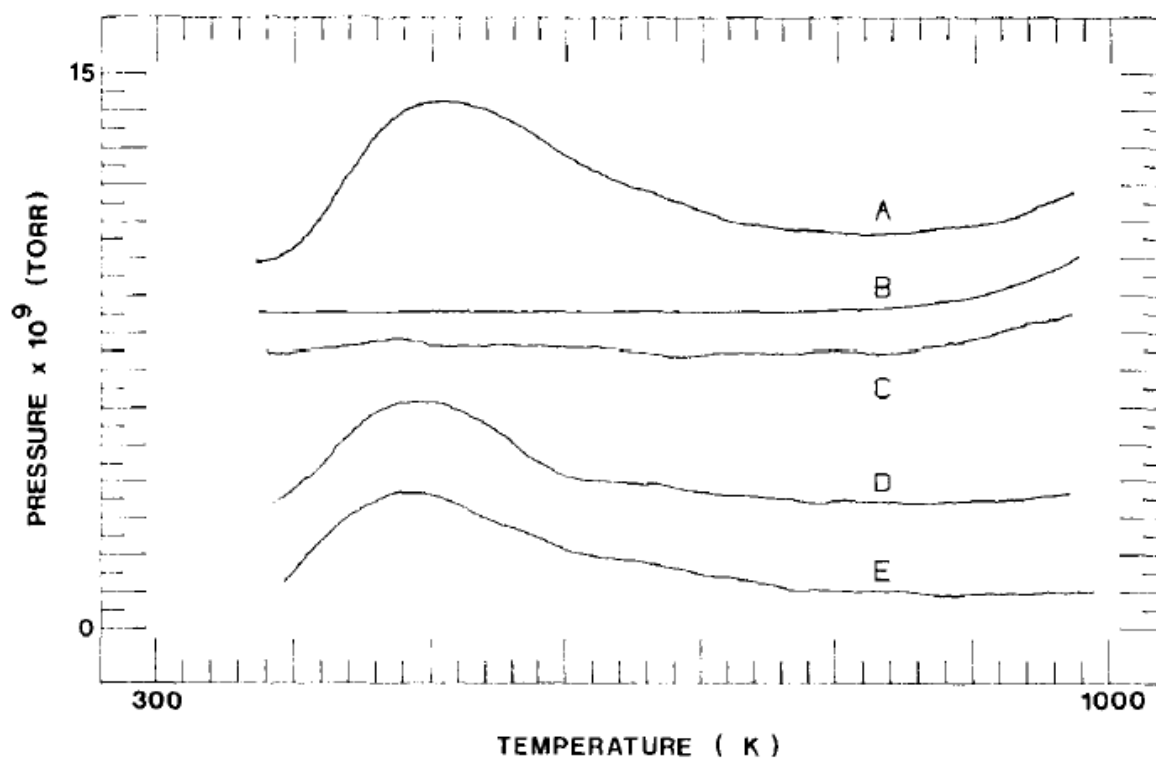


Figure 2.24 – TDS spectra of hydrogen from zirconium cleaned at 77°C and dosed at 27°C with (A) 2 days of background hydrogen, (B) background hydrogen immediately after spectrum (A), (C) 100 litres of hydrogen, (D) 10 litres of oxygen followed by 20 litres hydrogen, (E) 10 litres oxygen only⁸². Reprinted from Applied Surface Science, Vol. 24, Peterson W.J., Gilbert R.E., Hoflund G.B., The interaction of hydrogen with polycrystalline zirconium Part II. The effect of preadsorbed oxygen, pages 121-124, copyright 1985, with permission from Elsevier.

2.7 – MUZIC-2

The MUZIC-2 collaboration used a combination of theoretical^{65,94,95} and experimental studies^{17,56,96–103}, in order to establish a mechanistic understanding of corrosion and f_H in zirconium alloys. An in-depth summary of the collaboration was written by Romero et al.¹⁰⁴, which details all the different materials and techniques used. The collaboration found that f_H correlates with the kinetics of corrosion of zirconium alloys and is not constant during corrosion. f_H decreases with increasing n (from equation 1), and is lowest for materials with n approaching 0.5 (parabolic oxidation kinetics).

The correlation between f_H and oxidation rate has been attributed to changes in the electronic conductivity of the oxide formed during corrosion, which is related to the properties of the oxide and base metal. This is covered by Couet et al.⁶⁵, where they describe the development of a Coupled Current Charge Compensation model to describe the different oxidation kinetics based on the oxidation of the alloying elements present in zirconium alloys.

2.8 – References

1. Lustman B, Kerze Jr F. *Metallurgy of Zirconium.*; 1955.
2. Yeniscavich W, Wolfe RA, Lieberman RM. Hydrogen absorption by nickel enriched Zircaloy-2. *J Nucl Mater.* 1959;3:271-280.
3. Berry WE, Vaughan DA, White EL. Hydrogen pickup during aqueous corrosion of zirconium alloys. *Corrosion.* 1961;17:109-117.
4. Shishov VN, Nikulina AV, Markelov VA, et al. Influence of neutron irradiation on dislocation structure and phase composition of Zr-base alloys. In: Bradley ER, Sabol GP, eds. *Zirconium in the Nuclear Industry: 11th International Symposium, ASTM STP 1295.* ASTM International; 1996:603-622.
5. Motta AT, Yilmazbayhan A, Comstock RJ, et al. Microstructure and growth mechanism of oxide layers formed on Zr alloys studied with micro-beam synchrotron radiation. *J ASTM Int.* 2005;2(5):347-372. doi:10.1520/JAI12375.
6. Mardon JP, Charquet D, Senevat J. Influence of composition and fabrication process on out-of-pile and in-pile properties of M5 alloy. In: Sabol GP, Moan G, eds. *Zirconium in the Nuclear Industry: 12th International Symposium ASTM STP1354.* ASTM International; 2000:505-524.
7. Motta AT, Da Silva MJG, Yilmazbayhan A, Comstock RJ, Cai Z, Lai B. Microstructural characterization of oxides formed on model Zr alloys using synchrotron radiation. *J ASTM Int.* 2008;5(3). doi:10.1520/JAI101257.
8. Sabol GP, Kilp G, Balfour M, Roberts E. Development of a cladding alloy for high burnup. In: Van Swam L, Eucken C, eds. *Zirconium in the Nuclear Industry: Eighth International Symposium, ASTM STP 1023.* ASTM International; 1989:227-244.
9. Garner GL, Mardon JP. Alloy M5 in action. *Nucl Eng Int.* 2002;47(578):36-37.
10. de Gabory B, Dong Y, Motta AT, Marquis E a. EELS and atom probe tomography study of the evolution of the metal/oxide interface during zirconium alloy oxidation. *J Nucl Mater.* 2015;462:304-309. doi:10.1016/j.jnucmat.2015.03.043.
11. Bossis P, Lelièvre G, Barberis P, Iltis X, Lefebvre F. Multi-scale characterization of the metal-oxide interface of zirconium alloys. In: Sabol GP, Moan GD, eds. *Zirconium in the Nuclear Industry: 12th International Symposium ASTM STP 1354.* ASTM International; 2000:918-945.
12. Yilmazbayhan A, Motta AT, Comstock RJ, Sabol GP, Lai B, Cai Z. Structure of zirconium alloy oxides formed in pure water studied with synchrotron radiation and optical microscopy: relation to corrosion rate. *J Nucl Mater.* 2004;324(1):6-22. doi:10.1016/j.jnucmat.2003.08.038.

13. Wei J. Effect of hydrogen on the corrosion performance of zirconium alloys. 2012.
Available at: <https://www.escholar.manchester.ac.uk/api/datastream?publicationPid=uk-ac-man-scw:157531&datastreamId=FULL-TEXT.PDF>.
14. Adamson RB, Garzarolli F, Cox B, Strasser A, Rudling P. *ZIRAT 12 Special Topic Report 2007 - Corrosion Mechanisms in Zirconium Alloys*; 2007.
15. Rudling P, Strasser A, Garzarolli F. *IZNA 7 Special Topic Report: Welding of Zirconium Alloys*; 2007.
16. Couet A. Hydrogen Pick-up behaviour in zirconium alloys. 2011.
17. Couet A, Motta AT, Comstock RJ. Effect of alloying elements on hydrogen pick-up in zirconium alloys. In: Comstock RJ, Barberis P, eds. *Zirconium in the Nuclear Industry: 17th International Symposium, ASTM STP 1543*. ASTM International; 2015:479-514.
doi:10.1520/STP154320120215.
18. Cox B, Pemsler JP. Diffusion of oxygen in growing zirconia films. *J Nucl Mater*. 1968;28:73-78.
19. Sabol GP, Dalgaard S. The origin of the cubic rate law in zirconium alloy oxidation. *J Electrochem Soc*. 1975;122(2):316-317.
20. Billot P, Beslu P, Giordano A, Thomazet J. Development of a mechanistic model to assess the external corrosion of the Zircaloy claddings in PWRs. In: Van Swam L, Eucken C, eds. *Zirconium in the Nuclear Industry: 8th International Symposium, ASTM STP 1023*. ASTM International; 1989:165184.
21. Bradhurst DH, Heuer PM. The temperature dependence of the in-reactor oxidation of zirconium alloys in moist CO₂ atmospheres from 573–868K. *J Nucl Mater*. 1981;96(1):196-204. doi:[http://dx.doi.org/10.1016/0022-3115\(81\)90233-6](http://dx.doi.org/10.1016/0022-3115(81)90233-6).
22. Ocken H, Biederman RR, Hann CR, Westerman R. Evaluation models of Zircaloy oxidation in light of recent experiments. In: *Zirconium in the Nuclear Industry: 4th International Symposium, ASTM STP 681*. ASTM International; 1979:514-536.
23. Perkins RA, Busch RA. Corrosion of Zircaloy in the presence of LiOH. In: *Zirconium in the Nuclear Industry: Ninth International Symposium, ASTM STP 1132*. Publ by ASTM; 1991:595-611. Available at: <http://www.scopus.com/inward/record.url?eid=2-s2.0-0026399521&partnerID=tZOtx3y1>.
24. Garzarolli F, Jorde D, Manzel R, Politano JR, Smerd PG. Waterside corrosion of Zircaloy-clad fuel rods in a PWR environment. In: Franklin D, ed. *Zirconium in the Nuclear Industry: Fifth Conference, ASTM STP 754*. ASTM International; 1982:430-449.
25. Wei J, Frankel P, Polatidis E, et al. The effect of Sn on autoclave corrosion performance and

corrosion mechanisms in Zr–Sn–Nb alloys. *Acta Mater.* 2013;61(11):4200-4214.
doi:10.1016/j.actamat.2013.03.046.

26. Bouvier P, Godlewski J, Lucazeau G. A Raman study of the nanocrystallite size effect on the pressure–temperature phase diagram of zirconia grown by zirconium-based alloys oxidation. *J Nucl Mater.* 2002;300(2-3):118-126. doi:10.1016/S0022-3115(01)00756-5.
27. Bryner J. The cyclic nature of corrosion of Zircaloy-4 in 633 K water. *J Nucl Mater.* 1979;82:84-101.
28. Garde AM. Enhancement of aqueous corrosion of Zircaloy-4 due to hydride precipitation at the metal–oxide interface. In: Eucken CM, Garde AM, eds. *Zirconium in the Nuclear Industry: 9th International Symposium, ASTM STP 1132*. ASTM International; 1991:566-594.
29. Wei J, Frankel P, Blat M, et al. Autoclave study of zirconium alloys with and without hydride rim. *Corros Eng Sci Technol.* 2012;47(7):516-528.
doi:10.1179/1743278212Y.0000000055.
30. Bouineau V, Ambard A, Bénier G, et al. A new model to predict the oxidation kinetics of zirconium alloys in a pressurized water reactor. In: Kammenzind B, Limbäck M, eds. *Zirconium in the Nuclear Industry: 15th International Symposium, ASTM STP 1505*. ASTM International; 2009:405-429.
31. Cox B. Some thoughts on the mechanisms of in-reactor corrosion of zirconium alloys. *J Nucl Mater.* 2005;336(2-3):331-368. doi:10.1016/j.jnucmat.2004.09.029.
32. Beie H, Mitwalsky A, Garzarolli F, Ruhmann H, Sell H. Examinations of the corrosion mechanism of zirconium alloys. In: Garde AM, Bradley ER, eds. *Zirconium in the Nuclear Industry: 10th International Symposium, ASTM STP 1245*. ASTM International; 1994:615-643. doi:10.1520/STP15212S.
33. Arima T, Miyata K, Inagaki Y, Idemitsu K. Oxidation properties of Zr–Nb alloys at 500–600°C under low oxygen potentials. *Corros Sci.* 2005;47(2):435-446.
doi:10.1016/j.corsci.2004.06.011.
34. Pilling NB, Bedworth RE. The oxidation of metals at high temperature. *J Inst Met.* 1923;29:529-591.
35. Parise M, Sicardy O, Cailletaud G. Modelling of the mechanical behavior of the metal–oxide system during Zr alloy oxidation. *J Nucl Mater.* 1998;256(1):35-46. doi:10.1016/S0022-3115(98)00045-2.
36. Barberis P, Rebeyrolle V, Vermoyal JJ, Chabretou V, Vassault JP. CASTA DIVA: Experiments and modeling of oxide-induced deformation in nuclear components. *J ASTM Int.* 2008;5(5):612-630.

37. Hutchinson B, Hallstadius L. Oxidation of Zircaloy-2 studied using a wedge-shaped specimen. *J Nucl Mater.* 2013;432:437-443.
38. Bradhurst DH, Heuer PM. The influence of oxide stress on the breakaway oxidation of Zircaloy-2. *J Nucl Mater.* 1970;37:35-47.
39. Ortner SR, Swan H, LaFerrere A, et al. Study of Zircaloy corrosion to develop mechanistic understanding. In: *Fontevraud 8 - Contribution of Materials Investigations and Operating Experience to LWRs' Safety, Performance and Reliability.*; 2014.
40. Tejlund P, Andrén H-O. Oxidation induced localized creep deformation in Zircaloy-2. *J Nucl Mater.* 2014;444(1-3):30-34. doi:10.1016/j.jnucmat.2013.09.020.
41. Arashi H, Ishigame JM. Raman spectroscopic studies of the polymorphism in ZrO₂ at high pressures. *Phys Status Solidi.* 1982;71(2):313-321. doi:10.1002/pssa.2210710203.
42. Block S, Da Jornada JAH, Piermarini GJ. Pressure-temperature phase diagram of zirconia. *J Am Ceram Soc.* 1985;69(9):497-499.
43. Nechaev A. Corrosion of zirconium alloys in nuclear power plants. In: *IAEA-TECDOC-684.* Vienna: IAEA; 1993:177.
44. Ritchie I. Waterside corrosion of zirconium alloys in nuclear power plants. In: *IAEA-TECDOC-996.* Vienna; 1998:312.
45. Kysela J. Water chemistry and corrosion control of cladding and primary circuit components. In: *IAEA-TECDOC-1128.*; 1999:309.
46. Garvie R. The occurrence of metastable tetragonal zirconia as a crystallite size effect. *J Phys Chem.* 1965;147(1950):1238-1243. doi:10.1021/j100888a024.
47. Barberis P. Zirconia powders and Zircaloy oxide films: tetragonal phase evolution during 400°C autoclave tests. *J Nucl Mater.* 1995;226:34-43. doi:10.1016/0022-3115(95)00108-5.
48. Yao M, Zhou BX, Li Q, Liu WQ, Geng X, Lu YP. A superior corrosion behavior of Zircaloy-4 in lithiated water at 360°C/18.6MPa by β -quenching. *J Nucl Mater.* 2008;374(1-2):197-203. doi:10.1016/j.jnucmat.2007.08.002.
49. Ni N, Lozano-Perez S, Jenkins ML, et al. Porosity in oxides on zirconium fuel cladding alloys, and its importance in controlling oxidation rates. *Scr Mater.* 2010;62(8):564-567. doi:10.1016/j.scriptamat.2009.12.043.
50. Iwasawa M, Ohnuma T, Soneda N. Ab Initio Electronic Structure Study of α -Zirconium and hydrogen. *Mater Trans.* 2008;49(12):2765-2769. doi:10.2320/matertrans.MRA2008184.
51. Chandra K, Kulkarni AS, Ramanjaneyulu PS, et al. Determination of diffusion coefficients of hydrogen and deuterium in Zr-2.5% Nb pressure tube material using hot vacuum extraction-quadrupole mass spectrometry. *J Nucl Mater.* 2015;461:151-156.

doi:10.1016/j.jnucmat.2015.03.021.

52. Christensen M, Wolf W, Freeman C, et al. H in α -Zr and in zirconium hydrides: solubility, effect on dimensional changes, and the role of defects. *J Phys Condens Matter*. 2015;27(2):25402. doi:10.1088/0953-8984/27/2/025402.
53. Griessen R. Heats of solution and lattice-expansion and trapping energies of hydrogen in transition metals. *Phys Rev B*. 1988;38(6):3690-3698.
54. Motta AT, Chen L-Q. Hydride formation in zirconium alloys. *JOM*. 2012;64(12):1403-1408. doi:10.1007/s11837-012-0479-x.
55. Garzarolli F, Cox B, Rudling P. *ANT International Report: Corrosion and Hydriding*; 2012.
56. Couet A, Motta AT, Comstock RJ. Hydrogen pickup measurements in zirconium alloys: Relation to oxidation kinetics. *J Nucl Mater*. 2014;451(1-3):1-13. doi:10.1016/j.jnucmat.2014.03.001.
57. Kass S. Hydrogen pickup in various zirconium alloys during corrosion exposure in high-temperature water and steam. *J Electrochem Soc*. 1960;107(7):594-597. doi:10.1149/1.2427781.
58. Harada M, Kimpara M, Abe K. Effect of alloying elements on uniform corrosion resistance of zirconium-based alloys in 360°C water and 400°C steam. In: Eucken CM, Garde AM, eds. *Zirconium in the Nuclear Industry: 9th International Symposium, ASTM STP 1132*. ASTM International; 1991:368-391.
59. Takahashi K, Iwasaki T, Maruno Y. Effect of precipitates in oxide film on hydrogen pick-up of zirconium alloys. In: *Top Fuel 2016: LWR Fuels with Enhanced Safety and Performance*. ANS; 2016:1245-1254.
60. Hatano Y, Hitaka R, Sugisaki M, Hayashi M. Influence of size distribution of Zr (Fe, Cr)₂ precipitates on hydrogen transport through oxide film of Zircaloy-4. *J Nucl Mater*. 1997;248:311-314.
61. Annand K, Nord M, MacLaren I, Gass M. The Corrosion of Zr(Fe, Cr)₂ and Zr₂Fe Secondary Phase Particles in Zircaloy-4 under 350 °C pressurised water conditions. *Corros Sci*. 2017;128(January):213-223. doi:10.1016/j.corsci.2017.09.014.
62. Baek JH, Jeong YH. Depletion of Fe and Cr within precipitates during Zircaloy-4 oxidation. *J Nucl Mater*. 2002;304:107-116.
63. Pêcheur D, Lefebvre F, Motta AT, Lemaignan C, Wadier JF. Precipitate evolution in the Zircaloy-4 oxide layer. *J Nucl Mater*. 1992;189(3):318-332. doi:10.1016/0022-3115(92)90385-X.
64. Tejland P, Langhammer C, Andrén HO. On the black oxide colour of zirconium alloys. *J*

- Nucl Mater.* 2010;400(1):79-83. doi:10.1016/j.jnucmat.2010.02.013.
65. Couet A, Motta AT, Ambard A. The coupled current charge compensation model for zirconium alloy fuel cladding oxidation: I. Parabolic oxidation of zirconium alloys. *Corros Sci.* 2015;100:73-84. doi:10.1016/j.corsci.2015.07.003.
 66. Harada M, Wakamatsu R. The effect of hydrogen on the transition behavior of the corrosion rate of zirconium alloys. In: Kammenzind B, Limbäck M, eds. *Zirconium in the Nuclear Industry: 15th International Symposium, ASTM STP 1505*. ASTM International; 2009:101-117. doi:10.1520/JAI101117.
 67. Tupin M, Martin F, Bisor C, et al. Hydrogen diffusion process in the oxides formed on zirconium alloys during corrosion in pressurized water reactor conditions. *Corros Sci.* 2017;116:1-13. doi:10.1016/j.corsci.2016.10.027.
 68. Wood C. Developments in nuclear power plant water chemistry. In: *International Conference of Water Chemistry of Nuclear Reactor Systems 8*. Vol 1. British Nuclear Energy Society; 2000:1-6.
 69. Staudt U, Marchl T. Field experience with B-10-enriched boric acid. In: *International Conference of Water Chemistry of Nuclear Reactor Systems 8*. British Nuclear Energy Society; 2000:45-48.
 70. Manolescu A, Mayer P, Simpson C. Effect of lithium hydroxide on corrosion rate of zirconium-2.5 wt% niobium in 340 C water. *Corrosion.* 1982;38(1):23-31.
 71. Polley M, Garbett K, Pick M. *A Survey of the Effect of Primary Coolant pH on Westinghouse PWR Plant Radiation Fields.*; 1994. Available at: <http://www.epri.com/abstracts/Pages/ProductAbstract.aspx?ProductId=TR-104180>.
 72. Müller S, Lanzani L. Corrosion of zirconium alloys in concentrated lithium hydroxide solutions. *J Nucl Mater.* 2013;439(1-3):251-257. doi:10.1016/j.jnucmat.2012.07.030.
 73. Pêcheur D, Godlewski J, Billot P, Thomazet J. Microstructure of oxide films formed during the waterside corrosion of the Zircaloy-4 cladding in lithiated environment. In: Bradley ER, Sabol GP, eds. *Zirconium in the Nuclear Industry: Eleventh International Symposium ASTM STP 1295*. ASTM International; 1996:94-113.
 74. Ramasubramanian N. Lithium uptake and the corrosion of zirconium alloys in aqueous lithium hydroxide solutions. In: Eucken CM, Garde AM, eds. *Zirconium in the Nuclear Industry: Ninth International Symposium, ASTM STP 1132*. ASTM International; 1991:613-626.
 75. Yilmazbayhan A, Breval E, Motta AT, Comstock RJ. Transmission electron microscopy examination of oxide layers formed on Zr alloys. *J Nucl Mater.* 2006;349(3):265-281.

doi:10.1016/j.jnucmat.2005.10.012.

76. Oskarsson M, Ahlberg E, Pettersson K. Oxidation of Zircaloy-2 and Zircaloy-4 in water and lithiated water at 360°C. *J Nucl Mater.* 2001;295:97-108.
77. Cox B, Wu C. Dissolution of zirconium oxide films in 300°C LiOH. *J Nucl Mater.* 1993;199:272-284.
78. Cox B, Wu C. Transient effects of lithium hydroxide and boric acid on Zircaloy corrosion. *J Nucl Mater.* 1995;224:169-178.
79. Cox B, Ungurelu M, Wong YM, Wu C. Mechanisms of LiOH degradation and H₃BO₃ repair of ZrO₂ films. In: Bradley ER, Sabol GP, eds. *Zirconium in the Nuclear Industry: Eleventh International Symposium, ASTM STP 1295*. ASTM International; 1996:114-136.
80. Kido T, Wada S, Takahashi T, Uchida H, Komine I, Inoue Y. Behavior of lithium and boron in irradiated and unirradiated oxides formed on Zircaloy-4 claddings. In: Sabol GP, Moan G, eds. *Zirconium in the Nuclear Industry: 12th International Symposium, ASTM STP 1354*. ASTM International; 2000:773-792. doi:10.1520/STP14327S.
81. Gulbransen E, Andrew K. Solubility and decomposition pressures of hydrogen in alpha-zirconium. *JOM.* 1955;7:136-144.
82. Peterson WJ, Gilbert RE, Hoflund GB. The interaction of hydrogen with polycrystalline zirconium Part II. The effect of preadsorbed oxygen. *Appl Surf Sci.* 1985;24:121-124.
83. Chen W, Wang L, Lu S. Influence of oxide layer on hydrogen desorption from zirconium hydride. *J Alloys Compd.* 2009;469(1-2):142-145. doi:10.1016/j.jallcom.2008.01.157.
84. Khatamian D, Ling VC. Hydrogen solubility limits in α - and β -zirconium. *J Alloys Compd.* 1997;253-254:162-166.
85. Khatamian D. Effect of β -Zr decomposition on the solubility limits for H in Zr-2.5Nb. *J Alloys Compd.* 2003;356-357:22-26. doi:10.1016/S0925-8388(03)00094-X.
86. Asbury DA, Hoflund GB, Peterson WJ, Gilbert RE. TPD and ESD studies of the interaction of hydrogen and oxygen on polycrystalline zirconium. *Surf Sci.* 1987;185:213-226.
87. Wongsawaeng D, Jaiyen S. High-temperature absolute hydrogen desorption kinetics of zirconium hydride under clean and oxidized surface conditions. *J Nucl Mater.* 2010;403(1-3):19-24. doi:10.1016/j.jnucmat.2010.05.025.
88. Eliaz N, Eliezer D, Abramov E, Zander D, Koster U. Hydrogen evolution from Zr-based amorphous and quasicrystalline alloys. *J Alloys Compd.* 2000;305:272-281.
89. Huang J-H, Huang S-P. Hydriding of zirconium alloys in hydrogen gas. *Mater Sci Eng A.* 1993;161(2):247-253. doi:10.1016/0921-5093(93)90519-K.

90. Li YS, Wong PC, Mitchell K a. R. XPS investigations of the interactions of hydrogen with thin films of zirconium oxide II. Effects of heating a 26 Å thick film after treatment with a hydrogen plasma. *Appl Surf Sci.* 1995;89(3):263-269. doi:10.1016/0169-4332(95)00032-1.
91. Foord JS, Goddard PJ, Lambert RM. Adsorption and absorption of diatomic gases by zirconium: studies of the dissociation and diffusion of CO, NO, N₂, O₂ And D₂. *Surf Sci.* 1980;94:339-354.
92. Hoflund GB, Cox DF, Gilbert RE. An investigation of the interaction of polycrystalline zirconium with O₂, N₂, CO, and N₂O. Part I. *J Vac Sci Technol A Vacuum, Surfaces, Film.* 1983;1(4):1837-1842. doi:10.1116/1.572224.
93. Roustila A, Chene J, Severac C. XPS study of hydrogen and oxygen interactions on the surface of zirconium. *Alloy Compd.* 2003;357:330-335.
94. Lindgren M, Sundell G, Panas I, Hallstadius L, Thuvander M, Andrén HO. Toward a comprehensive mechanistic understanding of hydrogen uptake in zirconium alloys by combining atom probe analysis with electronic structure calculations. In: Vol STP 1543. ASTM International; 2015:515-539. doi:10.1520/STP154320120164.
95. Bell BDC, Murphy ST, Burr PA, et al. The influence of alloying elements on the corrosion of Zr alloys. *Corros Sci.* 2016;105:36-43. doi:10.1016/j.corsci.2015.12.022.
96. Aarholt T. Analytical microscopy of corroded zirconium alloys. 2017.
97. Garner A, Gholinia A, Frankel P, Gass M, MacLaren I, Preuss M. The microstructure and microtexture of zirconium oxide films studied by transmission electron backscatter diffraction and automated crystal orientation mapping with transmission electron microscopy. *Acta Mater.* 2014;80:159-171. doi:10.1016/j.actamat.2014.07.062.
98. Hu J, Garner A, Ni N, et al. Identifying suboxide grains at the metal–oxide interface of a corroded Zr–1.0%Nb alloy using (S)TEM, transmission-EBSD and EELS. *Micron.* 2015;69:35-42. doi:10.1016/j.micron.2014.10.004.
99. Motta AT, Couet A, Comstock RJ. Corrosion of zirconium alloys used for nuclear fuel cladding. *Annu Rev Mater Res.* 2015;45(1):311-343. doi:10.1146/annurev-matsci-070214-020951.
100. Setiadinata B. Corrosion and hydrogen pickup mechanisms of zirconium alloys. 2016.
101. Sundell G, Thuvander M, Andrén HO. Enrichment of Fe and Ni at metal and oxide grain boundaries in corroded Zircaloy-2. *Corros Sci.* 2012;65:10-12. doi:10.1016/j.corsci.2012.08.061.
102. Sundell G, Thuvander M, Yatim AK, Nordin H, Andrén HO. Direct observation of hydrogen and deuterium in oxide grain boundaries in corroded zirconium alloys. *Corros Sci.*

2015;90:1-4. doi:10.1016/j.corsci.2014.10.016.

103. Tejlund P, Andrén HO, Sundell G, et al. Oxidation mechanism in Zircaloy-2 - The effect of SPP size distribution. In: Comstock RJ, Barberis P, eds. *Zirconium in the Nuclear Industry: 17th International Symposium, ASTM STP 1543*. ASTM International; 2015:373-403. doi:10.1520/STP154320130052.
104. Romero J, Partezana J, Comstock RJ, Hallstadius L, Motta AT, Couet A. Evolution of hydrogen pickup fraction with oxidation rate on zirconium alloys. In: *Top Fuel 2015 - Reactor Fuel Performance*. European Nuclear Society; 2015:476-482. Available at: [https://www.euronuclear.org/events/topfuel/topfuel2015/transactions/topfuel2015-
transactions-oral-1.pdf](https://www.euronuclear.org/events/topfuel/topfuel2015/transactions/topfuel2015-transactions-oral-1.pdf).

3 – Experimental Techniques

Contents

3.1 – Transmission Electron Microscopy	41
3.1.1 – Sample Preparation For TEM.....	43
3.2 – Electron Energy Loss Spectroscopy	48
3.2.1 – Principal Component Analysis	50
3.2.2 – Multiple Linear Least Squares Fitting	54
3.3 – Thermal Desorption Spectroscopy	55
3.3.1 – Hydrogen Hot-Gas Extraction	59
3.4 – Secondary Ion Mass Spectroscopy	59
3.5 – Digital Scanning Calorimetry	60
3.6 – Samples Investigated	60
3.7 – References.....	62

I used various techniques in this project for analysing the as-received and oxidised samples, and in this chapter I will cover each of these techniques, starting with Transmission Electron Microscopy (TEM).

3.1 – Transmission Electron Microscopy

In a TEM high energy electrons (typically 200 – 300 kV) are used to image a sample, and are detected after passing through the sample. To ensure most of the electrons pass through and give a high-resolution image a Zr sample needs to be around 100nm thick. When electrons pass through the sample, they can either be transmitted through the sample with no deviation or they can be scattered. Scattering can occur due to electrons elastically/in-elastically scattering from the nuclei or the electron cloud of atoms in the sample. Diffraction patterns are formed by electrons elastically scattering from the electron cloud for example. Electron Energy Loss Spectroscopy (EELS) is an example of a technique used for analysing in-elastically scattered electrons.

The vast majority of TEM work I have carried out has been in Scanning TEM (STEM) mode. This technique is carried out by focussing the electron beam onto a small region of the sample and scanning the beam across the sample. Several images can be formed by the electrons depending on where the detectors are placed. A detector for the directly transmitted beam forms a bright field (BF) image. This beam consists of electrons which pass straight through the sample and electrons which are in-

elastically scattered. These in-elastically scattered electrons are used for EELS. The scattered electrons are collected by two annular detectors: the annular dark field (ADF) detector is used for the low-angle electrons, and the high angle annular dark field (HAADF) detector. The ADF detector can be used to detect diffraction contrast. The contrast for the HAADF detector has a strong dependence on the atomic number (Z) and this contrast is referred to as Z -contrast. Figure 3.1 shows a basic schematic of a STEM instrument with an EELS detector in place. For more general information about TEM, see Williams and Carter's book¹, and for more detail on EELS see Egerton's book².

STEM and EELS were carried out on a cold field emission source JEOL ARM-200F and general TEM work was carried out on a LaB₆ filament JEOL 2100. The acceleration voltage of the electrons was 200kV for both microscopes. For the ARM-200F the convergence angle (α in Figure 3.1) is 31 mrad, and the collection angle (β in Figure 3.1) is 41 mrad in STEM mode. HAADF images were obtained with two JEOL ADF detectors (located before the viewing screen) and a Gatan ADF (located just before the EELS detector).

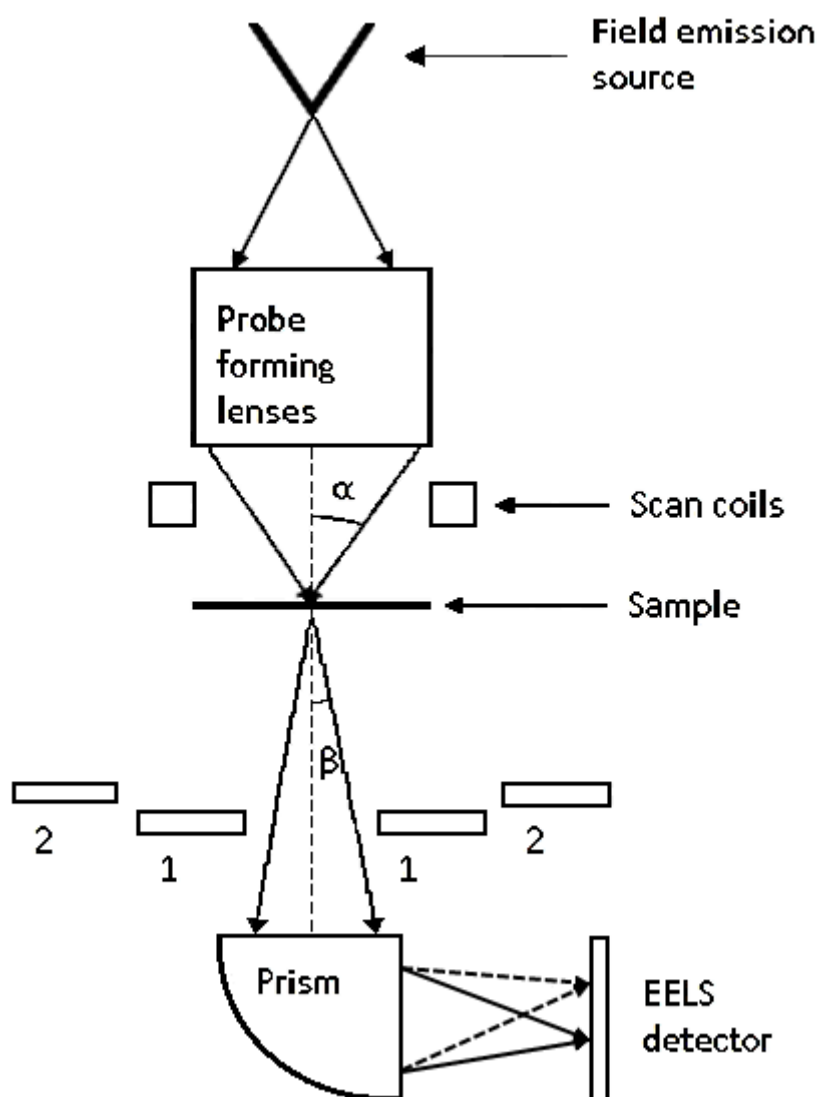


Figure 3.1 – STEM-EELS setup (not to scale)³. Detectors labelled 1 & 2 are ADF and HAADF detectors respectively. The dashed lines after the prism show electrons with lower energy. α is the convergence angle, and β is the collection angle. Reproduced with permission of IOP Publishing in the format Thesis/Dissertation via Copyright Clearance Center.

3.1.1 – Sample Preparation For TEM

For sample preparation I used the in-situ lift-out method⁴⁻⁷ with Focussed Ion Beam (FIB) milling. I used a FEI FIB200 for initial lift-out and a Zeiss NVision FIB-SEM for thinning to electron transparency. Both of these instruments use a gallium ion beam for milling the sample at 30kV. This method enables a large area to be prepared with a uniform cross-section.

The following list outlines the method I used for extracting a sample from my material:

1. A small piece of material (~5 x 5 mm) was mounted on an SEM stub using silver dag and coated with a layer of deposited gold to ensure good conduction from the surface of the sample to the equipment.

2. After loading into the FIB200 chamber a $15\text{ }\mu\text{m} \times 2\text{ }\mu\text{m} \times 2\text{ }\mu\text{m}$ layer of platinum was deposited to protect the sample from damage from the beam.
3. With a beam current of 7000 pA, 3 trenches were milled around the sample using the staircase function (Figure 3.2). I generally used a depth of $3\text{ }\mu\text{m}$, but increased this for the later oxide (which was thicker than $3\text{ }\mu\text{m}$) to $4\text{ }\mu\text{m}$.
4. Any re-deposited material was milled off using the cleaning cross section function. Depending on the thickness I used a beam current of 3000/5000 pA.
5. When the sample reached around $1\text{ }\mu\text{m}$ thick (Figure 3.3) I used a beam current of 1000 pA to obtain a flat surface. To stop the beam tails damaging the sample I tilted the sample by $\sim 2^\circ$.
6. After obtaining a flat surface I tilted the sample to 45° and I milled two slots at the bottom and to the side of the sample (Figure 3.4). I repeated this on the opposite side to leave the sample attached to the material by a small section.
7. The micromanipulator needle (MN) was then inserted (after I made sure the stage was below the MN insertion height) and the stage was moved into position for welding with the MN (Figure 3.5). I used the platinum again for this process.
8. I then milled the remaining connection away to separate the sample from the material completely (Figure 3.6).
9. The sample was then welded to a copper grid (Figure 3.7). I deposited platinum in 3 different regions to ensure a secure attachment was made; On the top, and by tilting each side I could deposit platinum on the join of the sample to the copper grid (Figure 3.8)
10. After this I used the NVision to mill the sample until it was electron transparent at 5kV (with the secondary electron image), shown in Figure 3.9). The NVision was used for this as it has a Scanning Electron Microscope (SEM) attached, which allowed me to monitor the sample face on during milling to stop me destroying the sample.
11. When the sample was electron transparent, a final 2kV, 250 pA cleaning was carried out to remove FIB damage from the sample.

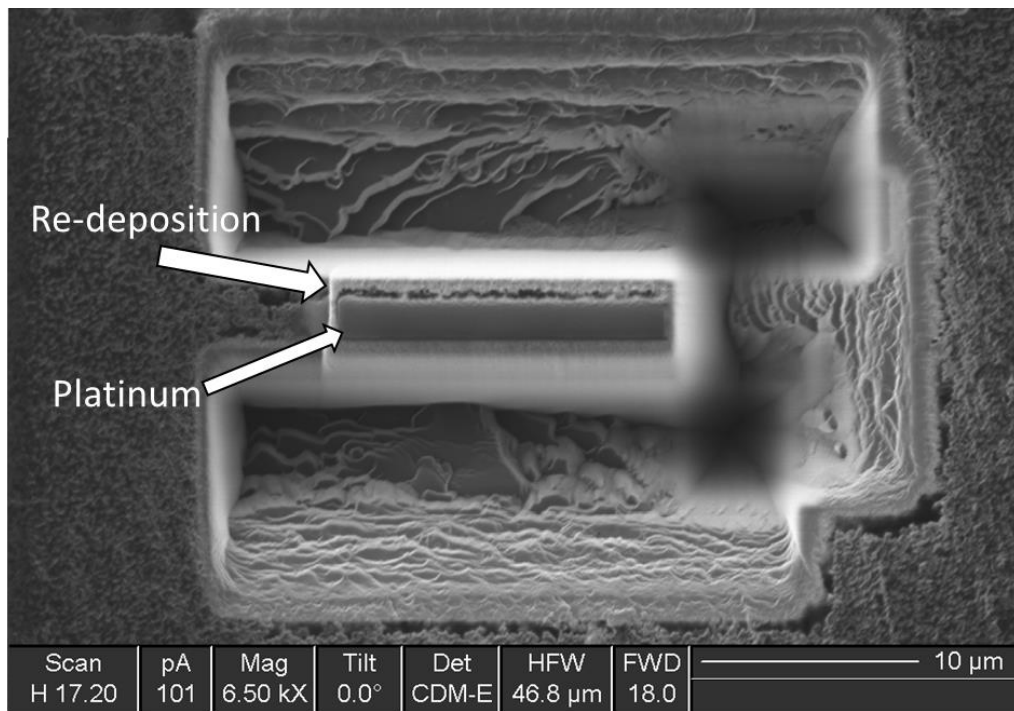


Figure 3.2 – Milled trenches around sample, which is covered by platinum. There is re-deposition above and below the sample.

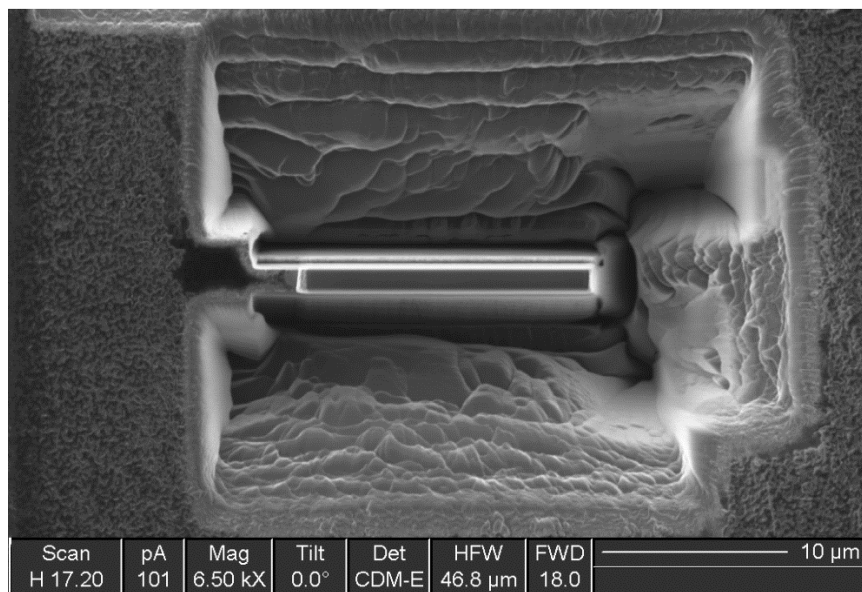


Figure 3.3 – Sample after applying the cleaning cross-sections to remove the re-deposited material.

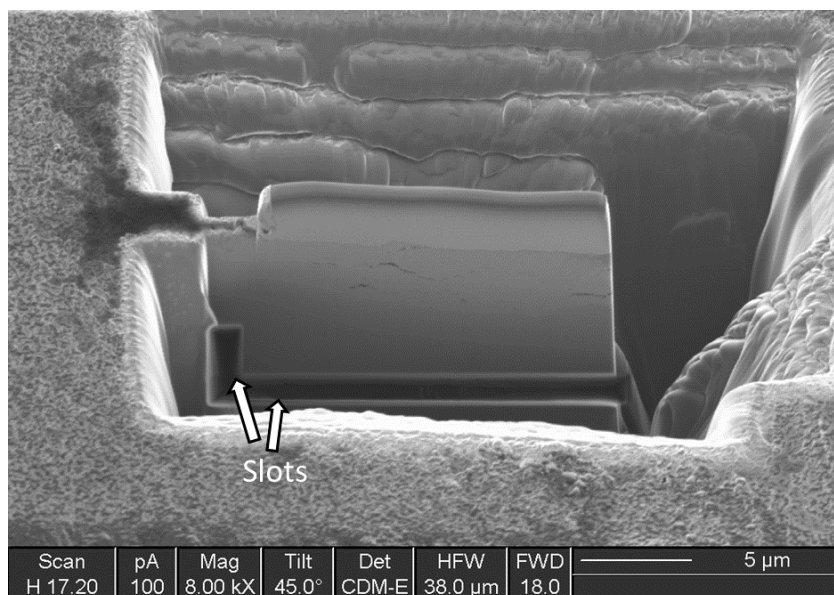


Figure 3.4 – Milled slots. The same pattern was milled on the opposite side to ensure the sample was free in those areas.

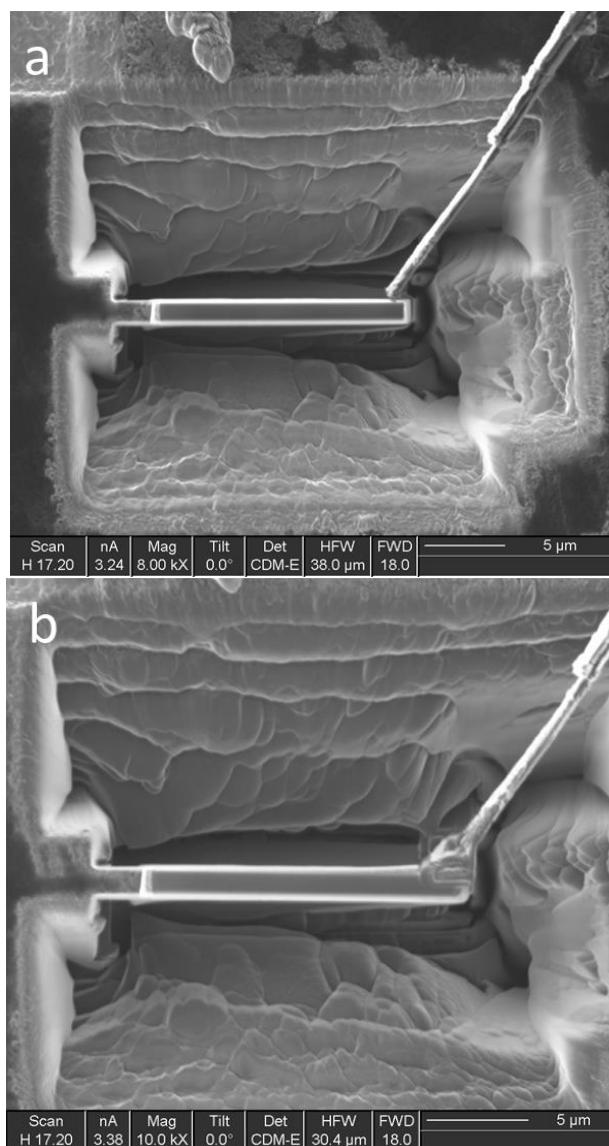


Figure 3.5 – (a) The micromanipulator needle in position for attachment to sample. (b) After platinum deposition.

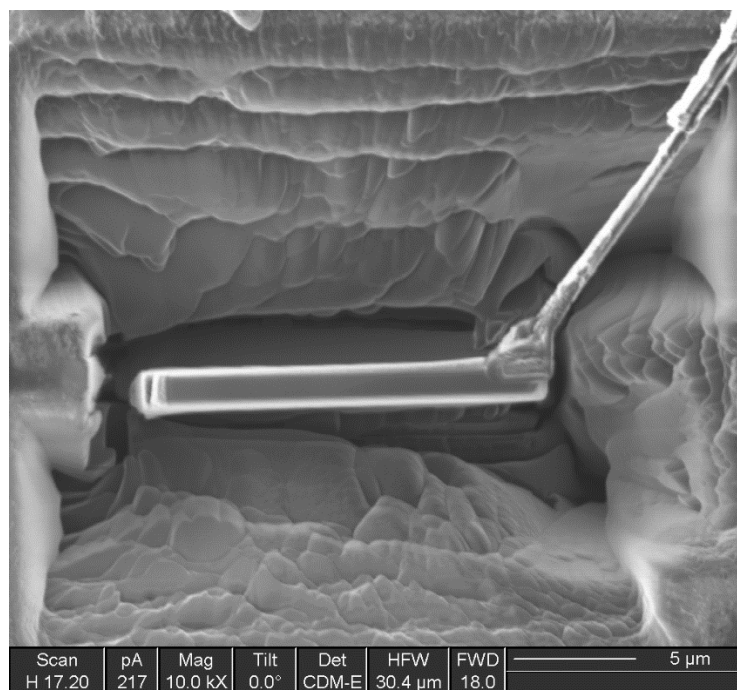


Figure 3.6 – Sample after having the link to the bulk severed.

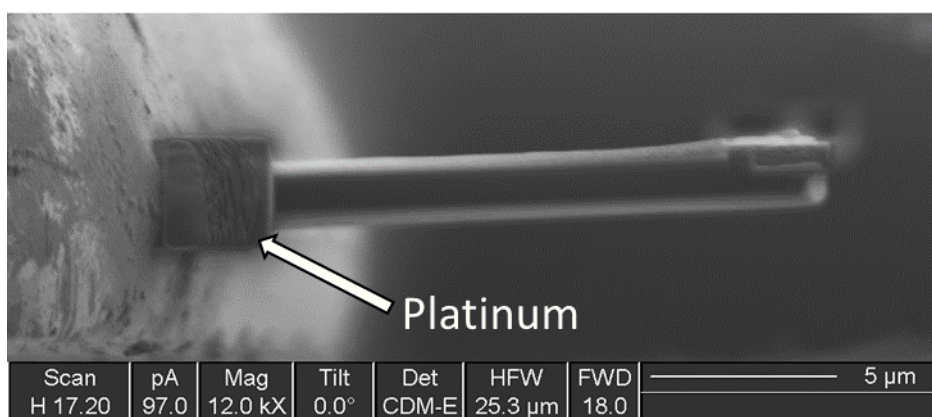


Figure 3.7 – Sample after the initial weld to the copper grid (on the left).

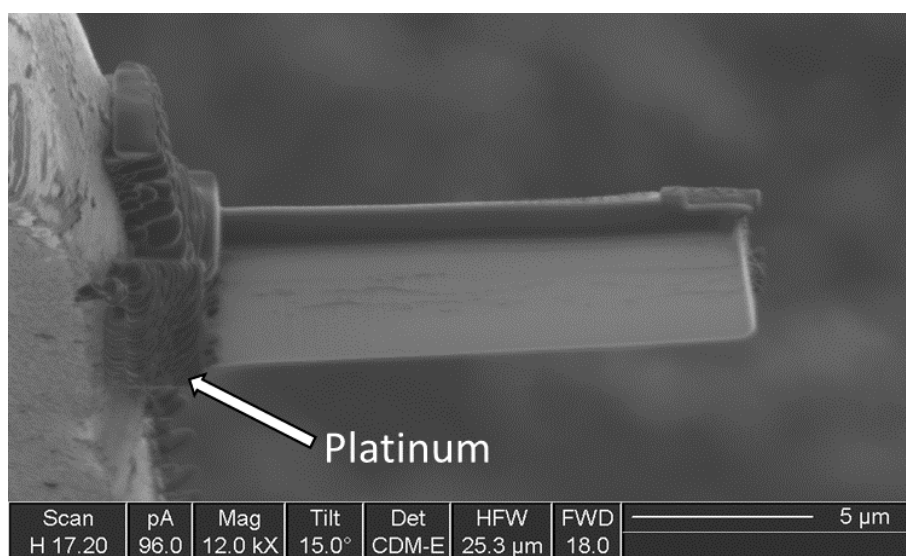


Figure 3.8 – Sample after a tilted weld.

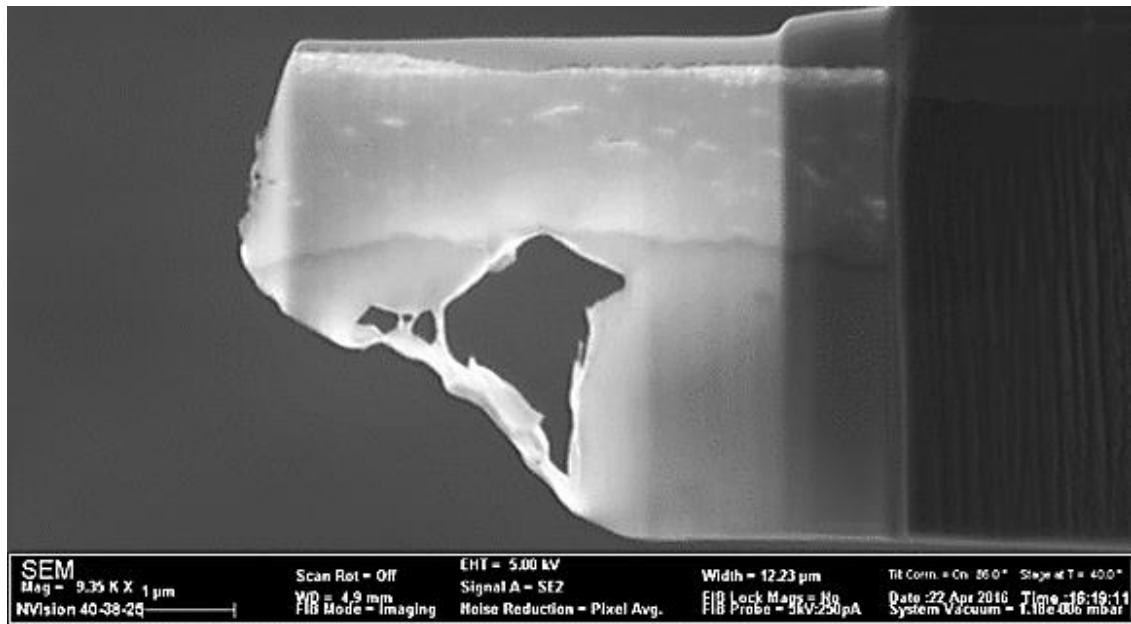


Figure 3.9 – Electron transparent sample after thinning in the NVision.

3.2 – Electron Energy Loss Spectroscopy

EELS uses the in-elastically scattered electrons from the directly transmitted beam for chemical analysis of a sample. The electrons can be separated according to the amount of energy lost by passing them through a magnetic field. A field of strength B , will cause the electron trajectory to be curved through an arc of radius $r = \frac{mv}{eB}$, where m , v , and e are the mass, velocity and charge of the electron respectively.

This means that the paths of faster moving electrons (lower energy loss) are curved less.

The EELS detector used on the ARM-200F is a Gatan Imaging Filter (GIF), specifically the Quantum GIF spectrometer, with 2048 channels.

An example of EELS data is shown in Figure 3.10. The vast majority of the electrons which reach the detector lose zero energy after passing through a sample (assuming it has been adequately thinned), forming the zero-loss peak (ZLP). After the ZLP there is the low-loss region, which covers an energy loss up to ~100 eV. The low-loss region contains peaks caused by the electrons interacting with the plasmons in the material. Spectra obtained in this region can be acquired on the order of minutes, with a spatial resolution of a few nm.

Above 100 eV is the core-loss region (so named because electron losses in this region are due to the electrons interacting with the core shell electrons in the sample), which has a much lower intensity than the ZLP. This means that to obtain a signal above the background for the core-loss we need to

increase the time per pixel. Table 3.1 shows the pixel time for the energy ranges examined, and peaks examined in those regions. I also included the dispersion used for each energy range. A dispersion of 0.05 eV/channel covers an energy range of 100 eV, and 0.25 eV/channel covers 500 eV. The lower dispersion is useful for low-loss work as it gives more accurate spectra, but higher dispersion is necessary for my core-loss work it would also not be possible to detect the O-K, Cr-L_{2,3} and the Fe-L_{2,3} edges on the same spectrum with the lower dispersion. Figures 3.11 and 3.12 show examples of the core-loss data. These data can be improved by using Principal Component Analysis (PCA), which I will talk about in the next section.

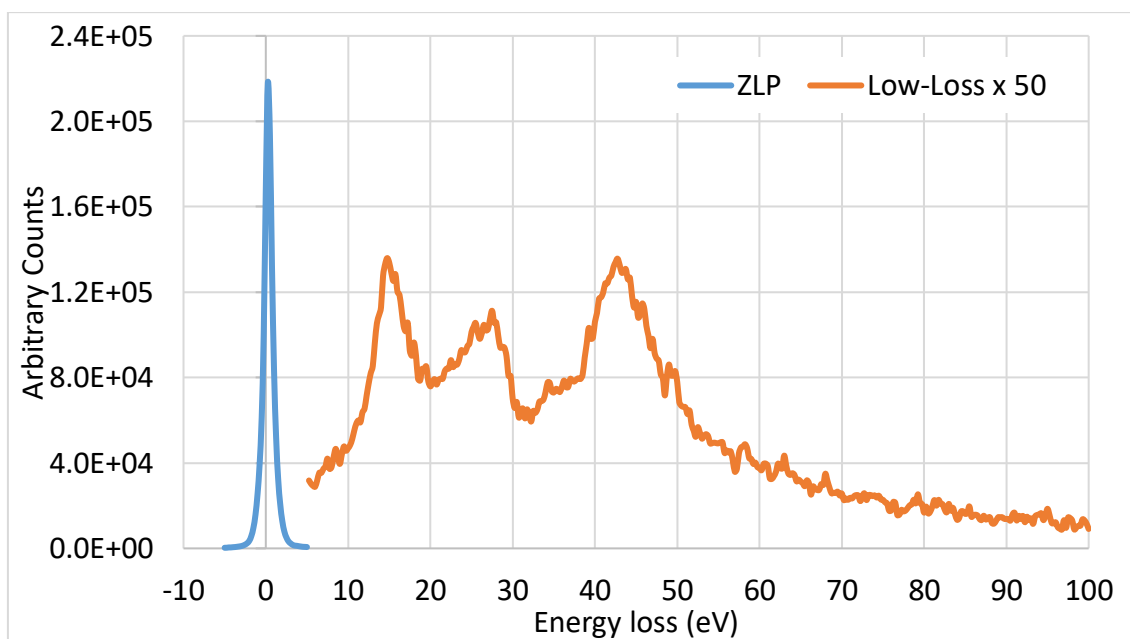


Figure 3.10 – Zero-loss peak (ZLP) and a magnified low-loss region.

Energy Range (eV)	Pixel Time (s)	Dispersion (eV/channel)	Peaks examined (energy in brackets)
0 – 100	1×10^{-5}	0.05, 0.25	ZLP and plasmons
0 – 500	1×10^{-5}	0.25	ZLP
460 – 960	0.01	0.25	O-K (532), Cr-L _{2,3} (575, 584), Fe-L _{2,3} (708, 721)
2050 – 2550	0.1	0.25	Zr-L _{2,3} (2222, 2307)

Table 3.1 – Energy ranges used in EELS experiments with their respective pixel times.

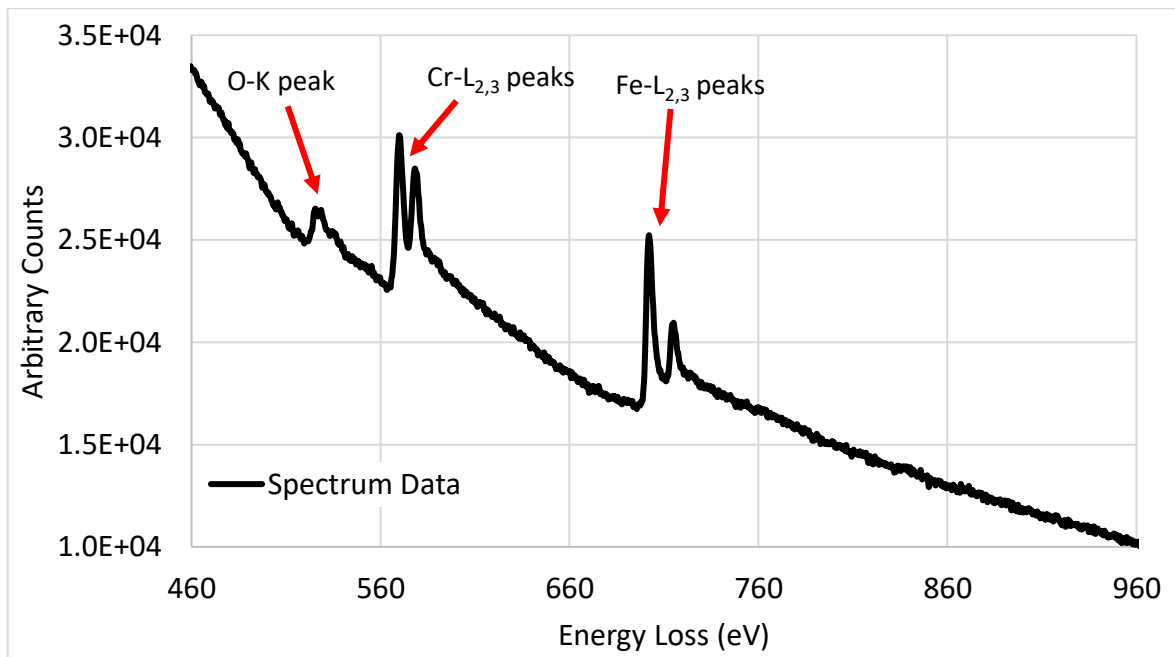


Figure 3.11 – Raw EELS data for the 460 – 960 eV range, showing the O-K, Cr-L_{2,3}, and Fe-L_{2,3} peaks.

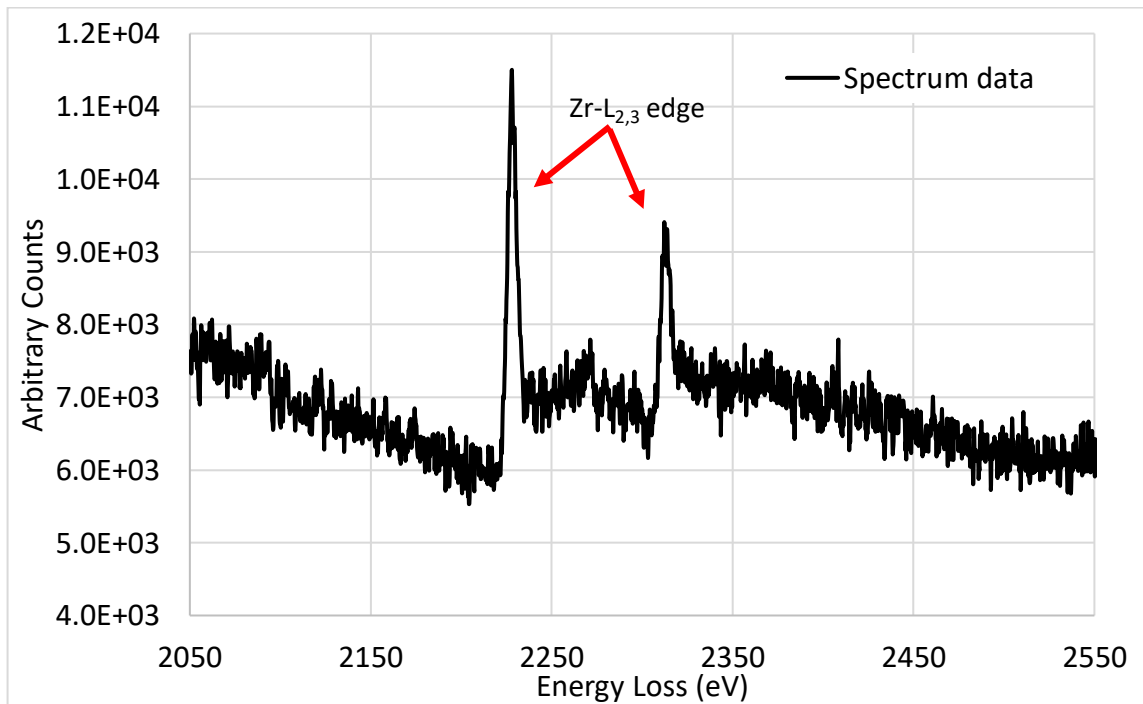


Figure 3.12 – Raw EELS data for the 2050 – 2550 eV range, showing the Zr-L_{2,3} peaks.

3.2.1 – Principal Component Analysis

Data acquired by EELS is in the form of a data-cube, where each pixel on a spectrum image (SI) has a corresponding EELS spectrum. Each spectrum can be decomposed into 2048 components, most of which contain noise. PCA is used to separate these components into orthogonal components that can be sorted in order of decreasing variance (known as a scree plot). Removing the components which only contain noise before reconstructing the data-cube gives much clearer spectra. I used a software

package called Hyperspy^{8,9} to carry out this work, which also allows x-ray spikes to be removed before carrying out PCA. An example of the process I used for carrying out PCA was:

1. Load original data into Hyperspy (Figure 3.13)
2. After aligning the spectrum with the ZLP, I carried out the x-ray spike removal (Figure 3.14).
3. Decompose the spectrum into orthogonal components.
4. Looking at the scree plot (Figure 3.15), the first 4 components will be useful. To determine if the 5th point is useful, the individual components can be plotted (Figure 3.16). Note that the first component is labelled as 0.
5. After determining that up to the 4th component (5th point in Figure 3.15) does not contain noise, the spectrum is re-constructed (Figure 3.17), which shows a much clearer spectrum.

The example here was for a line scan, but can be as easily applied to an EELS map.

Another method of processing the EELS data is to use Multiple Linear Least Squares (MLLS) fitting, which I will discuss in the next section.

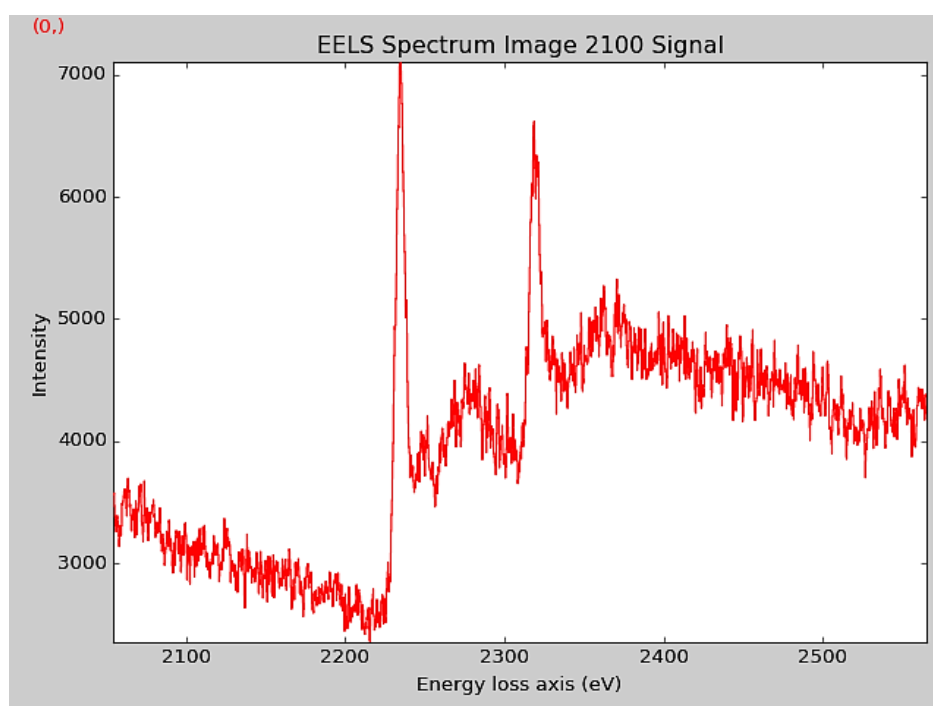


Figure 3.13 – Original EELS data for 2050 – 2550 eV loss.

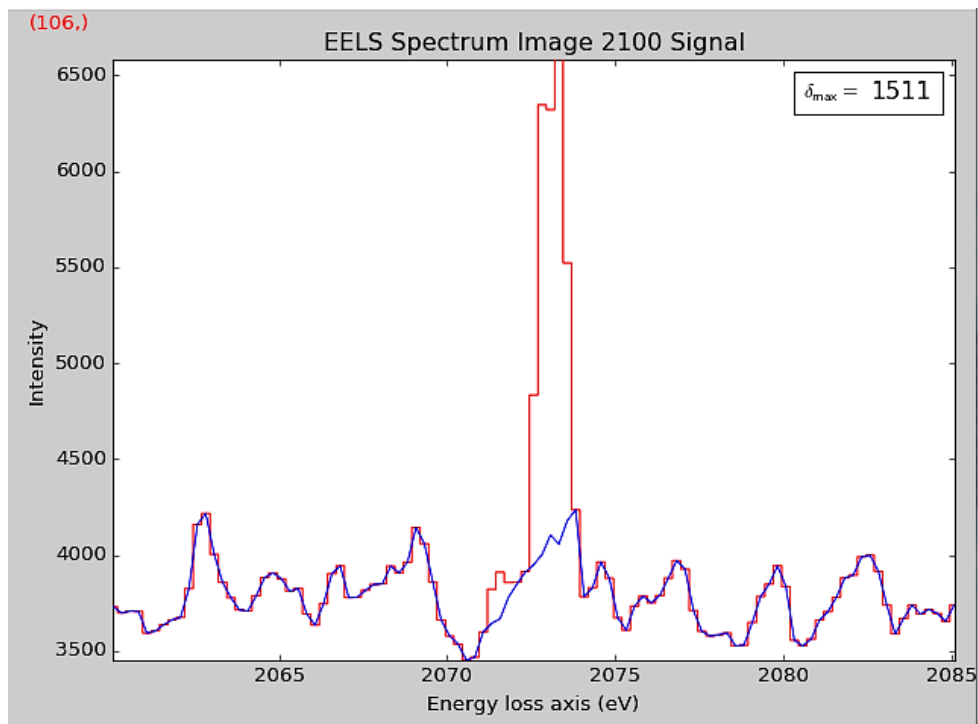


Figure 3.14 – Example of x-ray spike removal. The blue line shows the new spectrum after the spike removal.

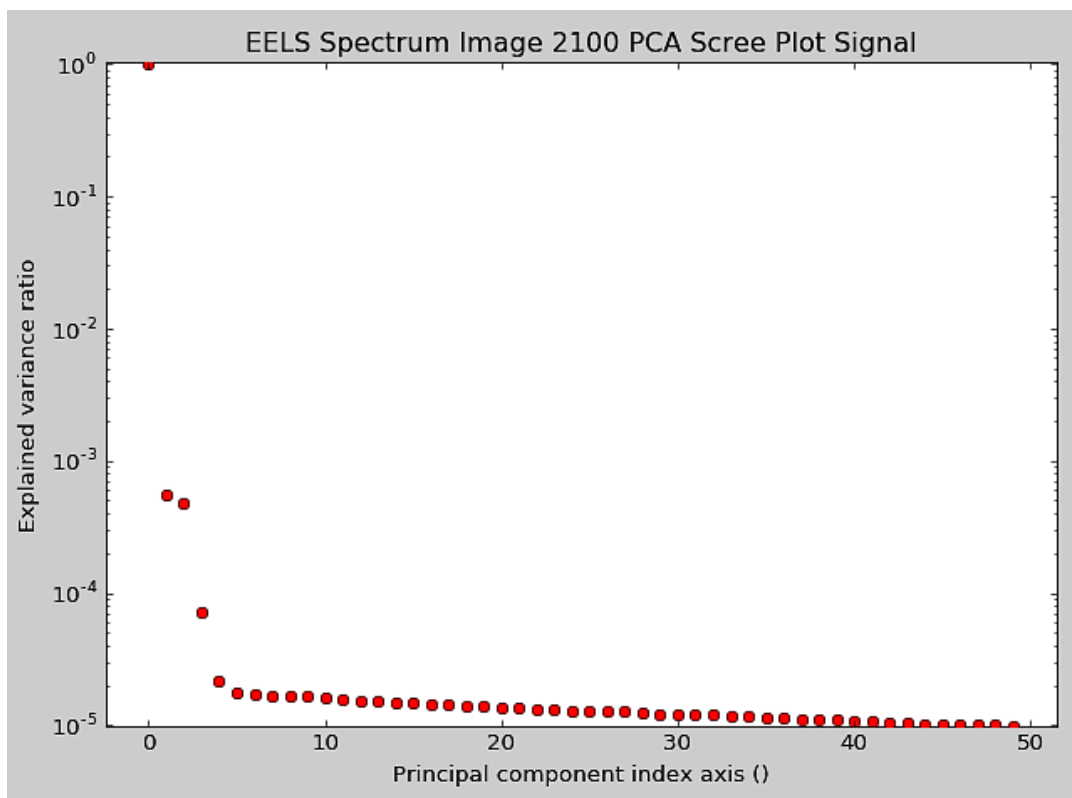


Figure 3.15 – Scree plot of individual components after PCA. The first 4 points (from the left) can definitely be used, but closer inspection must be done on the 5th and 6th.

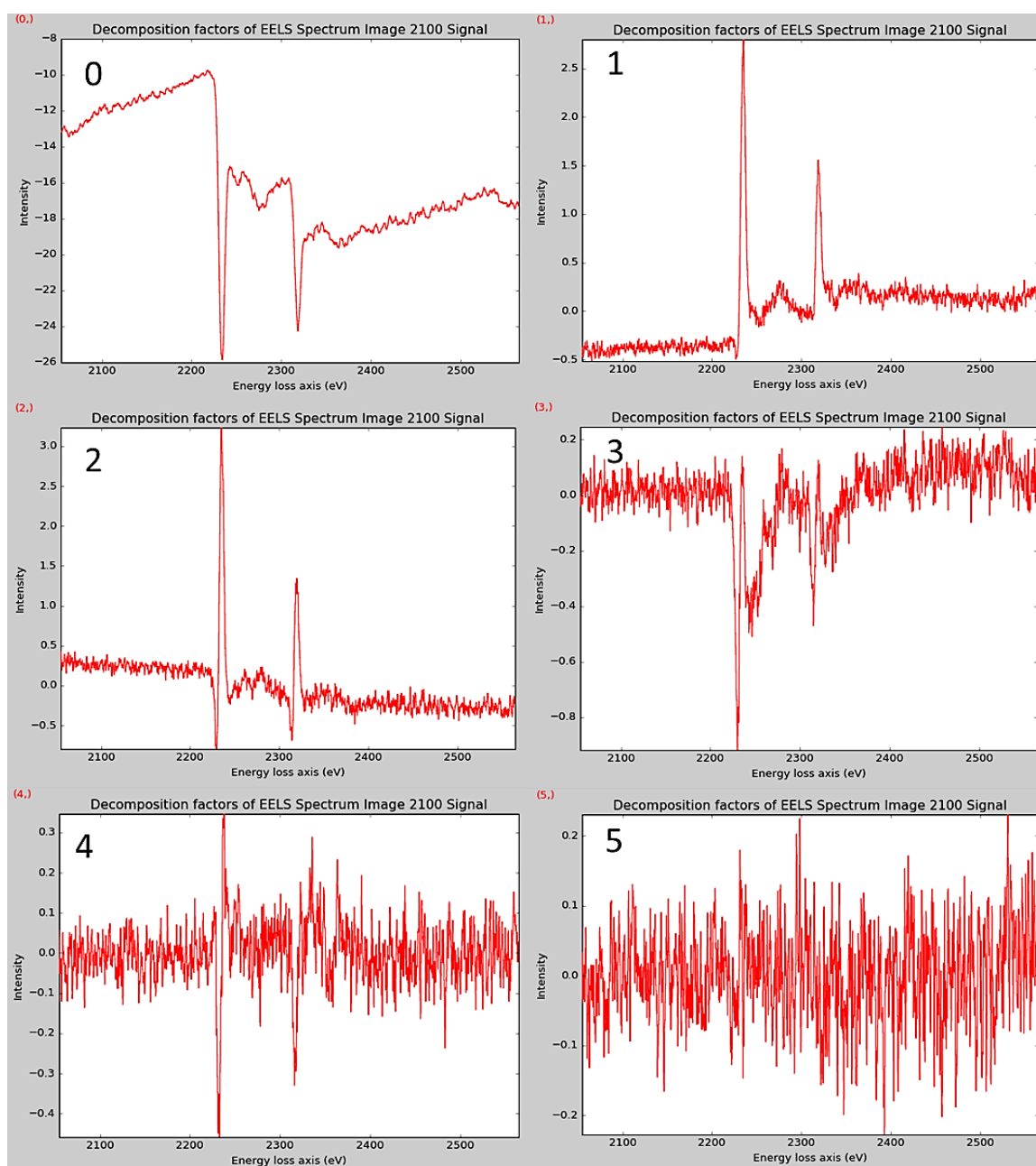


Figure 3.16 – The first 6 components after PCA. Spectrum 4 is the last spectrum with useful data, so in this case this would be the highest value I would use for re-constructing the data.

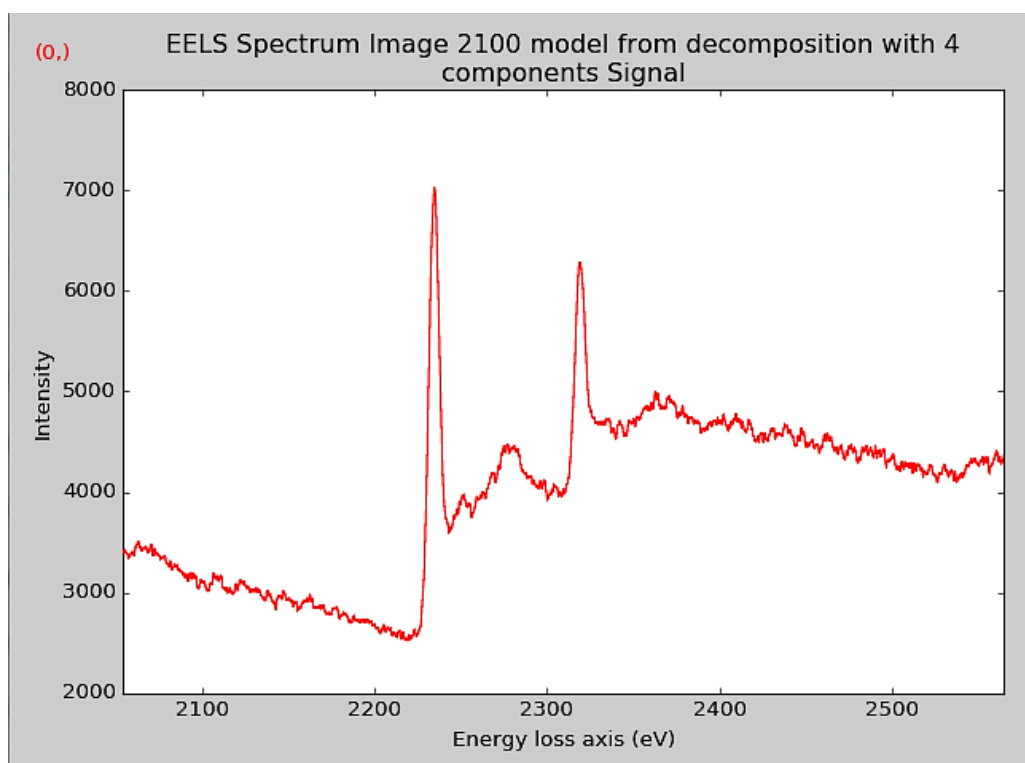


Figure 3.17 – Re-constructed EELS data after PCA. Note the significant reduction in noise.

3.2.2 – Multiple Linear Least Squares Fitting

MLLS¹⁰ is an analysis technique which takes a set of reference spectra (which I generate) and linearly fits them to an SI. This enabled me to separate and analyse the distribution of the different components at the oxide-metal (OM) interface. MLLS can use the plasmon peaks from the low-loss spectra to carry out the fitting, and obtaining spectra from 0 – 100 eV takes on the order of minutes for an area several μm^2 in size, which allowed an entire sample to be mapped quickly. I carried out MLLS using the analysis software Digital Micrograph (DM) made by Gatan Inc.

The different components I observed at the OM interface were the Zr metal, zirconia, a suboxide of zirconia (ZrO), an oxygen-saturated zirconium (OSZ) region, zirconium hydrides, and second phase particles (SPPs). I computed the thickness of the OSZ and ZrO regions from their respective phase maps by using Mercury Software's Avizo. This software enabled me to draw around the area of interest from the MLLS plot and extract that area for computing the thickness. I tracked the thickness of these regions as the oxidation time increased.

3.3 – Thermal Desorption Spectroscopy

Thermal Desorption Spectroscopy (TDS) is a technique used to analyse gases which are released from a sample when it is heated in ultra-high vacuum (5×10^{-9} mbar). I used a Hiden Analytical Thermal Programmed Desorption (TPD) workstation (shown in Figure 3.18 and 3.19). The samples sizes I used were of approximate dimensions 10mm x 10mm x 0.5 mm and were placed on an aluminium nitride wafer (~14 mm x 10 mm x 0.64 mm) on top of a molybdenum heater. I used the wafer to prevent the sample from becoming stuck to the heater during analysis. The sample and wafer are held in place by two pins to ensure good thermal contact between the sample and the heater (see Figure 3.20).



Figure 3.18 – Hiden Analytical TPD workstation.

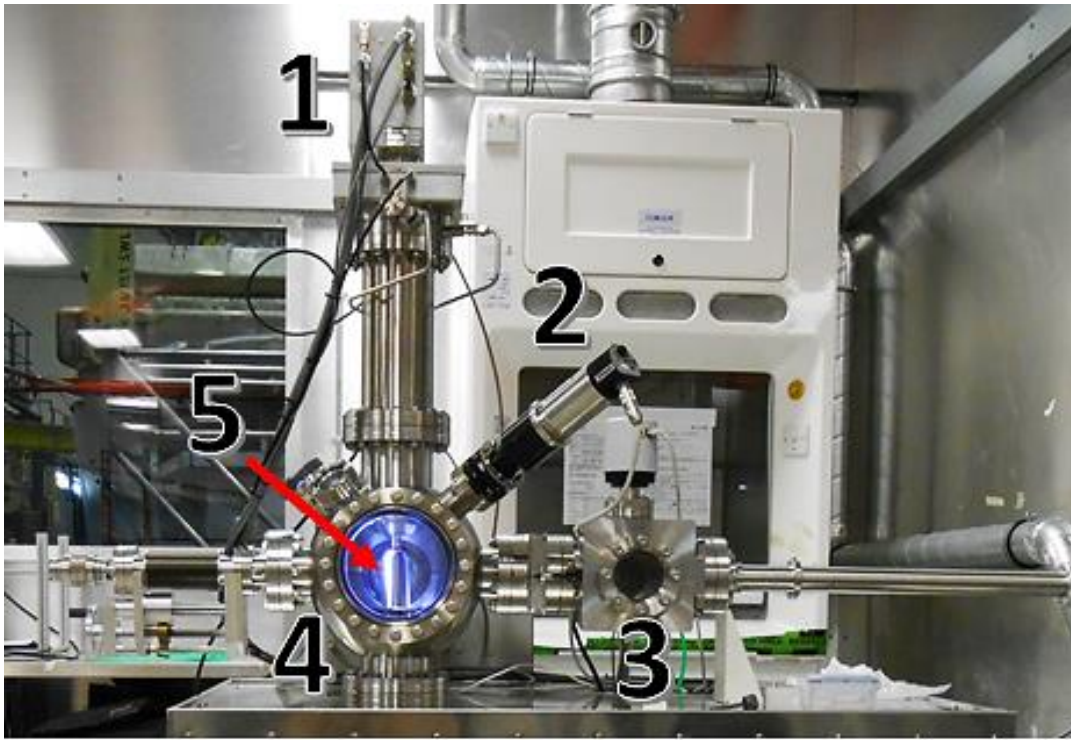


Figure 3.19 - Closer view of workstation. 1 – Residual gas analyser , 2 – Pyrometer, 3 – Sample exchange chamber, 4 – Main chamber, 5 – Heater.

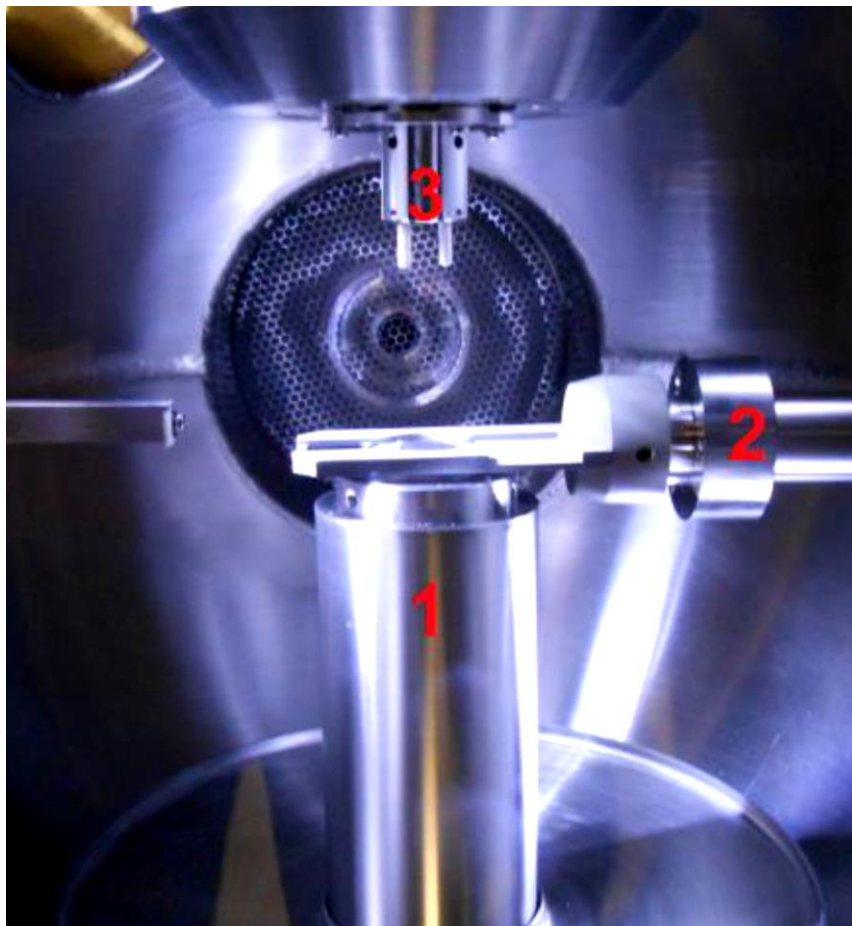


Figure 3.20 – View inside the main chamber. 1 – Heater, 2 – Transfer Rod, 3 – Holding pins.

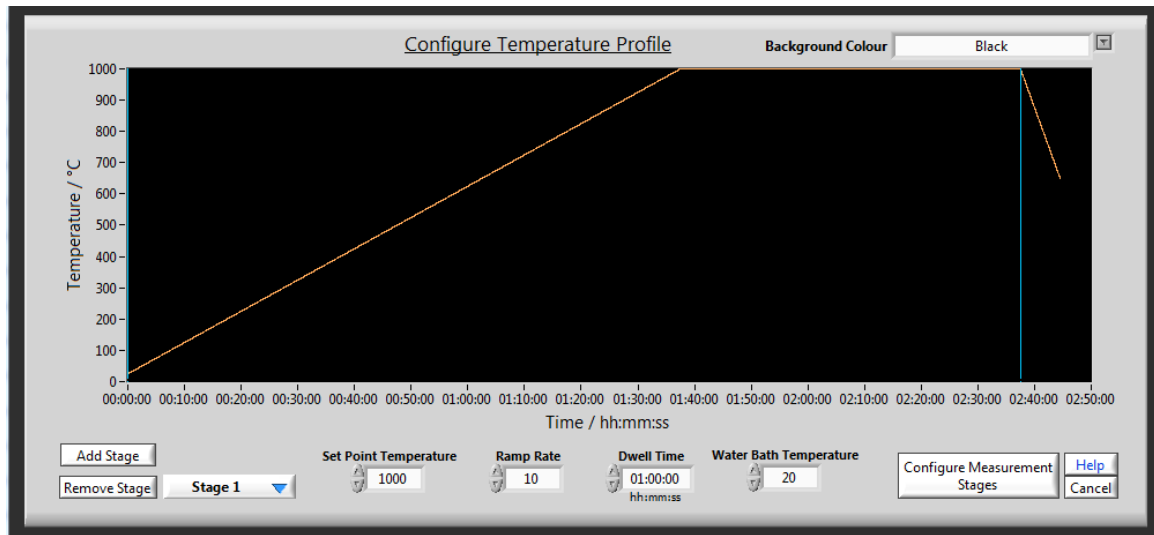


Figure 3.21 – Window for setting heating rate, end temperature and hold time.

The heater can be programmed to follow a particular heating rate up to 1000°C (Figure 3.12), with a maximum heating rate of 20°C. The temperature of the sample was measured with a pyrometer, which measures the intensity of infrared radiation to calculate the temperature of a sample. The pyrometer is setup to assume a perfect black-body (which has an emissivity of 1), which means that the measured temperature is lower than the real temperature. To calculate the temperature of the zirconium (T_{Zr}) from the measured temperature (T_M) we can use the following formula:

$$T_{Zr} = \left(\frac{1}{\epsilon_{Zr}}\right)^{\frac{1}{4}} * T_M \quad (1)$$

ϵ_{Zr} is the emissivity of zirconium. The value of the emissivity can depend on various parameters, such as the wavelength of light used in the experiment, or how well polished the sample is. For zirconium it has been found to vary from 0.2-0.5¹¹⁻¹⁴, which means the recorded pyrometer temperature needs to be scaled by 1.19-1.50 to give the true specimen temperature. For a T_M of 600°C the T_{Zr} could range from ~700°C – 900°C, with an error of 20-50%.

Gases which are desorbed are collected and analysed by a residual gas analyser. This uses a quadrupole mass spectrometer to select for individual mass-to-charge ratios, ranging from 1-50 amu. It can operate in two modes, Bar scan in which scans across the entire range of masses or Multiple Ion Detection (MID) where it scans across a pre-selected range of masses. A Bar scan is useful for identifying species that are present in an unknown sample, and MID is useful as it has a higher

resolution and will give more accurate readings. For a vast majority of the samples tested, I used MID scans and scanned the following masses:

- 2 – Hydrogen (H_2)
- 3 – Deuterium-Hydrogen (D-H)
- 4 – Deuterium-Deuterium (D_2)
- 17 – O-H
- 18 – H_2O or O-D
- 19 – HDO
- 28 – CO
- 44 – CO_2

These masses were chosen because during a bar scan these were the most common species to be desorbed, as shown in Figure 3.22. D-H and D_2 were not found in as-received samples, but I wanted to measure for these as I knew they would be present in samples exposed to deuterated water.

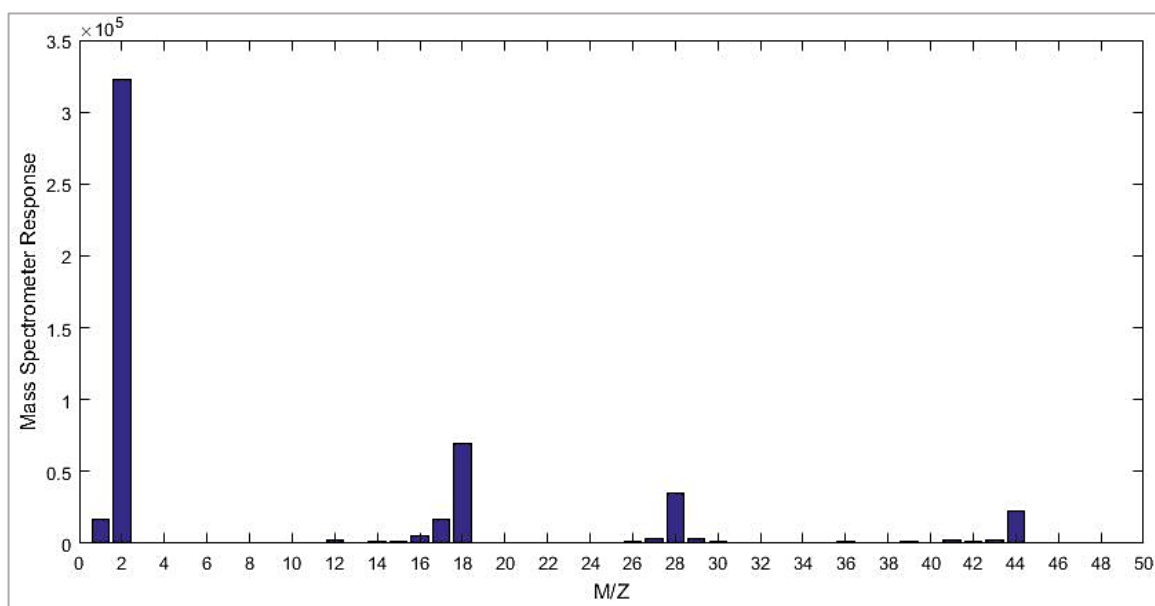


Figure 3.22 – Bar scan of as-received sample, showing the most common species desorbed during heating.

The detector sensitivity is controlled by changing the emission current, which ranges from 1-20 μA . The sensitivity is proportional to the current. If the number of counts exceeds 10^7 the detector will become saturated and shut off.

The general settings I used were as follows:

- Heating rate: 10 °C/min
- End temperature: 1000°C
- Hold time at end temperature: 1 hour
- Emission current: 5 μ A

3.3.1 – Hydrogen Hot-Gas Extraction

The software provided from Hiden allowed me to calculate the area under the hydrogen desorption curve, and this allowed me to compare the amount of hydrogen released from different samples. To quantify this as an actual amount of hydrogen I needed to compare my sample with another technique. Thanks to my collaboration in the MUZIC-2 project, Sousan Abolhassani at the Paul Scherrer Institute (PSI) agreed to carry out Hydrogen Hot-Gas Extraction (HHGE) on some of my samples¹⁵. This technique can determine how much hydrogen is in a sample in parts-per-million (ppm). Westinghouse also carried out similar tests on the samples exposed to pure water.

3.4 – Secondary Ion Mass Spectroscopy

Secondary Ion Mass Spectroscopy (SIMS) is a technique used for determining the chemical composition of samples to the nano-scale. It uses a primary ion beam to bombard a surface and cause the sample to emit charged particles, which can be analysed. A Cameca NanoSIMS 50 was used with a positively charge caesium beam to analyse samples exposed to both pure water and a high pH environment (which contained 50% D₂O). Samples exposed to pure water had a subsequent 31 day exposure to pure D₂O to act as a chemical tracer as the ratio of deuterium to hydrogen in nature is 10⁻⁴. This means any deuterium we detect over this ratio can only have come from the autoclave exposure.

From the data it is possible to calculate the diffusion coefficient of the hydrogen/deuterium in a sample, which gives me another method of determining the behaviour of hydrogen in the material. This is carried out in a Matlab application developed by Dr Kexue Li.

Samples were prepared by myself and Dr Thomas Aarholt and the data were obtained by Dr Li.

3.5 – Digital Scanning Calorimetry

To establish if there are any phase changes associated with hydrogen desorption during heating, a technique called Digital Scanning Calorimetry (DSC) was used^{16–18}. It measures the difference in thermal input from two crucibles, one of which contains the sample being tested and the other is empty, acting as a reference. The crucibles are maintained at the same temperature and if the sample is undergoing a phase change or oxidising then the input to the crucibles will be different as these processes are either endothermic or exothermic.

Samples were prepared by myself and the data collection by Dr David Crudden, on a Netzsch DSC 404 F1. This operates at a pressure of $\sim 10^{-4}$ mbar. Samples were $\sim 2 \times 2$ mm², and were heated at 10 K/min. We chose four samples to be tested by DSC: one un-oxidised sample and 3 oxidised samples, which were samples exposed to elevated pH water for 62 days, 91 days and 148 days as these are pre-transition, at transition and post-transition respectively.

3.6 – Samples Investigated

All the samples reported on were made from Zry-4. Sheets of Zry-4 were provided by Westinghouse, which were cut into 19 pieces, of dimension 25mm x 70 mm for oxidation. These samples had the following composition (in weight %): Sn-1.31; Fe-0.2; O-0.13; Cr-0.11; Zr-balance (The hydrogen content was given as 9 ppm). The samples were oxidised by AMEC Foster Wheeler (AFW) in a static autoclave. The water chemistry was 50% heavy water, containing 2 ppm Li, 95 ppm K and 1050 ppm B at 350°C (pH₃₅₀ = 8.82). These were compared to samples exposed to pure water at 360°C (pH₃₆₀=6.15) by Westinghouse Electric Company.

A selection of these samples was characterized by both STEM and by TDS/HHGE (See Table 3.1). All the TDS data was carried out by myself. Some of the STEM/EELS work on the samples exposed to pure water was carried out by Dr Aarholt for his doctoral thesis, and all the high pH samples were examined by me.

Two of the samples exposed to pure water (30 and 75 days pre-oxidation) were exposed for a further 31 days in pure D₂O for use in the NanoSIMS, giving a total oxidation time of 61 and 106 days. These were compared to two high pH samples (62 and 148 days).

AFW also provided electrolytically charged samples, which were charged for 5, 24 and 48 hours, using the method described by Wei et al¹⁹. The hydrogen content of these samples was examined by TDS.

Several strips of as-received Zry-4 were cut from the sheets and cold rolled to test how adding dislocations affected the hydrogen desorption.

Four samples were examined by DSC, one as-received piece and 3 oxidised in high pH, for 62, 91 and 148 days.

Table 3.2 shows a summary of the other samples examined and the techniques used.

Pure water					Elevated pH					
Oxidation time (days)	EELS	SIMS	TDS	HHGE	Oxidation time (days)	EELS	SIMS	TDS	HHGE	DSC
0			Yes	Yes	0			Yes	Yes	Yes
3	Yes			Yes	5	Yes		Yes		
7			Yes	Yes	15	Yes		Yes	Yes	
45	Yes		Yes	Yes	27	Yes		Yes		
61 (including 31 days D ₂ O)		Yes			45	Yes		Yes		
90	Yes		Yes	Yes	62	Yes	Yes	Yes		Yes
105	Yes			Yes	75	Yes		Yes		
106 (including 31 days D ₂ O)		Yes			91	Yes		Yes		Yes
120			Yes	Yes	123	Yes		Yes	Yes	
165	Yes		Yes	Yes	148	Yes	Yes	Yes		Yes
					176	Yes		Yes		
					211	Yes		Yes		
					243	Yes		Yes		

Table 3.1 – Samples exposed to pure water and high pH oxidised environments, and the techniques used to examine them.

Sample	Technique
Hydrogen charged (hours)	
5	TDS
24	TDS
48	TDS
Cold rolled (% reduction in thickness)	
7%	TDS
15%	TDS

Table 3.2 – Summary of other samples used for TDS.

3.7 – References

1. Williams D, Carter C. *Transmission Electron Microscopy: A Textbook for Materials Science*. 2nd ed. Springer; 2009. <https://books.google.co.uk/books?id=dXdrG39VtUoC>.
2. Egerton RF. *Electron Energy-Loss Spectroscopy in the Electron Microscope*. 3rd ed. Springer US; 2011. <https://books.google.co.uk/books?id=C8OZsABSk2sC&dq=Electron+energy->

loss+spectroscopy+in+the+electron+microscope&source=gbs_navlinks_s.

3. Egerton RF. Electron energy-loss spectroscopy in the TEM. *Reports Prog Phys.* 2009;72:25. doi:10.1088/0034-4885/72/1/016502
4. Aarholt T. Analytical microscopy of corroded zirconium alloys. 2017.
5. Mayer J, Giannuzzi LA, Kamino T, Michael J. TEM sample preparation and damage. *MRS Bull.* 2007;32(May):400-407.
6. Ni N. Study of oxidation mechanisms of zirconium alloys by electron microscopy. 2011. <https://ora.ox.ac.uk/objects/uuid:c60cdca2-e576-414a-8a10-eb3a60264998>.
7. Lozano-Perez S. A guide on FIB preparation of samples containing stress corrosion crack tips for TEM and atom-probe analysis. *Micron.* 2008;39(3):320-328. doi:10.1016/j.micron.2007.12.003
8. Peña F de la, Ostasevicius T, Fauske VT, et al. Hyperspy/Hyperspy V1.2. *doi.org*. doi:10.5281/ZENODO.345099
9. de la Peña F, Berger MH, Hocheplid JF, Dynys F, Stephan O, Walls M. Mapping titanium and tin oxide phases using EELS: An application of independent component analysis. *Ultramicroscopy.* 2011;111(2):169-176. doi:10.1016/j.ultramic.2010.10.001
10. Longo P. The use of MLLS fitting approach to resolve overlapping edges in the EELS spectrum at the atomic level. <http://www.gatan.com/use-mls-fitting-approach-resolve-overlapping-edges-eels-spectrum-atomic-level>.
11. Fong RWL, Paine M, Nitheanandan T. Total hemispherical emissivity of pre-oxidized and un-oxidized Zr-2 .5Nb pressure-tube materials at 600°C to 1000°C under vacuum. *CNL Nucl Rev.* 2016;5(1):85-93. doi:http://dx.doi.org/10.12943/CNR.2016.00006
12. Bechmann R, Carpenter LG, Mair WN, et al. The optical emissivity of titanium and zirconium. *Proc Phys Soc Sect B.* 1950;63(8):573-577.
13. Murphy E V, Havelock F. Emissivity of zirconium alloys in air in the temperature range 100-400°C. *J Nucl Mater.* 1976;60:167-176.
14. Lustman B, Kerze Jr F. *Metallurgy of Zirconium.*; 1955.
15. Abolhassani S, Bart G, Bertsch J, et al. Corrosion and hydrogen uptake in zirconium claddings irradiated in light water reactors. In: Comstock RJ, Barberis P, eds. *Zirconium in the Nuclear Industry: 17th International Symposium, ASTM STP 1543*. ASTM International; 2015:540-573. doi:10.1520/STP154320130007
16. Vizcaino P, Rios R, Banchik A. Hydrogen determinations in a zirconium based alloy with a DSC. *Thermochim Acta.* 2005;429:7-11. doi:10.1016/j.tca.2004.11.019

17. Khatamian D, Root JH. Comparison of TSSD results obtained by differential scanning calorimetry and neutron diffraction. *J Nucl Mater.* 2008;372(1):106-113.
doi:10.1016/j.jnucmat.2007.02.010
18. Setoyama D, Matsunaga J, Ito M, et al. Influence of additive elements on the terminal solid solubility of hydrogen for Zirconium alloy. *J Nucl Mater.* 2005;344(1-3):291-294.
doi:10.1016/j.jnucmat.2005.04.057
19. Wei J, Frankel P, Blat M, et al. Autoclave study of zirconium alloys with and without hydride rim. *Corros Eng Sci Technol.* 2012;47(7):516-528.
doi:10.1179/1743278212Y.0000000055

4 – Oxidation vs. pH

Contents

4.1 – Oxide Growth.....	65
4.2 – EELS Analysis	67
4.2.1 – Low-Loss EELS	68
4.2.2 – OSZ and ZrO in High pH Samples	72
4.2.3 – OSZ and pH.....	88
4.2.4 – SPP Oxidation	96
4.3 – Discussion	124
4.4 – Summary	130
4.5 – References	131

In this chapter I will be discussing the oxidation of Zircaloy-4 in different environments. First I will examine the oxide weight gain data. Then I will show the work carried out using STEM and EELS, and how I characterised the oxide-metal interface and SPPs using these techniques. These tests were carried out to examine changes in the microstructure (near the OM interface) and if they can be linked to the oxidising environment. The SPPs were examined to understand the process of oxidation in SPPs in Zircaloy-4 and if there is any difference in different pH environments.

4.1 – Oxide Growth

Figure 4.1 shows the oxide growth from the different environments. The oxide thickness is estimated from the weight gain, where 15 mg/dm^2 (milligrams per decimetre squared) is equivalent to $1 \text{ }\mu\text{m}$ of oxide growth^{1,2}. There were 19 samples exposed to high pH and they were weighed after each exposure, which was limited to a maximum of 30 days to replenish the water in the autoclave.

It can be seen that for either environment the oxide thickness at transition is approximately $2.2 \text{ }\mu\text{m}$, but for the pure water samples the transition occurs around 100 days versus 130 days for the elevated pH samples. This is only an estimate as we are lacking data at the transition points for both environments.

The oxidation rate of the pure water/360°C samples is greater than that of the elevated pH/350°C samples. We can assess the contribution to this from the difference in exposure temperatures by using an Arrhenius analysis. Figure 4.2 shows the mathematical fit to the pre-transition data in each environment.

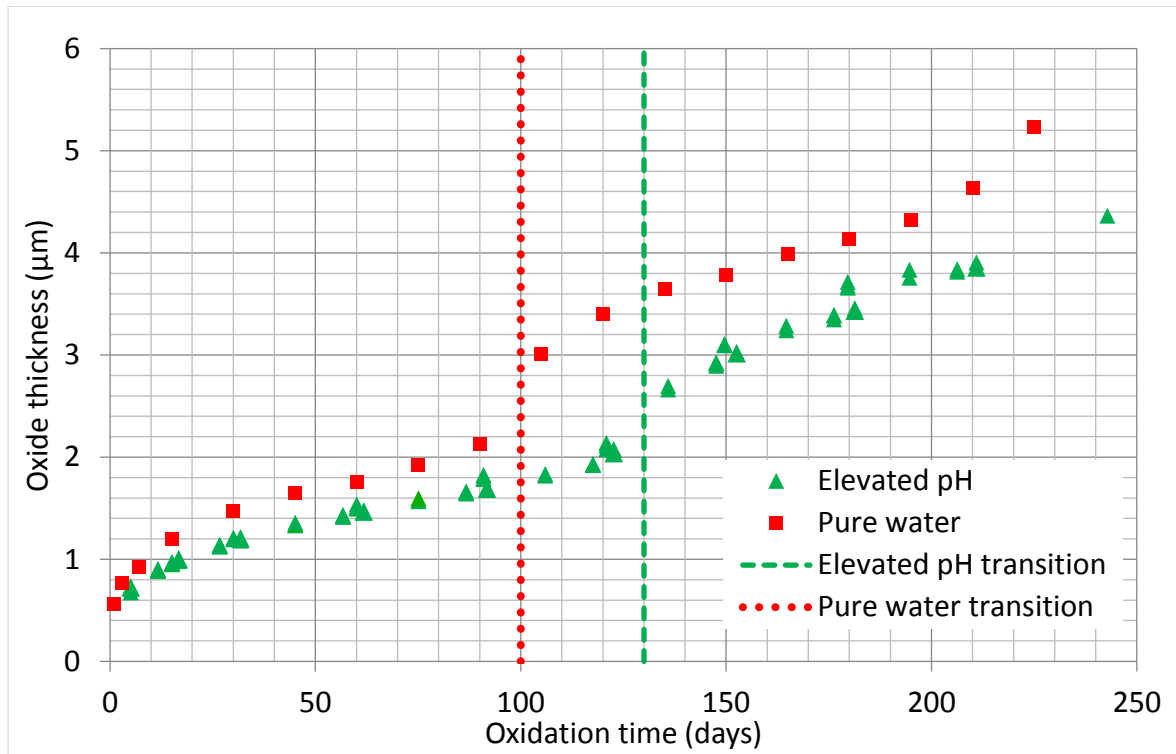


Figure 4.1 - Comparison of samples oxidized in pure water at 360°C vs samples oxidized in elevated pH at 350°C.

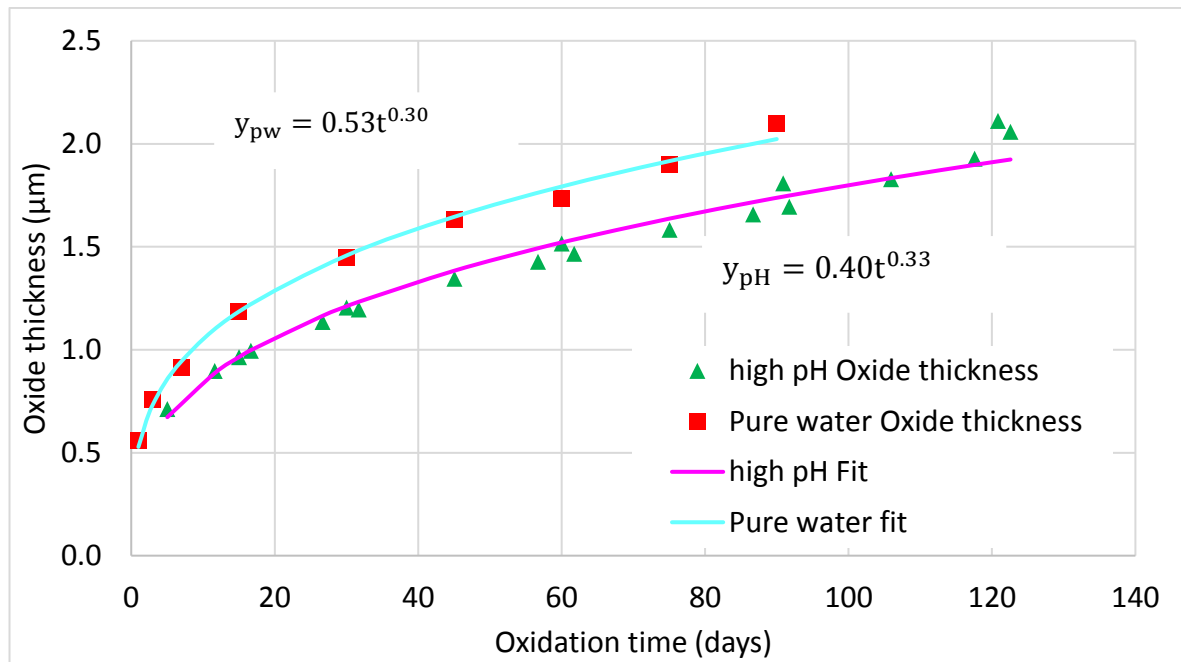


Figure 4.2 – Pre-transition oxide growth with the Matlab fit for the data.

The oxide growth equations are:

$$y_{pH} = 0.40t^{0.33} \quad y_{pw} = 0.53t^{0.30} \quad (3.1)$$

Where y_{pH} is the oxide thickness (in μm) for the high pH environment, y_{pw} is the oxide thickness (in μm) in pure water, and t is the time in days. The rate of oxidation is then:

$$\frac{dy_{pH}}{dt} = 0.13t^{-0.67} \quad \frac{dy_{pw}}{dt} = 0.16t^{-0.70} \quad (3.2)$$

For the same oxide thickness (for example 1 μm), the time in the high pH environment is 16.1 days, and for pure water it is 8.3 days. Putting these values into equation 3.2 gives

$$\frac{dy_{pH}}{dt}(16.1 \text{ days}) = 0.02 \mu\text{m/day} \quad \frac{dy_{pw}}{dt}(8.3 \text{ days}) = 0.036 \mu\text{m/day} \quad (3.3)$$

The ratio of these is:

$$\frac{\frac{dy_{pH}}{dt}}{\frac{dy_{pw}}{dt}} = 0.55 \quad (3.4)$$

This equation is related to the free energy of oxidation by:

$$\exp\left\{\frac{\Delta G}{R}\left(\frac{1}{T_{pH}} - \frac{1}{T_{pw}}\right)\right\} = \frac{\frac{dy_{pH}}{dt}}{\frac{dy_{pw}}{dt}} = 0.55 \quad (3.4)$$

$T_{pH}=350^\circ\text{C}$ and $T_{pw}= 360^\circ\text{C}$, making the left hand side of (3.4) become:

$$\exp(-3.05 * 10^{-6} * \Delta G) = 0.55 \quad (3.5)$$

$$\Delta G = 194 \text{ kJ/mol} \quad (3.6)$$

This value for the activation energy is higher than that found in the literature, which ranges from 55 – 177 kJ/mol³⁻⁷. In Figure 2.4 I showed the results obtained by Bouineau et al⁸, and the approximate oxide growth equations. By carrying out the same analysis as above the activation energy for those experiments is approximately 110 kJ/mol. This would indicate that the difference in oxidation rate for my experiments is due in part to the temperature difference and to the pH of the oxidising environment. It is not possible to tell how much each part contributes to the difference, although as the activation energy is close to that found in the literature, I would estimate that the pH effect is quite small. It should be noted that the oxidation is reduced in the lithium containing environment, which is the opposite of that found in the literature^{2,9-13}. From the findings of the MUZIC-2 collaboration¹⁴, the samples exposed to a higher pH should have a lower hydrogen pick-up as n in equation (3.1) is slightly higher for the high pH oxide growth.

4.2 – EELS Analysis

In this section I am going to show and discuss the results I obtained from the STEM-EELS experiments I carried out. I am going to start with the low-loss data and the characterisation of the OM interface, followed by the SPP observations I have made.

Throughout this analysis I will be ignoring the effects of multiple scattering in thicker regions of samples. This will have an effect on the quantification of these regions although it is small enough to ignore.

4.2.1 – Low-Loss EELS

I showed an example of a low-loss EELS data in Figure 3.10, and another example is shown in Figure 4.3. Each pixel in the Spectrum Image (SI) contains an EELS spectrum, and an example is shown at the bottom on the figure, showing the plasmon peaks in the oxide. Each of the regions shown in Figure 4.3 has its own corresponding plasmon peak, which are shown in Figure 4.4.

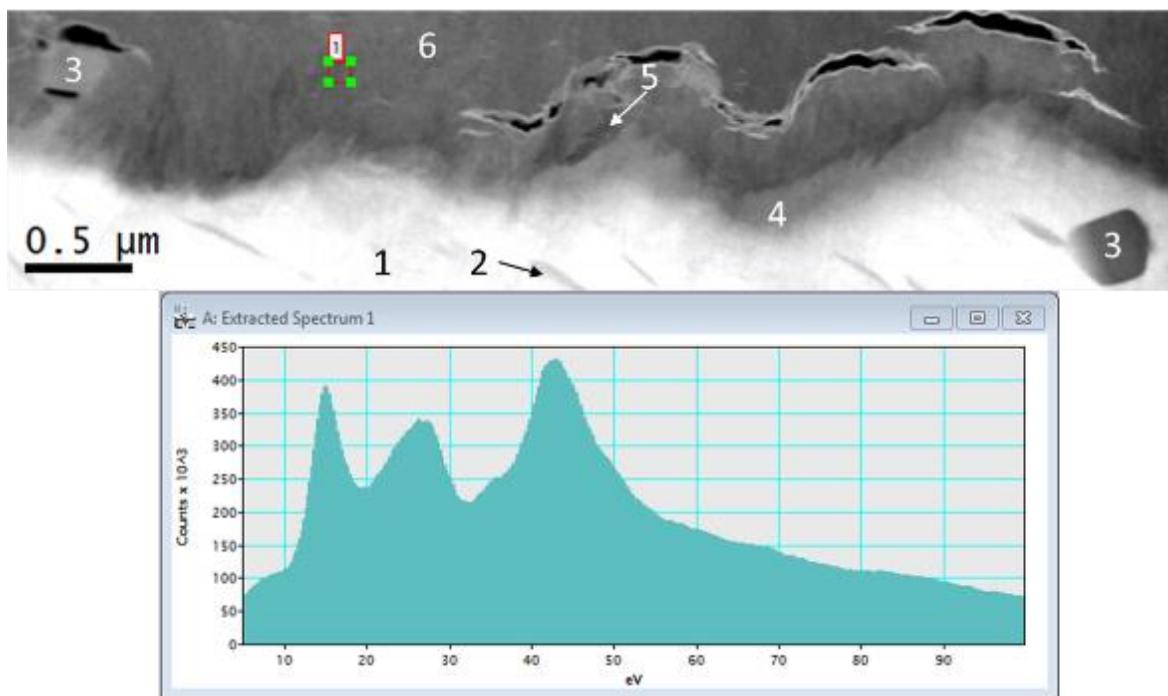


Figure 4.3 – EELS data from oxide on sample exposed to $\text{pH}_{350}=8.82$ for 91 days ($1.83\mu\text{m}$). SI (top) with the extracted spectrum from the red box below. The labelled regions are: 1 – Metal, 2 – Hydride, 3 – SPP (one in the oxide and one in the metal), 4 – Oxygen Saturated Zirconium (OSZ), 5 – ZrO , 6 – Oxide.

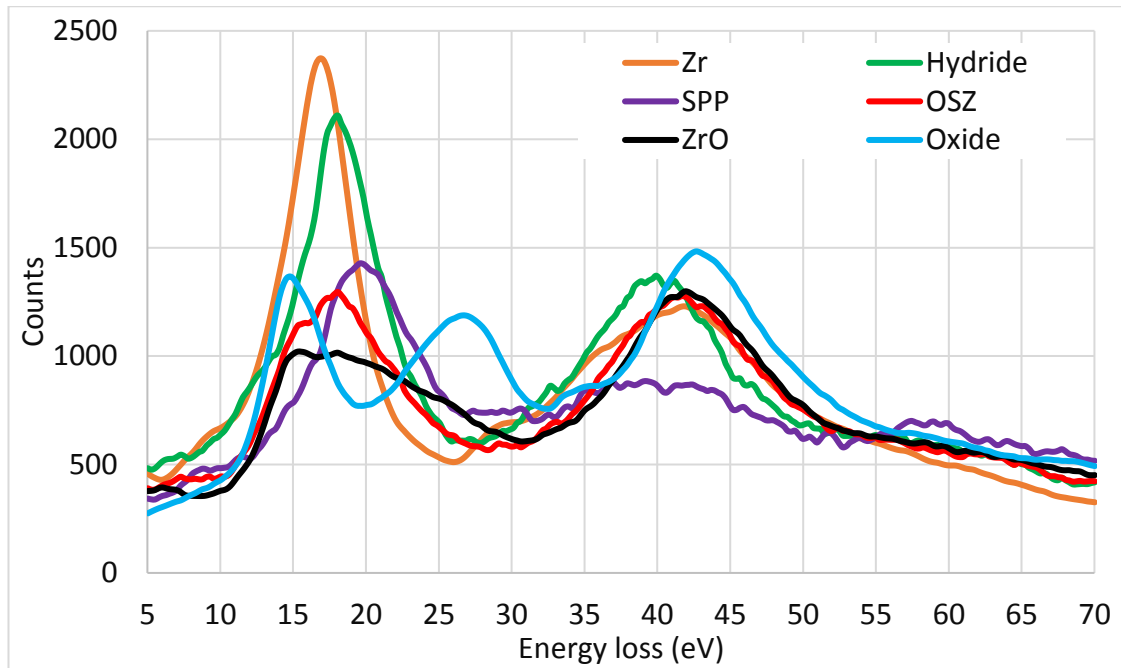


Figure 4.4 – Plasmon peaks for the different regions labelled in Figure 4.3.

Using the MLLS function on DM I obtained a series of images showing the fits of each spectrum to the original SI, which is shown in Figure 4.5. The most interesting aspect of these images is the separation of the ZrO and OSZ regions and how they change as the metal corrodes more (see the next section for more details). In this particular sample the ZrO layer was fairly uniform in thickness, whereas the OSZ region has a large variation across this region, and is thicker below the cracks than for the regions which are not.

Figure 4.6 shows how the plasmon peaks change in SPPs at different positions in the oxide, which means that I didn't use just one peak for the SPPs during my analysis.

The dispersion generally used for low-loss EELS was 0.05 eV/channel, which allowed me to achieve better fits with the MLLS function, as the scan has a range of 100 eV for this dispersion. Figure 4.7 shows the difference between 0.05 eV/channel and 0.25 eV/channel, which was used for core-loss EELS (and the SI in Figure 4.3). 0.25 eV/channel is used so that the O-K, Cr-L_{2,3} and the Fe-L_{2,3} edges can be detected on the same spectrum acquisition.

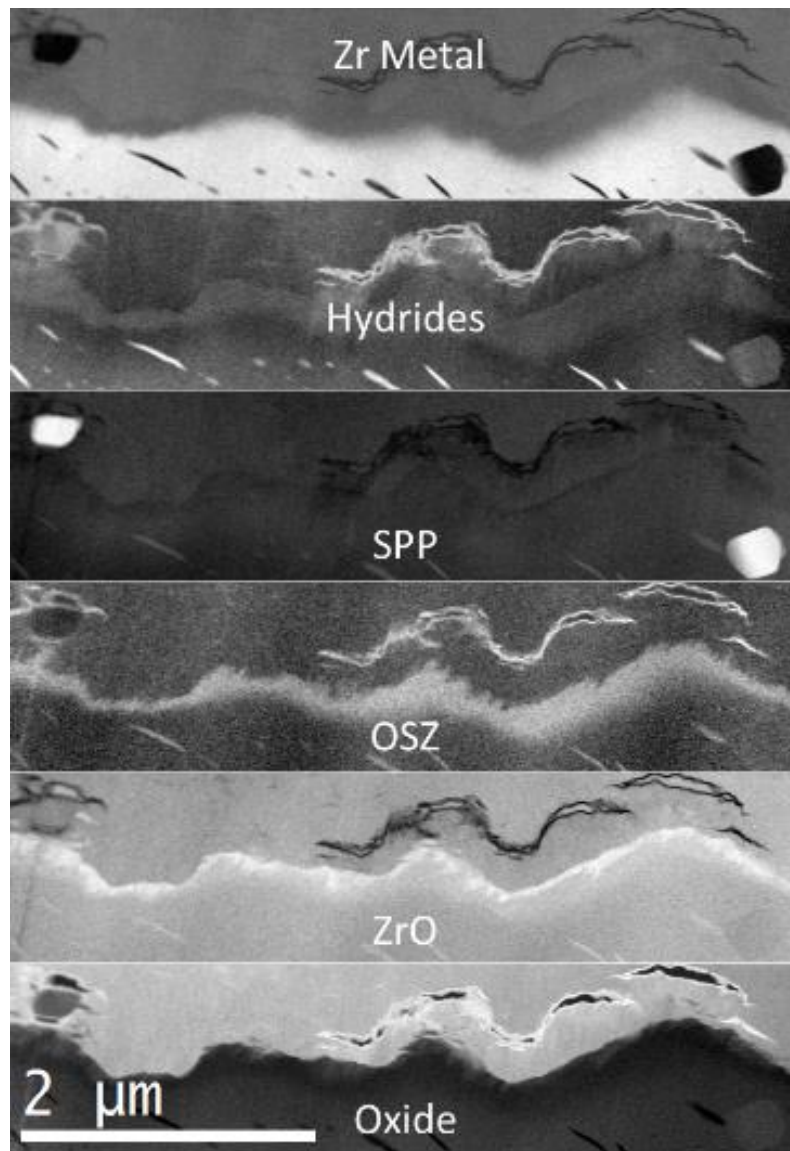


Figure 4.5 – MLLS fit for the 6 regions in Figure 4.3. From top to bottom: Metal, Hydrides, SPPs, OSZ, ZrO, and Oxide. Lighter areas show the strongest match to the input spectrum.

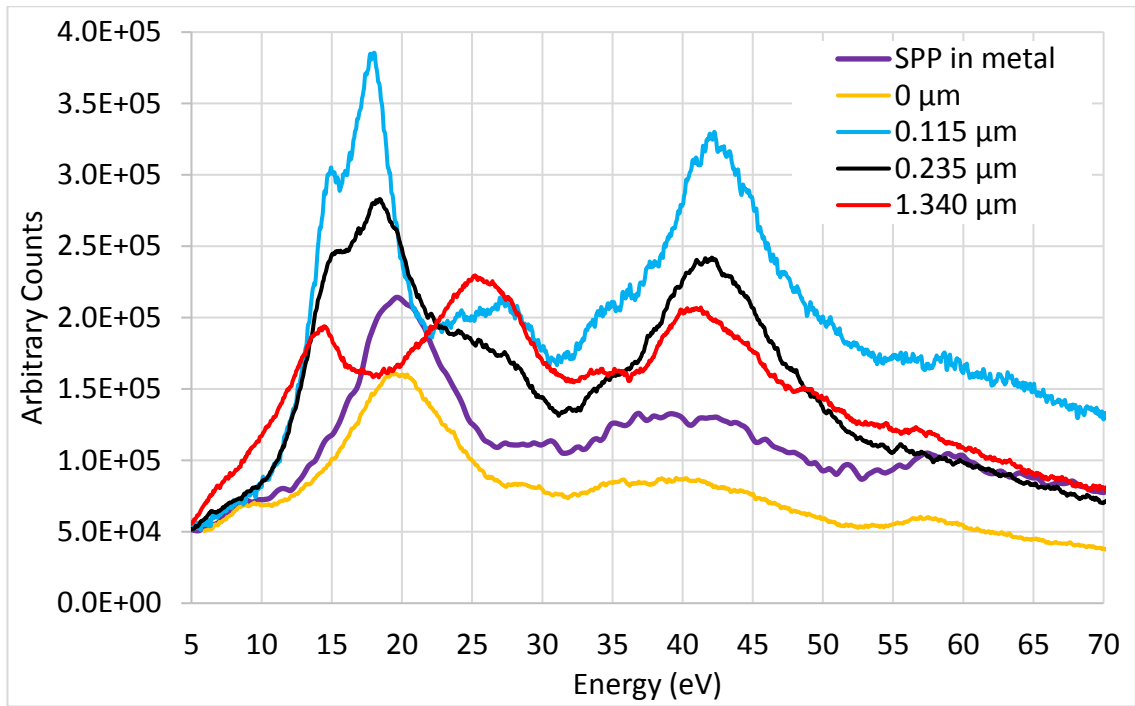


Figure 4.6 – Plasmon peak for SPPs at different distances from the OM interface.

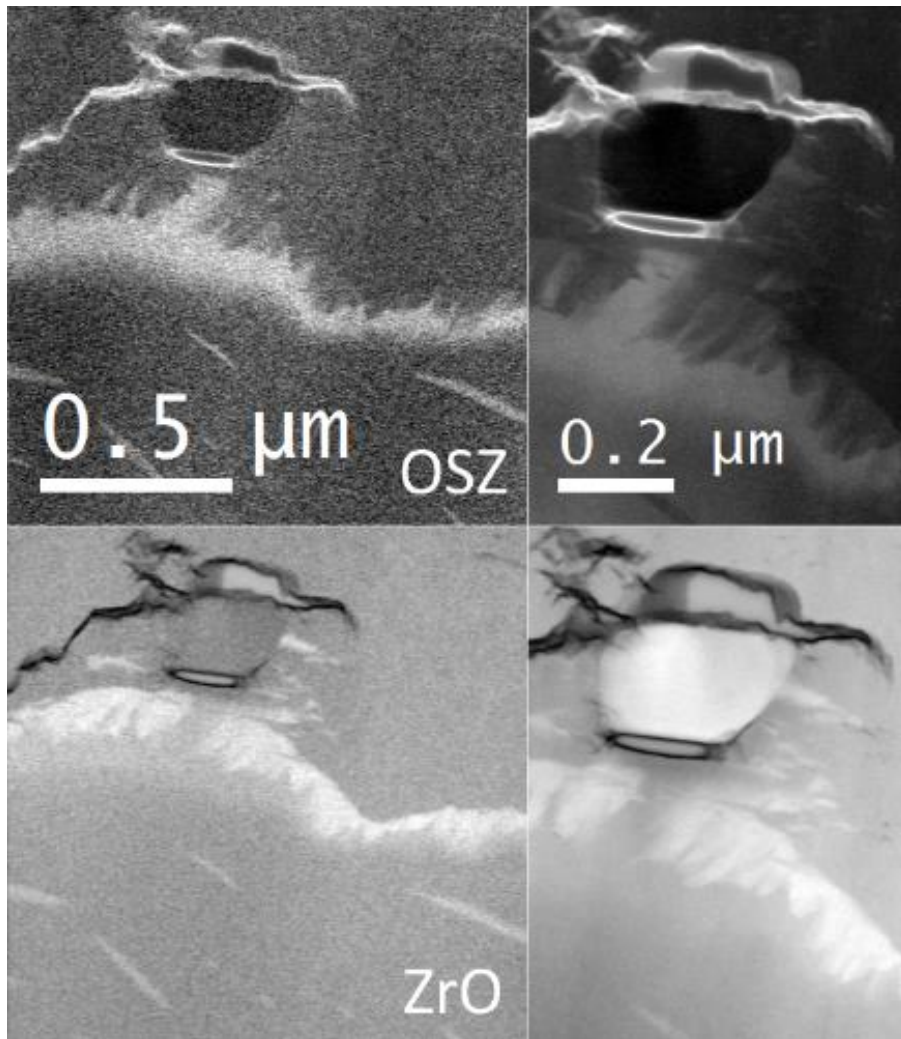


Figure 4.7 – MLLS fits for OSZ (top) and ZrO (bottom) of the SPP to the left of Figure 4.3. Comparison between images acquired using 0.25 eV/channel (left) with 0.05 eV/channel (right).

4.2.2 – OSZ and ZrO in High pH Samples

I am now going to discuss my observations of the OM interface, and in particular the OSZ and ZrO thickness as a function of oxidation time. The samples shown in this section were all oxidised at $\text{pH}_{350} = 8.82$. I will show 4 OM interfaces from pre-transition samples (15, 27, 62, and 123 days), and 3 post-transition samples (148, 211, and 240 days). I am going to compare the OM interface regions in samples exposed to different pH levels in the next section and will be showing the results for the 45 and 90 day (for pure water) and 45 & 91 day (for high pH) oxides there.

Figures 4.8 & 4.9 show dark field (DF) images of different lift-outs from the 15 day sample (average oxide thickness = $0.96\ \mu\text{m}$). It can be seen from both samples that there are some small cracks formed already (and one large one in Figure 4.8) and significant undulations in the OM interface.

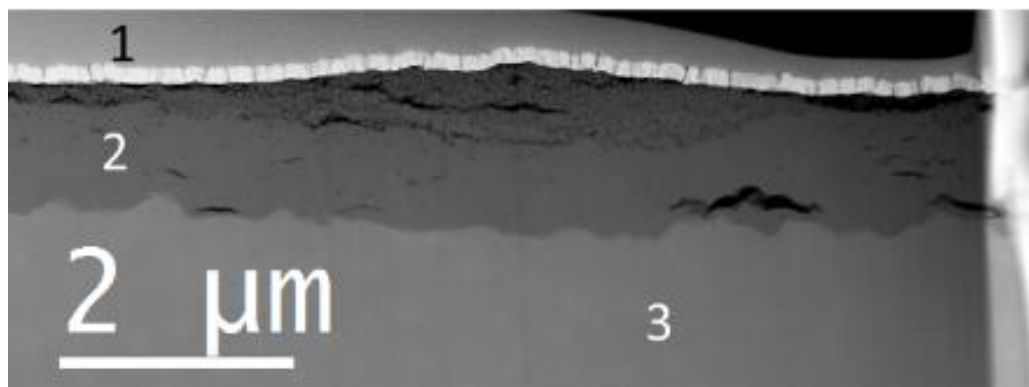


Figure 4.8 – OM interface region of a sample exposed to high pH water at 350°C for 15 days. The numbered regions are: 1 – Protective platinum layer (the lighter region underneath is a protective gold layer), 2 – Oxide, 3 – Metal.

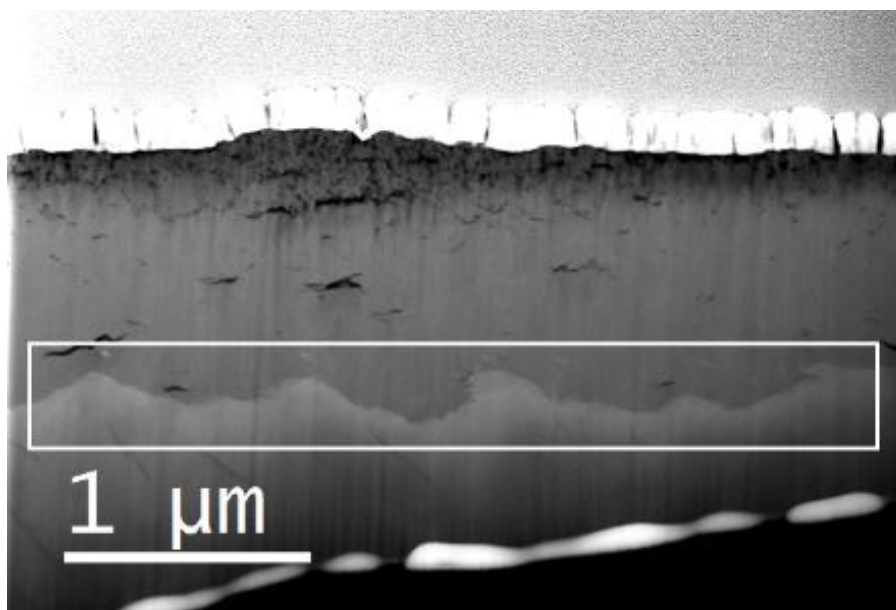


Figure 4.9 – Another region of oxide on a sample exposed to high pH water at 350°C for 15 days. The white box shows the area analysed with low-loss EELS.

Figure 4.10 shows a montage of MLLS fits of the OSZ in the area highlighted in Figure 4.9. The OSZ is a continuous layer, with varying thickness for this sample, and the same was found for the other 15 day sample. Figure 4.11 shows the MLLS fits for ZrO for the same region. This shows that the ZrO has the previously seen saw-tooth shape in places, and also has more continuous regions and one solid block (top right). The blocky region is not necessarily different in kind to the saw-tooth regions as it could represent a section through a saw-tooth projecting out of the plane of the section, or it could result from several saw-toothed regions widening and merging.

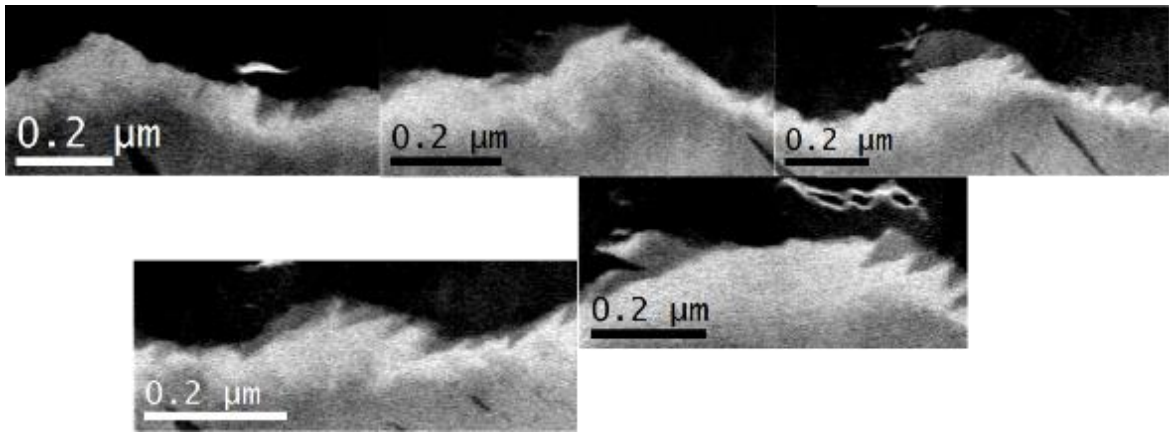


Figure 4.10 – MLLS fit of the OSZ from Figure 4.9. (The lower two images fit to the right of the upper three images).

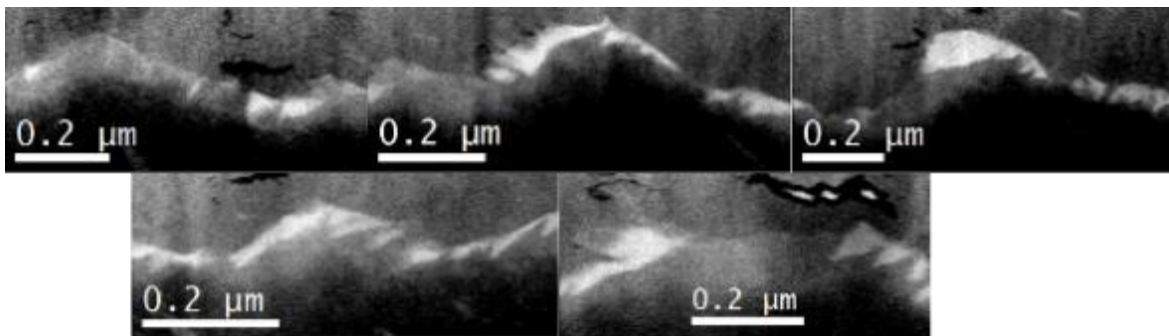


Figure 4.11 – MLLS fit of the ZrO region from Figure 4.9. (Again the lower two images fit to the right of the upper three images).

Figures 4.12 and 4.13 show DF images of two 27 day oxide samples (average oxide thickness = $1.14\mu\text{m}$). The oxide has similar undulations as the 15 day sample. There are not many more small cracks than the 15 day sample, but both images contain at least one significant crack, which is probably sample to sample variation rather than due to prolonged exposure to the oxidising medium. The sample in Figure 4.12 also contains several SPPs (shown by the MLLS fit in Figure 4.14), which I will discuss further in section 4.2.4.

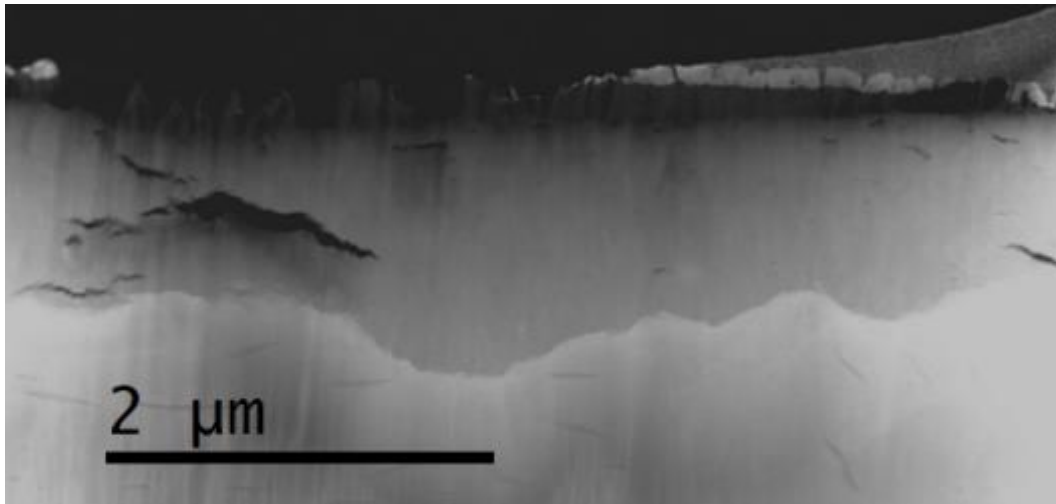


Figure 4.12 – Dark field image of oxide on sample exposed to high pH water at 350°C for 27 days (average oxide thickness = 1.15μm).

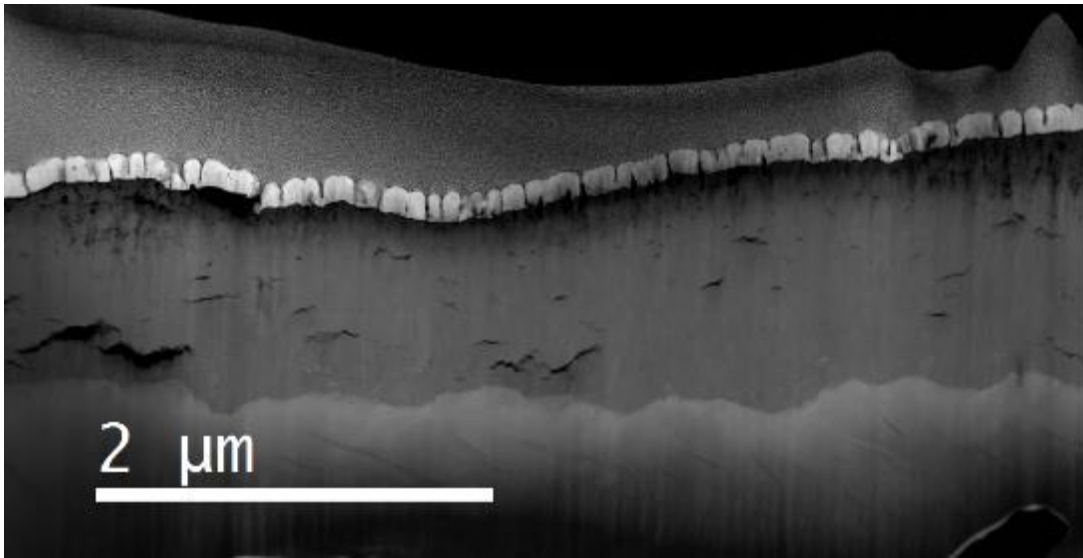


Figure 4.13 – Dark field image of oxide on sample exposed to high pH water at 350°C for 27 days (average oxide thickness = 1.15μm).

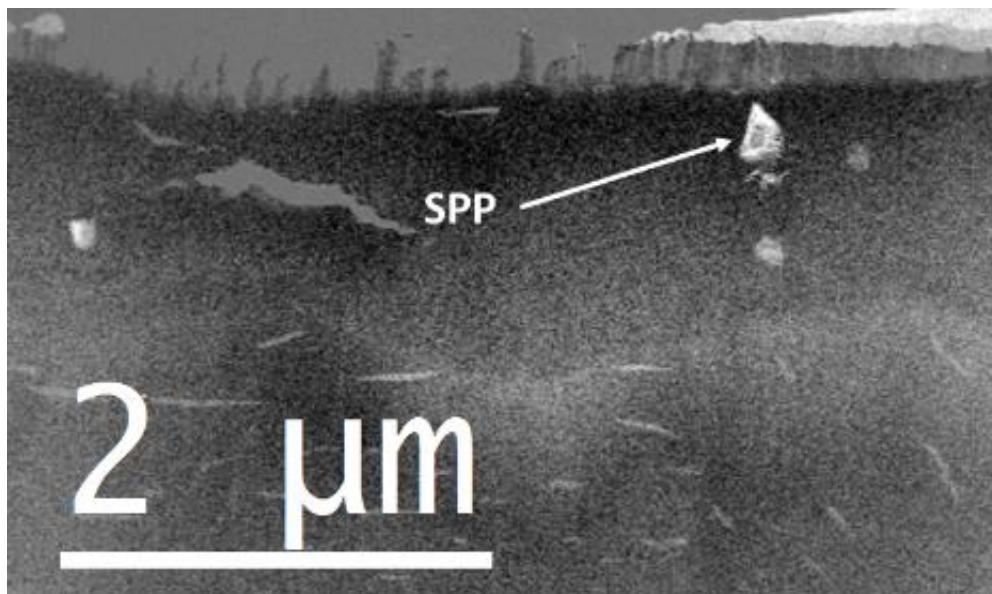


Figure 4.14 – MLLS fit for SPPs in oxide from Figure 4.12. (The MLLS fit to the SPPs also picks out some of the hydrides in the metal).

Figures 4.15 and 4.16 show the OSZ and ZrO regions respectively for the sample shown in Figure 4.13. These show that the OSZ in this sample is thinner than in the 15 day sample. The ZrO is more continuous in places, and retains the saw-tooth shape throughout, although there are a few indistinct regions. Again this is likely to be sample to sample variation.

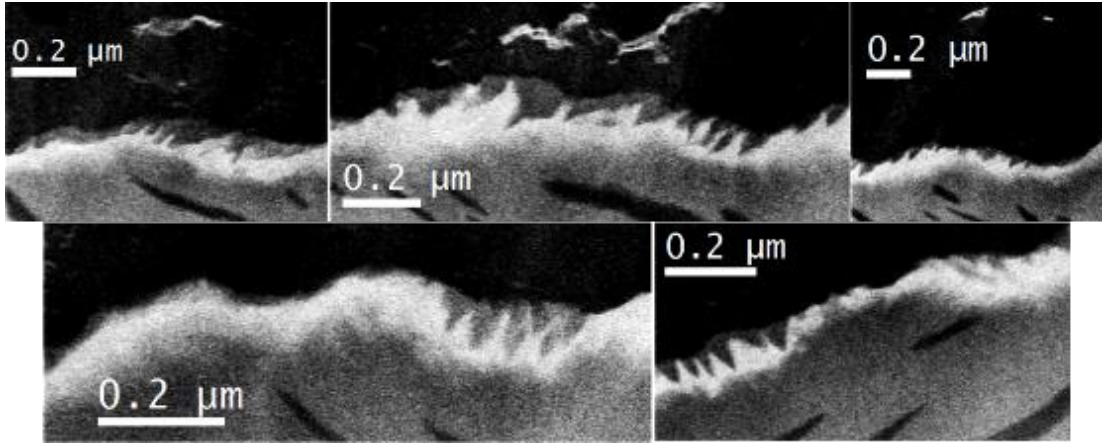


Figure 4.15 – MLLS fits for OSZ across the OM interface for the sample shown in Figure 4.13.

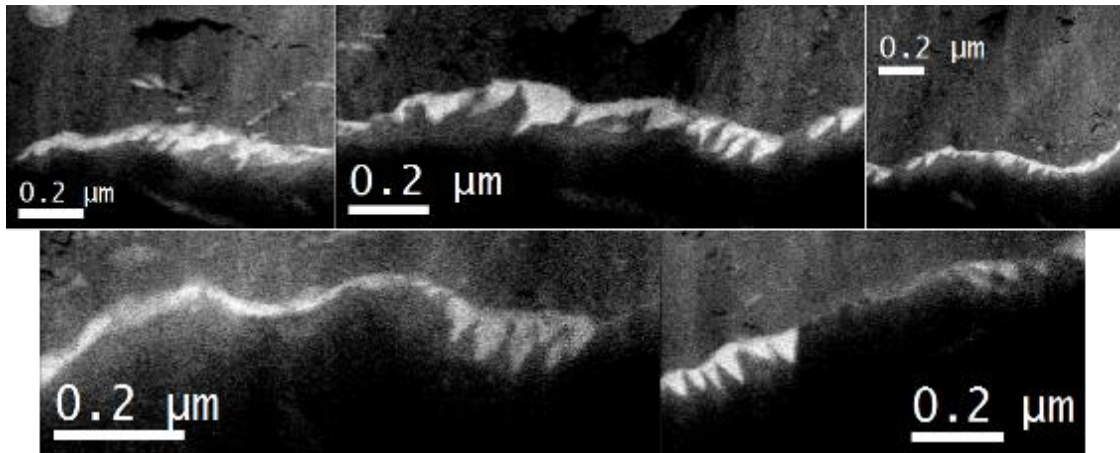


Figure 4.16 – MLLS fits for ZrO across the OM interface for the sample shown in Figure 4.13.

Figure 4.17 shows a DF image of a 62 day sample (average oxide thickness = $1.47 \mu\text{m}$), and Figures 4.18 & 4.19 show the OSZ and ZrO fits from the highlighted region, taken with 0.25 eV/channel dispersion. This sample shows a few large cracks near the oxide and some smaller ones at various depths in the oxide. From the MLLS plots it can be seen that the OSZ and ZrO layers are thicker beneath the cracks, which have previously been shown to form above delays in the OM interface^{15,16}. The ZrO is much less continuous in this sample, but still contains the saw-tooth shape seen in other samples. There is also another large block of ZrO, and in this case it is separated from the rest of the ZrO + OSZ region.

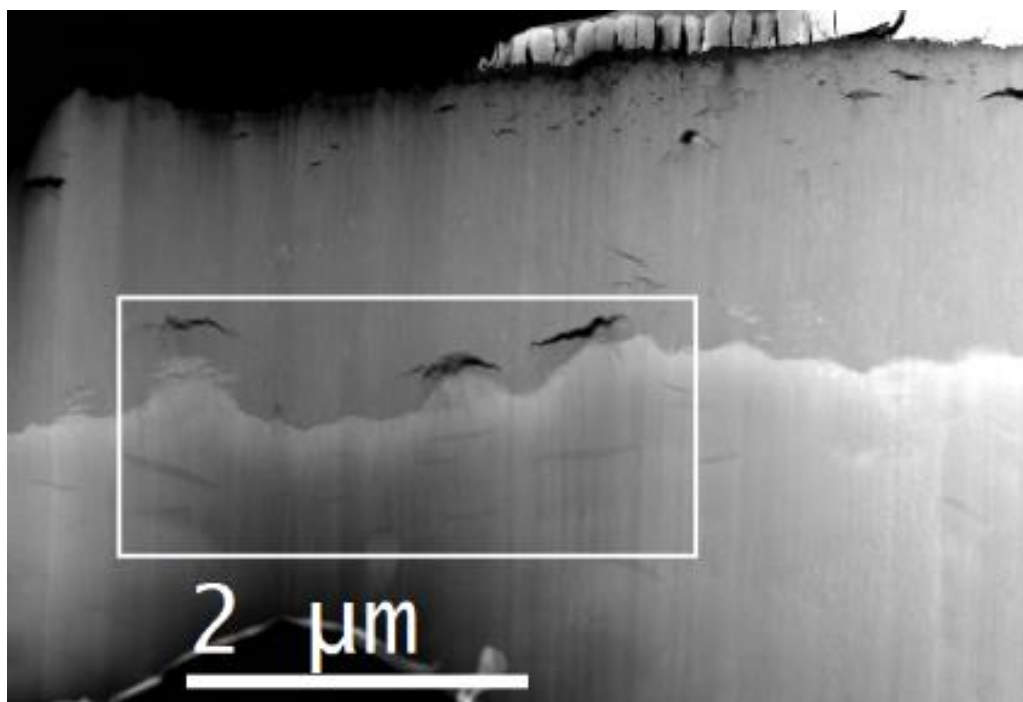


Figure 4.17 – Dark field image of oxide on sample exposed to high pH water at 350°C for 62 days (average oxide thickness = 1.47 μm). The white rectangle shows the area analysed by low-loss EELS.

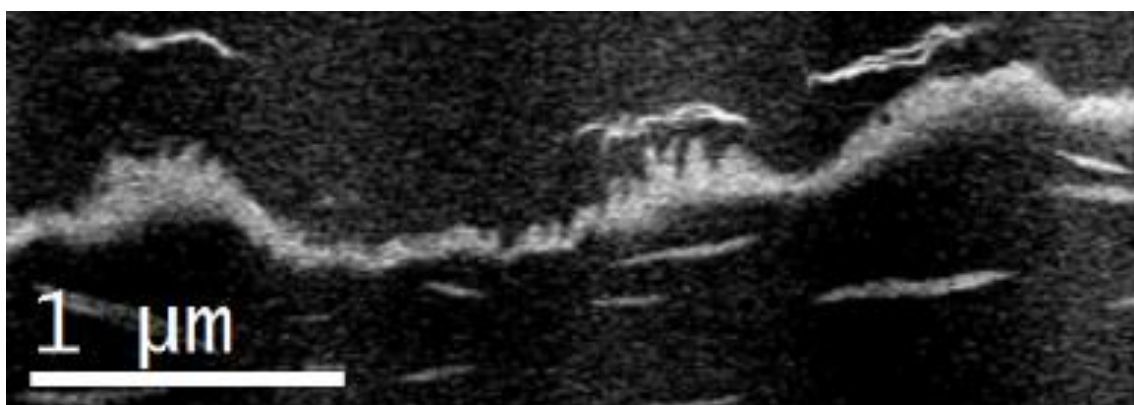


Figure 4.18 – OSZ fit of the highlighted region in Figure 4.17. The spear like objects in the lower half are hydrides in the metal.

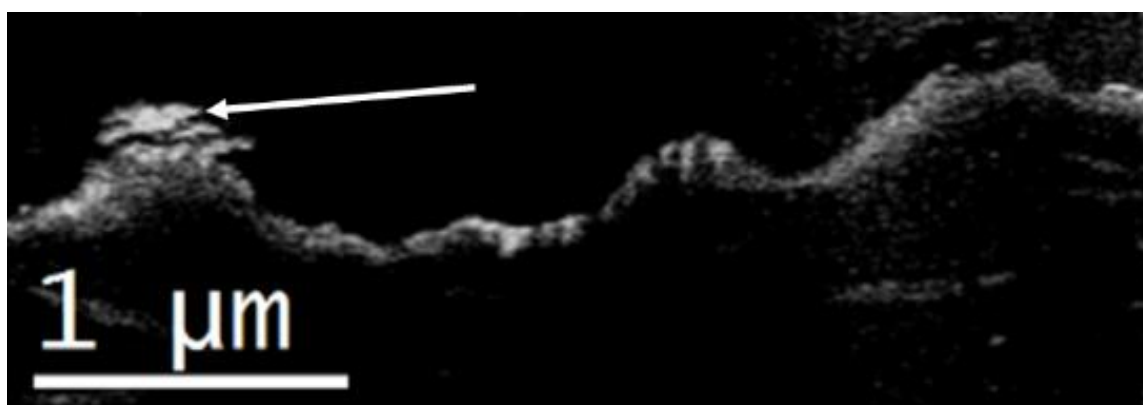


Figure 4.19 – ZrO fit of the highlighted region in Figure 4.17. The white arrow indicates a region of ZrO separated from the rest of the ZrO + OSZ region.

Figures 4.20 & 4.21 show DF images from two 123 day samples (average oxide thickness = 2.06 μm). In Figure 4.20 there are two large cracks near the OM interface, and the MLLS plots for the OSZ (Figure 4.22) shows that it is thicker underneath the crack. It appears that in regions where the rate of formation of zirconia is lower, a higher amount of OSZ + ZrO forms. The MLLS fit for the ZrO of region (a) in Figure 4.22 is shown in Figure 4.23, and it can be seen that the ZrO is not a continuous layer in this region. For region (b) of Figure 4.22 the MLLS could not fit a ZrO peak to the selected area, but by examining the Zr metal fit (Figure 4.24a) and reversing the grey-scale of the image (Figure 4.24b) the ZrO can be seen. In the area underneath the crack there is little ZrO but away from the crack the ZrO is thicker.

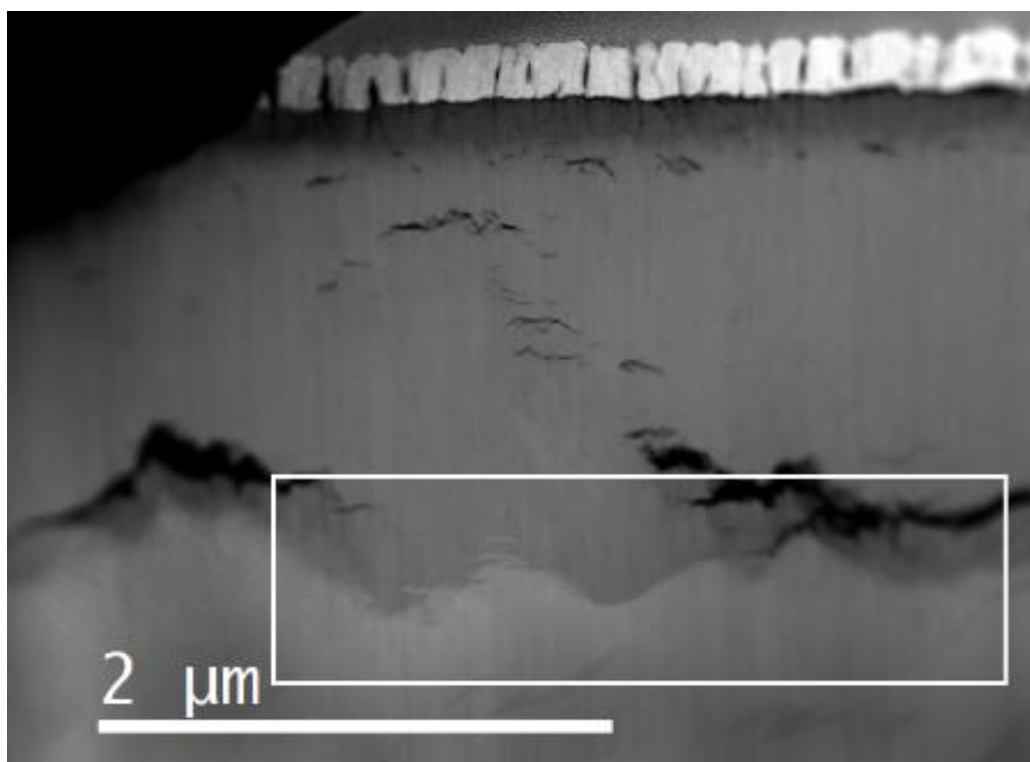


Figure 4.20 – OM interface of 123 day sample (average oxide thickness = 2.08 μm). The blurry region to the left is due to the sample being slightly bent.

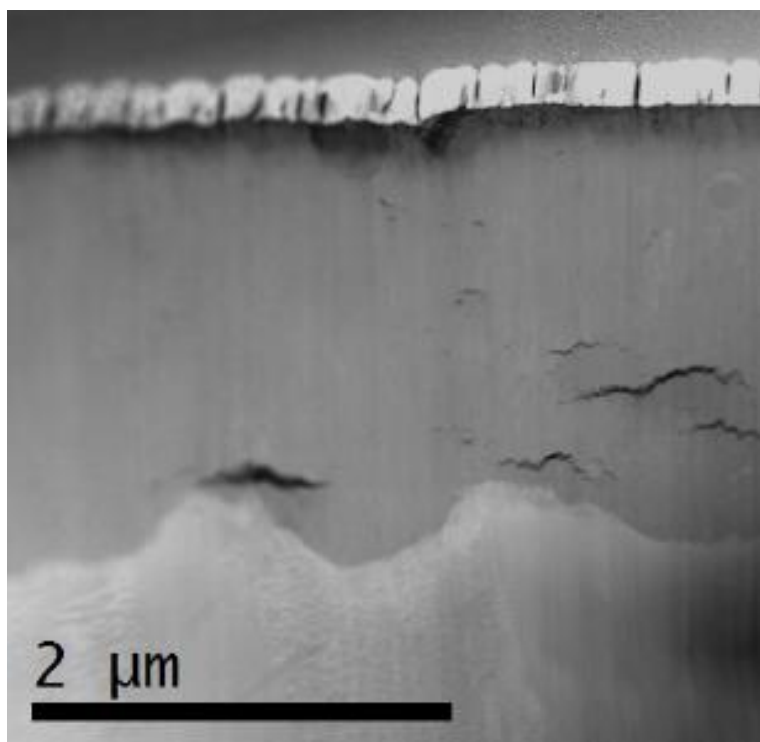


Figure 4.21 – OM interface of 123 day oxide (average oxide thickness = $2.08\ \mu\text{m}$).

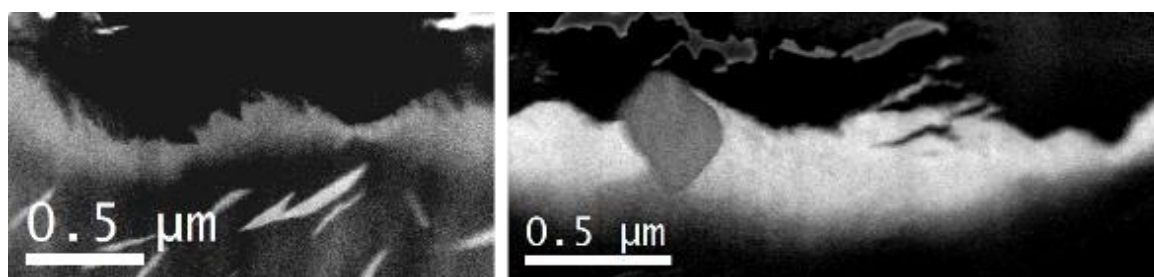


Figure 4.22 – MLLS fit for OSZ of the highlighted region in Figure 4.20. The left-hand image is the area between the cracks, and the right-hand image is the area underneath the right-hand crack.

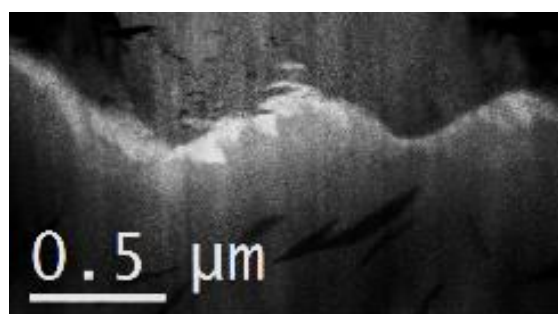


Figure 4.23 – ZrO fit in the same region as the left-hand image of Figure 4.22.

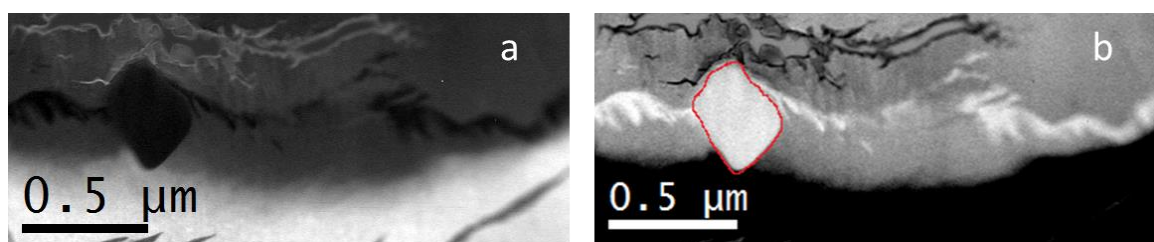


Figure 4.24 – MLLS fit for Zr (a) in the same region as the right-hand image in Figure 4.22. After reversing the grey-scale the ZrO can be more easily seen (b). The SPP on the OM interface is highlighted in red.

The sample in Figure 4.21 shows two cracks near the OM interface, although they are much smaller than in Figure 4.20 but still show a delay in the oxide front. The MLLS fits of the OSZ (Figure 4.25) show again that under the cracks the OSZ is thicker, and Figure 4.26 shows the ZrO is far more continuous in this sample than Figure 4.20.

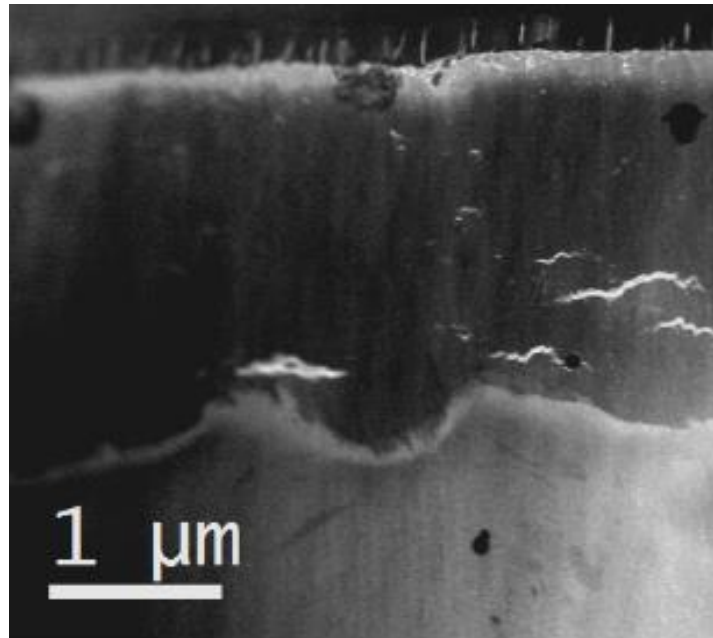


Figure 4.25 – OSZ fit for Figure 4.21. There is a match for a region where the sample meets the gold layer, which is an artefact.

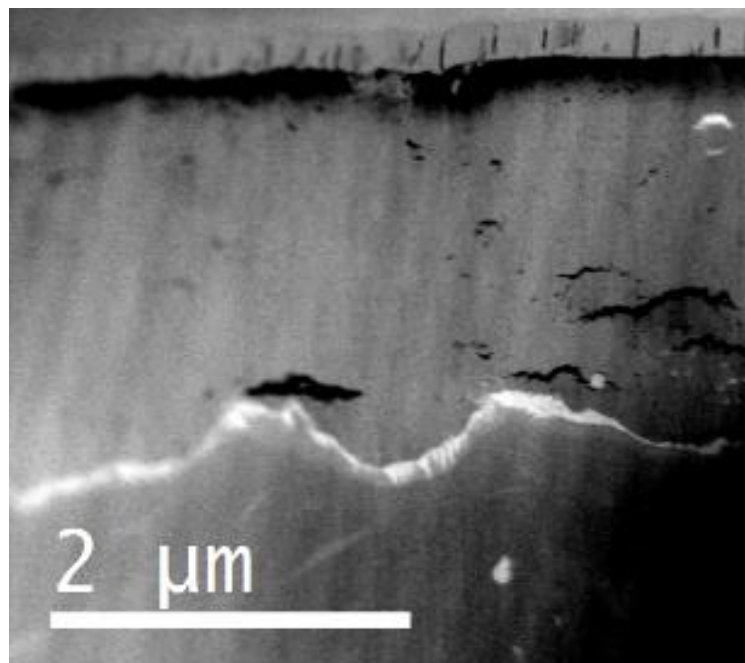


Figure 4.26 – ZrO fit for Figure 4.21. The ZrO layer is continuous in this region.

The rest of the samples are in the post-transition region. The 148 day sample (average oxide thickness = 2.92 μm) was extracted shortly after transition. Regions of oxide are shown in Figures 4.27 & 4.28.

There are extensive cracks throughout both of these samples. There was little to no ZrO present at this stage of oxidation, as the MLLS show in Figures 4.29 – 4.31, and no ZrO was detected in the sample shown in Figure 4.28 (and for the other 148 day samples I examined).

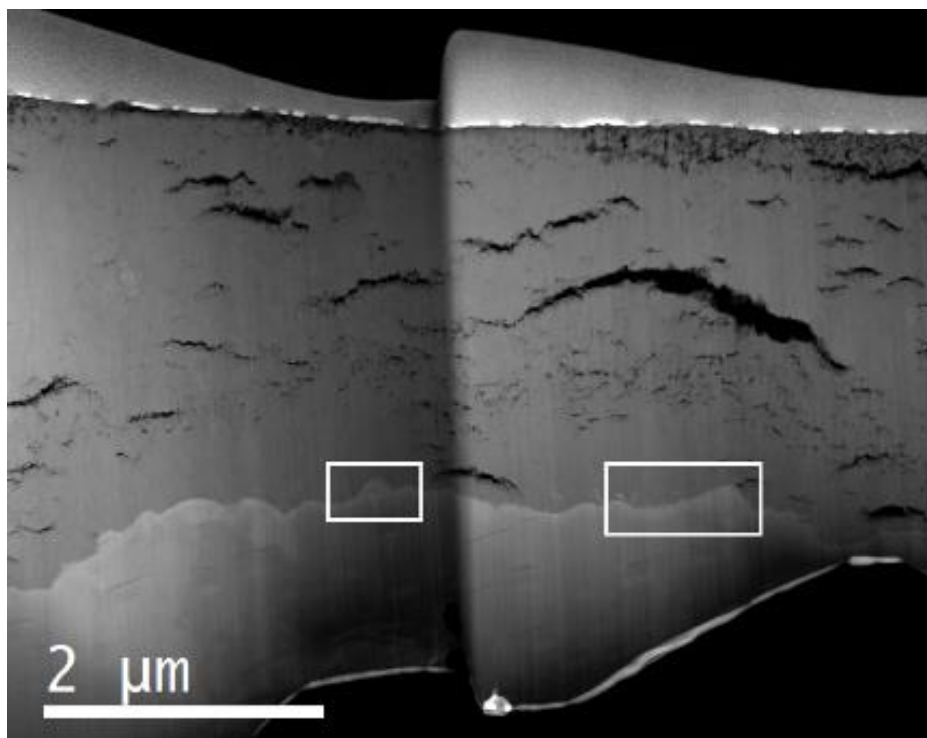


Figure 4.27 – Dark field image of post-transition oxide on sample exposed to high pH water at 350°C for 148 days (average oxide thickness = 2.92 μm). The white boxes show where MLLS was carried out.

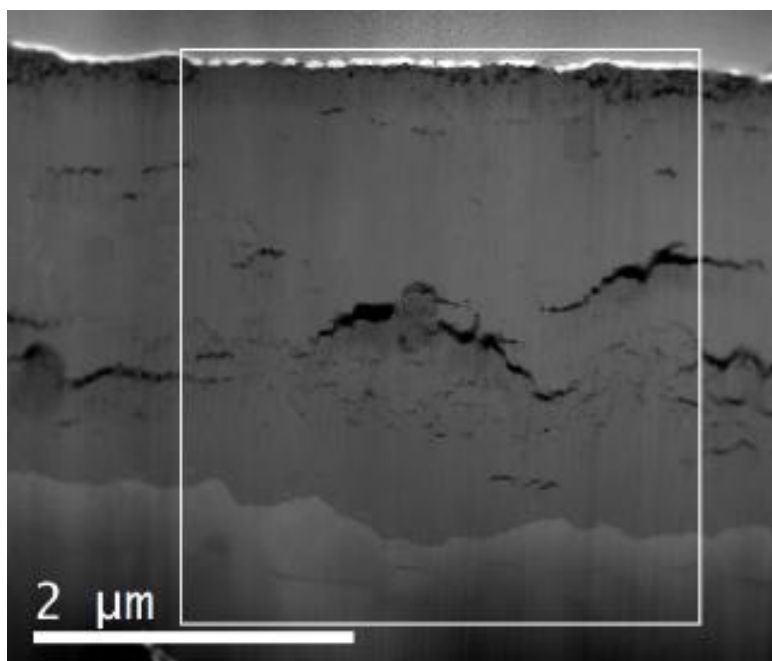


Figure 4.28 – Another part of 148 day oxide, with the white box showing the fitted region.

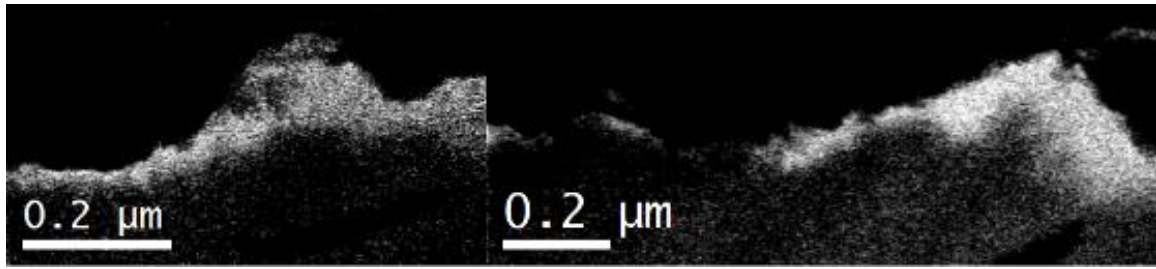


Figure 4.29 – OSZ fit for areas shown in Figure 4.27.

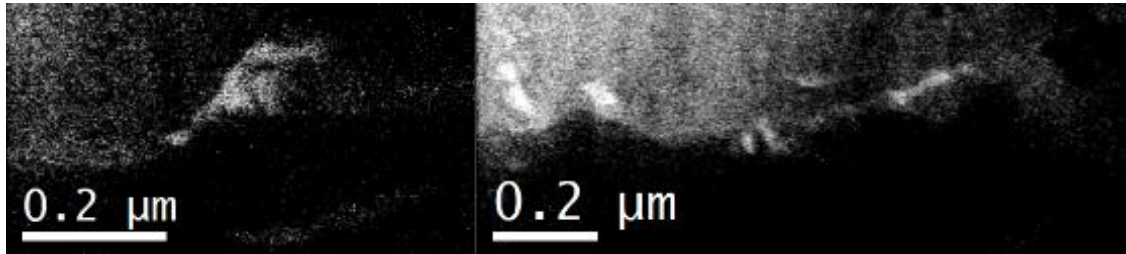


Figure 4.30 – ZrO fit for areas shown in Figure 4.27, showing little ZrO in these regions.

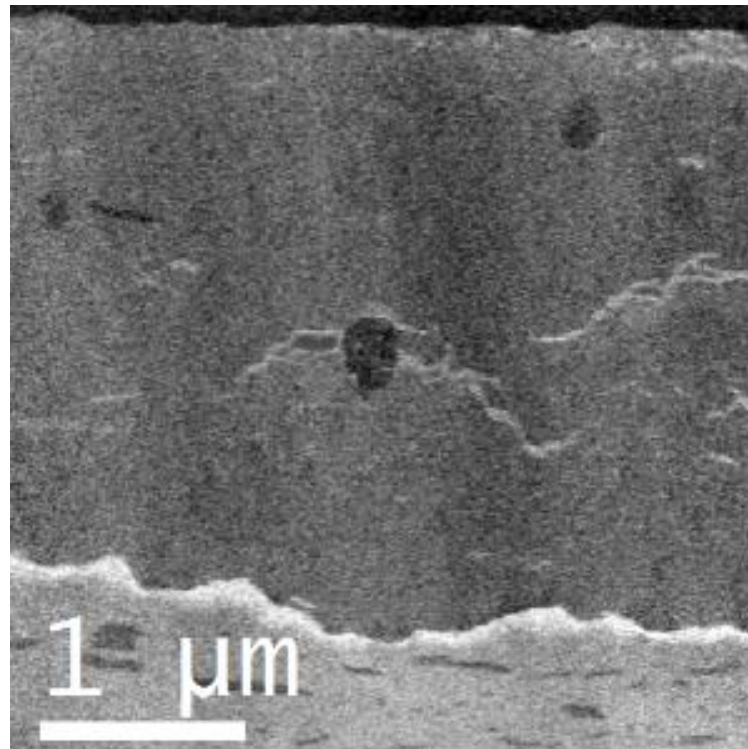


Figure 4.31 – OSZ fit for Figure 4.28.

The 211 day post-transition sample (average oxide thickness = $3.88\ \mu\text{m}$) was extracted during a period of slow oxide growth in the second half of the second cycle of oxidation. Figures 4.32 & 4.33 show there were extensive cracks throughout the samples. The layer of cracks in the middle of the oxide formed in the first cycle of oxidation. The MLLS fits (Figure 4.34 – 4.37) show that both the OSZ

and ZrO have returned to the pre-transition thickness and the ZrO has regions which are continuous. There are more examples of thicker regions of OSZ beneath cracks.

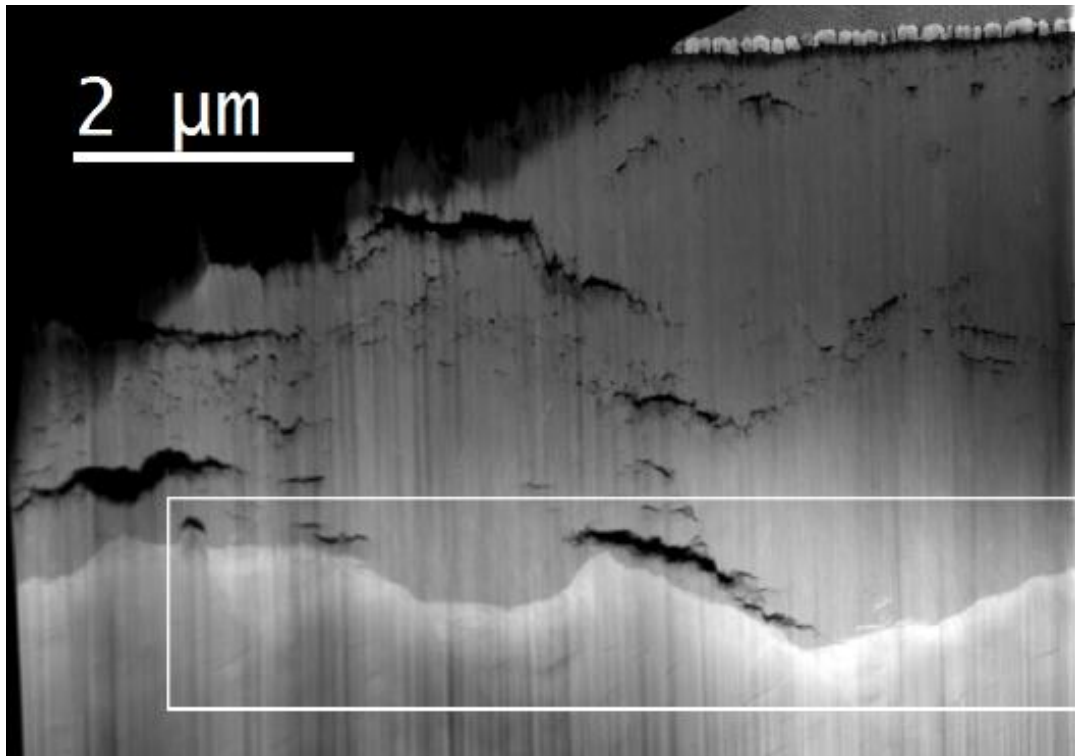


Figure 4.32 – 211 day oxide. The white area is where EELS was carried out. The black vertical stripes are artefacts from sample preparation.

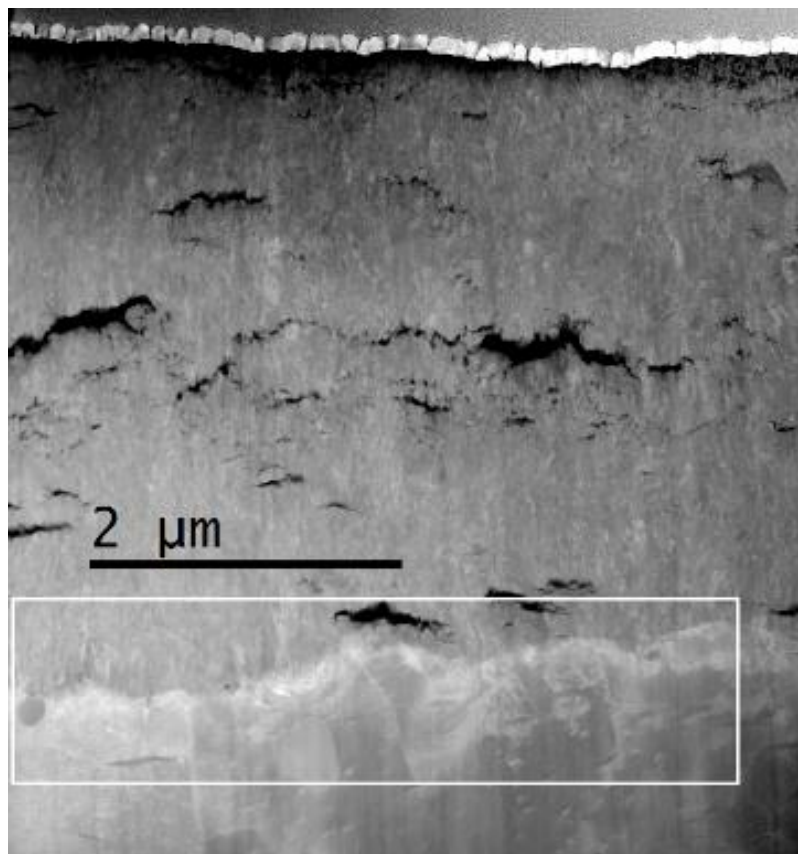


Figure 4.33 – 211 day oxide. The white area is where EELS was carried out.

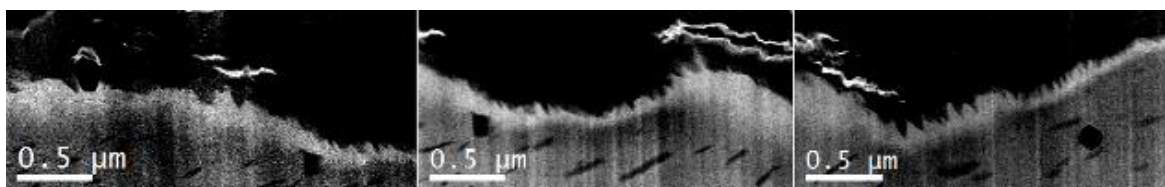


Figure 4.34 – OSZ fit for Figure 4.32.

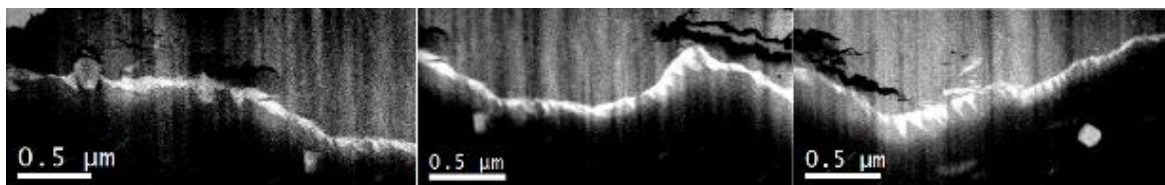


Figure 4.35 – ZrO fit for Figure 4.32, showing that a continuous layer has been re-formed.

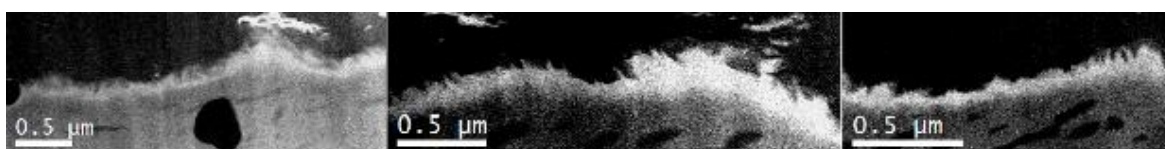


Figure 4.36 – OSZ fit for Figure 4.33.



Figure 4.37 – ZrO fit for Figure 4.33, again showing a continuous layer in places.

Figures 4.38 & 4.39 show regions of the oxide on the 243 day sample (average oxide thickness = $4.37\mu\text{m}$). Both figures show regions of oxide which are much thinner than given by the weight gain. The sample in Figure 4.38 shows a relatively small number of cracks, with the largest in a layer associated with the pre-transition oxide. None of the cracks are particularly large. The sample in Figure 4.39 shows more cracks, which are longer and show some connectivity. A second layer of large cracks may be forming in this area of the oxide.

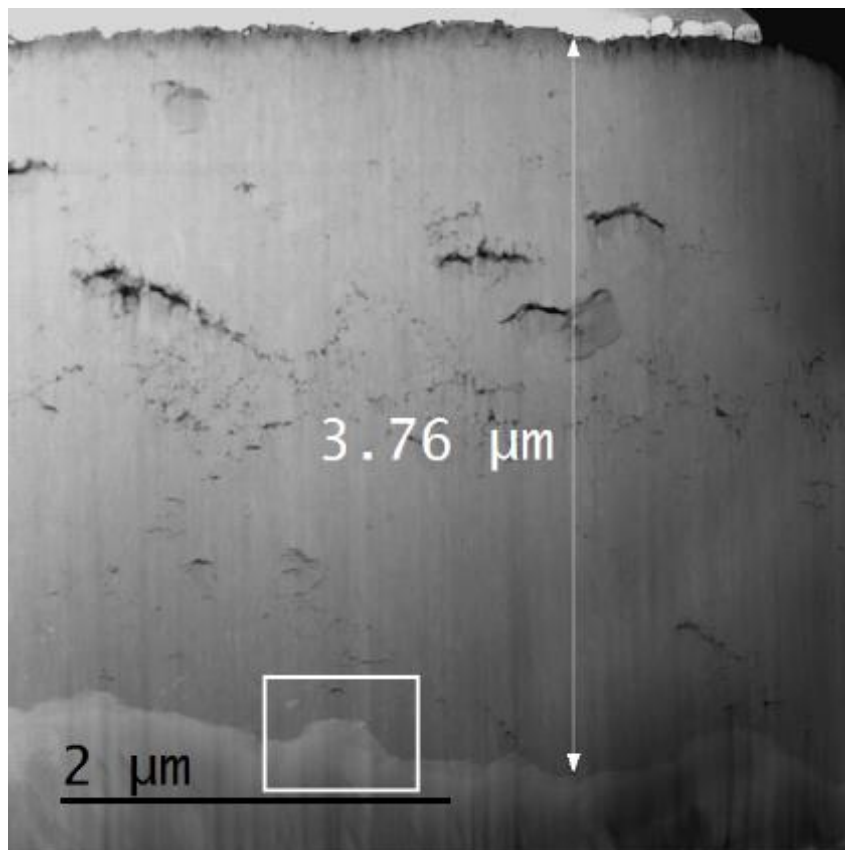


Figure 4.38 – Oxide on sample exposed to high pH water for 243 days, in area much thinner than the weight gain indicated. The white box shows an area analysed with EELS.

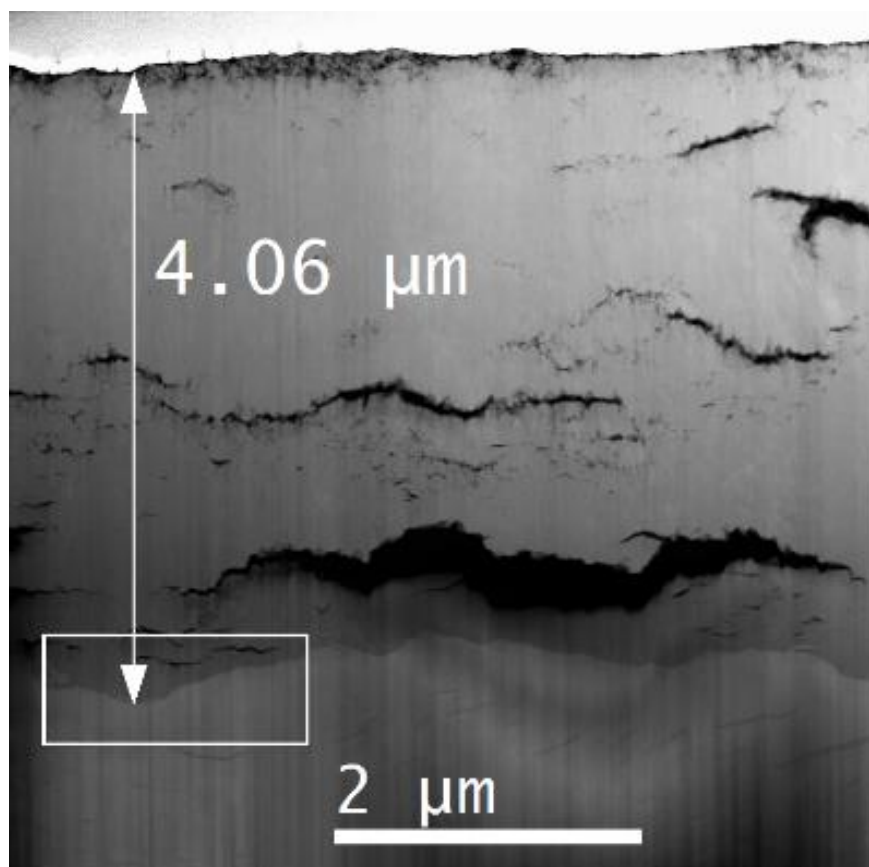


Figure 4.39 – Oxide on sample exposed to high pH water for 243 days in area with thicker oxide than in Figure 4.38 but still much thinner than average. The large crack was made slightly wider (up the page) by the milling process. EELS was carried out in the white box.

During the MLLS fitting an interesting phenomenon was encountered for these samples. Figures 4.40 – 4.43 show several MLLS fits of the same area, each with a different selection of spectra fitted to it. Figure 4.40 shows the results with all the components present; Zr metal, Zr hydrides, OSZ, ZrO and ZrO₂. The OSZ region is not well defined when it is characterised by the OSZ spectrum alone. In this area the shape of the OSZ region is better understood by comparing the Zr and ZrO maps. In the Zr map the darkest region (between the metal and oxide) shows the outline of the OSZ + ZrO region, while the brightest part of the ZrO map shows the portion of the combined region which is not OSZ. Taking into account the shape of the ZrO from its respective map then we can imagine what the OSZ layer looks like. The region of intermediate brightness in the ZrO map also corresponds to the OSZ. If the EELS spectra are deconvoluted without the OSZ component (Figure 4.39), the OSZ appears as the region of intermediate contrast in the Zr, ZrO and hydride maps.

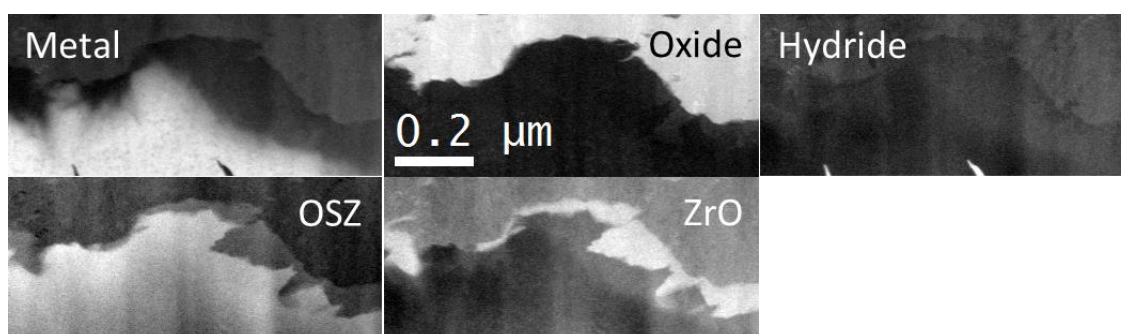


Figure 4.40 – MLLS fit of area shown in Figure 4.38. From top-left clockwise: Metal, ZrO₂, hydride, ZrO, OSZ.

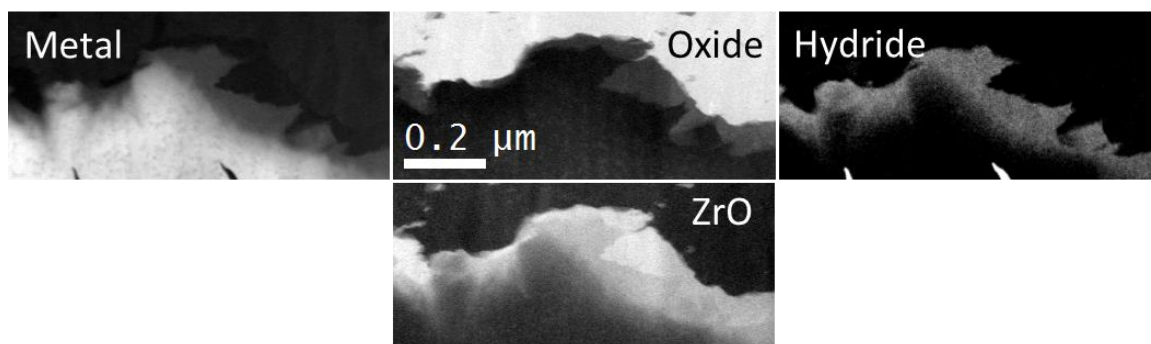


Figure 4.41 – MLLS fit for the same area without using the OSZ spectrum.

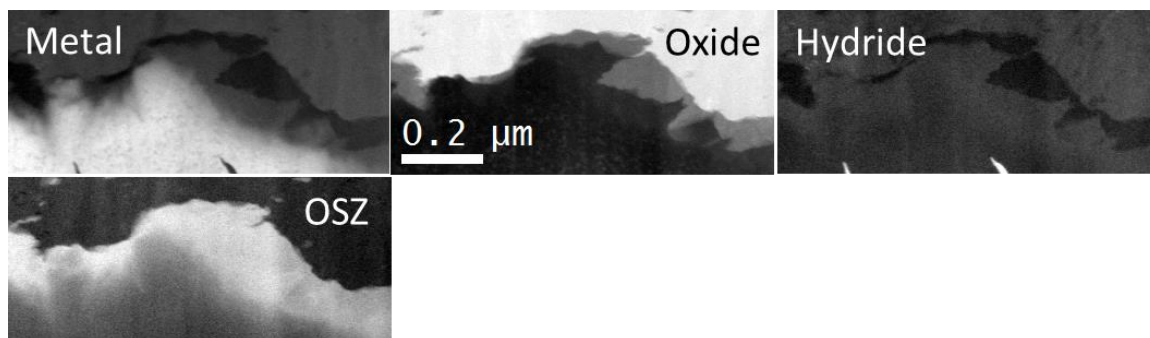


Figure 4.42 – MLLS fit for the same area without using the ZrO spectrum.

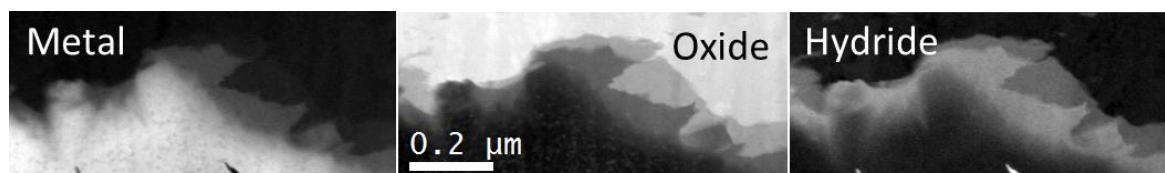


Figure 4.43 – MLLS fit for the same area without using either the OSZ or the ZrO spectra.

To calculate the thickness of the OSZ and ZrO regions I used Avizo to draw around the median of the OSZ/ZrO fit (see Figure 4.44) and extract that area shown in Figure 4.45. Using Gatan DM I drew a profile box around this area (Figure 4.46) and used this to calculate the mean and standard deviation of the thickness of the OSZ and ZrO layers.

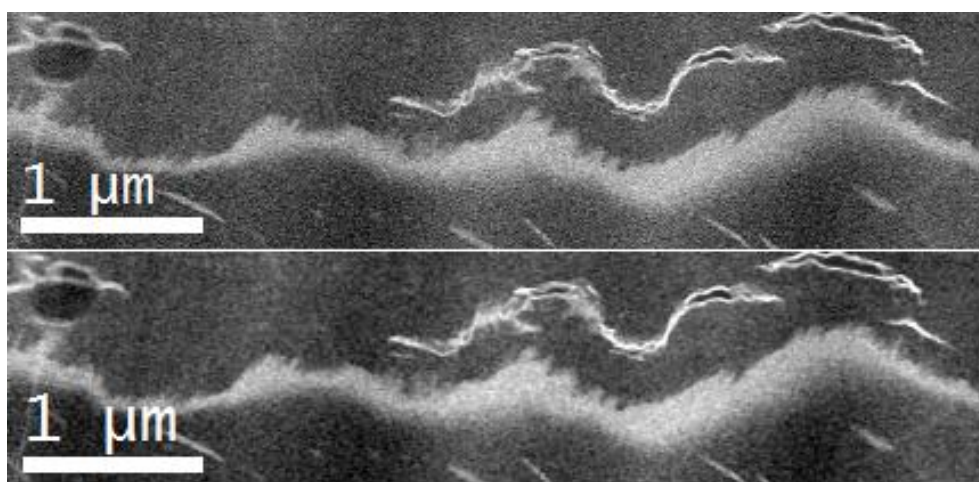


Figure 4.44 – Original MLLS image (top) and after a median filter (bottom). This is the MLLS fit of the EELS SI from Figure 4.3.



Figure 4.45 – Extracted region from Figure 4.44 used to compute the thickness of the OSZ layer.

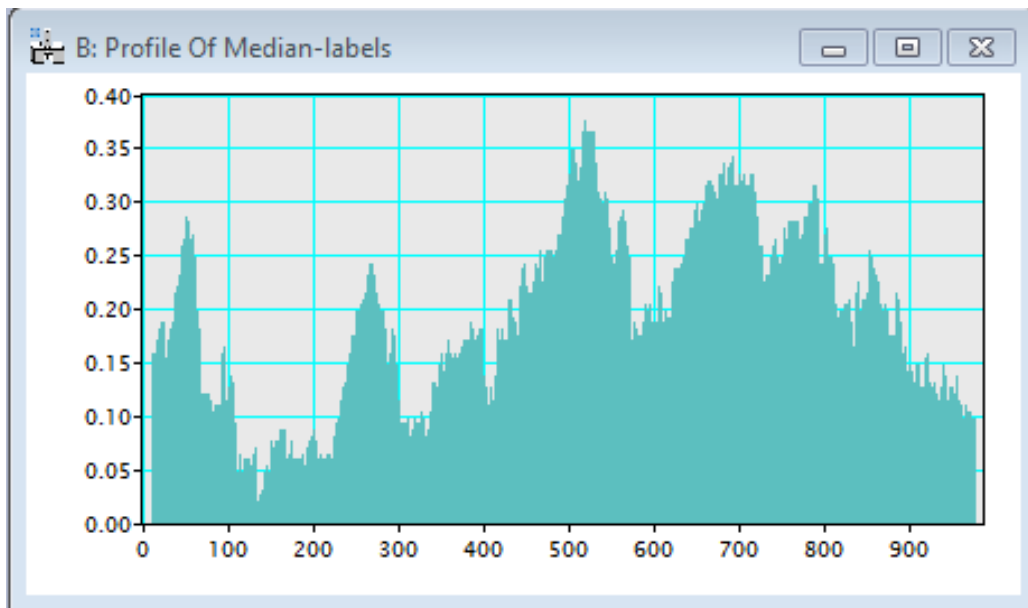


Figure 4.46 – Profile drawn around the extracted region in Figure 4.45.

Figure 4.47 shows a graph with the calculated thicknesses of the OSZ and ZrO regions for the high pH samples, as a function of the oxide thickness. Both layers increase in thickness as the oxide grows, up to around 90 days where it stays constant, within error. After transition, where the oxidation rate is high, the OSZ and ZrO are consumed by the rapidly oxidising zirconium and this leads to a small layer of OSZ and virtually no ZrO in the 148 day sample (2.93 μm oxide). The graph shows that for the first micron of oxide growth in both cycles no ZrO was observed. After 148 days both regions build up again. In the 243 day sample (4.37 μm oxide) the regions are thinner regions than in the 211 day sample, which may be due to the 243 day samples being in the early stages of a second transition. There is a slight misrepresentation with Figure 4.47, in that the ZrO layer is generally not continuous. For that reason it is better to look at the OSZ and ZrO as single layer, which I will refer to as the suboxide layer from now on. A plot of the suboxide layer as a function of oxide thickness is shown in Figure 4.48.

The next section will examine the effect of pH on the growth of the suboxide layer.

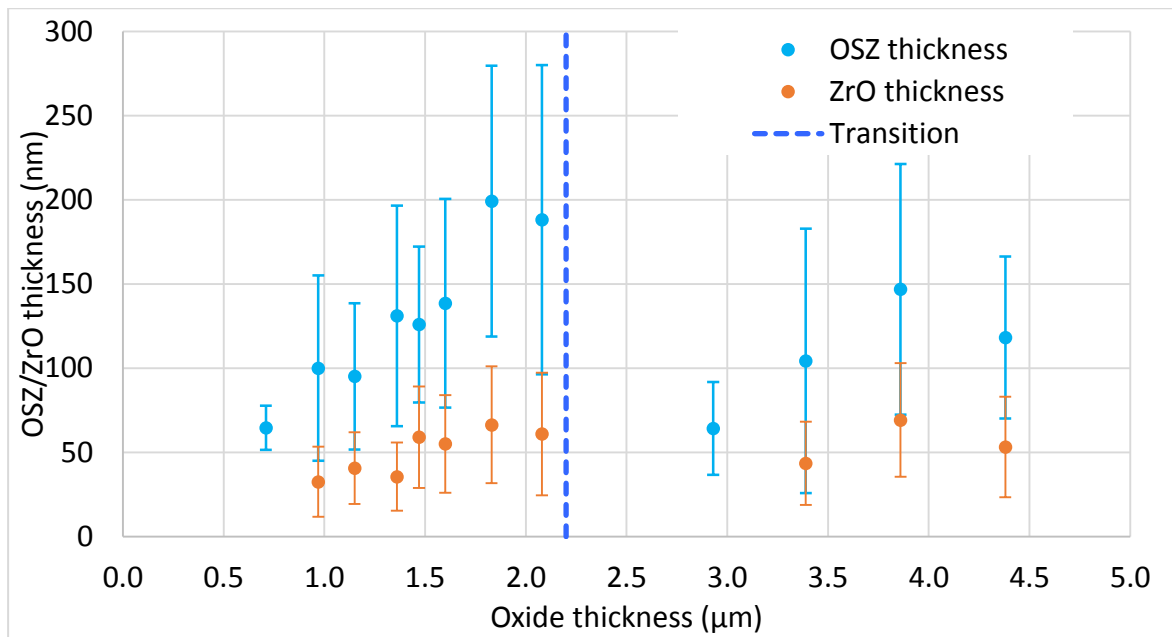


Figure 4.47 – Variation in the thicknesses of the OSZ + ZrO regions during oxidation in high pH water. The error bars are the standard deviation of the data.

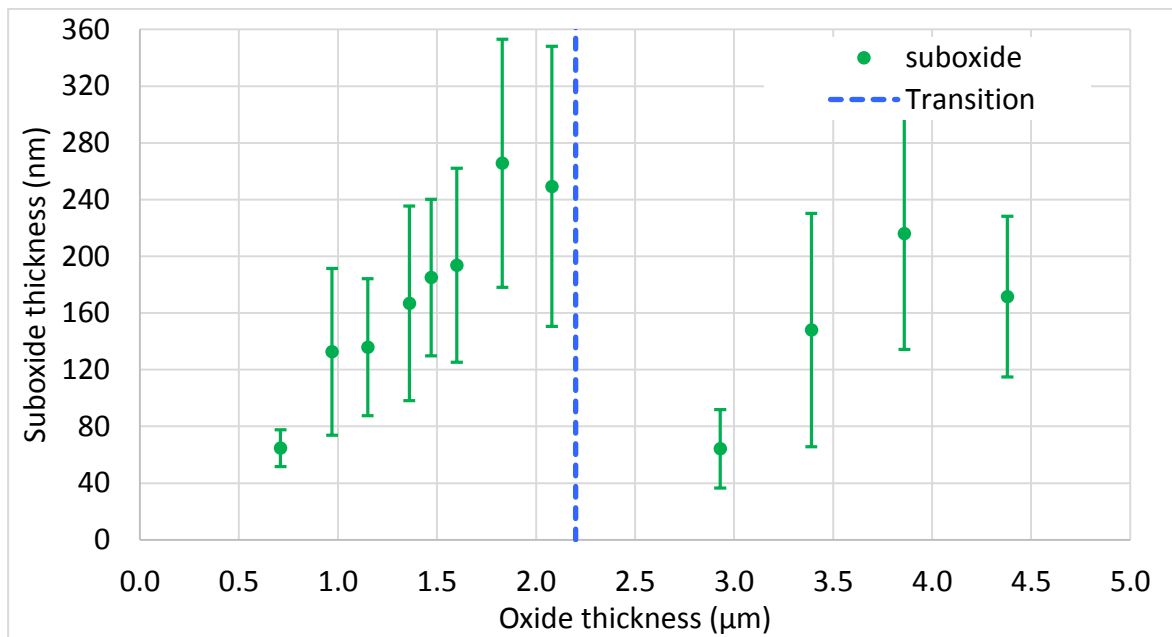


Figure 4.48 – Total suboxide thickness vs oxide thickness.

4.2.3 – OSZ and pH

Figures 4.49 & 4.50 show samples oxidised for 45 days in pure water (average oxide thickness = 1.65 μm and a high pH (average oxide thickness = 1.34 μm) respectively. The portion of oxide on the pure water sample is thinner than average, while the portion of high pH oxide is roughly as thick as quoted. Both regions show a few large cracks, with several smaller cracks throughout the oxide. While both images show regions of oxide with varying thickness, the image of the high pH sample shows much more variation. The area of oxide shown varies from just over 1 μm thick up to 1.8 μm at the thickest.

The pure water sample varies from 1-1.5 μm by comparison. This is not necessarily true for the entire samples, and may reflect the effects of the orientations of the underlying metal grains.

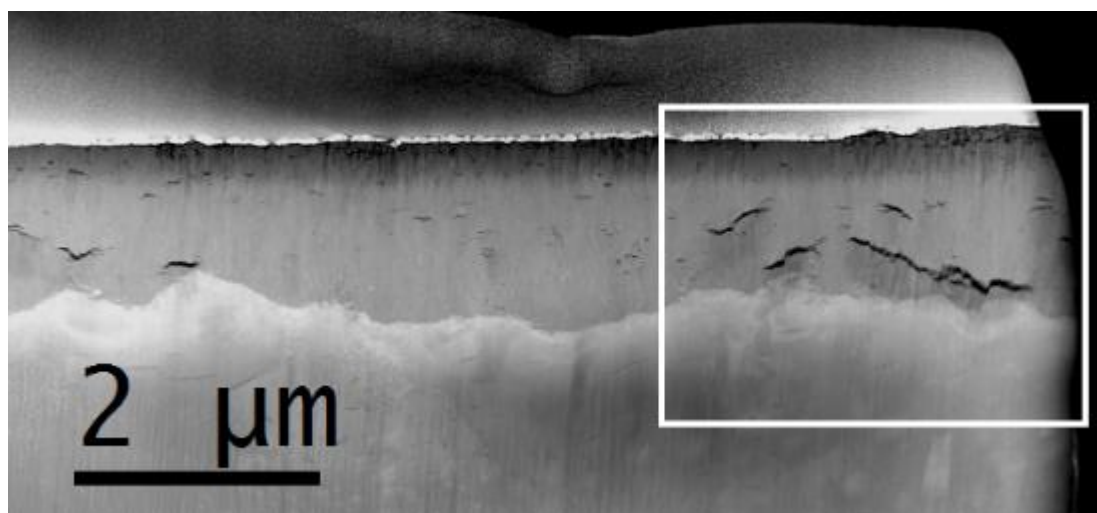


Figure 4.49 – 45 day pure water oxide. The white box is the area analysed with MLLS. (Courtesy of Thomas Aarholt¹⁷)

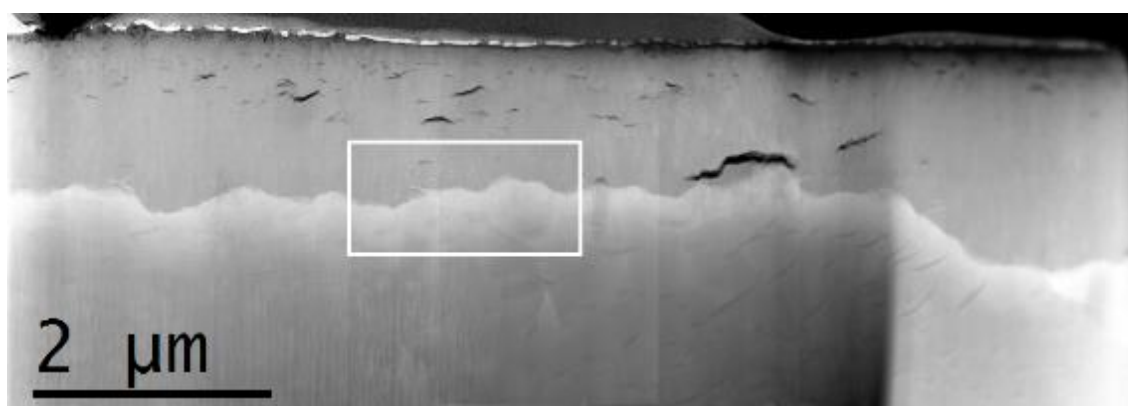


Figure 4.50 – 45 day oxide for a high pH sample. The white box shows the MLLS fit region.

The MLLS fits of the white regions in Figures 4.49 & 4.50 are shown in Figures 4.51 & 4.52 respectively. The dispersion on the acquired spectrum in Figure 4.52 was 0.25 eV/channel, which is why the image is of a lower quality. Figure 4.4 shows that the OSZ and hydride plasmon peaks are similar, and in this region they matched up to a greater extent than normal, which is why the hydrides appear in this image.

Figures 4.51 & 4.52 show that both samples have a fairly continuous ZrO layer and consistent OSZ layers. The ZrO in both had some atypical features. The ZrO in the pure water sample had a region underneath a crack which does not have the usual saw-tooth shape, but has what look like fingers protruding back into the oxide. The high pH sample has something similar, although it is a much

smaller. For these samples the combined OSZ + ZrO layer was thicker for the pure water sample, but again this is not necessarily true throughout the samples as only small regions have been analysed.

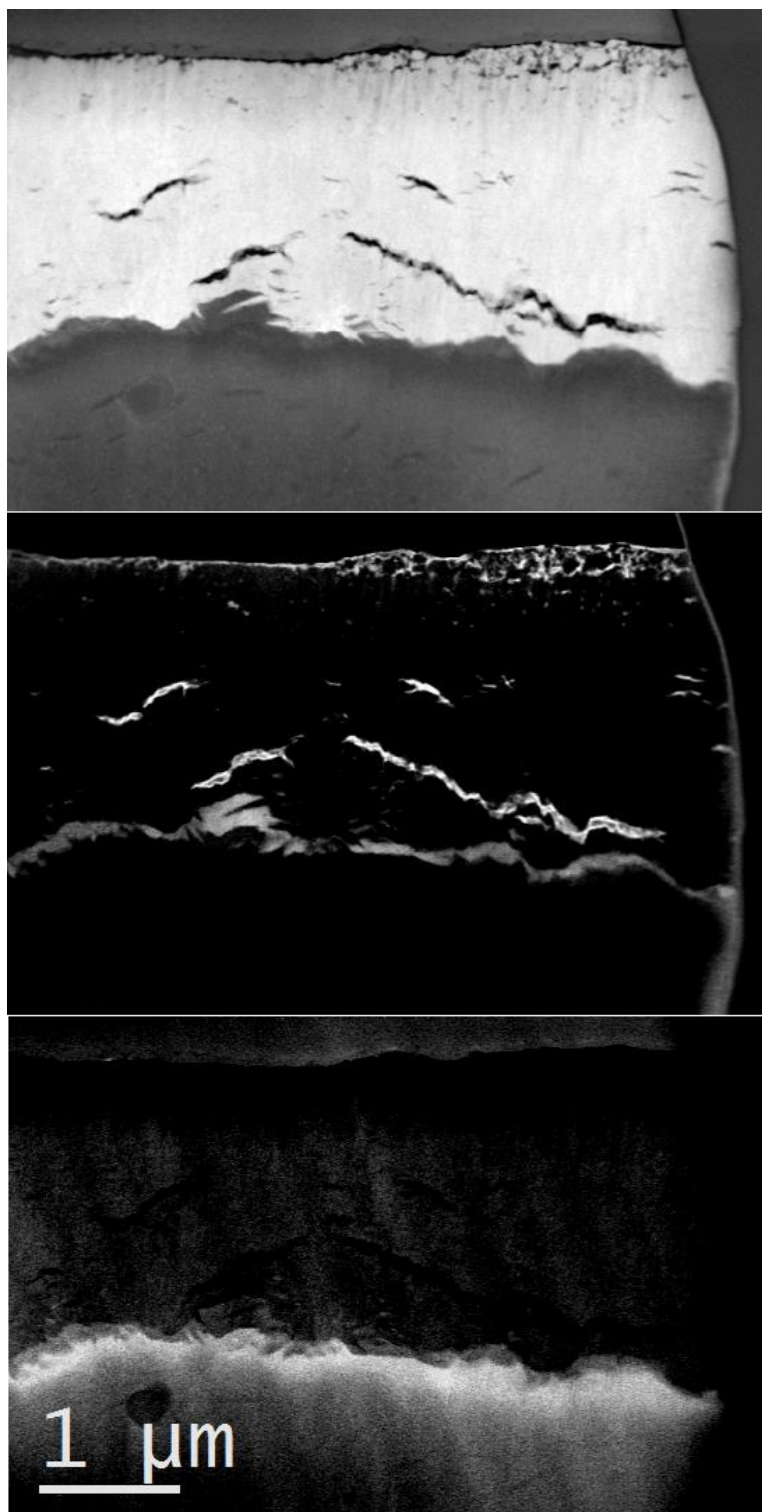


Figure 4.51 – MLLS fit for ZrO₂ (top), ZrO (middle) and OSZ (bottom) of the white box in Figure 4.49 from oxide formed in pure water.

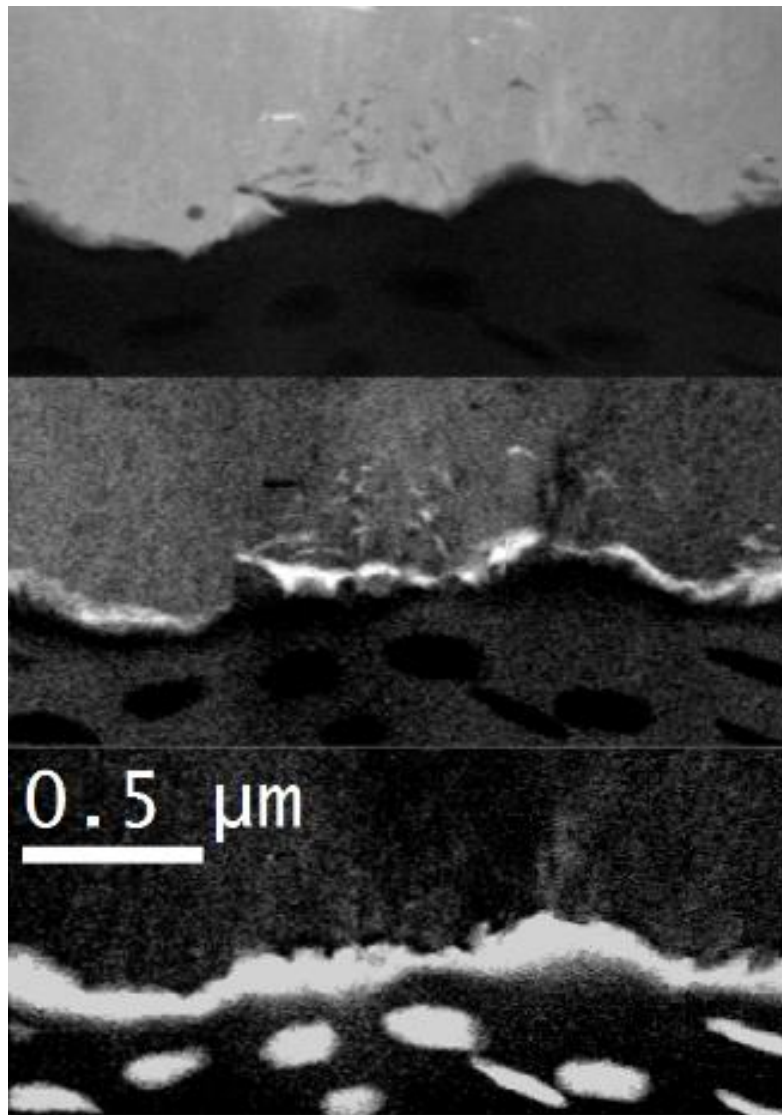


Figure 4.52 – MLLS fit for ZrO_2 (top), ZrO (middle) and OSZ (bottom) of the white box in Figure 4.50 from oxide formed in high pH water.

I will now look at samples oxidised for 90 days in pure water (average oxide thickness = $2.13 \mu\text{m}$) and 91 days in high pH (average oxide thickness = $1.81 \mu\text{m}$). Figure 4.53 shows a sample oxidised for 90 days in pure water. The OSZ and ZrO fits of the regions highlighted in Figure 4.53 are shown in Figures 4.54 & 4.55. This shows the OSZ layer is slightly thinner in the area where the oxide is thicker, and the ZrO thickness is uniform regardless of oxide thickness, with the characteristic saw-tooth shape. Again there are regions of ZrO that are surrounded by oxide, but I think this is result of the projection of the sample.

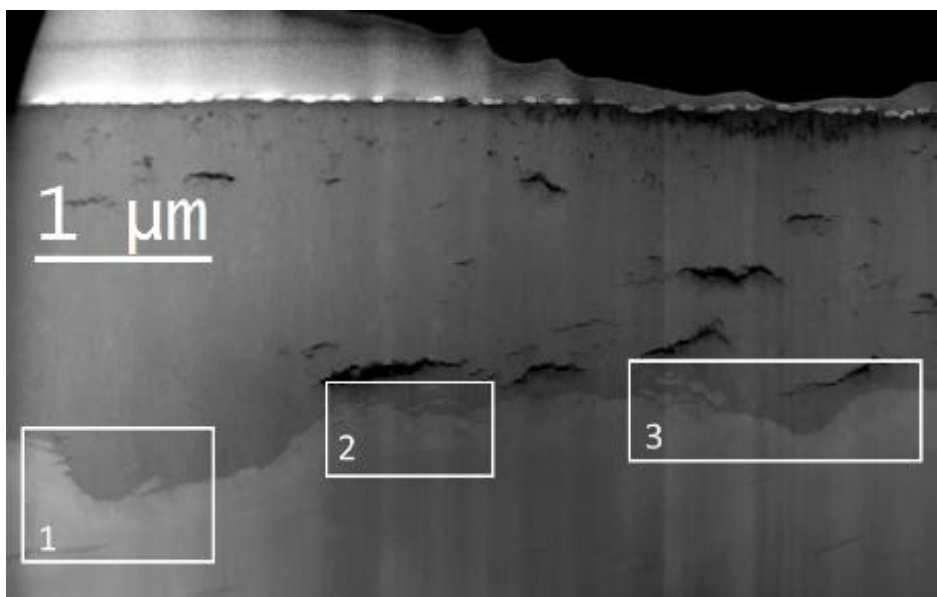


Figure 4.53 – Oxide formed by exposure for 90 days in pure water. The white boxes were examined by EELS, shown in Figures 4.54 & 4.55. The EELS spectrum was acquired at 0.05 eV/channel.

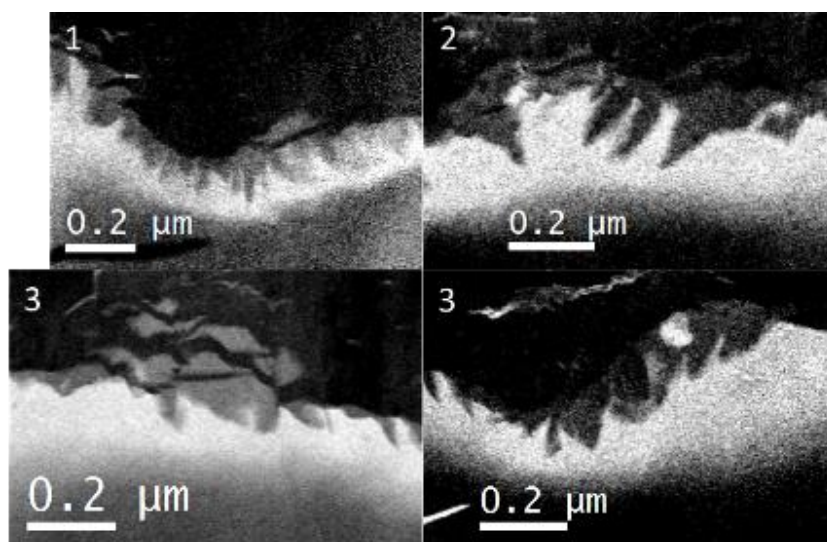


Figure 4.54 – OSZ fits of the numbered regions of Figure 4.53.

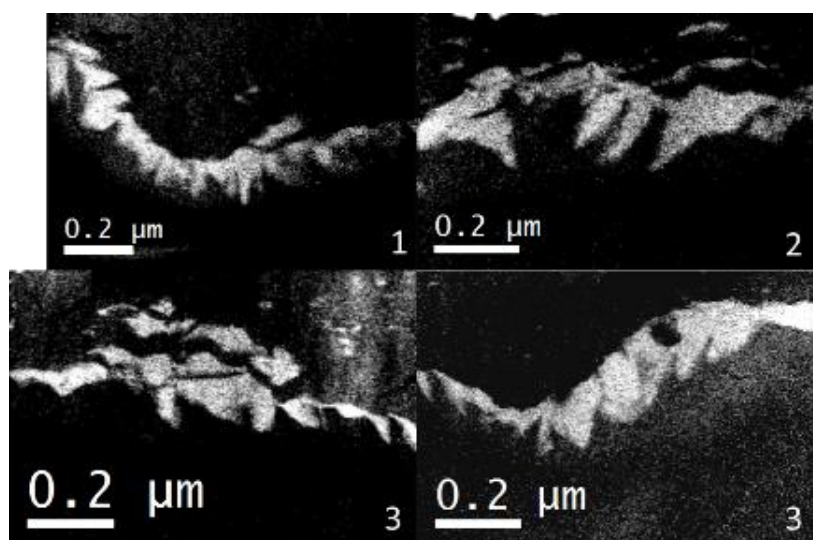


Figure 4.55 – ZrO fits of the numbered regions in Figure 4.53.

Figure 4.56 shows the OM interface for a 91 day oxide from high pH. There are several large cracks in this sample, with one particularly long one near the OM interface, with the OM interface following a similar route to the crack. The oxide in this sample was again slightly thinner than expected from the weight gain measurements, and there was only a match up at the thickest part of the oxide. The OSZ and ZrO fits have been shown previously in Figure 4.5, and are reproduced in Figure 4.57. The ZrO layer is similar to that seen in the pure water sample in that it is continuous, and has the saw-tooth shape in places, but is slightly smoother elsewhere. The OSZ layer varies here depending on the thickness of the oxide layer, it is thicker at delays in the oxidation front and thinner at protuberances.

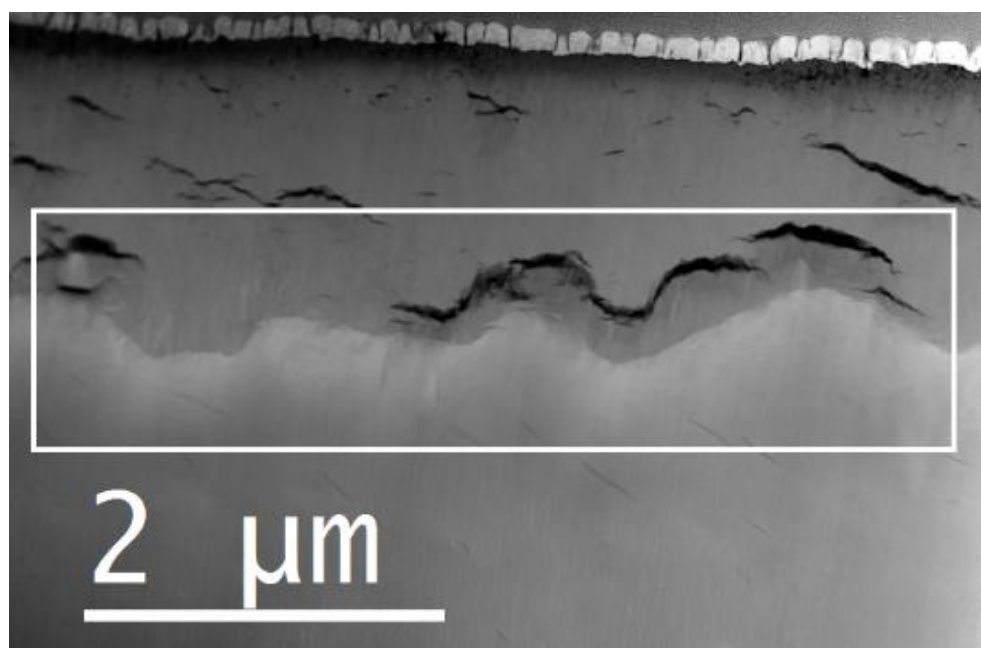


Figure 4.56 – Oxide formed by 91 days in high pH. The white box is the area shown in Figure 4.3, and shown again in Figure 4.57. The EELS spectrum was acquired at 0.25 eV/channel.

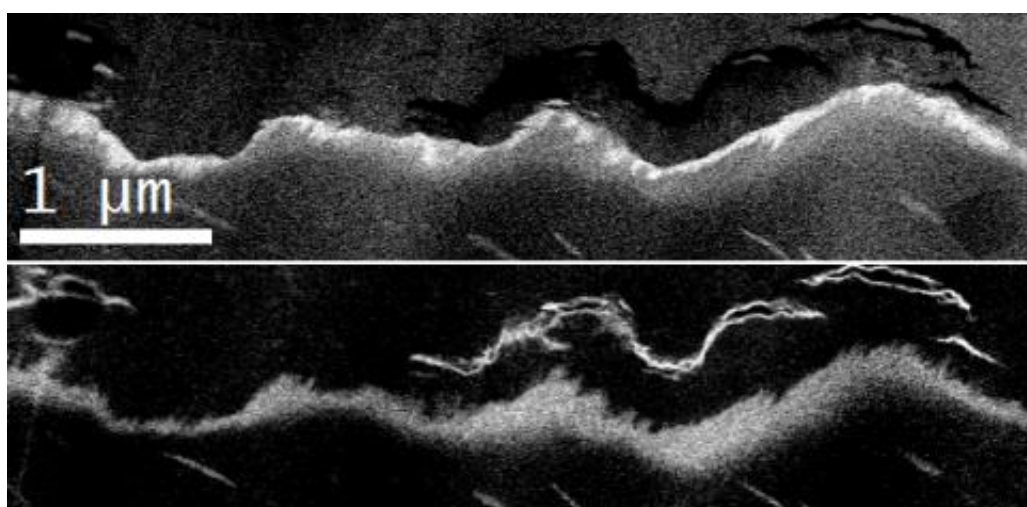


Figure 4.57 – ZrO (top) and OSZ (bottom) MLLS fits of the region shown in Figure 4.56

There is an SPP on the left side of Figure 4.56 with a crack above and below it. There is a delay in the OM interface here, which is probably caused by the SPP. I carried out low-loss EELS in this region (which was originally shown in Figure 4.7), and is shown in Figure 4.58. There is a clear delay in oxidation underneath the SPP as there is a strip of OSZ extending up to the OM interface. There is another example here of the ZrO extending into the oxide, which seems to occur in older oxides.

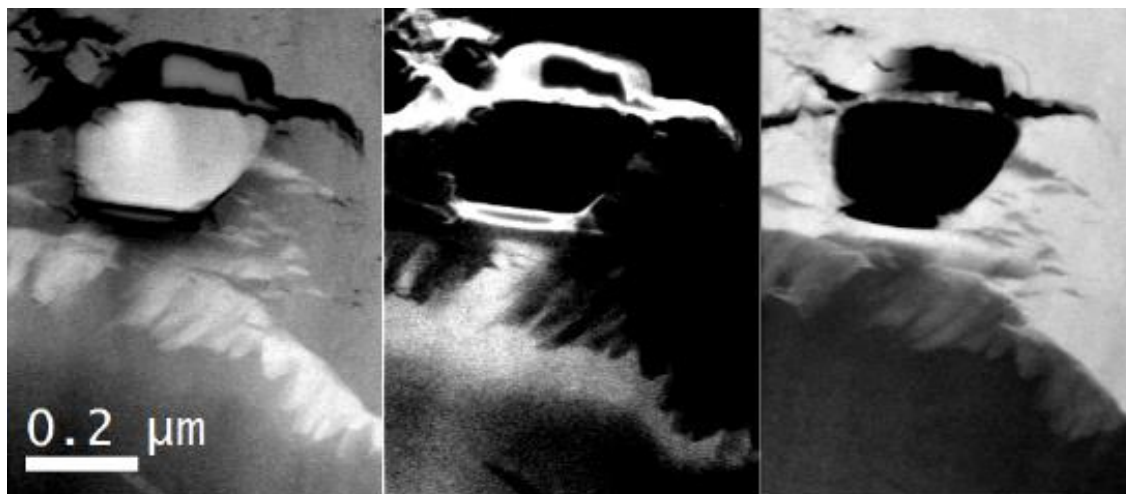


Figure 4.58 – MLLS fits for SPP to the left of Figure 4.56. The fits from left to right are: ZrO, OSZ, and oxide.

Using the same method for the OSZ + ZrO thickness mentioned previously, I computed the suboxide thickness of several samples exposed to pure water, and compared it with samples exposed to a high pH which is shown in Figures 4.59. The suboxide regions were thicker in the pure water samples at a given time. In Figure 4.59 the pure water values have been scaled by taking the ratio of the equations in equation (3.2). After scaling the suboxide thickness is constant within error (except for the 45 day samples) for samples oxidised for a similar amount of time. This indicates that the suboxide growth is affected by the oxide growth rate but not by the pH of the oxidising environment, i.e. neither the ZrO₂ growth rate nor the suboxide growth rate were affected by the pH range tested.

Another way to visualise the trend of the suboxide thickness is to plot it against the locally measured oxide thickness, which is shown in Figure 4.60. This shows that regardless of pH, the suboxide increases in thickness as the oxide grows until the oxide reaches about 1.8 μm. It is unknown what happens between 1.8 μm and transition. The oxidation rate increases at transition and the suboxide layer is reduced in thickness. As the oxidation rate starts decreasing again the suboxide layer builds

back up again. As the suboxide growth was similar in both environments it is likely that the difference in the bulk oxide growth was due to the difference in temperature and not pH.

Throughout this section I have shown images which contain Secondary Phase Particles (SPPs), and in the next section I will show the examination of these SPPs with EELS.

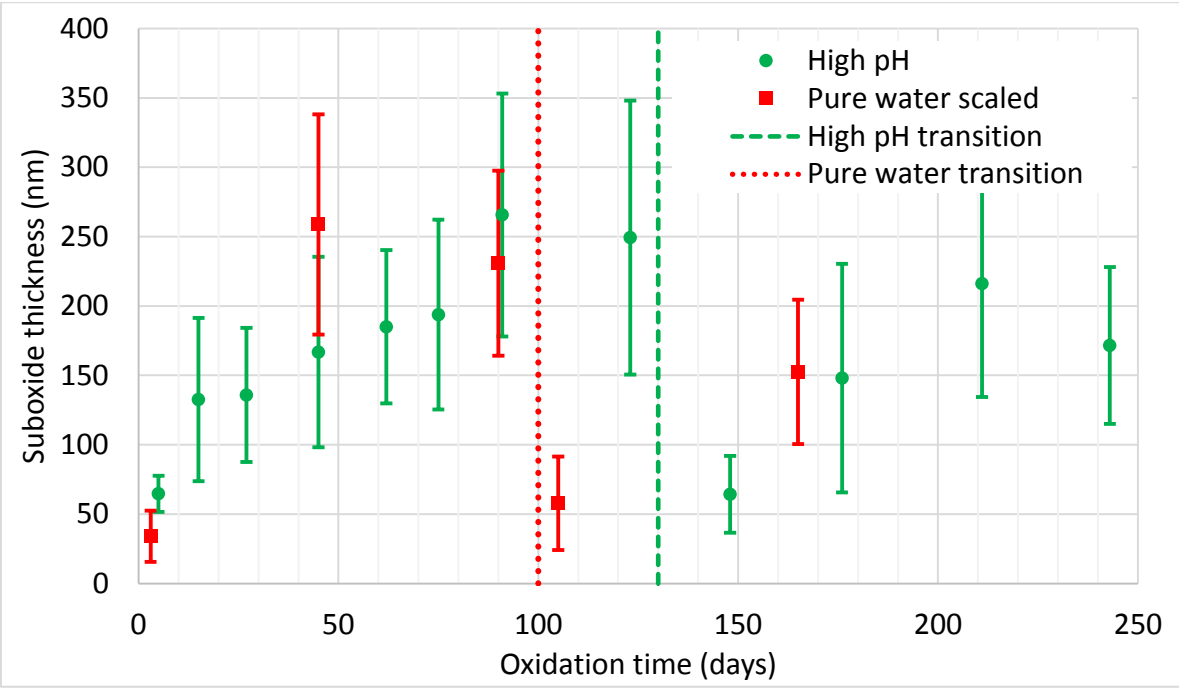


Figure 4.59 – Suboxide thickness vs oxidation time for high pH and pure water samples.

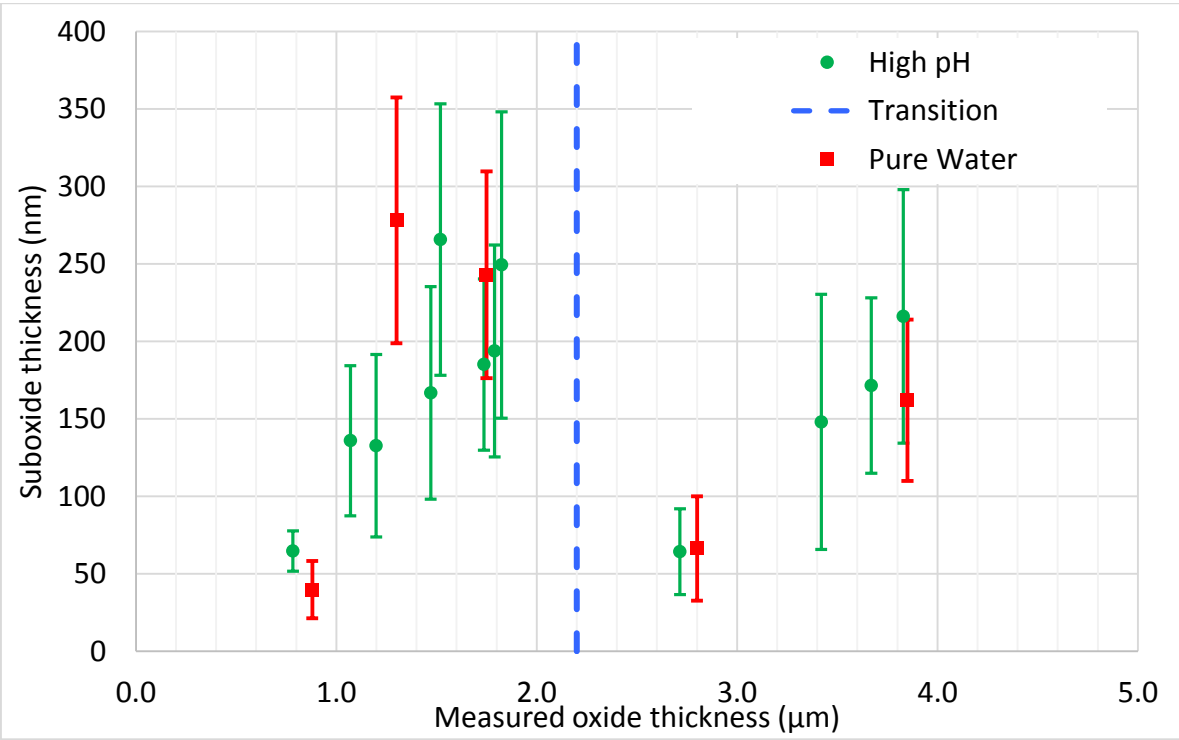


Figure 4.60 – Suboxide thickness vs oxide thickness for high pH and pure water samples. Transition was approximated to 2.2 μm .

4.2.4 – SPP Oxidation

I have used core-loss EELS to examine the SPPs that were present in the TEM foils I made. This is due to the core-loss signal containing much more quantitative information about the Cr and Fe in the SPPs than in the low-loss signal. The vast majority of the SPPs were in the oxide, and I will present them in order of increasing distance from the OM interface (therefore increasing exposure to the oxidising environment) to examine if there is any difference in oxidation behaviour in the different environments. There are several methods of determining the oxidation state of a metal from EELS^{18–22}. The first method I will use is the energy difference between the O K-edge onset and the respective onset of the L₃-edge of the metal, which increases as the oxidation state increases. This will be referred to as $\Delta E(\text{Cr})$ and $\Delta E(\text{Fe})$ for Cr and Fe respectively. The second is the narrowing of the FWHM of the L₃ peak as the oxidation state increases. The third method is the L₃/L₂ intensity ratio, calculated from their respective areas. I computed the L₃/L₂ ratio using the Oxide Wizard script developed by Yedra et al.²³, with an integration window of 2 eV. Table 4.1 summarises the values of $\Delta E(\text{Cr})/\Delta E(\text{Fe})$, the FWHM, and the L₃/L₂ ratio for Cr, Cr³⁺, Fe, and Fe²⁺, which I will refer to as the 3 parameters. I have decided that only if I find all of these values to match the literature then I can say with confidence that either the Cr or Fe have oxidised.

Species	ΔE (eV) ^{19,20}	FWHM (eV) ²²	L ₃ /L ₂ ratio
Cr	43	4.3	1.38 ¹⁸ , 1.2 ²²
Cr ³⁺	46.5	3.2	1.63 ¹⁹ , 1.7 ²²
Fe	176	3.5	2.99 ²⁰ , 3.0 ²²
Fe ²⁺	177	2.4	3.99 ²⁰ , 4.1 ²²

Table 4.1 – Values of ΔE , FWHM, and L₃/L₂ ratio for Cr and Fe and their +2 ions.

I will first present SPPs that were in the metal. Figure 4.61 shows a DF image of two SPPs in the metal, the green line shows where the EELS spectra were obtained. The light areas under both SPPs are areas where the sample was thicker due to the SPPs being milled less than the surrounding zirconium metal. Figure 4.62 shows part of the EELS spectrum obtained across the SPP, showing the presence of Cr and Fe, and a small amount of O from surface oxidation. The FWHM I obtained for

Cr is ~ 4.5 eV and for Fe is 4 eV, both of which are slightly higher than the literature values. This is probably because the samples I looked at were thicker than is ideal. The L_3/L_2 ratios for Cr and Fe were 1.45 and 2.95 respectively. The Cr value is slightly higher than the literature values, but is close enough to be taken as the un-oxidised value for these experiments.

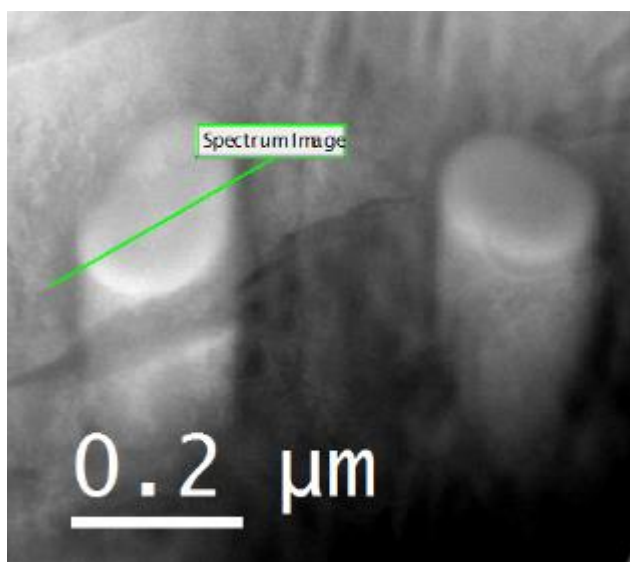


Figure 4.61 – Two SPPs in the metal. The green line shows where the spectrum was obtained.

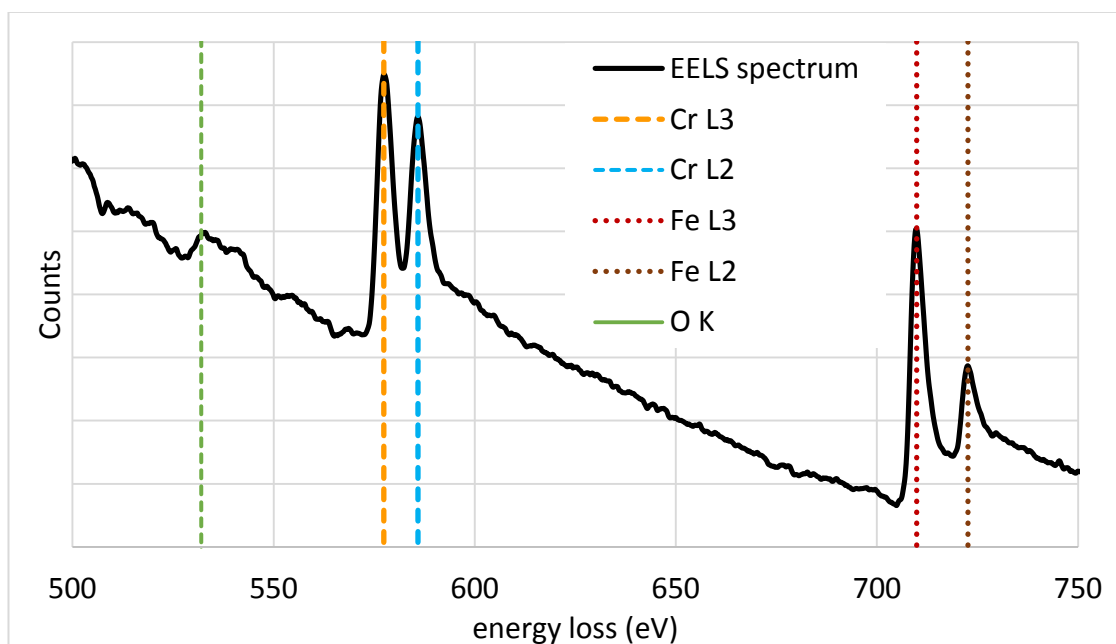


Figure 4.62 – Core-loss EELS across SPP shown in Figure 4.61. The O-K edge, Cr- $L_{2,3}$ and Fe- $L_{2,3}$ edges are indicated.

Using the quantification tool in DM I was able to extract the relative amount of Cr and Fe present, and the Fe/Cr ratio is shown in Figure 4.63. The average for this SPP is 1.545, which is similar to the value of 1.7 found by Pêcheur et al²⁴. Of the SPPs in the metal that I have examined the average Fe/Cr ratio was 1.323, which included two SPPs at the OM interface (one is shown in Figure 4.64), with a

range between 1.026 – 1.546. The Fe/Cr ratio was constant across each individual SPP I examined, and are consistent with the literature values^{24–26}.

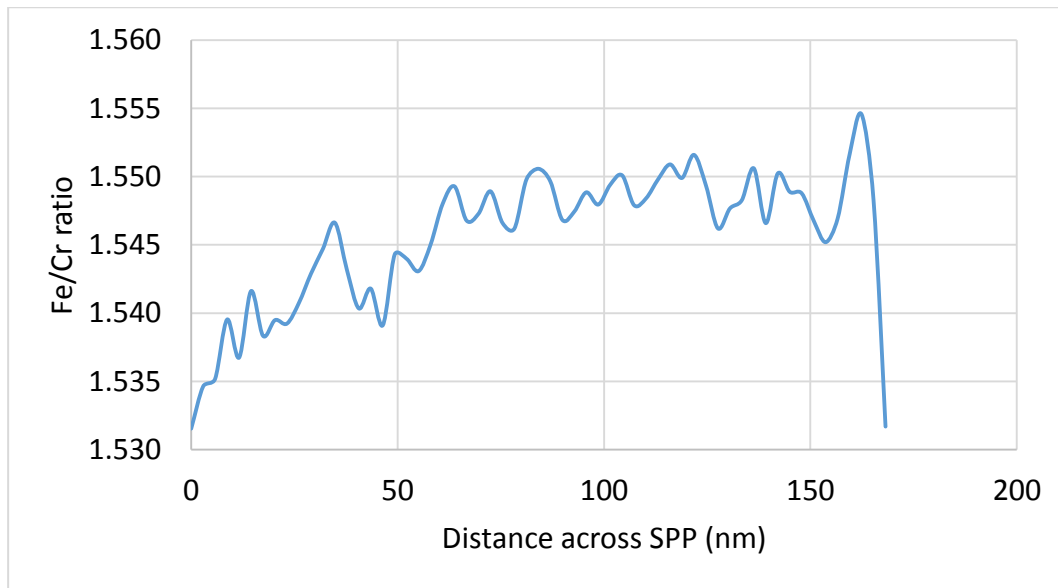


Figure 4.63 – Fe/Cr ratio across SPP shown in Figure 4.61.

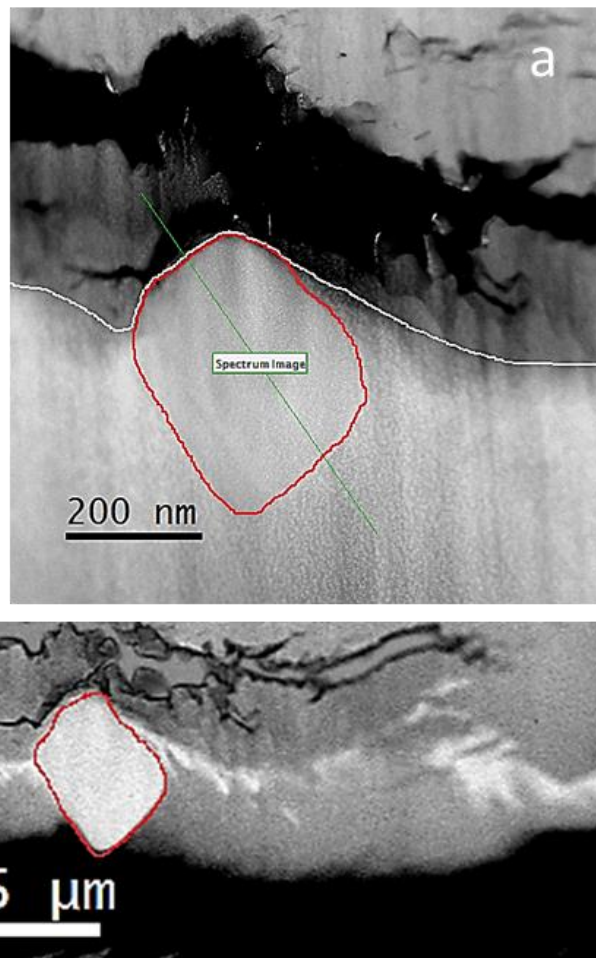


Figure 4.64 – An SPP on the OM interface, which I have circled with a red outline in both parts. a) the white line shows where the OM interface is. b) is from Figure 4.24b, showing the SPP surrounded by OSZ and ZrO.

Figure 4.64 shows an SPP which was just below the OM interface (on the metal side) of a 122 day high pH oxide, which was previously shown in Figure 4.24. This SPP is surrounded by OSZ with the bottom left corner still in contact with Zr metal. I took a line scan across the SPP after zooming in on the edge near the OM interface to examine what happens to the Zr, Cr and Fe at the edge of the SPP nearest the oxide. Figure 4.65 shows the Survey Image, and the red dots show the points where I extracted the EELS spectra, which are shown in Figures 4.66 & 4.67. Figure 4.66 shows spectra from 500 – 750 eV, showing that there has been a small amount of surface oxidation of the SPP. Table 4.2 shows the 3 parameters mentioned previously. The results indicate that there is some oxidation of Cr at the edge of the SPP compared to the bulk of the SPP, while the Fe is un-oxidised.

Looking at the Fe-L_{2,3} edges in Figure 4.66 shows that there is less Fe compared to Cr at the edge of the sample as the peaks are reduced significantly. This is backed up by examining the Fe/Cr ratio, which is 0.66 at the edge compared to 1.35 throughout the SPP. The Fe/Cr ratio did not vary significantly from the centre to the edge of the metallic SPP, so this redistribution is caused by oxidation.

The Zr-L_{2,3} edges are displayed in Figure 4.67, which shows that the zirconium is un-oxidised in the centre of the SPP, but oxidised at the edge of the SPP. This results shows that Zr oxidises before the Cr/Fe in the SPP, which is consistent with the results of Pêcheur et al.

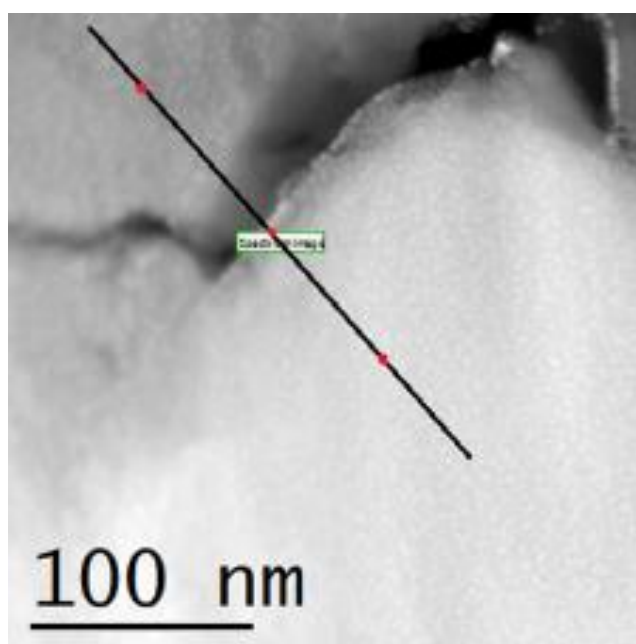


Figure 4.65 – The closer line scan on the SPP from Figure 4.64. The red dots show the parts where I extracted the spectra for Figures 4.66 & 4.67.

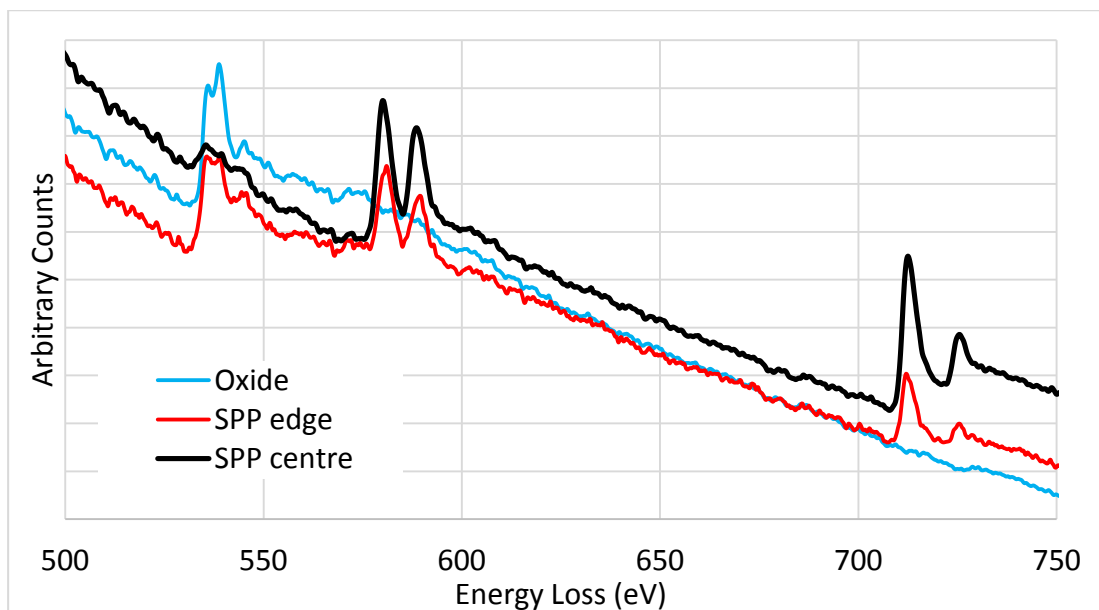


Figure 4.66 – O K-edge, Cr $L_{2,3}$ -edges and Fe $L_{2,3}$ -edges for the points shown in Figure 4.65

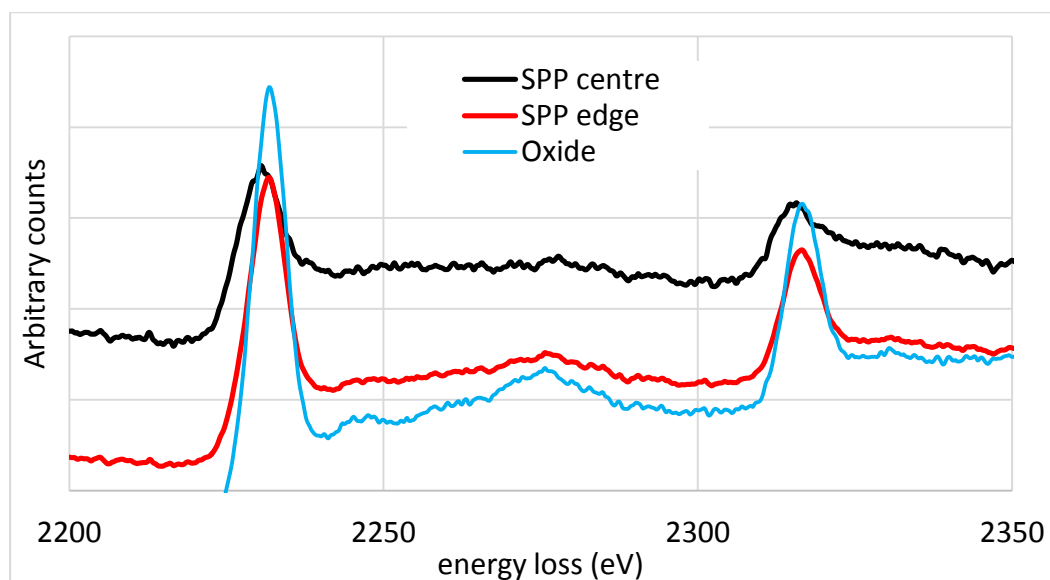


Figure 4.67 – Zr- $L_{2,3}$ edges for points shown in Figure 4.65.

	Centre	Edge
$\Delta E(\text{Cr})$	43.75	44.25
Cr FWHM	4.5	4.25
Cr L_3/L_2 ratio	1.55	1.64
$\Delta E(\text{Fe})$	176.25	176.25
Fe FWHM	4.5	4.25
Fe L_3/L_2 ratio	3.74	3.38

Table 4.2 – Summary of the Cr and Fe parameters for the spectra shown in Figure 4.66.

Figure 4.68 shows an SPP which has just been submerged in oxide. The closest part of the SPP to the OM interface is $\sim 40\text{nm}$, and the top of the SPP is $\sim 290\text{ nm}$ from the OM interface. It is in a pure water oxide so has been exposed from between 15 seconds (at the closest point) and 3 hours (at the top of the SPP), which I estimated this from the oxide growth rate. Even after such a short time there is a clear indication of O being incorporated into the SPP, which is shown by the relative composition maps of O, Cr, and Fe in Figure 4.69. There is a region to the left where there is a clear gradient of all 3 elements; the Fe/Cr ratio (shown in Figure 4.70) ranges from 0.743 in the blue region, to 1.230 in the red/orange region, to 1.530 in the yellow region. The O/Fe ratio in the same region decreases from 13.2 to 0.84.

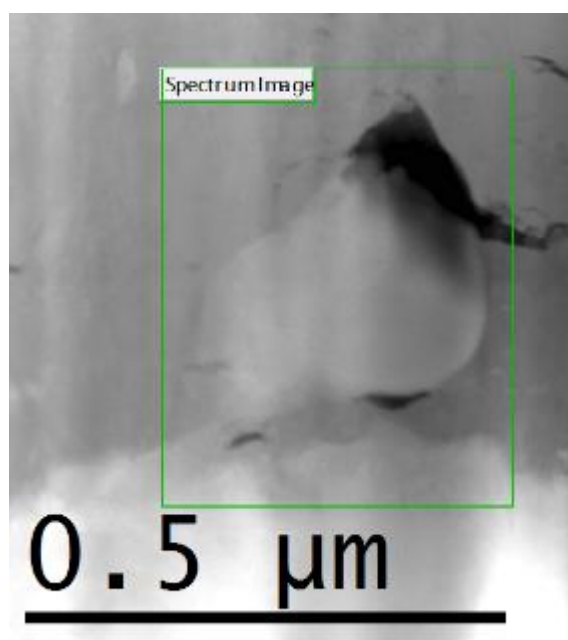


Figure 4.68 – SPP 40 nm from OM interface in a 165 day pure water oxide.

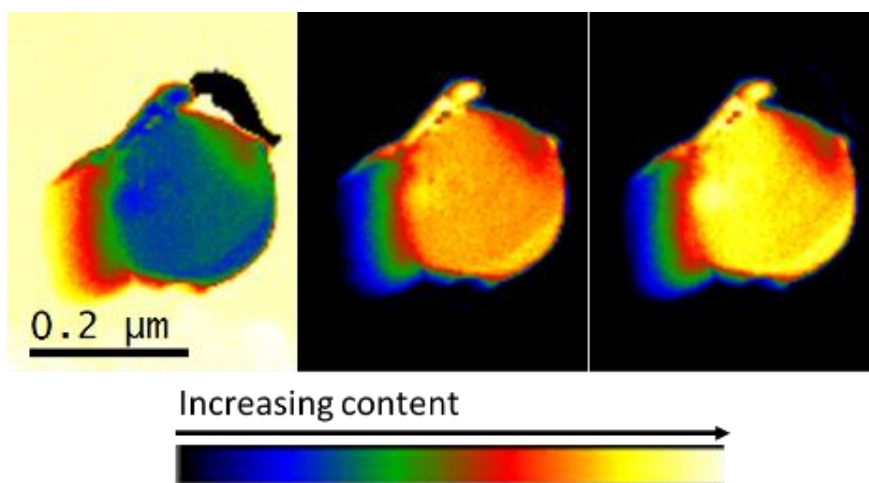


Figure 4.69 - Relative composition maps (from left to right) for O, Cr and Fe of the SPP shown in Figure 4.68.

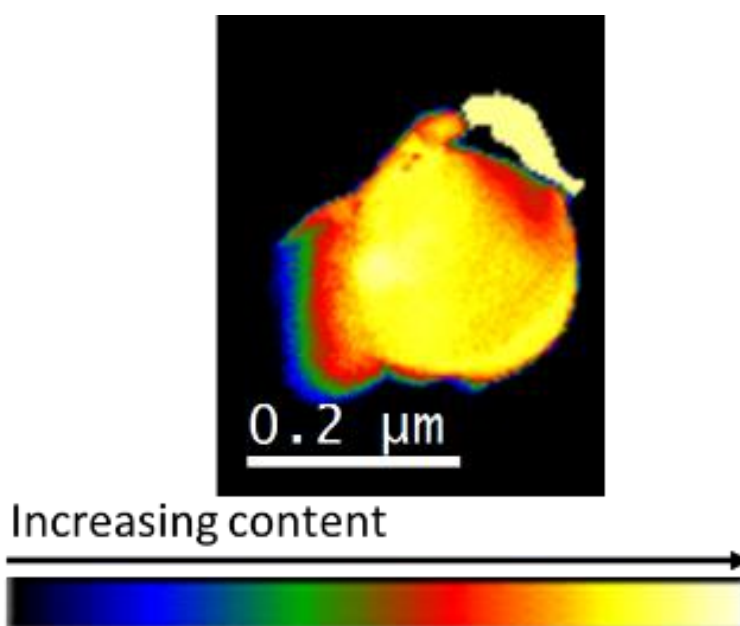


Figure 4.70 – Fe/Cr ratio of SPP from Figure 4.68.

Figure 4.71 shows EELS spectra for the different coloured regions in Figure 4.70. The crack is at the top of the SPP and shows a much stronger Cr and Fe signal, which means that Cr and Fe will migrate to cracks after leaving SPPs. As mentioned earlier the O content decreases the closer to the centre of the SPP we look, the O K-edge is reduced significantly in the yellow region (higher Fe/Cr ratio). In the crack there is a splitting of the O K-edge. Table 4.3 shows the results of the 3 parameters for Cr and Fe. It shows that from just using the $\Delta E(\text{Cr})$ and $\Delta E(\text{Fe})$ and their FWHM the Cr and Fe are un-oxidised. However the L_3/L_2 ratio indicates that there might be some oxidation of the Cr and Fe in the SPP, particularly where the O content is higher. It should be noted though that the Cr and Fe content are much lower in the blue region, and the L_2 edges for both are much lower than the rest of the SPP, which explains the higher L_3/L_2 ratio in that region.

The O which is present in the SPP will react with the Zr before oxidising the Cr and Fe. This is confirmed by examining the Zr spectra in Figure 4.72. I have summarised the onset energies for the 5 spectra showing Zr in Table 4.4, which shows that the blue line is at the same oxidation state as the oxide (Zr^{4+}), the green and red lines are at an intermediate oxidation state (Zr^{2+}), and the yellow line is un-oxidised.

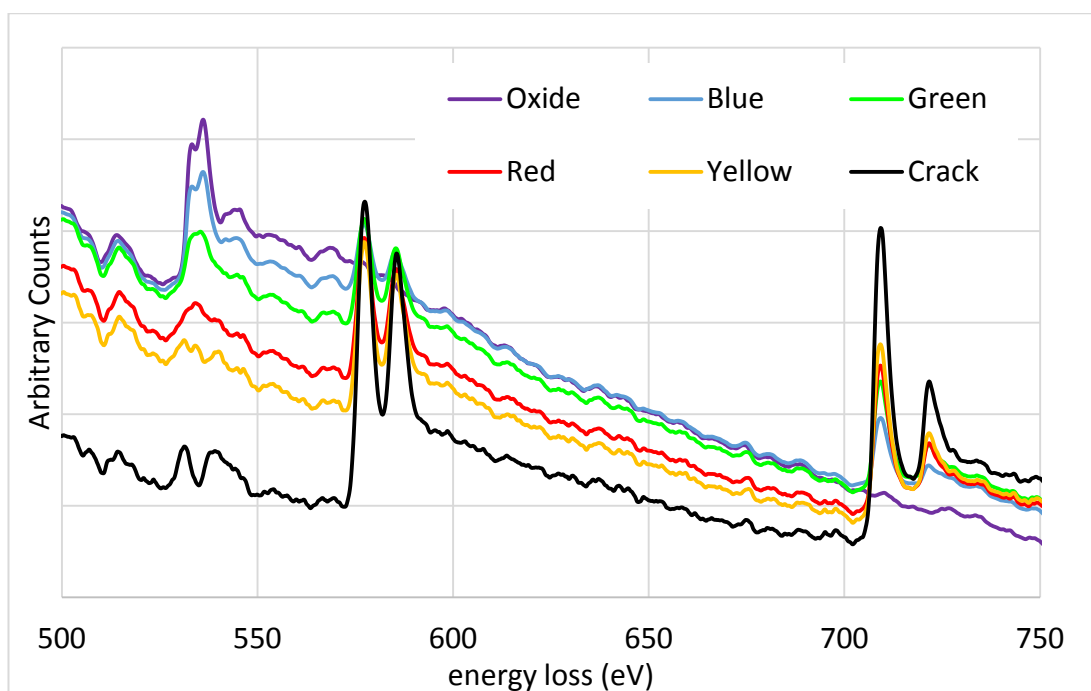


Figure 4.71 – EELS spectra in each of the coloured regions shown in Figure 4.70. The spectrum labelled ‘Crack’ was obtained at the top of the SPP where the O content was low.

	Blue	Green	Red	Yellow	Crack
$\Delta E(\text{Cr})$	43.5	43.5	43.5	43.5	43.5
Cr FWHM	4.5	4.5	4.5	4.75	4.5
Cr L_3/L_2 ratio	1.79	1.67	1.6	1.52	1.66
$\Delta E(\text{Fe})$	175.5	175.5	175.5	175.5	175.5
Fe FWHM	4	4.5	4.5	4.75	4.75
Fe L_3/L_2 ratio	3.61	3.22	3.19	3.26	3.41

Table 4.3 – Summary of the Cr and Fe parameters for the spectra shown in Figure 4.71.

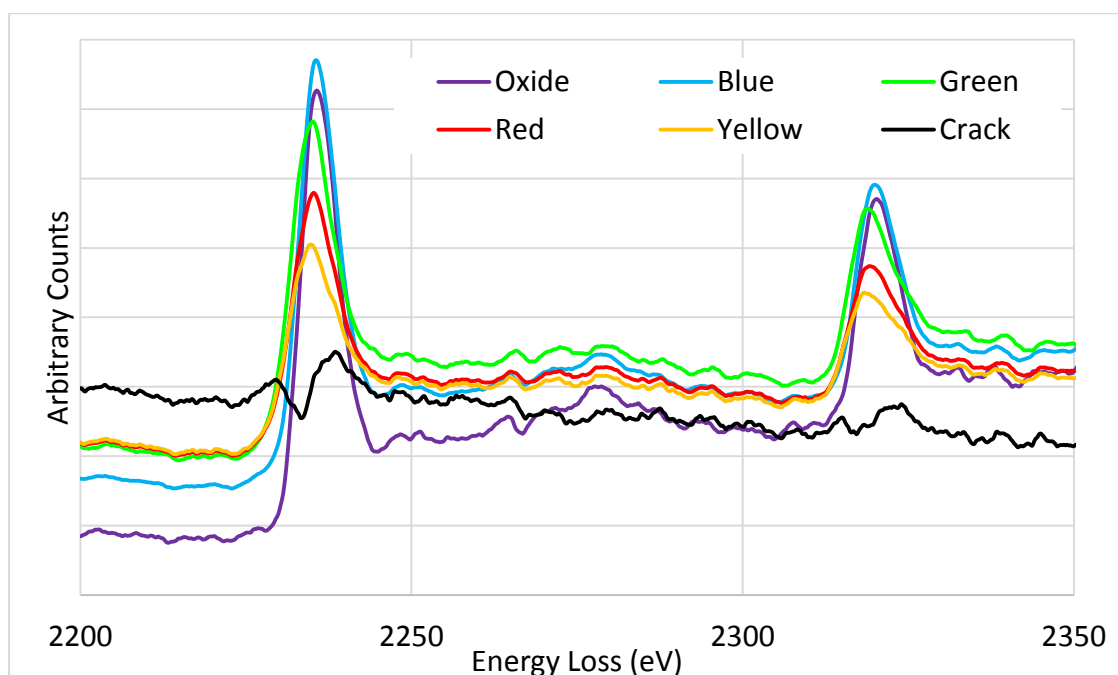


Figure 4.72 – EELS spectra showing the Zr $L_{2,3}$ -edges at the same points in Figure 4.71.

Line	Onset energy (eV)
Oxide	2232.98
Blue	2232.73
Green	2231.48
Red	2231.73
Yellow	2230.98

Table 4.4 – Zr onset energies for spectra in Figure 4.72.

The SPP shown in Figure 4.73 is 90 nm from the OM interface in a 91 day high pH oxide (average oxide thickness = 1.81 μm), and extends 192 nm from the OM interface, which means it has been in the oxide for between 16 minutes and 7.5 hours. The whiter area on the left of the SPP is due to that region being slightly thicker. I took two line scans across the SPP, one horizontal and one vertical. The horizontal line scans are shown in Figure 4.74, which shows that the zirconium in the SPP is un-oxidised as it is at a lower energy compared to the zirconium in the oxide (at the top and bottom of the line scan). The Cr and Fe are not oxidised even at the left and right edges of the SPP, and the average Fe/Cr ratio in this line scan was 1.954, with a range of 1.714 – 2.147.

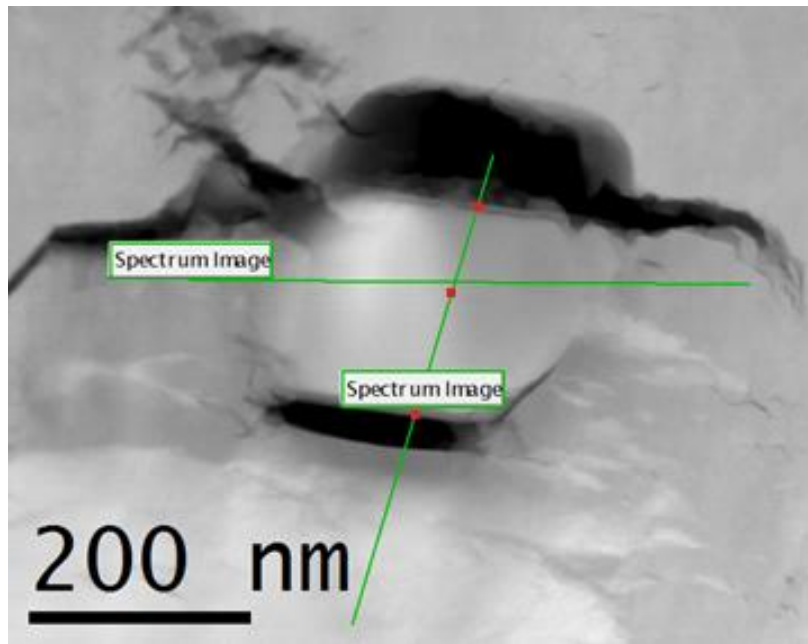


Figure 4.73 – SPP 90 nm from the OM interface in 1.83 μ m oxide formed after 91 days in high pH water. The green lines show where the initial line scans were taken. The red points show the locations from which the spectra in Figure 4.76 were extracted.

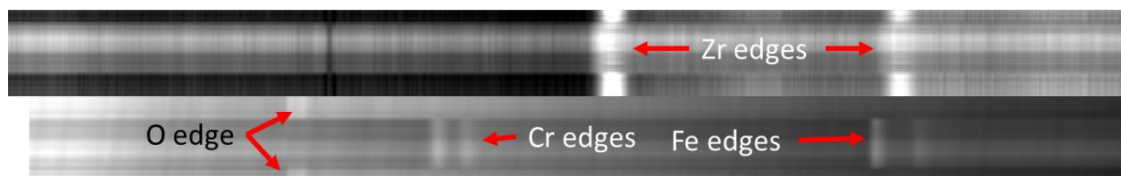


Figure 4.74 – Horizontal line scans for SPP in Figure 4.73. The Zr-L edges are shown at the top and the O-K, Cr-L and Fe-L edges at the bottom. Moving from left to right in these images moves to a higher energy loss, and moving from top to bottom is each pixel of the line scan

Figures 4.75 & 4.76 shows the Zr and O/Cr/Fe spectra for the points indicated on the vertical line scan on Figure 4.73. The shift in energy of the Zr L_3 peaks in Figure 4.75 shows that the Zr at the Top and Bottom of the sample is oxidised, and the Zr in the middle is un-oxidised. This is confirmed by there being no O K-edge (at 532 eV) on the ‘SPP Centre’ spectrum in Figure 4.76.

Table 4.5 summarises the 3 parameters for the Top, Centre and Bottom of the SPP. The Cr L_3/L_2 ratio is higher than that shown in the literature, which on its own would indicate that oxidation has occurred, but this is contradicted by the $\Delta E(\text{Cr})$ and FWHM results. The $\Delta E(\text{Fe})$ is roughly constant, and on its own would indicate that the Fe is oxidised, but the constant nature of the Fe FWHM and the much lower L_3/L_2 ratio shows that the Fe remains un-oxidised.

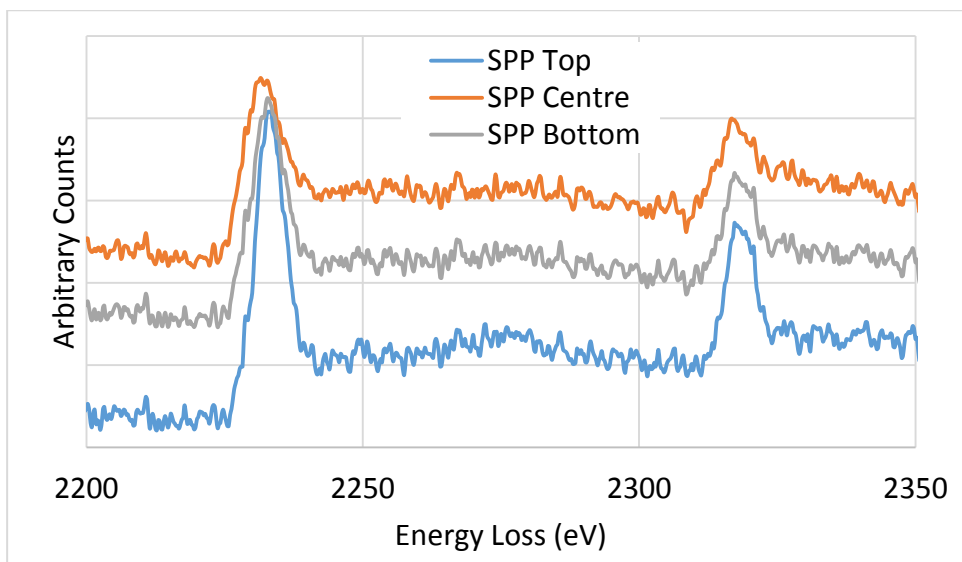


Figure 4.75 – Zr spectra from indicated points in Figure 4.73, showing Zr oxidation at the Top and Bottom of the SPP.

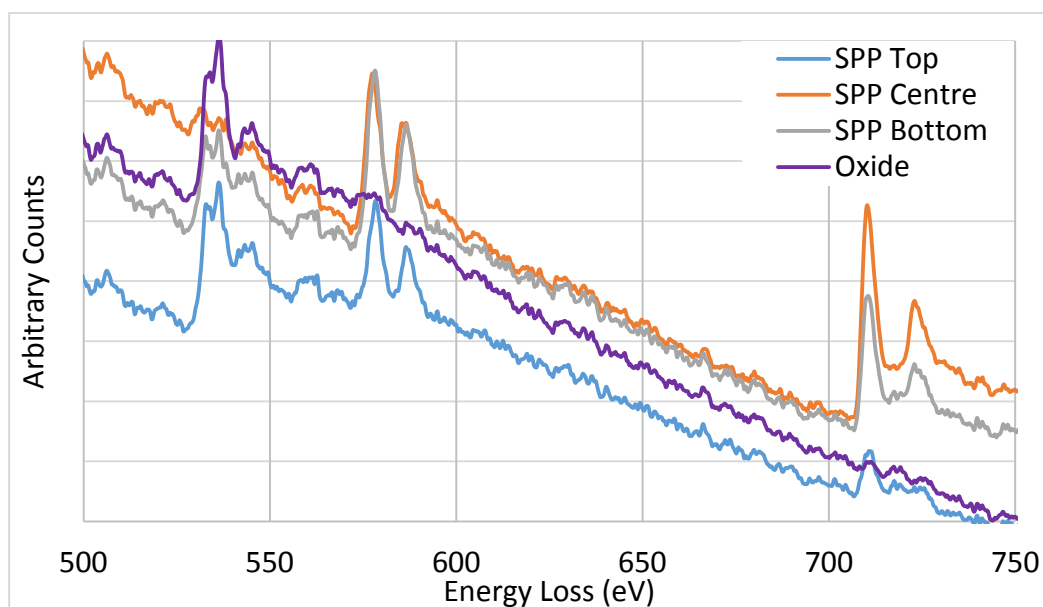


Figure 4.76 – EELS spectra at the indicated points in the vertical line scan from Figure 4.73.

	Top	Centre	Bottom
$\Delta E(\text{Cr})$	44.25	43.5	44
Cr FWHM	4	4.5	4
Cr L_3/L_2 ratio	1.91	1.78	1.72
$\Delta E(\text{Fe})$	177.25	177	177
Fe FWHM	4.5	4.5	4.5
Fe L_3/L_2 ratio	-	3.02	2.68

Table 4.5 – Summary of Cr and Fe for the line scans shown in Figure 4.76.

Along the vertical line scan the Fe/Cr ratio in the SPP was 2.146 (range = 1.206 – 2.351), but this drops to about 0.6 at the Top and at the Bottom it is 1.206. After carrying out small line scans at the top and bottom of the SPP I observed the Fe depletion in progress. Figure 4.77 shows where the line scan at the bottom of the sample was carried out, and Figure 4.78 shows the EELS spectra for the points indicated. This shows that the amount of Fe compared to Cr increases at the edge of the SPP as the Fe peaks are relatively larger compared to Cr at the edge. The Fe/Cr ratio at these 3 points is 1.967, 0.895, and 2.808. Table 4.6 shows the 3 parameters for each of the points in Figure 4.77. For Cr the $\Delta E(\text{Cr})$ there is a hint of oxidation at the Middle and Bottom of the line scan, and the Cr L_3/L_2 ratio on its own indicates clearly that oxidation has occurred at the Middle and Bottom. Although this is not confirmed by the FWHM data. The $\Delta E(\text{Fe})$ values are the same as Fe^{2+} , indicating oxidation has occurred, but this is clearly refuted by the FWHM and L_3/L_2 ratio, which are much closer to the un-oxidised values.

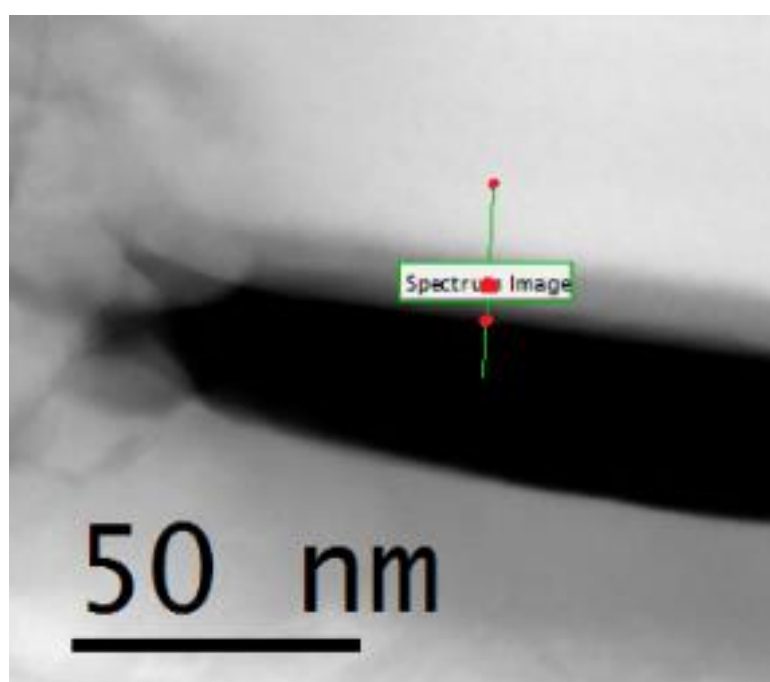


Figure 4.77 – Line scan at the bottom of the SPP. The red dots show where I have extracted the EELS spectra shown in Figure 4.78.

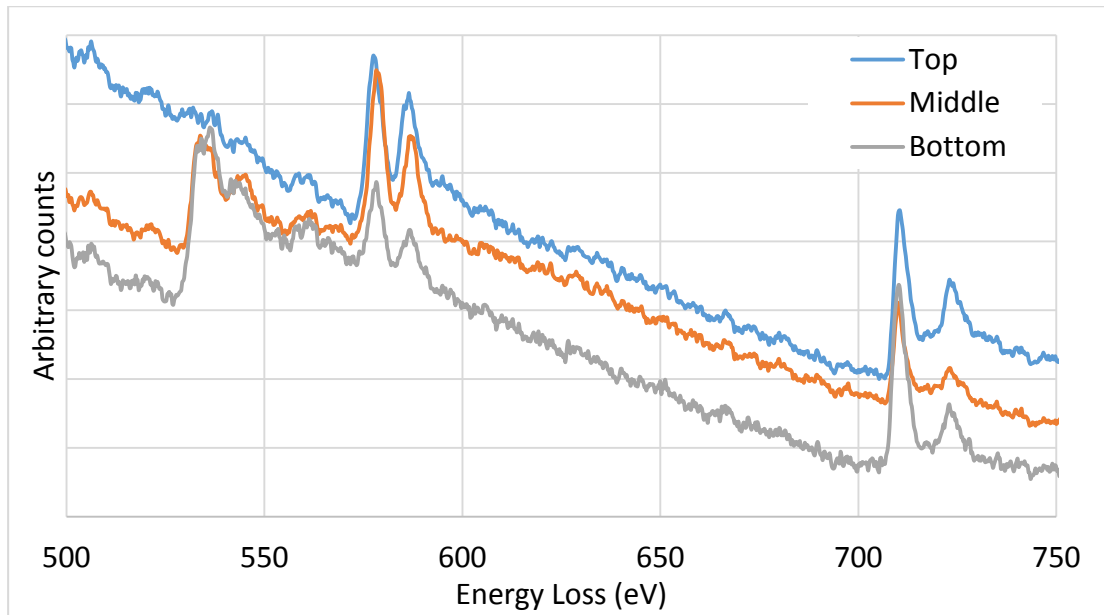


Figure 4.78 – EELS spectra of the points shown in Figure 4.77. The Fe segregation is clear as there is an increase in the amount of Fe compared to Cr at the edge of the SPP.

	Top	Middle	Bottom
$\Delta E(\text{Cr})$	43.5	45	44.75
Cr FWHM	3.75	4	4
Cr L_3/L_2 ratio	1.69	1.84	1.88
$\Delta E(\text{Fe})$	177.5	177.5	177
Fe FWHM	3.5	3.25	3.75
Fe L_3/L_2 ratio	2.48	2.85	3.42

Table 4.6 – Summary of Cr and Fe for line scans shown in Figure 4.78.

Figure 4.79 shows two SPPs which are 330 nm from the OM interface, in 1) a sample exposed to pure water (average oxide thickness = 3.99 μm after 165 days), and 2) a high pH sample (average oxide thickness = 1.15 μm after 27 days). For SPP 1 the distance from the top of the crack to the OM interface is 570 nm, which means it been exposed to oxide from 5-31 hours. For SPP 2 the distance was ~600 nm to the top of the SPP, which means it has been exposed to oxide for 14-85 hours.

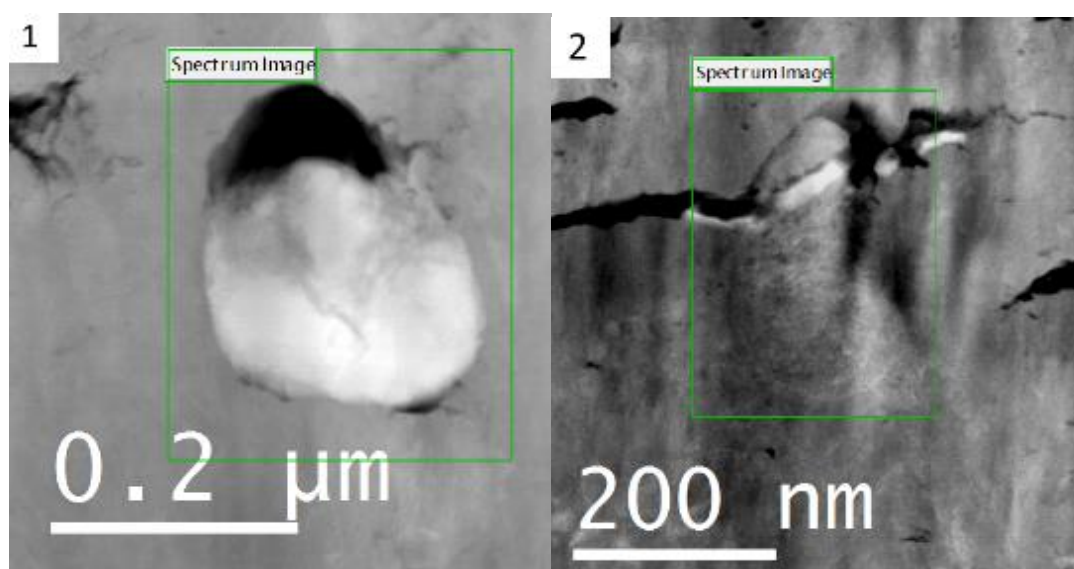


Figure 4.79 – SPPs which are approximately 300 nm from the OM interface; 1) in a pure water sample, and 2) a high pH sample.

Figure 4.80 shows the relative composition maps for O, Cr and Fe for SPP 1. Both Cr and Fe have segregated to the large crack at the top of the SPP, and the Fe/Cr ratio is 1.21 throughout the SPP, even in the crack. Table 4.7 shows the 3 parameters for 3 areas of the SPP, the crack where the Cr and Fe is high, the middle of the SPP, and in the area in the centre where the Cr and Fe content is lower. These results show that for this SPP neither the Cr nor the Fe have been oxidised.

Figure 4.81 shows that the Zr in the SPP has started oxidising in places where the O content is slightly higher (and the Cr and Fe has been depleted), but most of the Zr in the SPP is still un-oxidised.

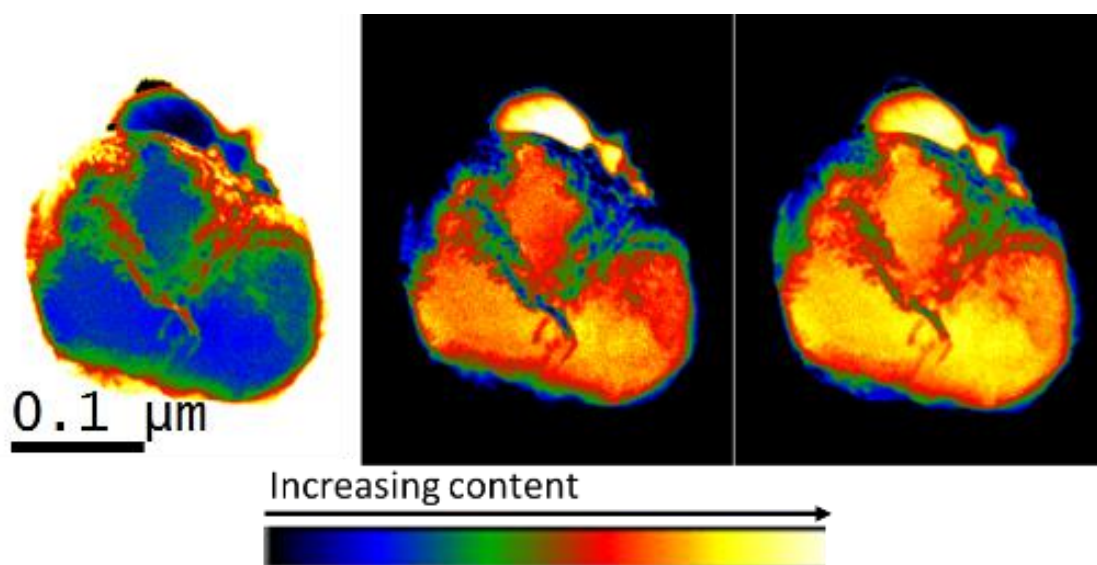


Figure 4.80 – Relative composition maps (from left to right) of O, Cr and Fe in SPP 1 from Figure 4.79.

	Crack	Middle of SPP	High O
$\Delta E(\text{Cr})$	43.75	43.5	43.5
Cr FWHM	4	3.75	4.5
Cr L_3/L_2 ratio	1.57	1.56	1.62
$\Delta E(\text{Fe})$	175.25	175.25	175.25
Fe FWHM	3.75	3.5	4
Fe L_3/L_2 ratio	3.37	3.04	3.25

Table 4.7 – Summary of Cr and Fe for SPP 1.

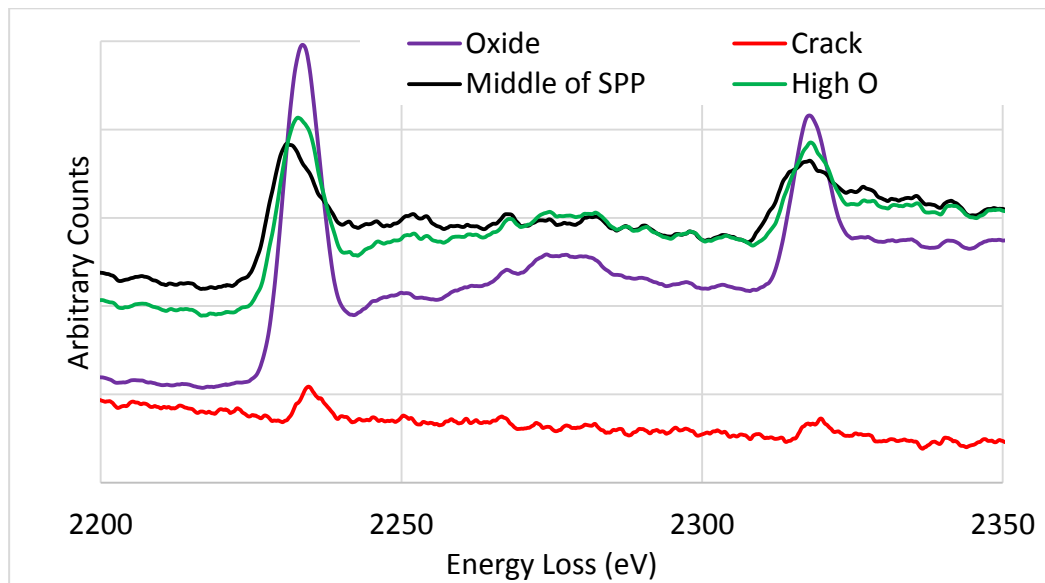


Figure 4.81 – Zr spectra for various points in SPP 1. The high O region is in the centre of the SPP where the Cr and Fe is reduced.

Figure 4.82 shows the relative composition maps for O, Cr and Fe for SPP 2, which shows there is little Cr or Fe left in the SPP and that most of it has migrated to the cracks. Table 4.8 summarises the 3 parameters, which shows the Cr has possibly oxidised in the ‘High Cr’ region, as both the FWHM and the L_3/L_2 ratio are similar to the literature values for Cr^{3+} . The $\Delta E(\text{Cr})$ is between the values given in the literature. The High Cr region was in the crack, and the O K-edge had the same shape as previously shown in Figure 4.71, which can be seen in Figure 4.83. The Fe was un-oxidised throughout the SPP and in the cracks, which can be understood by the lack of any O peak in the High Fe region. The Fe/Cr ratio in the SPP was ~ 0.6 , but increased to over 7 in the crack.

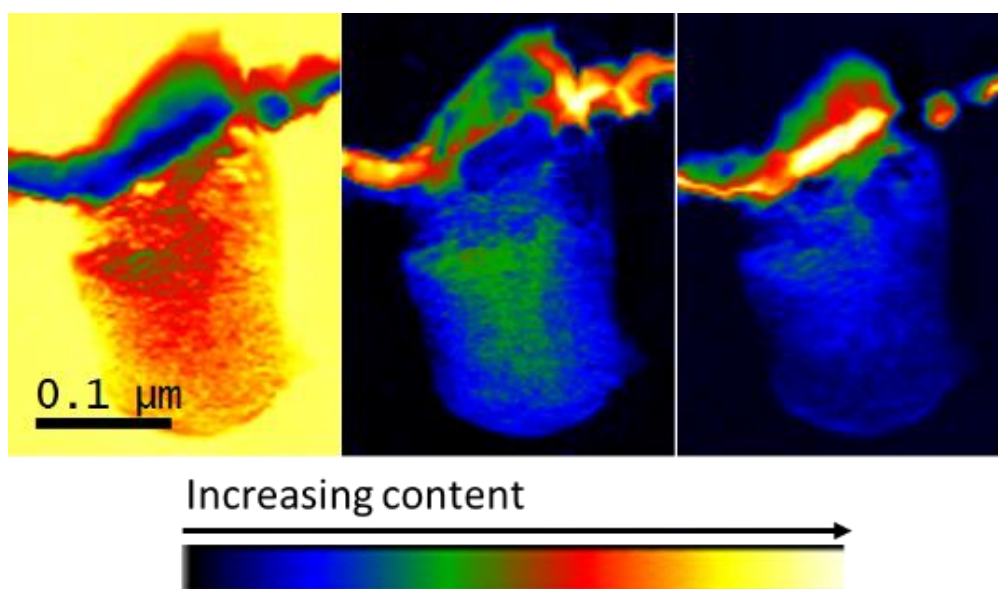


Figure 4.82 – Relative composition maps (from left to right) of O, Cr and Fe for SPP 2 from Figure 4.79.

	High Cr	Middle of SPP	High Fe
$\Delta E(\text{Cr})$	44.5	44.25	43.5
Cr FWHM	3.25	4	3.5
Cr L_3/L_2 ratio	1.62	1.77	1.66
$\Delta E(\text{Fe})$	-	176.25	176.25
Fe FWHM	-	3.25	3.5
Fe L_3/L_2 ratio	-	2.81	2.92

Table 4.8 – Summary of Cr and Fe for SPP 2.

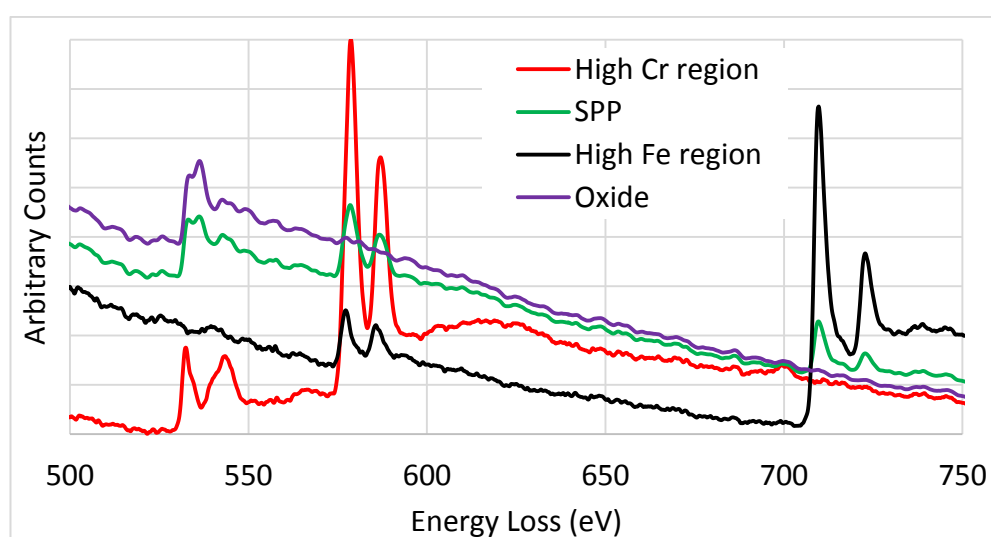


Figure 4.83 – EELS spectra for the regions examined in Table 4.8. Note the shape of the O K-edge is similar to the one shown on the ‘Crack’ spectrum in Figure 4.71.

The Zr in SPP 2 has completely oxidised in comparison (see Figure 4.84), which is not surprising as it has spent far longer exposed to the oxide compared to the Zr in SPP 1.

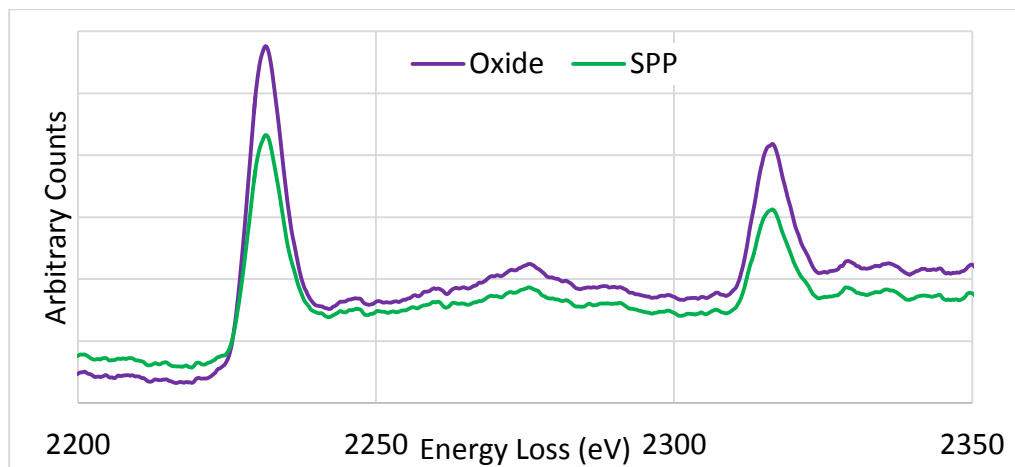


Figure 4.84 – Zr spectra in the SPP and Oxide, showing that the Zr is oxidised in SPP 2.

Figure 4.85 shows an SPP (previously shown in Figure 4.14) which was around 600 nm from the OM interface in a sample exposed to high pH for 27 days (average oxide thickness = 1.15 μm). It extended to 870 nm from the OM interface, meaning it has been in the oxide for 3.5-11 days. It is interesting to note that there is no crack at the top of this SPP, as cracks usually form at the top of the SPP as they are incorporated into the oxide. From the Zr EELS spectrum, the Zr in the entire SPP has oxidised (as shown in Figure 4.86), and this is true for the rest of the SPPs I will show.

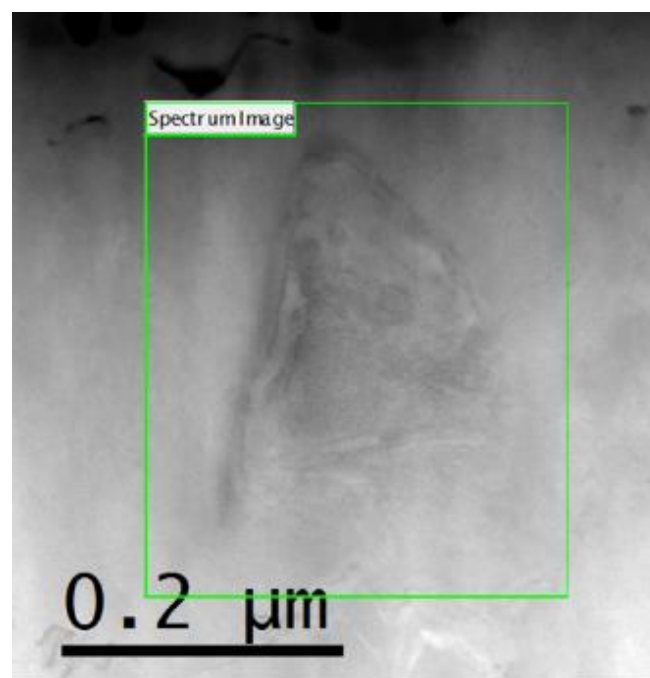


Figure 4.85 – SPP 600 nm from OM interface in a high pH oxide.

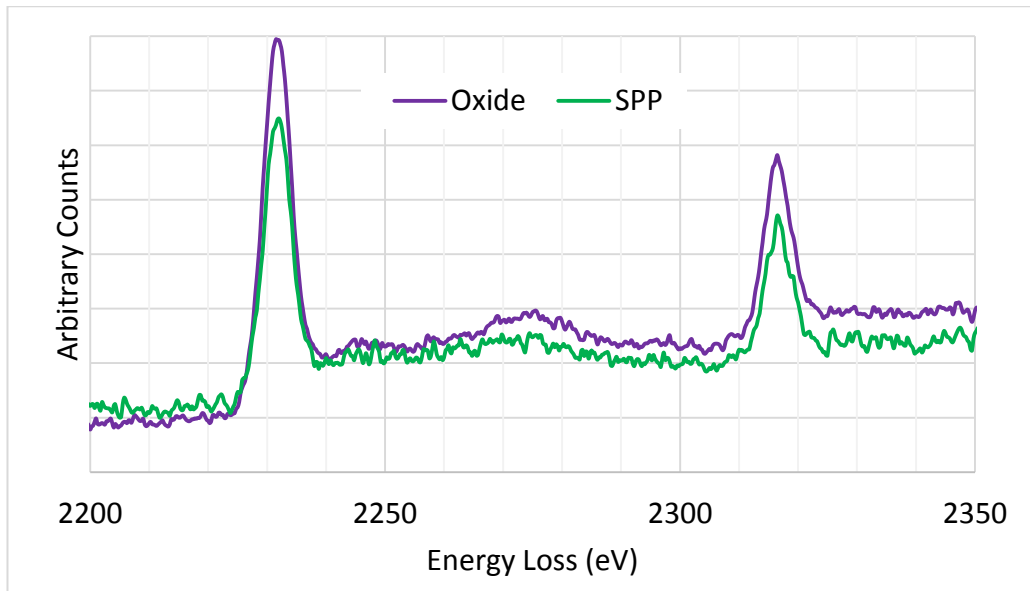


Figure 4.86 – Zr spectra in the SPP and oxide for the SPP shown in Figure 4.85.

The relative composition maps for O, Cr and Fe are shown in Figure 4.87, showing portions where the Cr is segregated from the Fe, and a large region near the top with a lower oxygen content. Table 4.9 shows the 3 parameters, which shows that in a region of low Fe and high Cr, the Cr has started oxidising. The L_3/L_2 ratio alone indicates that the Cr has oxidised elsewhere in this SPP, but the other parameters contradict this. In the centre of the SPP and in the presence of Fe, Cr has not oxidised, and the Fe has not oxidised in any part of the SPP, even though there is some O present in the High Fe region (see Figure 4.88).

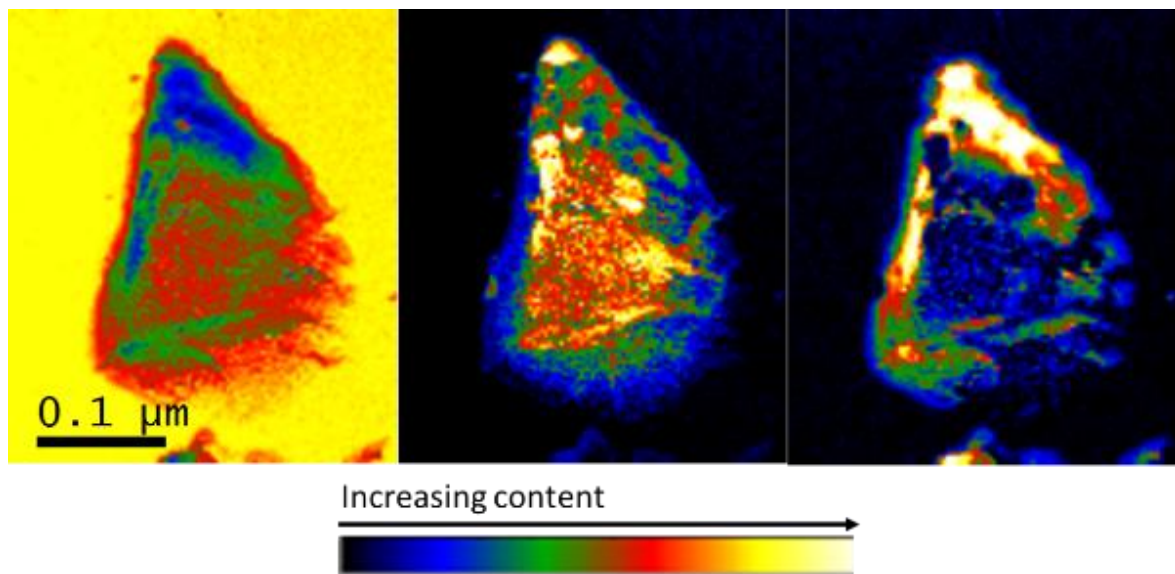


Figure 4.87 – Relative composition maps (from left to right) of O, Cr and Fe for SPP from Figure 4.85.

	High Cr	Middle of SPP	High Fe
$\Delta E(\text{Cr})$	44.5	43.5	43.5
Cr FWHM	3.5	4	4
Cr L_3/L_2 ratio	1.82	1.68	1.89
$\Delta E(\text{Fe})$	-	-	175.5
Fe FWHM	-	-	4
Fe L_3/L_2 ratio	-	-	3.38

Table 4.9 – Cr and Fe oxidation behaviour for SPP in Figure 4.85.

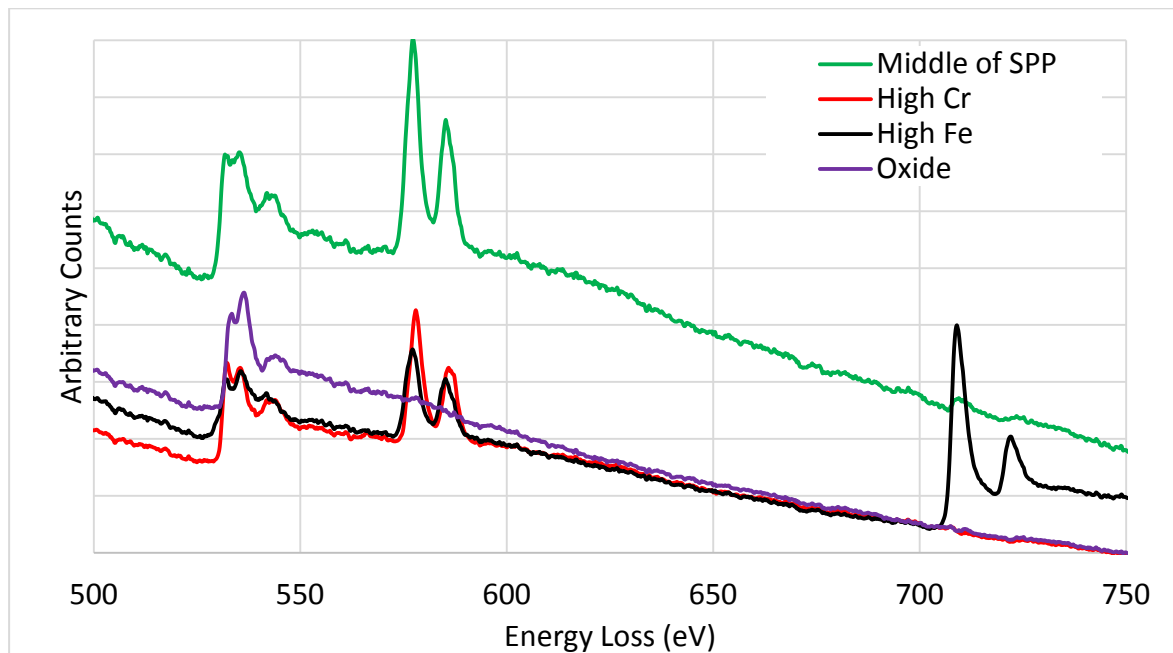


Figure 4.88 – EELS spectra of regions in SPP in Figure 4.85.

The Fe/Cr ratio in this SPP varied significantly. In the High Cr region at the top there was extremely little Fe, the average Fe/Cr ratio = 0.017 (range = 0.001 – 0.032), in the high Fe region at the top of the SPP the average = 3.194 (range = 1.946 – 5.414), and in the strip on the left hand side with a high Fe content the average = 5.741 (range = 3.418 – 8.597). In the middle of the SPP the average Fe/Cr ratio = 0.324 (range = 0.058 – 1.073).

Figure 4.89 shows an SPP in a pure water oxide for 165 days (average oxide thickness = 3.99 μm), which is between 0.65-1.18 μm from the OM interface (2-15 days). Figure 4.90 shows the O, Cr and Fe relative composition maps, which show that the particle has much more O present than those previously shown, but only where the Cr has stayed in the SPP. There is virtually no Fe left in the SPP, and it has migrated to crack above the SPP. The 3 parameters are shown in Table 4.10, which

again shows some variability for Cr. The Cr L_3/L_2 ratio indicates oxidation in the middle of the SPP and in the High Cr region, but the FWHM is larger than the Cr value (possibly due to the sample being too thick in this region). The value of $\Delta E(\text{Cr})$ is slightly higher in those areas than for Cr, although it is much lower than that for Cr^{3+} . Cr is not oxidised in the high Fe region, which again shows no O peak in its EELS spectrum (see Figure 4.88). This suggests that the Fe is stabilising the Cr from oxidising. Figure 4.88 also shows the splitting of the O K-edge in the region of a crack with a high Cr content, as seen previously in Figures 4.69 & 4.81.

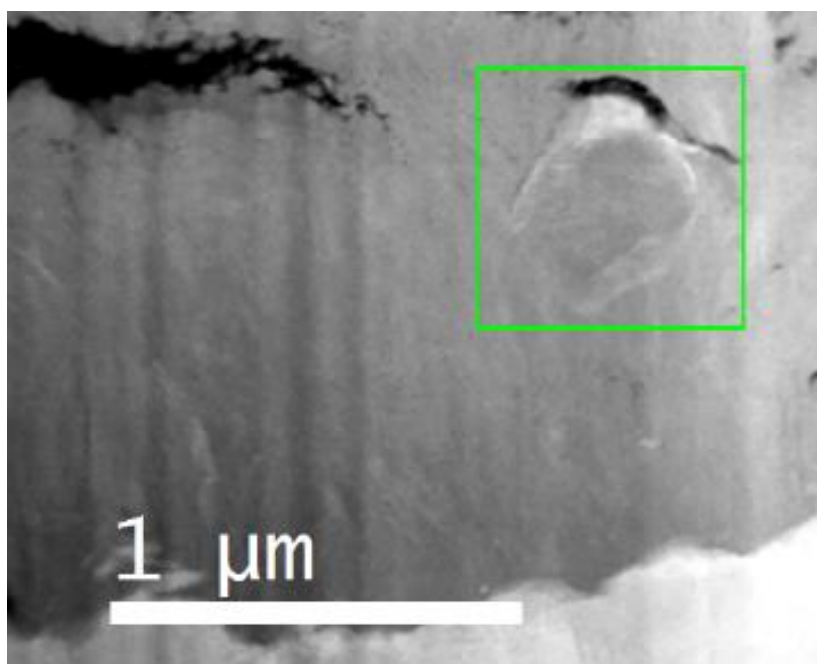


Figure 4.89 – SPP in pure water 165 day oxide. The green box shows the area where the SI was obtained.

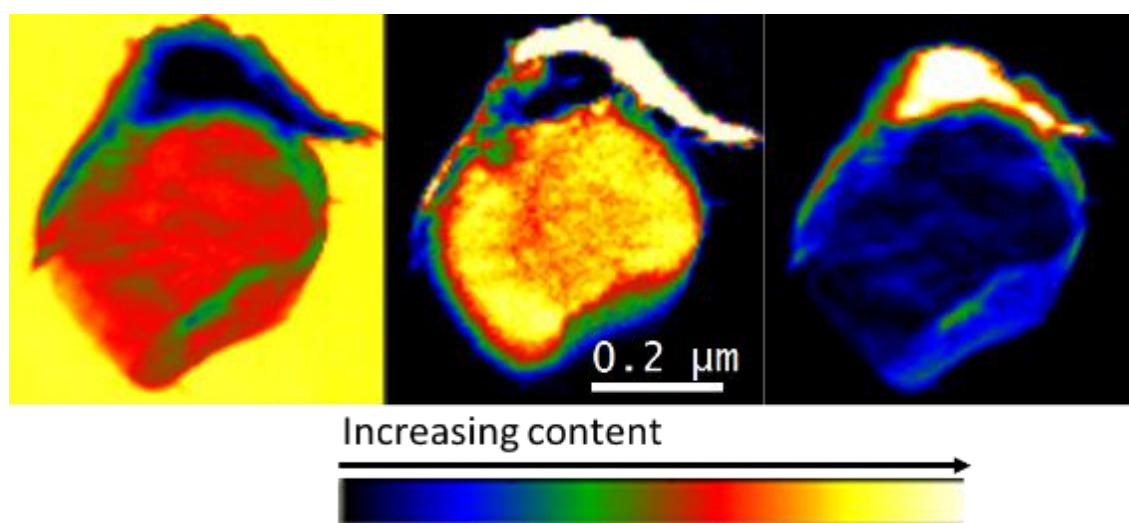


Figure 4.90 – Relative composition maps (from left to right) of O, Cr and Fe for SPP from Figure 4.89.

	High Cr	Middle of SPP	High Fe
$\Delta E(\text{Cr})$	44.5	44.25	43.75
Cr FWHM	4	3.75	4
Cr L_3/L_2 ratio	1.83	1.74	1.59
$\Delta E(\text{Fe})$	-	175.25	175.25
Fe FWHM	-	3.25	3.88
Fe L_3/L_2 ratio	-	2.95	3.1

Table 4.10 – Cr and Fe oxidation behaviour for SPP in Figure 4.89.

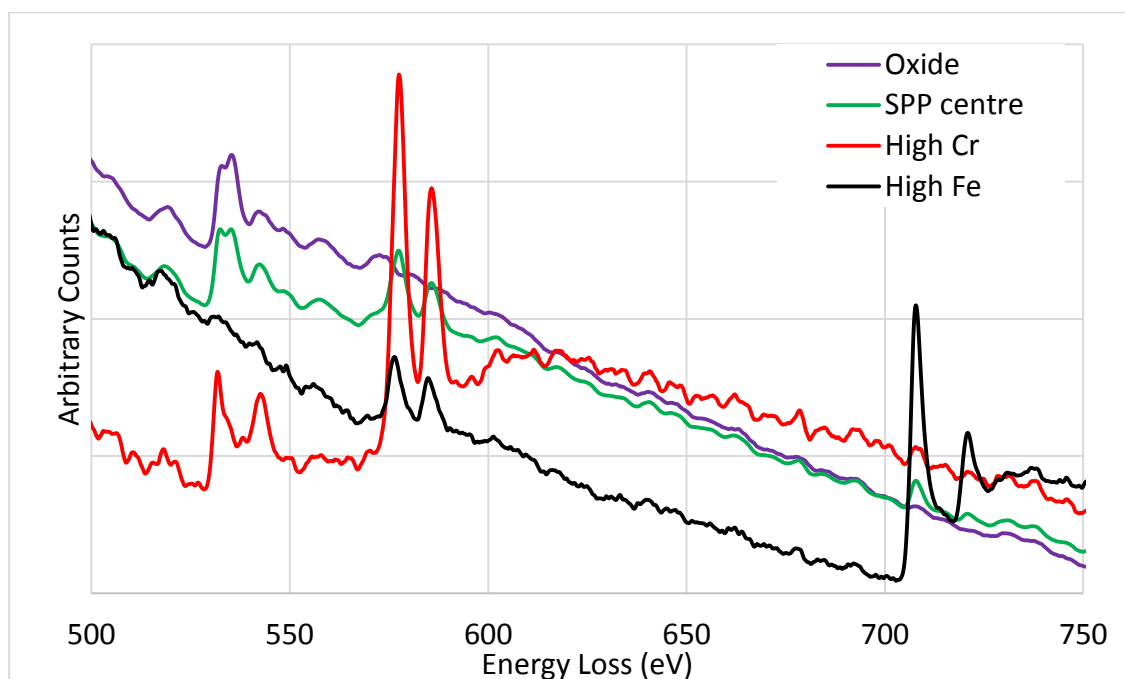


Figure 4.91 – EELS spectra for 4 regions of the SPP in Figure 4.89.

The Fe/Cr ratio varies drastically in the SPP, as shown in Figure 4.92. In the centre of the SPP the average ratio is 0.073 (range = 0.005-0.155), at the bottom of the SPP the average ratio is 0.507 (range = 0.319 – 0.781), along the strip to the top-left it is 1.253 (range = 1.118 – 1.593), across the green/red/yellow region the average is 4.000 (range = 3.376 – 5.872) and the brightest region is 8.217 (range = 6.984 – 9.262).

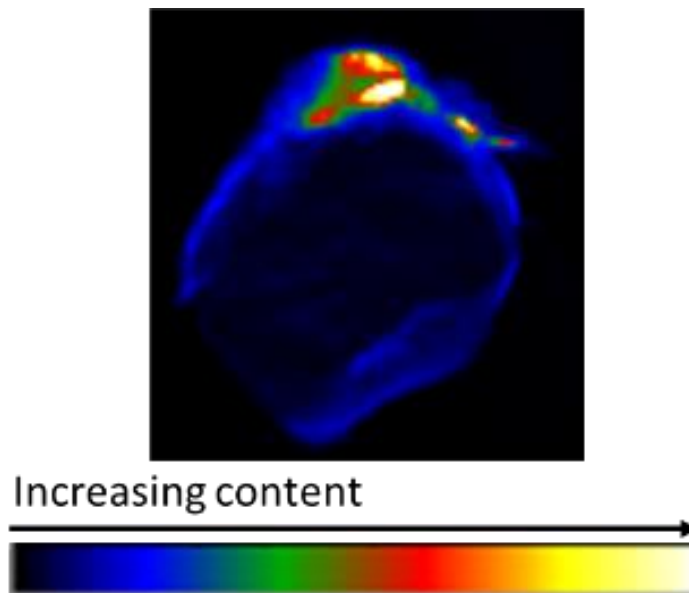


Figure 4.92 – Fe/Cr ratio map of SPP from Figure 4.89.

Figure 4.93 shows an SPP 1.55 μm from the OM interface in a sample exposed to high pH for 123 days (average oxide thickness = 2.08 μm), which is 170 nm tall, so has been in the oxide for between ~64-85 days. The relative composition maps for O, Cr and Fe are shown in Figure 4.94, which shows the same phenomenon as was shown in the previous SPPs. The Fe and Cr have migrated to the crack, and the Fe and Cr are un-oxidised in the High Fe region in the crack, shown in Figure 4.95 and Table 4.11, where there is no O peak in the High Fe region. The Cr data is again contradictory, as the L_3/L_2 ratio indicates oxidation has occurred, even in the High Fe region, the $\Delta E(\text{Cr})$ is slightly higher than the un-oxidised, hinting at oxidation, and the FWHM values show no oxidation has occurred. It is probable that there is some oxidation in the middle of the SPP and the High Cr region, but not throughout.

Again the Fe/Cr ratio varies across the SPP. In the centre of the SPP the Fe/Cr ratio has an average of 0.122 (range = 0.030 – 0.209), and in the crack the average = 4.135 (range = 1.922 – 6.160)

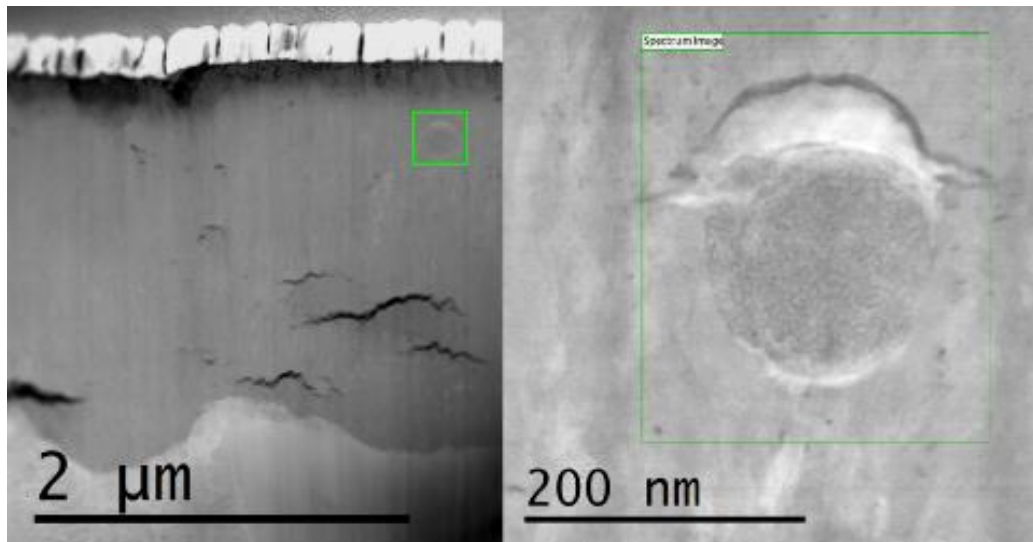


Figure 4.93 – SPP 1.55 μm from OM interface in a 123 day high pH oxide (left), with a close up DF image (right), showing a filled crack above it.

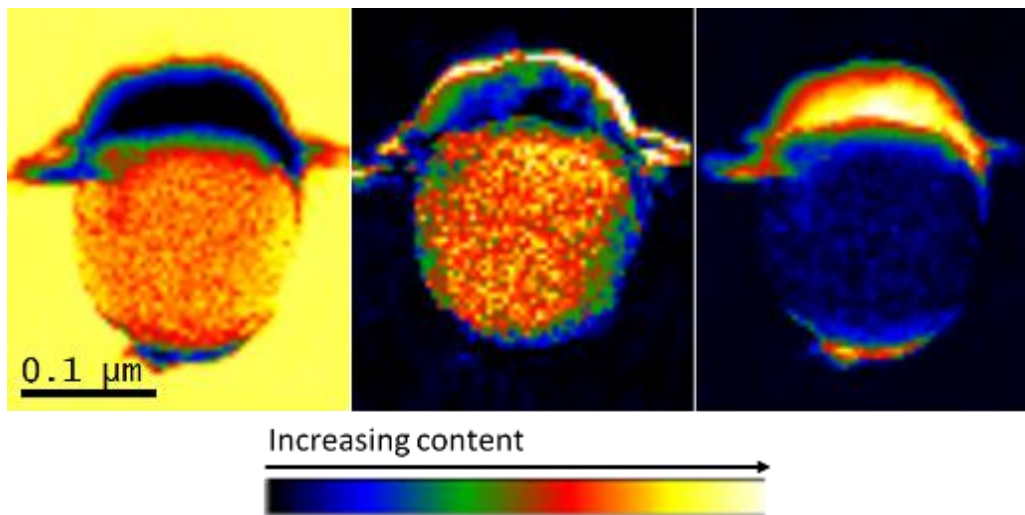


Figure 4.94 – Relative composition maps (from left to right) of O, Cr and Fe for SPP from Figure 4.93.

	High Cr	Middle of SPP	High Fe
$\Delta E(\text{Cr})$	44.75	44.75	44
Cr FWHM	3.75	3.75	4.25
Cr L_3/L_2 ratio	2.03	1.97	1.84
$\Delta E(\text{Fe})$	-	-	176.5
Fe FWHM	-	-	3.75
Fe L_3/L_2 ratio	-	-	3.28

Table 4.11 – Cr and Fe oxidation behaviour for the SPP shown in Figure 4.93.

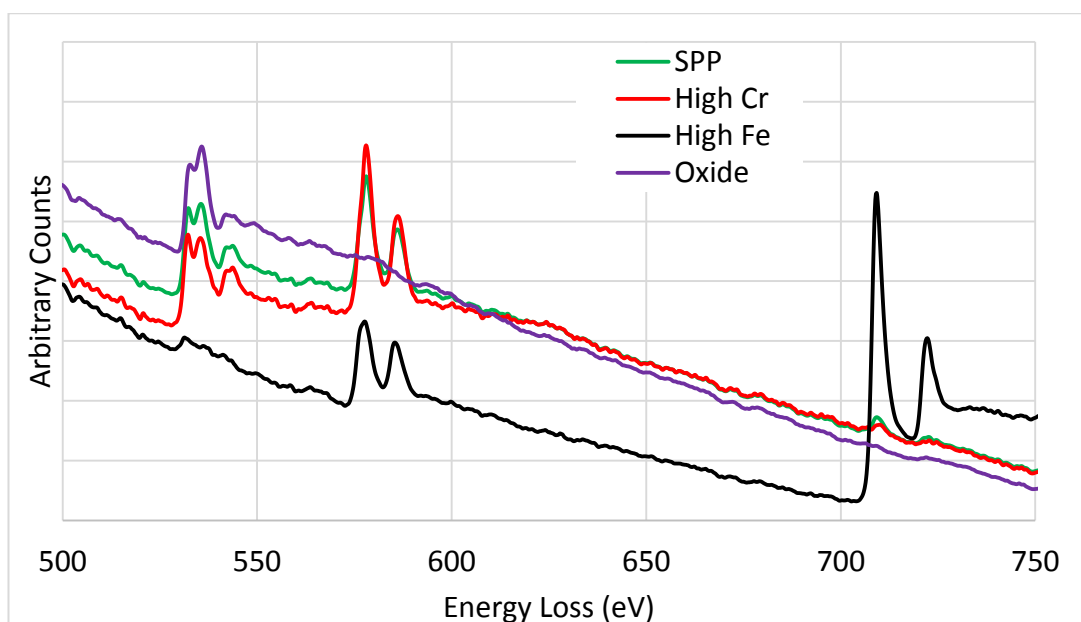


Figure 4.95 – EELS spectra at four points of the SPP shown in Figure 4.93.

Figure 4.96 shows an SPP 2.1 μm from the OM interface in a sample exposed to high pH for 148 days (average oxide thickness = 2.93 μm), which is 260 nm tall, equating to approximately 125 – 131 days in the oxide. The DF image to the right shows bright areas in the cracks at the top and bottom of the SPP, which are as usual filled with Cr and Fe, as shown in the composition maps in Figure 4.97. As seen previously there is relatively little Cr or Fe left in the SPP, and in this SPP the Cr which is left has been oxidised (see Table 4.12). The region with high Cr has partially oxidised, again based on the fact that the $\Delta E(\text{Cr})$ is in between the Cr and Cr^{3+} values and the L_3/L_2 ratio is in the oxidised range. Neither the Cr nor the Fe have oxidised in the High Fe region. This is expected as the O content in this region is much lower than elsewhere in the map.

The Fe/Cr ratio is shown in Figure 4.98, and shows that the Fe/Cr ratio is higher in the cracks than anywhere else. There are areas in the SPP where there is no Fe left, and the average in this area = 0.122 (range = 0 – 0.362). In the brighter blue region to the bottom-right of the SPP the average = 1.164 (range = 0.913 – 1.408), the green area has an average = 1.710 (range = 1.650 – 1.813), the red/yellow region has an average = 3.156 (range = 2.519 – 3.43) and the yellow/white region average = 3.923 (range = 3.661 – 4.112).

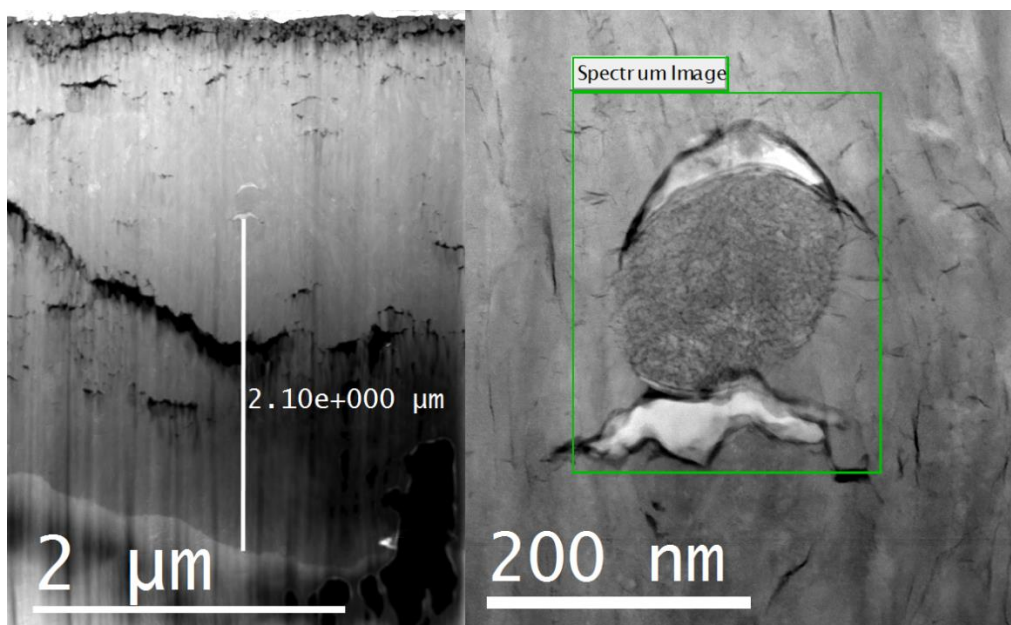


Figure 4.96 – Left; an SPP 2.1 μm from the OM interface in a high pH oxide. Right; close up of the SPP, the green box shows the area of analysis by EELS.

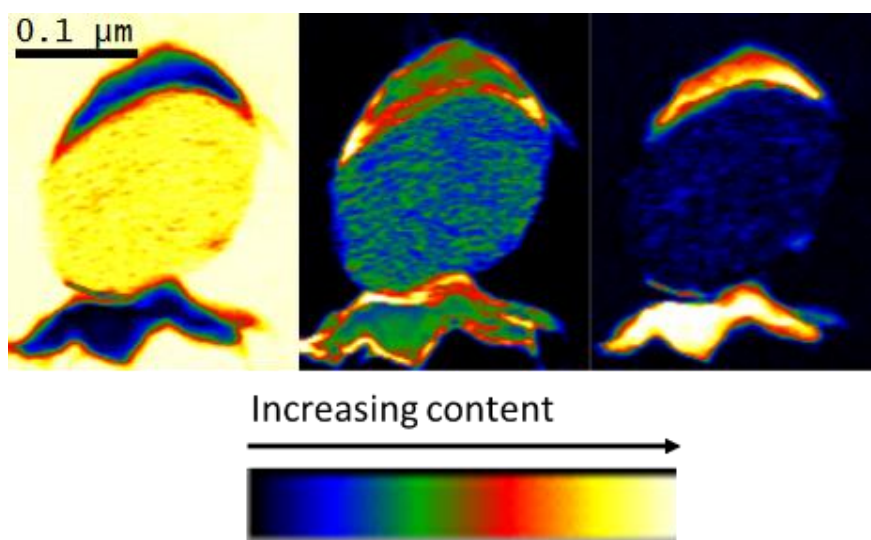


Figure 4.97 – Relative composition maps (from left to right) of O, Cr and Fe for SPP from Figure 4.93.

	High Cr	Middle of SPP	High Fe
$\Delta E(\text{Cr})$	44.75	45	43.25
Cr FWHM	3.75	3.25	4.75
Cr L_3/L_2 ratio	1.76	1.72	1.57
$\Delta E(\text{Fe})$	-	-	176
Fe FWHM	-	-	4.0
Fe L_3/L_2 ratio	-	-	3.28

Table 4.12 – Cr and Fe oxidation behaviour for SPP in Figure 4.96.

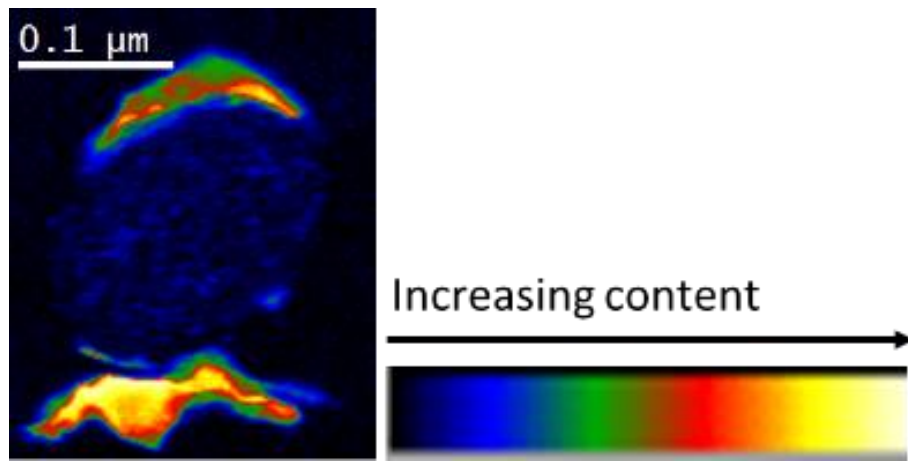


Figure 4.98 – Fe/Cr ratio of SPP in Figure 4.96.

Figure 4.99 shows an SPP 2.45 μm from the OM interface in a sample exposed to high pH for 211 days (average oxide thickness = 3.86 μm), which measures 490 nm from the top of the upper crack to the bottom of the lower crack. This has been in the oxide from between ~132 – 147 days.

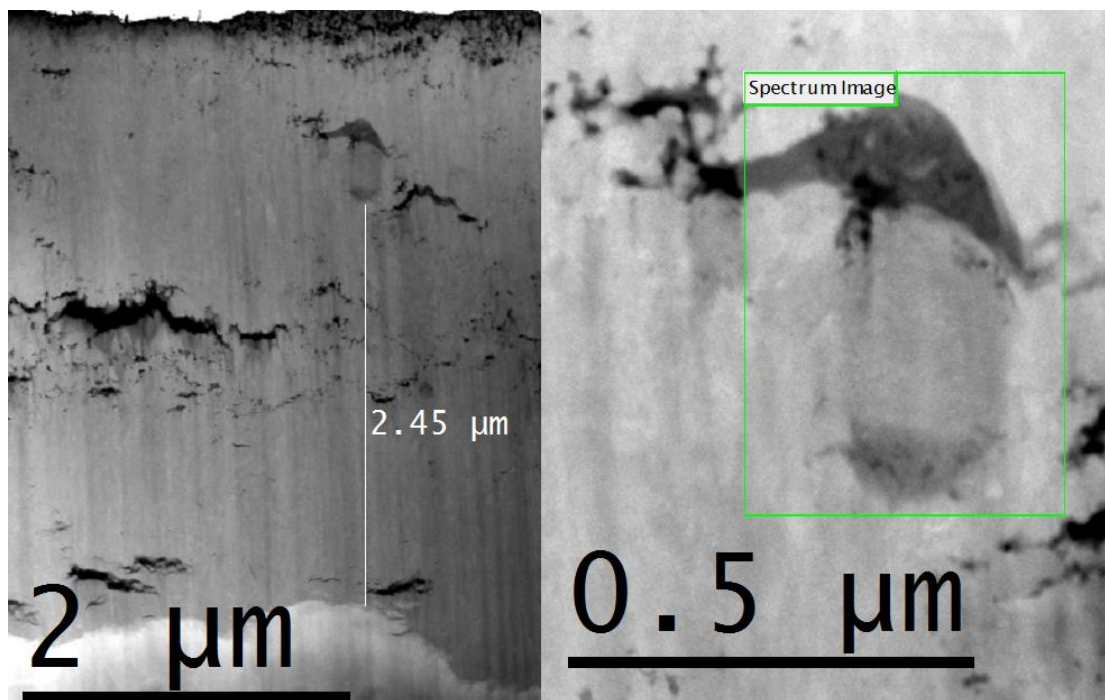


Figure 4.99 – SPP 2.45 μm from OM interface in high pH oxide (left), and close up DF showing where the EELS spectra were collected (right).

Figure 4.100 shows the relative composition maps for O, Cr and Fe, showing a slightly different behaviour for the Fe and Cr. This time the Fe has migrated further from the SPP compared to the Cr and there is a large concentration in the crack to the upper left of the SPP. There is virtually no Fe left in the SPP. Table 4.13 shows the 3 parameters for the four indicated regions in Figure 4.100; 1) High Cr, 2) Medium Cr/Fe, 3) Middle of SPP, and 4) High Fe. The L_3/L_2 ratio for both Cr and Fe indicates

that both have oxidised. $\Delta E(\text{Cr})$ is again between the values for Cr and Cr^{3+} , and $\Delta E(\text{Fe})$ is close to the value for Fe^{2+} . The FWHM is higher for both Cr and Fe because this sample was slightly thicker than the one shown in Figure 4.93. This is the first case where I am confident that both elements are oxidised throughout.

The Fe/Cr ratio is virtually zero in the centre of the SPP, and increases to 0.122 in the High Cr region (range = 0.069 – 0.187). In the Medium Cr/Fe region the Fe/Cr ratio increases to an average of 0.879 (range 0.816 – 0.941), and in the High Fe region the average = 2.700 (range = 1.055 – 2.984).

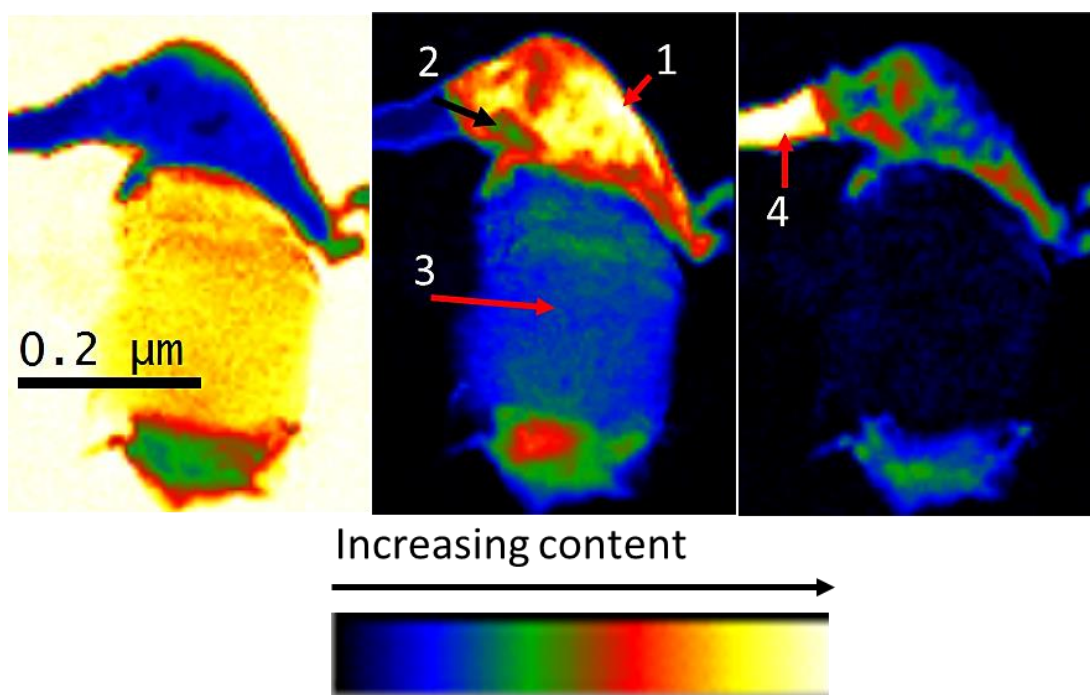


Figure 4.100 – Relative composition maps (from left to right) of O, Cr and Fe for SPP from Figure 4.99. The four indicated areas are: 1) High Cr, 2) Medium Cr/Fe, 3) Middle of SPP, and 4) High Fe.

	High Cr	Medium Cr/Fe	Middle of SPP	High Fe
$\Delta E(\text{Cr})$	44.75	44.75	44.75	-
Cr FWHM	3.75	3.63	3.5	-
Cr L_3/L_2 ratio	1.97	2.05	1.84	-
$\Delta E(\text{Fe})$	-	176.75	-	176.75
Fe FWHM	-	4.13	-	3.88
Fe L_3/L_2 ratio	-	4.28	-	4.32

Table 4.13 – Cr and Fe oxidation behaviour for SPP in Figure 4.99.

Figure 4.101 shows an SPP 4.03 μm from the OM interface in a sample exposed to pure water for 165 days (average oxide thickness = 3.99 μm), which is approximately 260 nm tall, meaning it has been in the oxide for $\sim 163 - 189$ days. The O, Cr, and Fe composition maps are shown in Figure 4.102. This shows the familiar behaviour seen in the previous SPPs, the vast majority of the Fe is only in the cracks, some Cr has stayed in the SPP, where it is oxidised, along with the Cr in the High Cr region (which is in a crack). Table 4.12 shows the oxidation behaviour, the Fe L_3/L_2 ratio again indicates that the Fe has oxidised, although the $\Delta E(\text{Fe})$ value is lower than the previous SPP. The higher value for the FWHM for both Cr and Fe could be again due to the sample being too thick in this region.

There is some Fe left in the SPP, and the Fe/Cr ratio in the SPP = 0.094 (range = 0.007 – 0.289), in the High Cr region the average = 0.94 (range = 0.694 – 1.303) and in the High Fe region the average = 3.6 (range = 2.348 – 5.1).

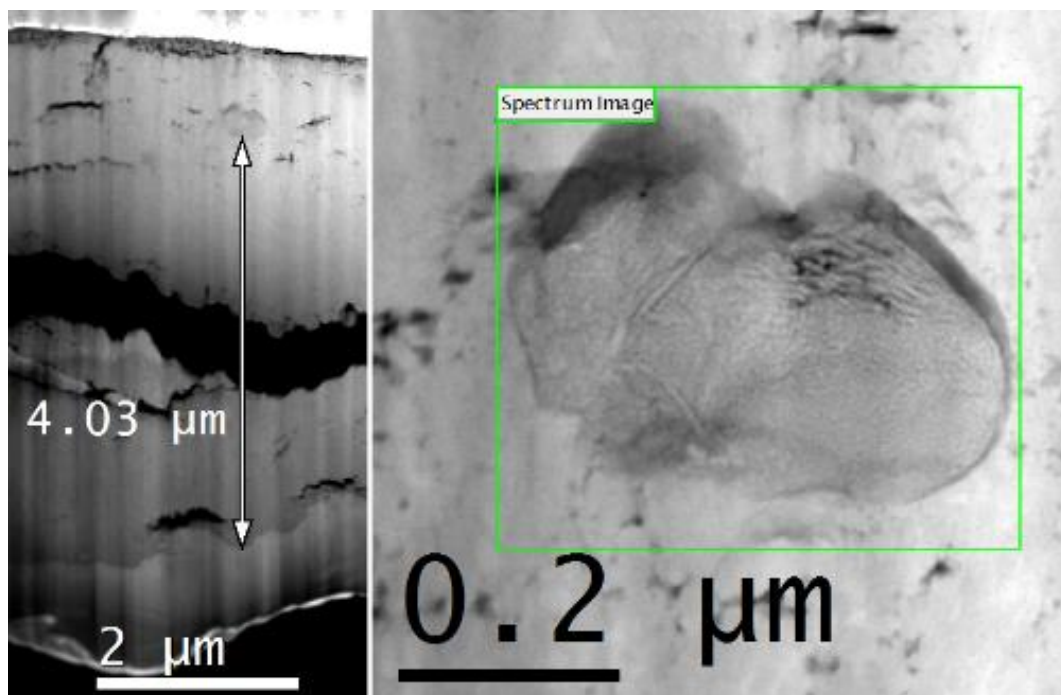


Figure 4.101 – SPP 4.03 μm from the OM interface in a pure water oxide.

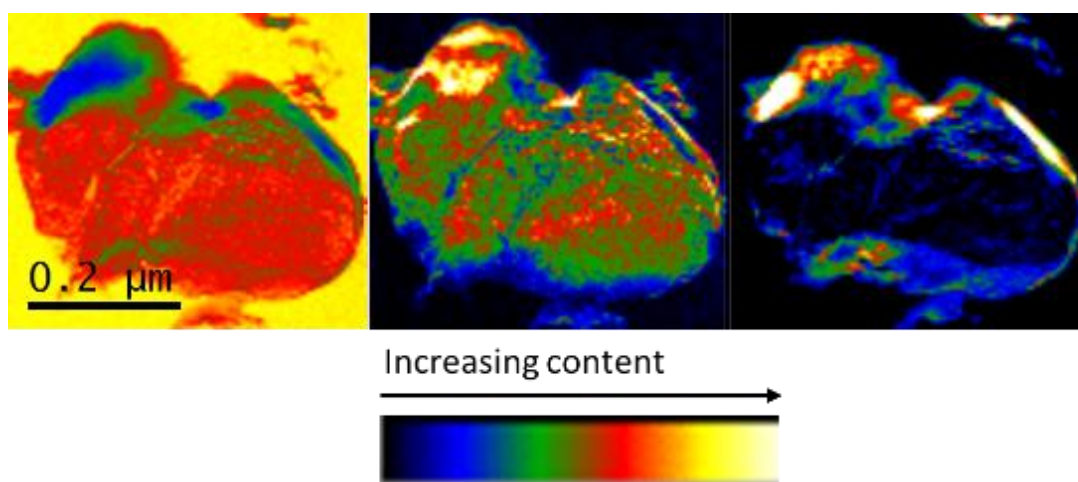


Figure 4.102 – Relative composition maps (from left to right) of O, Cr and Fe for SPP from Figure 4.101.

	High Cr	Middle of SPP	High Fe
$\Delta E(\text{Cr})$	44.75	44.5	44.75
Cr FWHM	3.5	3.5	3.5
Cr L_3/L_2 ratio	2.13	2.12	1.96
$\Delta E(\text{Fe})$	176	-	175.5
Fe FWHM	3.88	-	4
Fe L_3/L_2 ratio	4.07		4.04

Table 4.14 - Cr and Fe oxidation behaviour for SPP in Figure 4.101.

4.3 – Discussion

In section 4.1 I showed that the difference in oxidation rates during pre-transition oxidation was due in part to the difference in the exposure temperature and the difference in the pH. As the activation energy was not significantly higher than that found in the literature I estimate that most of the difference is due to temperature and the pH has a smaller effect. This was confirmed by my observations of the suboxide growth as a function of measured oxide thickness, which was independent of the environment. This means that oxidation is not limited by the availability of protons in the oxidising water. The available protons are used for charge balance with the electrons liberated during corrosion, either by the electrons flowing through the oxide to form hydrogen gas, or by the inward migration of protons to form hydrides. Therefore, if changing the number of available protons does not change the oxidation rate, the rate of electron transport must be much higher than the proton transport through the oxide. This would also indicate that the amount of hydrogen pick-up in the pre-

transition regime would be similar as both materials have similar hydrogen transport rates. This will be discussed in the next chapter. The value of n in equation (3.1) was higher for the high pH environment, which means that the hydrogen pick-up fraction should be lower towards the end of the second cycle. This will also be discussed in the next chapter.

In Figures 4.40 – 4.43 I showed the various MLLS fits I carried out on a 243 day high pH oxide, in which it proved difficult to determine where exactly the OSZ region was. I am not sure why the OSZ region behaved like this for this sample, but a possible reason for this is that in these regions the sample is approaching a second transition, where the ZrO and OSZ are fully oxidised into zirconia by the rapidly increasing oxygen content at the OM interface.

There are two pieces of evidence that I have found that indicate that this is the reason. The first is that the shape of the plasmon peaks for the ZrO is slightly altered in both the 243 day samples I looked at, as shown in Figure 4.103. The ZrO₂ plasmon peaks contain two peaks at approximately 15 eV and 27 eV, and for ZrO there is a broad peak in this energy range. For the ZrO in the 243 day sample there is a shoulder forming at the higher energy range, which indicates that it is starting to oxidise further. The second piece of evidence is that there is a region in the sample shown in Figure 4.32 (reproduced in Figure 4.104) which after carrying out MLLS shows little ZrO (shown in Figure 4.105), which is still present along the OM interface under the large crack shown in Figure 4.104.

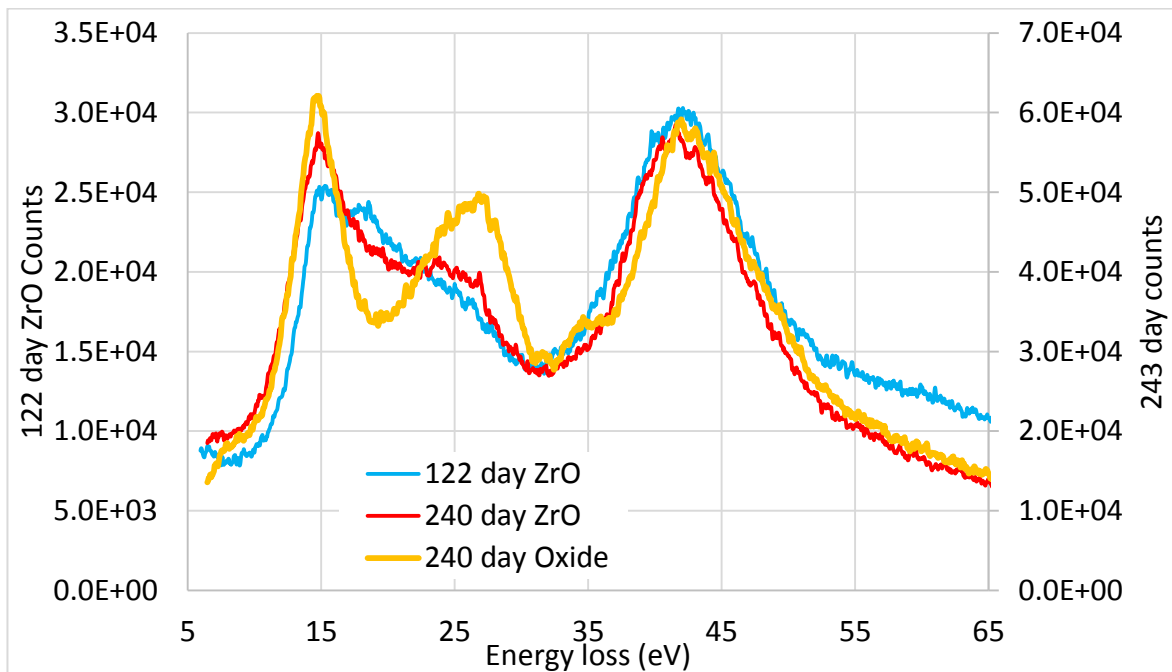


Figure 4.103 – ZrO plasmon peaks for 122 day and 243 oxide, with ZrO₂ peak for 243 day sample. Compared to the 122 day peak, the lower energy 243 day ZrO peak is starting to split towards the two peaks present in the ZrO₂.

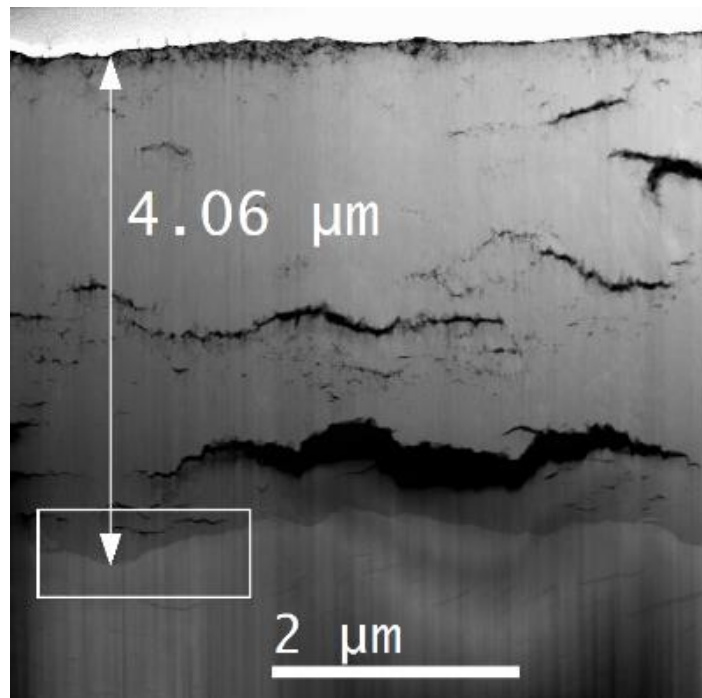


Figure 4.104 – 243 day oxide, reproduced from Figure 4.39. EELS was carried out in the white box, shown in Figure 4.105.

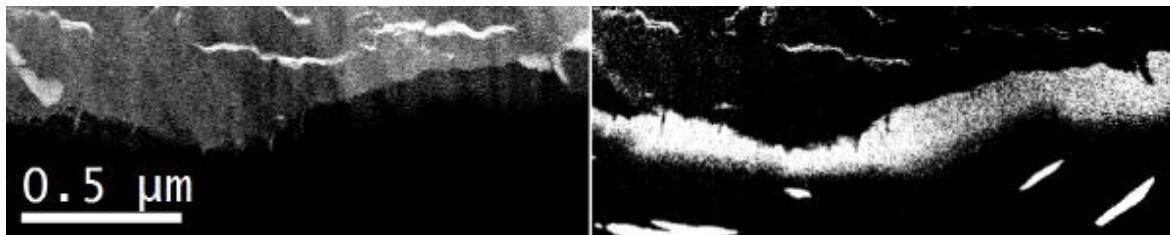


Figure 4.105 – MLLS fit for ZrO (left) and OSZ (right, with hydrides).

In section 4.2.4 I showed the results of the EELS examination of SPPs near the OM interface and at various depths in the oxide. I measured the Fe/Cr ratio on the SPPs I examined, and Figure 4.106 shows this ratio in the centre of the SPP and at the cracks formed around the SPP as a function of distance from the OM interface. The Fe/Cr ratio in the centre of the SPP shows the same trend shown by Takahashi et al.^{24–26}, and is virtually zero after 0.8 μm into the oxide. The Fe/Cr ratio in the cracks initially increases as Fe migrates faster from the SPP than Cr, except for in one SPP (SPP1 in Figure 4.79) which had a uniform Fe/Cr ratio in the SPP and crack. After this the Cr content increases in the cracks.

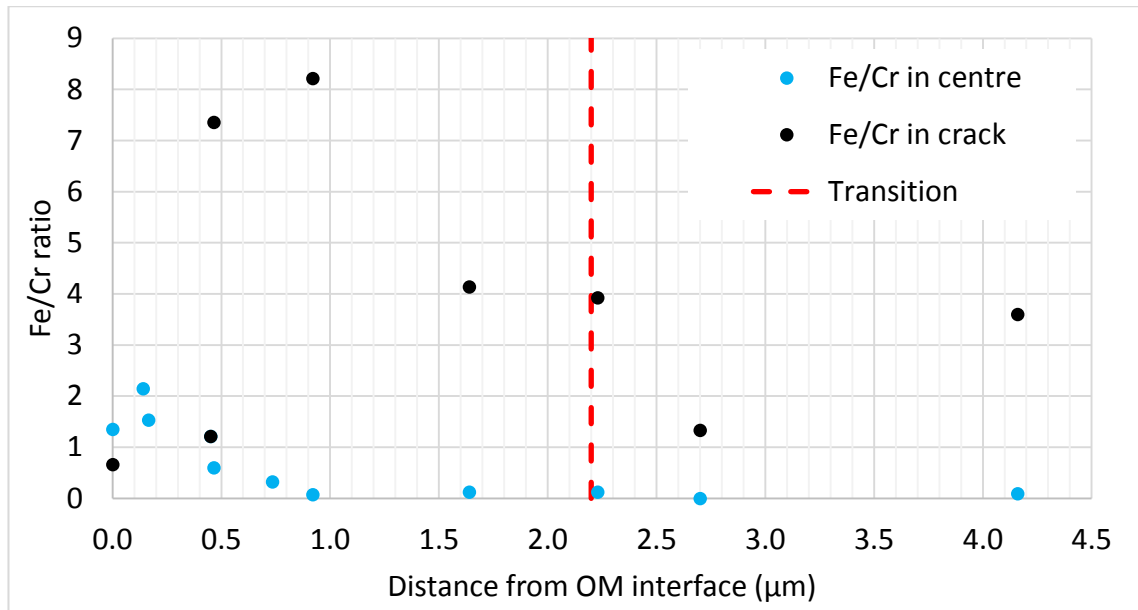


Figure 4.106 – Fe/Cr ratio for SPP at various distances from OM interface.

From the composition maps shown for the various SPPs it is possible to show the relative amount of O in the middle of the SPP and in the cracks, which is shown in Figure 4.107. Note the composition maps assume that the amount of O + Cr + Fe = 100%, and does not take into account the Zr present. It can be seen that there is an increase in the O content in the crack after the SPP distance from the OM interface passes 2.2 μm (the oxide thickness at transition). This is the SPP shown in Figure 4.99, which was the first one which showed that both Fe and Cr were oxidised. The increase in the O content in the crack for this SPP could be the reason the Fe/Cr ratio in the crack drops for this SPP.

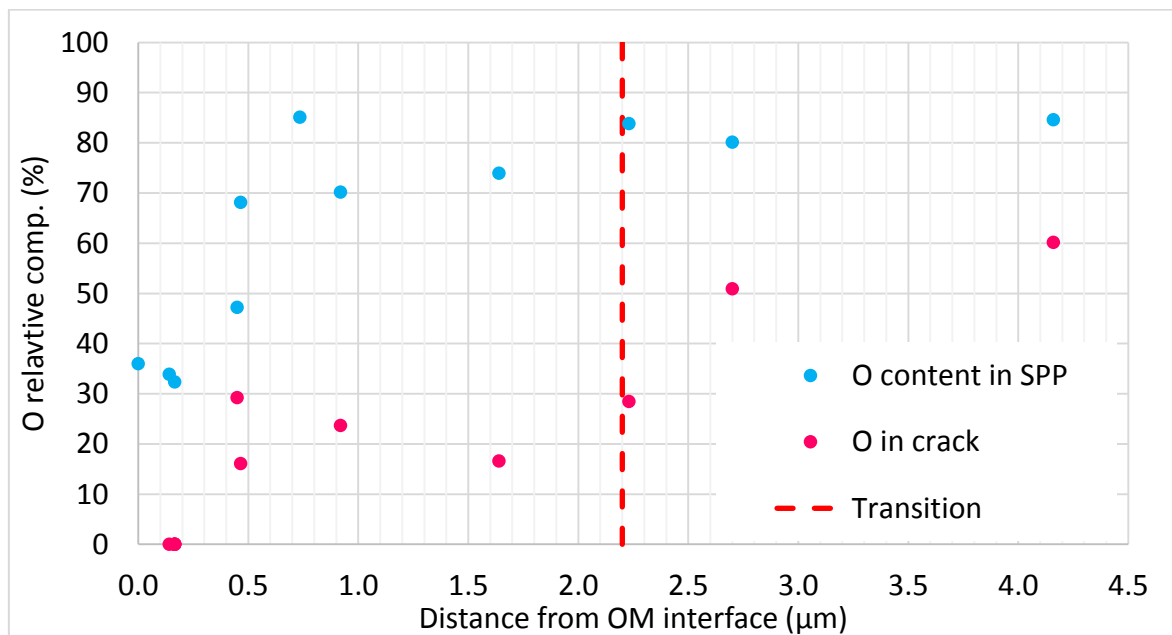


Figure 4.107 – O composition (relative) vs SPP distance from OM interface.

I used 3 different parameters to quantify if the Cr and Fe was oxidised in the SPPs, which has proved useful as a single parameter was somewhat inconsistent. The FWHM data (shown in Figure 4.108) was sensitive to the sample thickness so is only really useful if all samples are of the same thickness. The Fe results were constantly above the value for Fe and never decreased below 3.2, although there was a general trend for the peak to narrow. The Cr FWHM in the middle of the SPP (green points in Figure 4.108) shows a clear tendency to narrow, although the Cr FWHM in the cracks for high Cr regions broadens (red points with yellow borders).

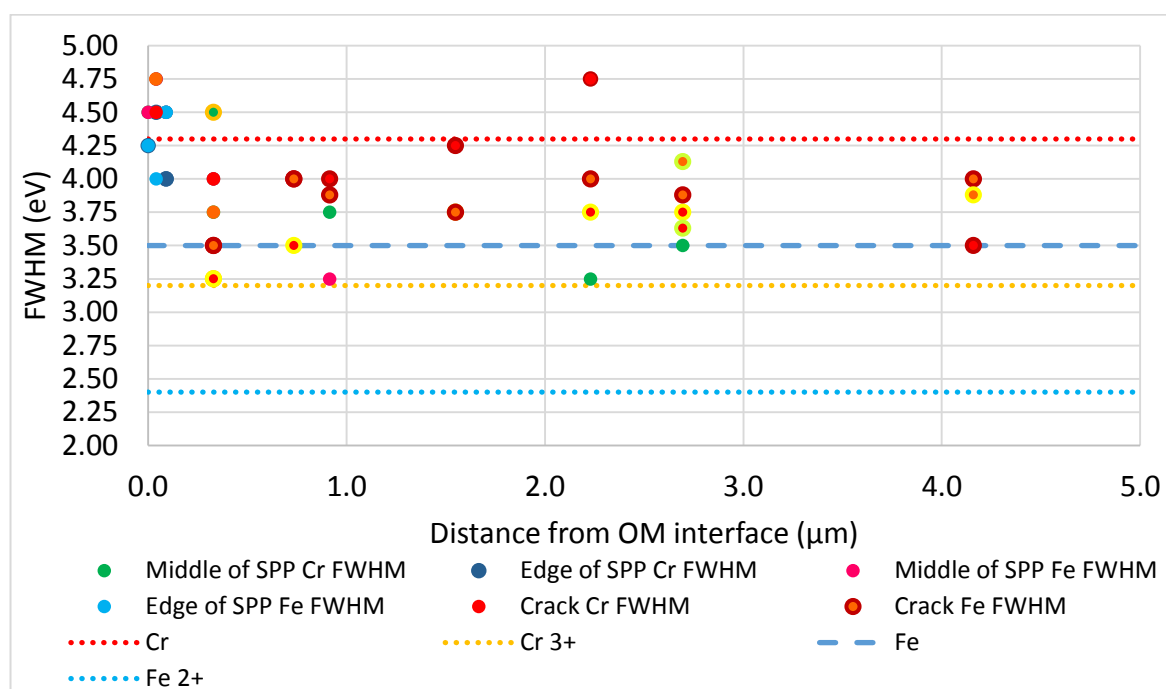


Figure 4.108 – FWHM values for Cr and Fe for the SPPs shown in section 4.2.4. Points with a yellow border are in a high Cr region, dark red is a high Fe region, orange is the High O region in SPP1 in Figure 4.79, and the light green is for a medium Cr/Fe region.

Figure 4.109 shows a plot of the values of $\Delta E(\text{Cr})$ (a) and $\Delta E(\text{Fe})$ (b) against the distance of the SPP from the OM interface. The $\Delta E(\text{Cr})$ for example has not been found to reach the value for Cr^{3+} (46.5 eV), which would have led me to believe that Cr did not oxidise at all in these tests, or that it only reaches Cr^{2+} , which has an energy shift of ~ 45 eV¹⁹. This was true for the Cr measurements at various points in the SPPs. The $\Delta E(\text{Fe})$ values were slightly more consistent, and there is a trend for the Fe shift in the crack to increase. In the middle of the SPP and there does not appear to be one, although there were not many points for these as Fe migrates away from these regions quickly.

The L_3/L_2 ratio was the most consistent of the 3 parameters, in that there was a noticeable increase as the SPPs were in the oxide for longer (see Figure 4.110) but was still not easy to interpret on its own.

For future work it would be useful to carry out measurements of the three parameters mentioned on pure samples of Cr, Cr³⁺, Fe and Fe²⁺ to obtain a standard to compare results with.

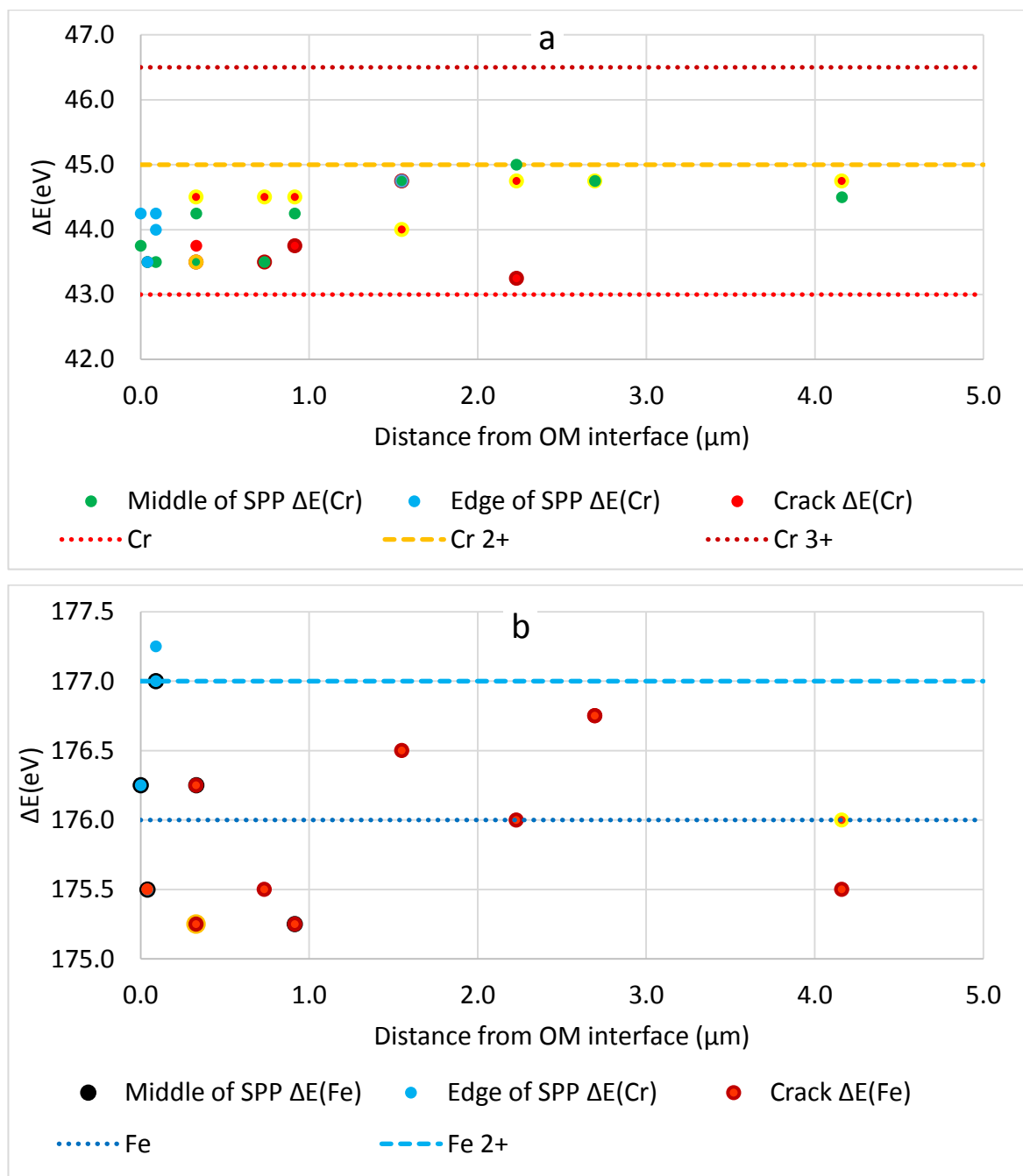


Figure 4.109 - $\Delta E(\text{Cr})$ (a) and $\Delta E(\text{Fe})$ (b) values for all the SPPs shown in section 4.2.4. The orange border is for a high O region in SPP1 from Figure 4.79, the yellow border signifies high Cr regions, and the dark red border is in high Fe regions.

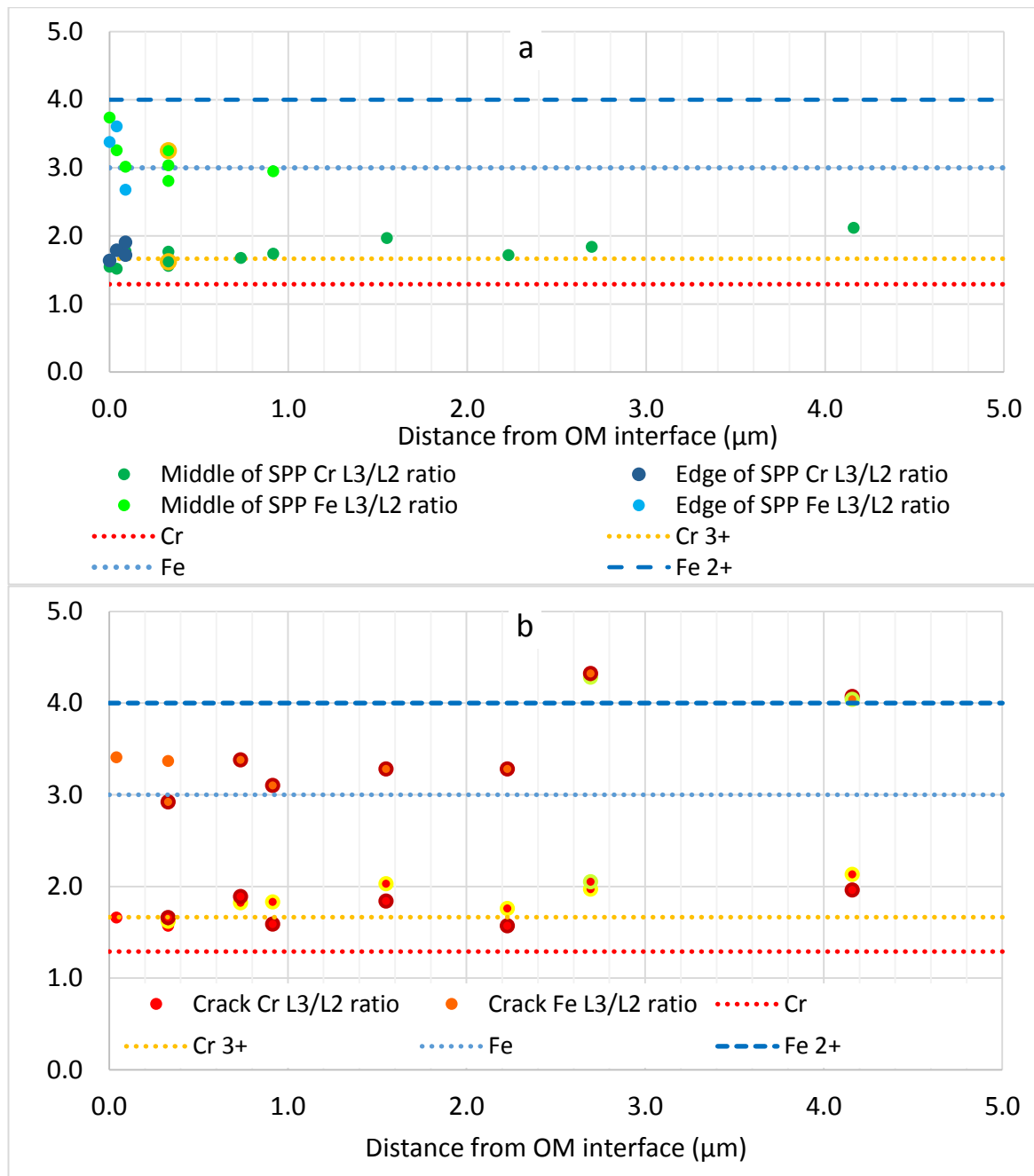


Figure 4.110 – L_3/L_2 ratio for Cr and Fe vs SPP distance from OM interface. In a) the orange border is for a high O region in SPP1 from Figure 4.79. In b) the yellow border signifies high Cr regions, dark red high Fe regions, and light green medium Fe/Cr.

4.4 – Summary

I have shown in this chapter that the oxidation of Zircaloy-4 is not affected by the pH range tested of the oxidising water; first by comparing the oxidation rates, then by examining the OM interface and the growth of the OSZ and ZrO layers as oxidation occurs. The OSZ and ZrO layers show a cyclical nature, in that they both gradually get thicker as the oxidation time increases, before being consumed just after transition, and then re-growing in the second stage of oxidation.

The SPPs generally show the same oxidation behaviour. Cracks form above and below the SPPs as they are passed by the OM interface. Zr in the SPP is oxidised first, with oxidation at the surface of the SPP as the SPP encounters the OM interface, even while part of the SPP may be in contact with the metal. The solubility of metals in oxides is very low, so the metallic Cr and Fe migrate out of the oxidised regions of the SPP. As the OM interface moves further into the metal, leaving the SPP within the oxide, Zr oxidation progresses further into the SPP, the metallic Cr and Fe migrate into the cracks surrounding the SPP. As the OM interface moves further away from the SPP and the oxygen potential increases, Cr begins to oxidise, and metallic Fe migrates away from the oxidised Cr.

In the cracks the Cr will start oxidising in regions of low Fe first (after around 10 days). In regions with Cr and Fe together, the Cr does not oxidise in Fe until the SPP has been in the oxide for over 130 days (2.1 μm oxide thickness). Fe was not oxidised in the crack at 2.1 μm but was at 2.45 μm , which means it oxidises in between these regions. There did not appear to be any effect of pH on the oxidation of the SPPs.

4.5 – References

1. Hillner E, Franklin DG, Smee J. Long-term corrosion of Zircaloy before and after irradiation. *J Nucl Mater.* 2000;278(2-3):334-345. doi:10.1016/S0022-3115(99)00230-5.
2. Yilmazbayhan A, Breval E, Motta AT, Comstock RJ. Transmission electron microscopy examination of oxide layers formed on Zr alloys. *J Nucl Mater.* 2006;349(3):265-281. doi:10.1016/j.jnucmat.2005.10.012.
3. Billot P, Beslu P, Giordano A, Thomazet J. Development of a mechanistic model to assess the external corrosion of the Zircaloy claddings in PWRs. In: Van Swam L, Eucken C, eds. *Zirconium in the Nuclear Industry: 8th International Symposium, ASTM STP 1023*. ASTM International; 1989:165184.
4. Bradhurst DH, Heuer PM. The temperature dependence of the in-reactor oxidation of zirconium alloys in moist CO₂ atmospheres from 573–868K. *J Nucl Mater.* 1981;96(1):196-204. doi:http://dx.doi.org/10.1016/0022-3115(81)90233-6.
5. Ocken H, Biederman RR, Hann CR, Westerman R. Evaluation models of Zircaloy oxidation in light of recent experiments. In: *Zirconium in the Nuclear Industry: 4th International Symposium, ASTM STP 681*. ASTM International; 1979:514-536.
6. Perkins RA, Busch RA. Corrosion of Zircaloy in the presence of LiOH. In: *Zirconium in the Nuclear Industry: Ninth International Symposium, ASTM STP 1132*. Publ by ASTM;

1991:595-611. Available at: <http://www.scopus.com/inward/record.url?eid=2-s2.0-0026399521&partnerID=tZOtx3y1>.

7. Garzarolli F, Jorde D, Manzel R, Politano JR, Smerd PG. Waterside corrosion of Zircaloy-clad fuel rods in a PWR environment. In: Franklin D, ed. *Zirconium in the Nuclear Industry: Fifth Conference, ASTM STP 754*. ASTM International; 1982:430-449.
8. Bouineau V, Ambard A, Bénier G, et al. A new model to predict the oxidation kinetics of zirconium alloys in a pressurized water reactor. In: Kammenzind B, Limbäck M, eds. *Zirconium in the Nuclear Industry: 15th International Symposium, ASTM STP 1505*. ASTM International; 2009:405-429.
9. Müller S, Lanzani L. Corrosion of zirconium alloys in concentrated lithium hydroxide solutions. *J Nucl Mater.* 2013;439(1-3):251-257. doi:10.1016/j.jnucmat.2012.07.030.
10. Pêcheur D, Godlewski J, Billot P, Thomazet J. Microstructure of oxide films formed during the waterside corrosion of the Zircaloy-4 cladding in lithiated environment. In: Bradley ER, Sabol GP, eds. *Zirconium in the Nuclear Industry: Eleventh International Symposium ASTM STP 1295*. ASTM International; 1996:94-113.
11. Ramasubramanian N. Lithium uptake and the corrosion of zirconium alloys in aqueous lithium hydroxide solutions. In: Eucken CM, Garde AM, eds. *Zirconium in the Nuclear Industry: Ninth International Symposium, ASTM STP 1132*. ASTM International; 1991:613-626.
12. Cox B, Ungurelu M, Wong YM, Wu C. Mechanisms of LiOH degradation and H₃BO₃ repair of ZrO₂ films. In: Bradley ER, Sabol GP, eds. *Zirconium in the Nuclear Industry: Eleventh International Symposium, ASTM STP 1295*. ASTM International; 1996:114-136.
13. Cox B, Wu C. Transient effects of lithium hydroxide and boric acid on Zircaloy corrosion. *J Nucl Mater.* 1995;224:169-178.
14. Romero J, Partezana J, Comstock RJ, Hallstadius L, Motta AT, Couet A. Evolution of hydrogen pickup fraction with oxidation rate on zirconium alloys. In: *Top Fuel 2015 - Reactor Fuel Performance*. European Nuclear Society; 2015:476-482. Available at: <https://www.euronuclear.org/events/topfuel/topfuel2015/transactions/topfuel2015-transactions-oral-1.pdf>.
15. Ni N, Lozano-Perez S, Sykes JM, Smith GDW, Grovenor CRM. Focussed ion beam sectioning for the 3D characterisation of cracking in oxide scales formed on commercial ZIRLOTM alloys during corrosion in high temperature pressurised water. *Corros Sci.* 2011;53(12):4073-4083. doi:10.1016/j.corsci.2011.08.013.
16. Platt P, Wedge S, Frankel P, Gass M, Howells R, Preuss M. A study into the impact of interface roughness development on mechanical degradation of oxides formed on zirconium alloys. *J Nucl Mater.* 2015;459:166-174. doi:10.1016/j.jnucmat.2015.01.028.

17. Aarholt T. Analytical microscopy of corroded zirconium alloys. 2017.
18. Daulton TL, Little BJ. Determination of chromium valence over the range Cr(III)-Cr(VI) by electron energy loss spectroscopy. *Ultramicroscopy*. 2006;(106):561-573. doi:10.1016/j.ultramic.2006.02.005.
19. Arévalo-López ÁM, Alario-Franco MÁ. Reliable method for determining the oxidation state in chromium oxides. *Inorg Chem*. 2009;48(24):11843-11846. doi:10.1021/ic901887y.
20. Tan H, Verbeeck J, Abakumov A, Van Tendeloo G. Oxidation state and chemical shift investigation in transition metal oxides by EELS. *Ultramicroscopy*. 2012;116:24-33. doi:10.1016/j.ultramic.2012.03.002.
21. Colliex C, Manoubi T, Ortiz C. Electron-energy-loss-spectroscopy near-edge fine structures in the iron-oxygen system. *Phys Rev B*. 1991;44(20):11402-11411. doi:10.1103/PhysRevB.44.11402.
22. Leapman RD, Grunes LA, Fejes PL. Study of the L23 edges in the 3d transition metals and their oxides by electron-energy-loss spectroscopy with comparisons to theory. *Phys Rev B*. 1982;26(2):614-635. doi:10.1103/PhysRevB.26.614.
23. Yedra L, Xuriguera E, Estrader M, et al. Oxide Wizard: An EELS application to characterize the white lines of transition metal edges. *Microsc Microanal*. 2014;20:698-705. doi:10.1017/S1431927614000440.
24. Pêcheur D, Lefebvre F, Motta AT, Lemaignan C, Wadier JF. Precipitate evolution in the Zircaloy-4 oxide layer. *J Nucl Mater*. 1992;189(3):318-332. doi:10.1016/0022-3115(92)90385-X.
25. Takahashi K, Iwasaki T, Maruno Y. Effect of precipitates in oxide film on hydrogen pick-up of zirconium alloys. In: *Top Fuel 2016: LWR Fuels with Enhanced Safety and Performance*. ANS; 2016:1245-1254.
26. Baek JH, Jeong YH. Depletion of Fe and Cr within precipitates during Zircaloy-4 oxidation. *J Nucl Mater*. 2002;304:107-116.

5 – Hydrogen Measurements

Contents

5.1 – Digital Scanning Calorimetry	134
5.2 – Thermal Desorption Spectroscopy	138
5.2.1 – Initial Findings	138
5.2.2 – Calibration Tests	140
5.2.3 – Cold Rolled Samples	143
5.2.4 – Hydrogen Charged Samples	144
5.2.5 – Impact of Oxide on Hydrogen Desorption	146
5.2.6 – Effect of pH on Hydrogen Content	149
5.2.7 – Hydrogen Content of Samples Oxidised at High pH	150
5.3 – Hydrogen Content Measurements by Westinghouse and PSI	153
5.4 – NanoSIMS Results	157
5.4.1 – Diffusion Profiles	157
5.4.2 – 3D Profiles	161
5.5 – Discussion	164
5.6 – Summary	166
5.7 – References	167

In this chapter I will discuss the hydrogen analysis of my samples. I used DSC to determine the phase changes which occur during heating, along with TDS to observe the hydrogen desorption behaviour. The TDS results were combined with HHGE data from Westinghouse and PSI to calibrate the TDS for future use in quantifying the amount of hydrogen in a sample. I will first review the data from the DSC tests, followed by the TDS results.

5.1 – Digital Scanning Calorimetry

The DSC tests were carried out to determine what phase changes occur during heating of Zircaloy-4 samples. Figure 5.1 shows the baseline subtracted results of the samples tested with DSC. Except for the 148 day sample there is a large drop in the DSC output after about 300°C. This is followed by a large increase starting at around 820°C, with a shoulder around 840°C and a maximum at 870°C. One of these processes is an exothermic reaction and the other is endothermic. The dip in the DSC outputs is due to the exothermic oxidation of the zirconium, as evidenced by their weight gain (Table 5.1) and from FIB cross sections (Figures 5.2 & 5.3).

This means that the large increase at 820°C is an endothermic process, and from the Zr-H phase diagram (Figure 5.4¹) this is due to the $\alpha \rightarrow \beta$ phase change, which occurs at 863°C for pure zirconium. The addition of hydrogen lowers the transition temperature, although over 200 ppm of hydrogen is needed for it to drop to 820°C. The other alloying elements present (Sn, Fe, O, & Cr) cause a shift in the transition temperature. Sn² & O³ both cause an increase of 10°C each, and Fe⁴ & Cr⁵ both cause a 20 & 10°C decrease in the temperature respectively. It seems unlikely that the phase transition would start at 820°C, but it is possible for the phase change to occur at the shoulder at 840°C.

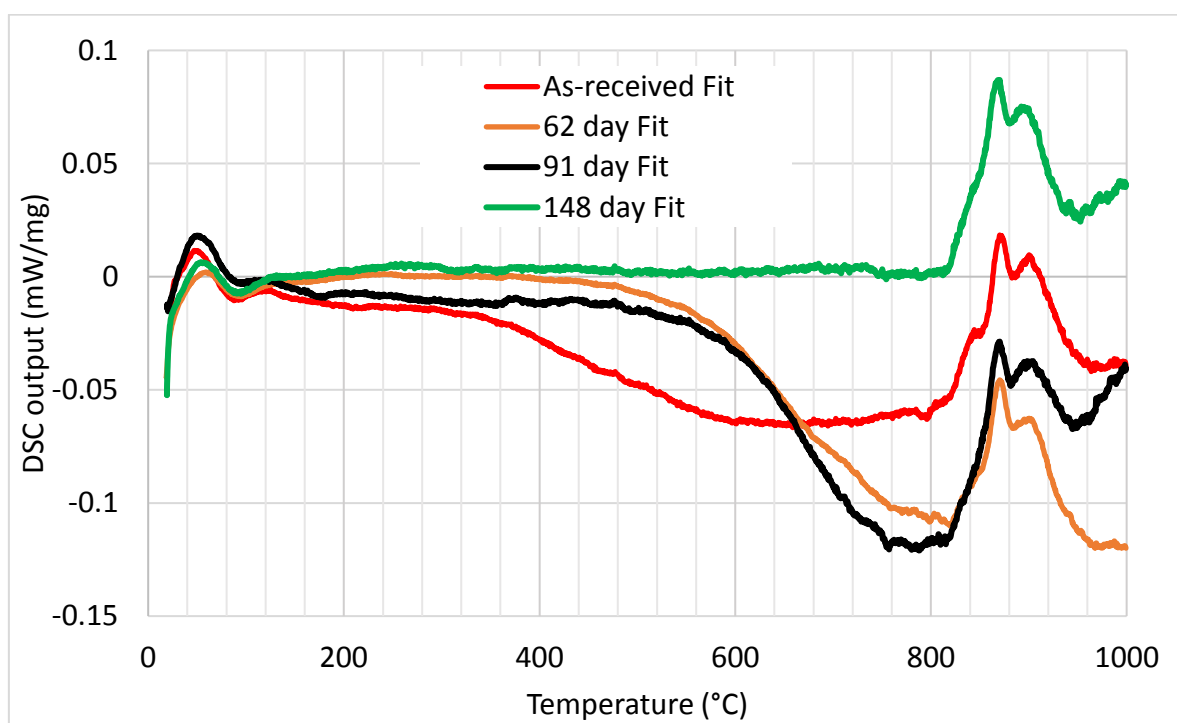


Figure 5.1 – Baseline subtracted DSC results. The large peak starting at ~820°C is the $\alpha \rightarrow \beta$ transition.

Oxidation time (days)	Oxide thickness after autoclave (μm)	Weight Gain from DSC (mg)	Oxide thickness after DSC (μm)	Total oxide thickness (μm)
0	0	0.09	0.46	0.46
62	1.46	0.41	1.35	2.81
91	1.7	0.25	1.44	3.14
148	2.9	0	0.00	2.90

Table 5.1 – Weight gain of samples after DSC exposure and calculated oxide thickness.

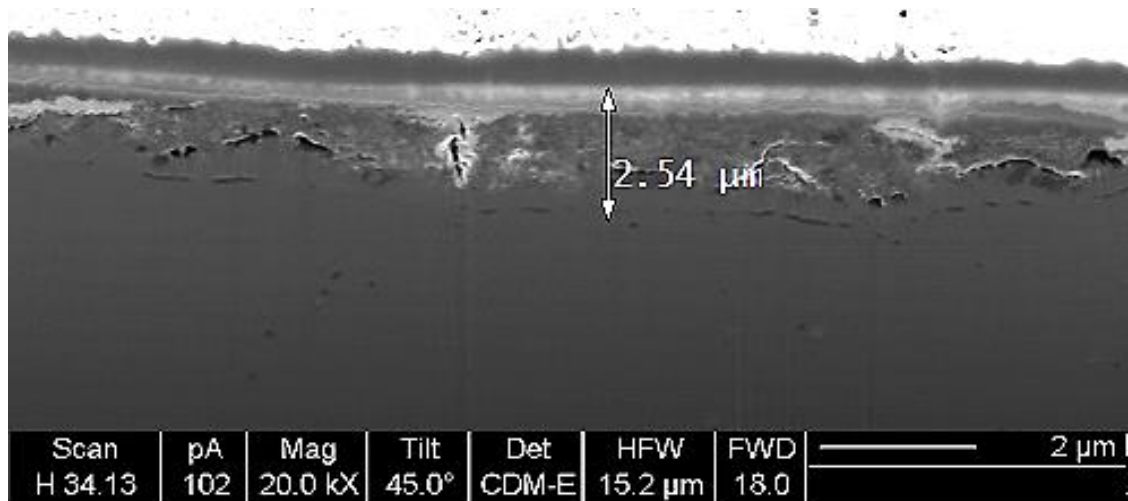


Figure 5.2 – FIB cross-section from 62 day oxide sample after DSC. We can see that the oxide is much thicker than expected after autoclave oxidation.

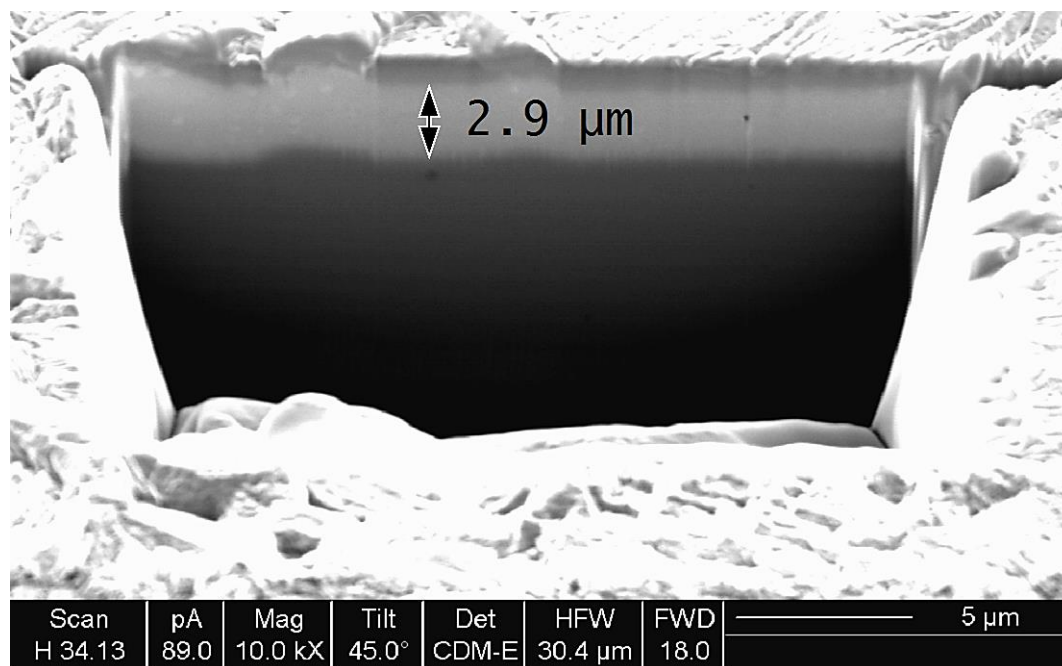


Figure 5.3 – FIB cross section from 148 day oxide sample after DSC. There was no additional oxide growth for this sample.

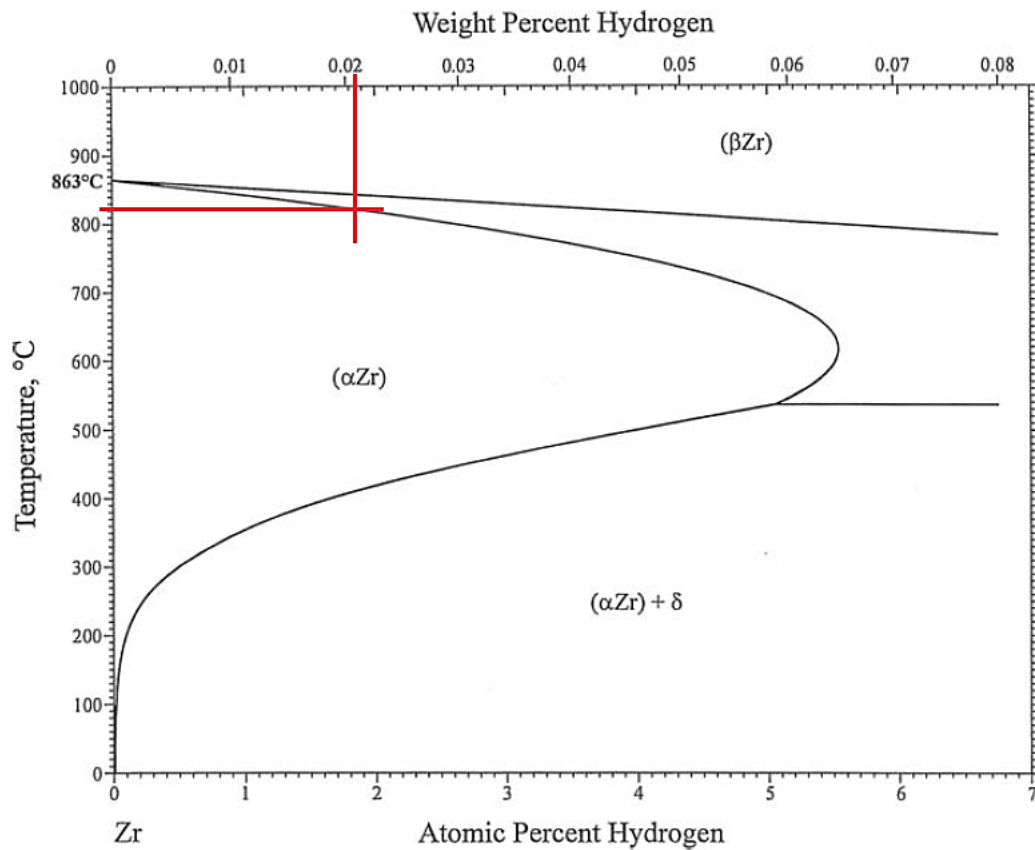


Figure 5.4 – Zr-H phase diagram for low H.¹ The red lines show the hydrogen content needed for the $\alpha \rightarrow \beta$ phase change to occur at 820°C.

A closer look at the 148 day DSC data (see Figure 5.5) shows that there is an endothermic reaction which starts at around 180°C, peaks at 260°C before decreasing and staying roughly constant after 320°C. Previous DSC experiments⁶⁻¹¹ have shown that these observations are due to hydride dissolution, which starts at approximately 180°C and finishes anywhere between 300 – 450°C, with hydrogen contents ranging from 15 -700 ppm, at heating rates from between 2 – 30°C/min.

Having ascertained where the transition temperatures occur during heating, I will now discuss the results I obtained from TDS.

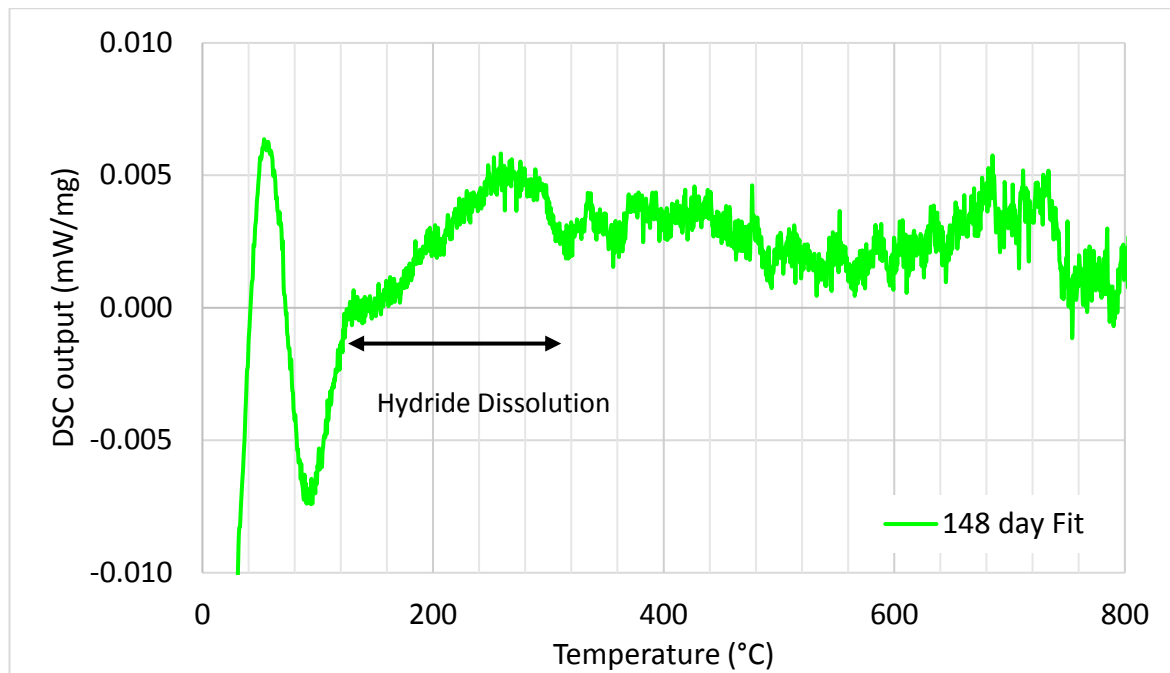


Figure 5.5 – Close up of 147 day oxide DSC output.

5.2 – Thermal Desorption Spectroscopy

I will start this section by showing the calibration tests, where the detector sensitivity was established, and also what effect the heating rate had on the hydrogen desorption. Then I will move onto samples which were mechanically deformed to introduce dislocations. This is followed by hydrogen charged samples. Then I will look at oxidised samples, in pure water at 360°C ($\text{pH}_{360}=6.15$) and at 350°C ($\text{pH}_{350}=8.82$). The latter samples were also tested with the oxide removed to test the effect of the oxide layer on hydrogen desorption.

5.2.1 – Initial Findings

Figure 5.6 shows a typical hydrogen desorption plot from an as-received sample. The temperature shown is the temperature as measured by the pyrometer (using an emissivity, $\epsilon = 1$). There are two peaks for the hydrogen desorption, a small one around 350°C and another at about 650°C. The first is probably hydrogen from the surface (as seen by Tupin et al.¹²) and the second peak is due to the difference in free energy (referred to as ΔF) between hydrogen in metal and in gas phase becoming positive between 600-700°C¹³. The temperature at which the second peak starts is indicated by the black line in Figure 5.6, which indicates the temperature at which this change occurs is ~500°C, where it can also be seen that the gradient of the temperature curve decreases (shown more clearly in Figure

5.7). This may be due to some of the heat going into the sample being removed by the hydrogen as it leaves the sample.

The temperature data shown do not take into account the true emissivity of the sample which is why it is lower than the value expected from the temperature of the heating stage. Figure 5.8 shows the same output as Figure 5.6 with the temperature after taking into account the emissivity. This indicates that the emissivity must be greater than 0.4 as the sample cannot be hotter than the maximum heater temperature (1000°C), and less than 0.5 (from the literature¹⁴⁻¹⁷). For an emissivity between 0.4 – 0.5 the large peak starts between 598 – 632°C and peaks at 798 – 843°C (Note that there are no peaks caused by the $\alpha \rightarrow \beta$ phase change). For the rest of this chapter the temperature displayed will be the measured temperature (with $\varepsilon = 1$) unless specified.

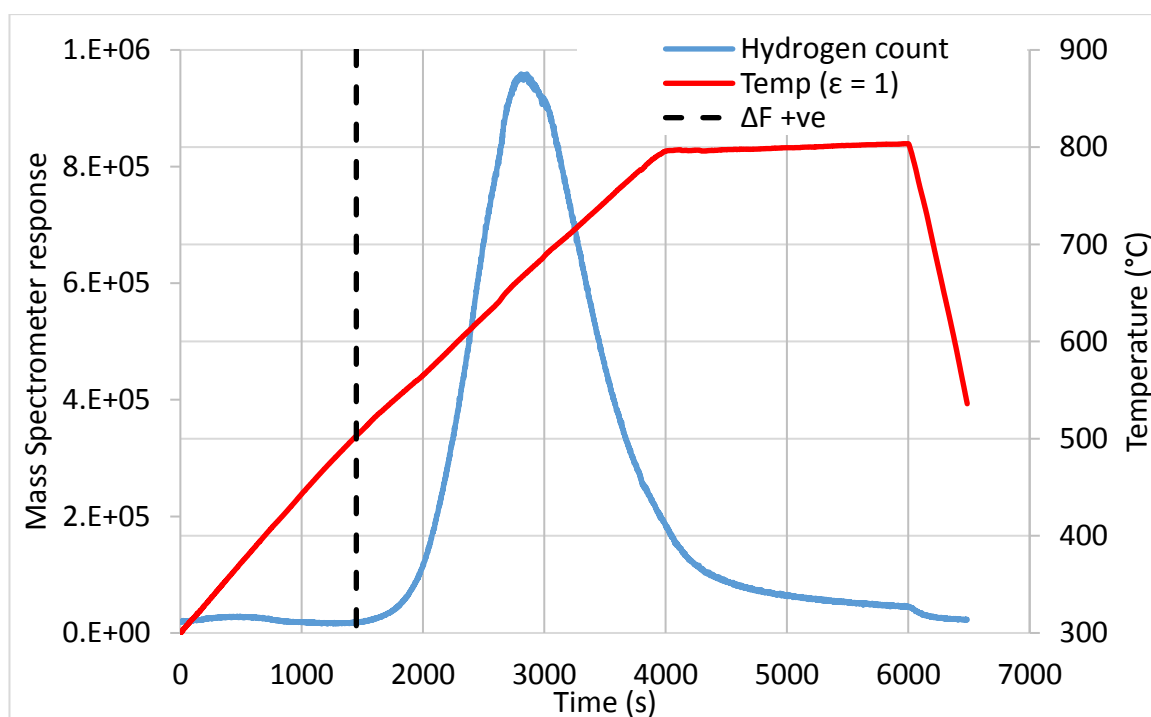


Figure 5.6 - Hydrogen desorption from an as-received sample heated at 10°C/min, emission current = 10 μ A. The temperature of the sample is measured on the right-hand axis and the hydrogen count is measured on the left-hand axis.

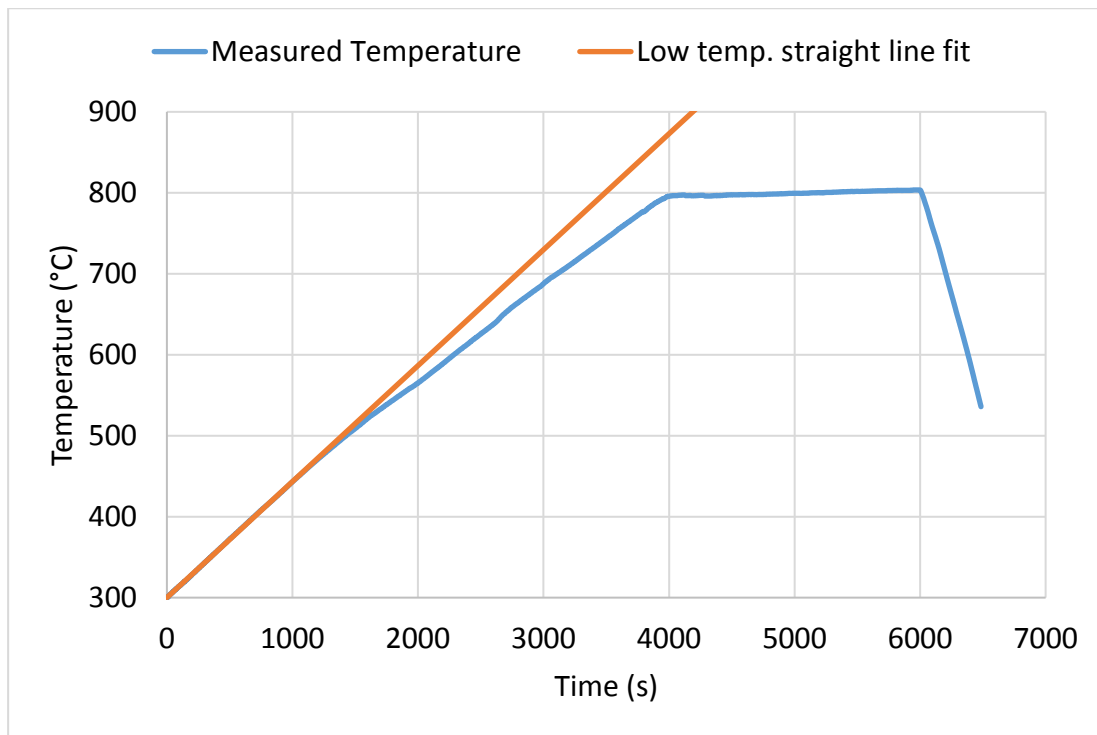


Figure 5.7 – Graph showing that the measured temperature gradient decreases at ~500°C.

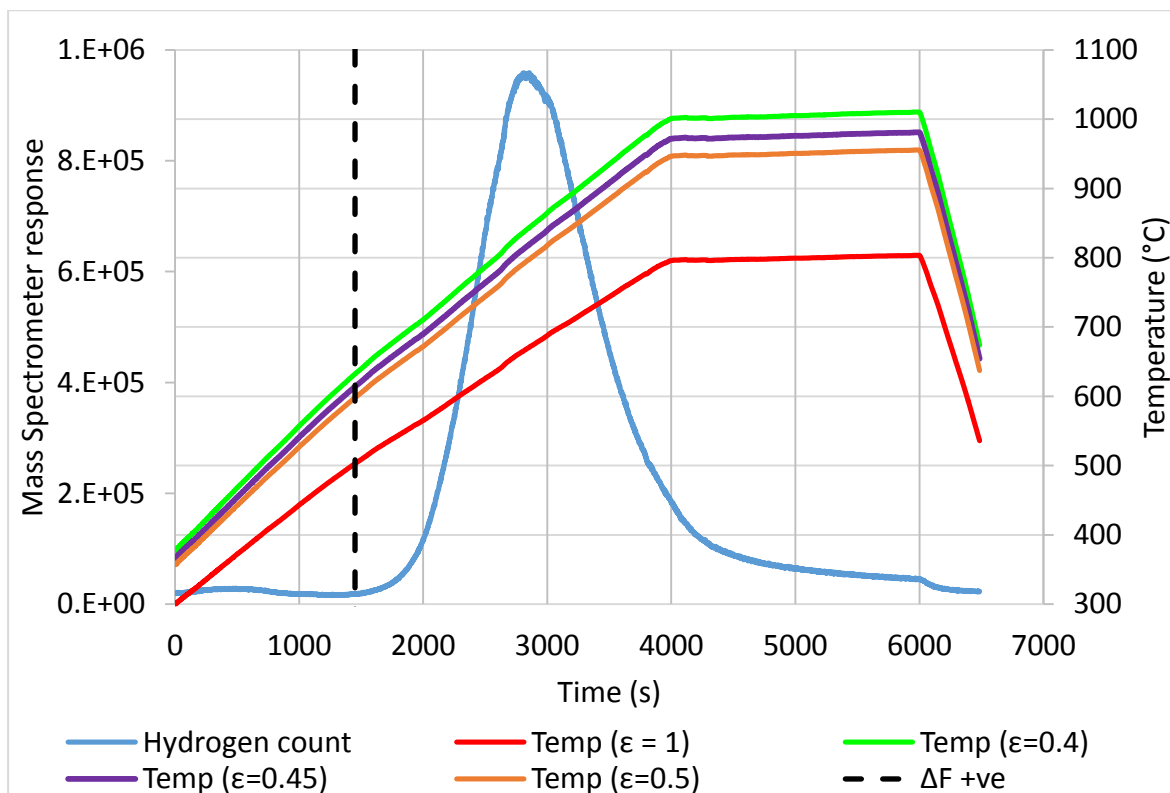


Figure 5.8 – Hydrogen desorption from as-received sample, with the temperature scaled by emissivity.

5.2.2 – Calibration Tests

To calibrate the system, I tested samples at various emission currents (which changes the detector sensitivity) and different heating rates. For the emission current tests the heating rate was set at 10°C per minute and covered the full range of current (i.e. 1–20 μ A), shown in Figure 5.9.

The way to compare spectra is to take the area under each curve and divide it by the sample volume. This method gives the amount of hydrogen desorbed from the sample. Figure 5.10 shows the amount of hydrogen per sample plotted against the emission current, along with the high temperature peak value. This shows that the amount of hydrogen detected is proportional to the emission current. The proportionality shown in Figure 5.10 is used to compare samples tested at different emission currents by taking the ratio of the emission currents used. This is useful as the detector of the RGA in the TDS becomes saturated when the number of counts for a given mass-to-charge ratio exceeds 10^7 , which means I used a lower emission current for samples with a higher hydrogen content. Note that the peak temperature is not affected by the emission current.

After correcting for the emission current I found that there is a sample-to-sample variation of 9%.

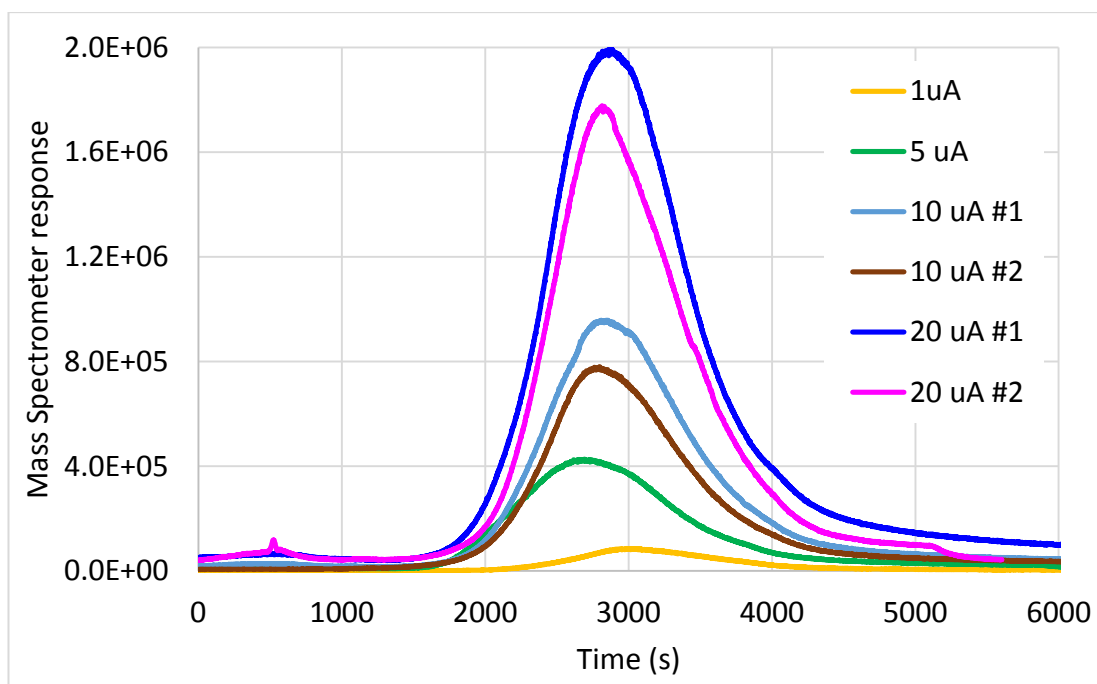


Figure 5.9 – Effect of emission current on desorption spectra.

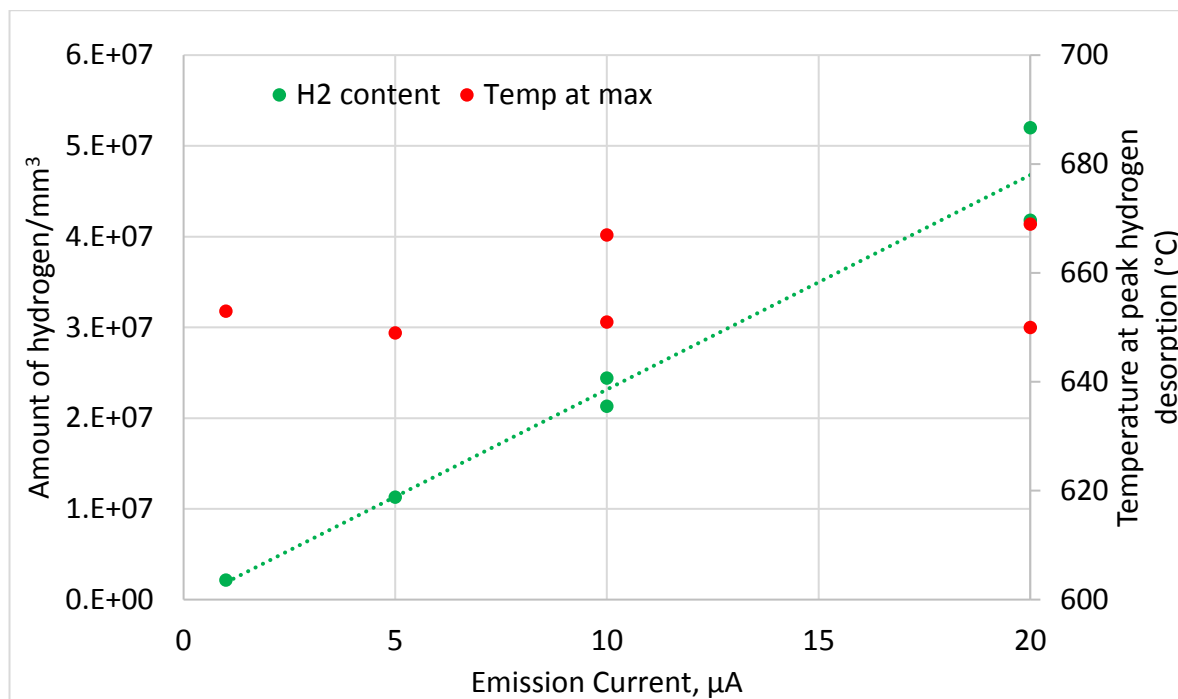


Figure 5.10 – Hydrogen content (Integrated area of TDS curve per volume of sample) against emission current. There is a clear trend between the amount of hydrogen detected and the emission current. The right-hand axis shows the temperature when the hydrogen reaches its peak desorption.

I tested samples at 5, 10, and 20°C/min with an emission current of 10 μA , and the results are shown in Figures 5.11 and 5.12, which shows that increasing the heating rate makes the peak narrower and the peak value higher. The amount of hydrogen detected does not vary much with heating rate but it can be seen that the temperature at the peak increases with heating rate. This means we can compare samples annealed at different rates. This is useful because I used a different heating rate for some of the oxidised samples to ensure all the hydrogen was desorbed.

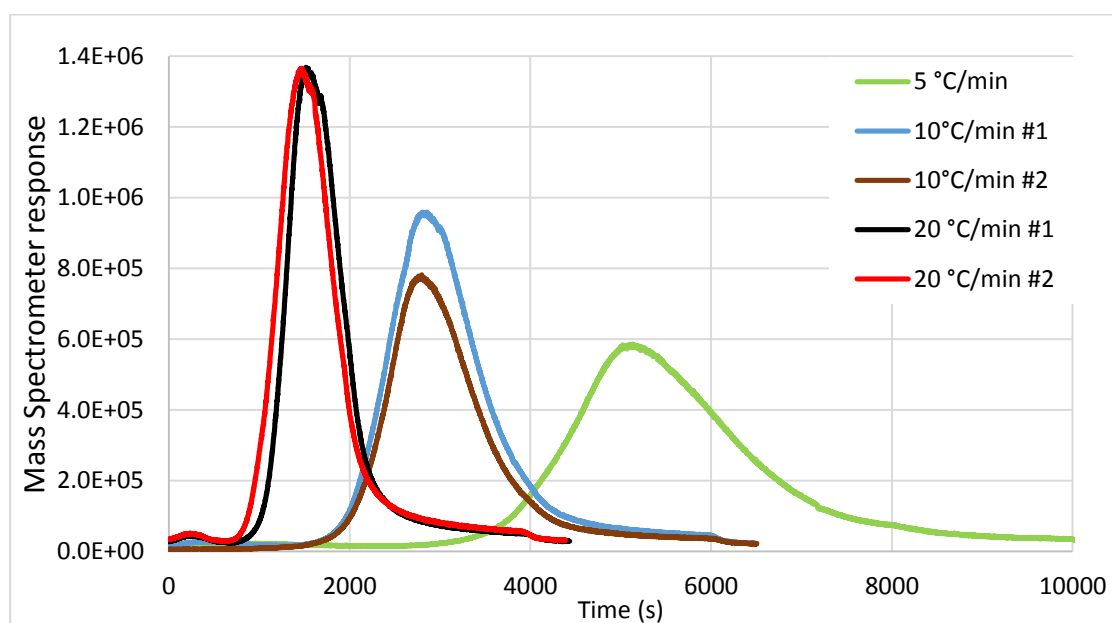


Figure 5.11 – Hydrogen desorption at different heating rates.

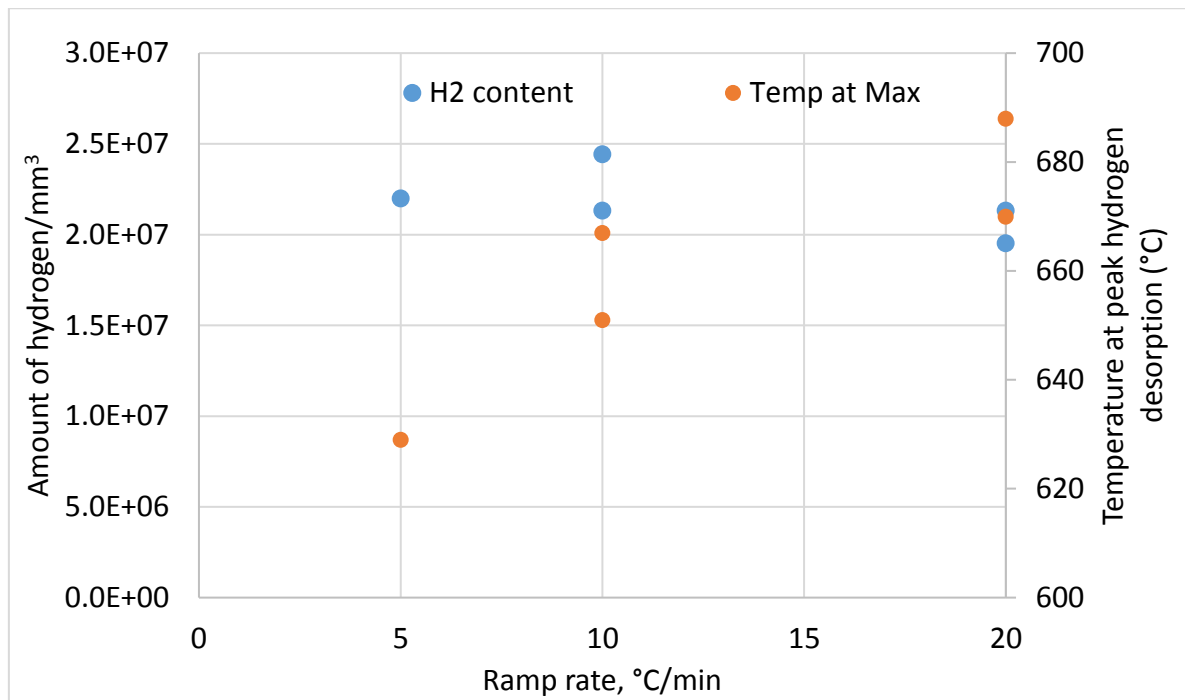


Figure 5.12 – Amount of hydrogen vs ramp rate, and temperature at peak hydrogen desorption.

5.2.3 – Cold Rolled Samples

I mechanically strained samples of as-received Zircaloy-4 to test how adding dislocations affected the amount of hydrogen desorbed. The results of these tests are shown in Figures 5.13 and 5.14, and it can be seen that the peak is broadened and the main peak is shifted to a lower temperature. This is consistent with the findings by Dupim et al.¹⁸, who showed that cold rolling leads to a lower dehydrogenation temperature.

The temperature curves (dashed lines in Figure 5.13) show that all 3 samples reach a different maximum temperature according to the pyrometer. For the sample with a 7% reduction in thickness, this is likely due to the sample being thinner than the as-received sample, meaning that for the thinned sample the top surface can reach a higher temperature. For the sample with a 15% reduction it was probably not pushed into the holding pins with as much force as the other two, which would mean not as much heat could be transferred to it.

Even though during straining no extra hydrogen is added 15% more hydrogen desorbed during the tests in the sample reduced in thickness by 15%. It is likely that introducing dislocations adds a rapid diffusion path for the hydrogen, allowing it to reach the surface more quickly.

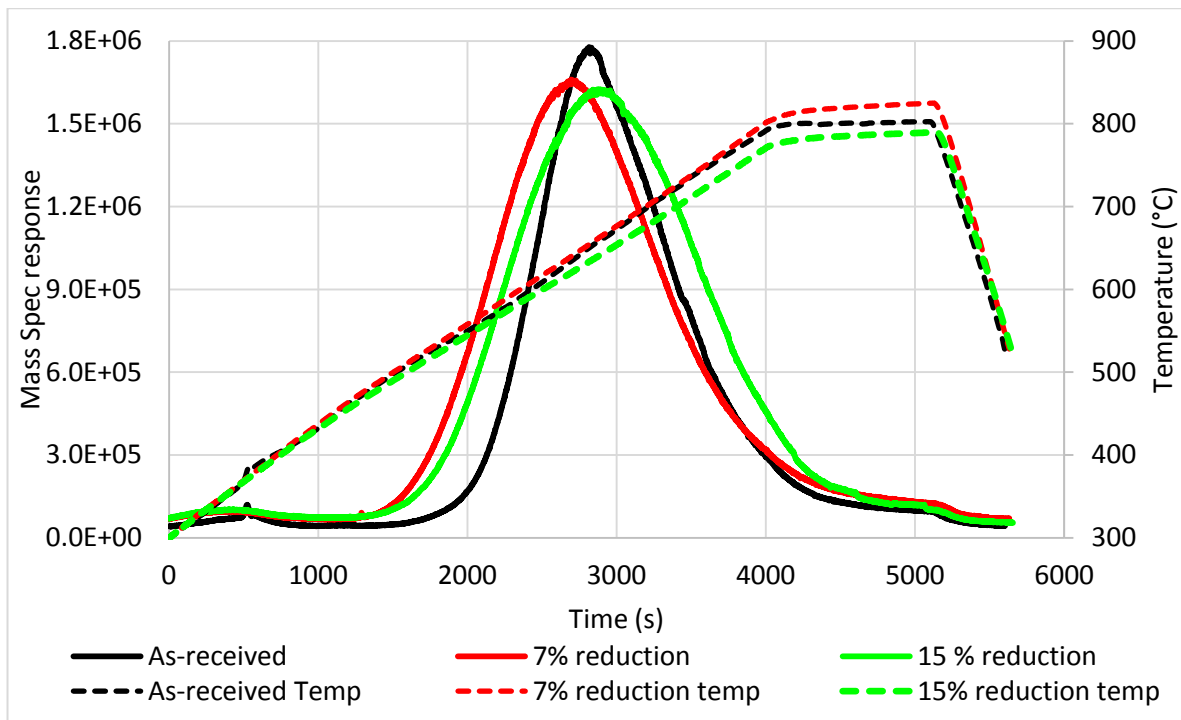


Figure 5.13 – Comparison of an as-received sample to rolled samples, ramp rate = 10 °C/min, emission current = 20 μ A. The value of reduction refers to the sample thickness.

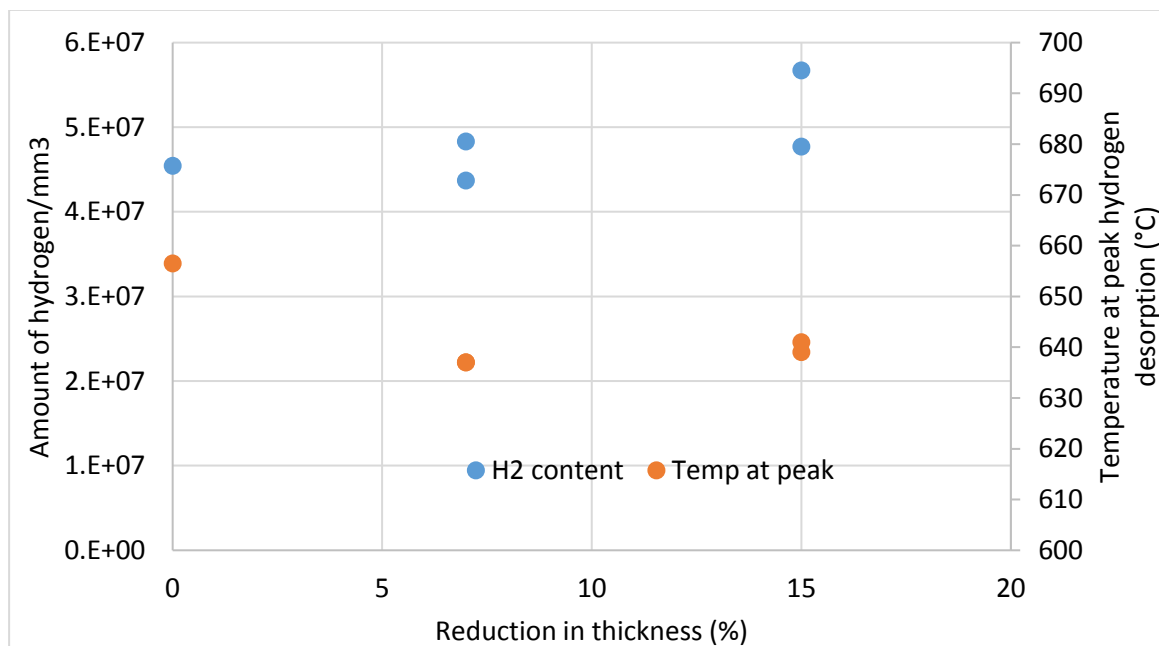


Figure 5.14 – Amount of hydrogen vs reduction in thickness, and temperature at peak hydrogen desorption.

5.2.4 – Hydrogen Charged Samples

Figure 5.15 shows the desorption spectra for samples electrolytically charged with hydrogen. The detector was set to the lowest sensitivity (1 μ A) as their high hydrogen content saturated the detector at any other setting. A spectrum from an as-received sample has been included, corrected for the emission current. No new peaks are produced, but the major peak increases in height and width, which is expected given the hydrides produced at the surfaces, which are approximately 10 μ m thick (see

Figures 5.16 & 5.17). The peak of the hydrogen desorption also shifts to lower temperature with longer charging time, shown in Figure 5.18. This can be explained by examining the work carried out by Gulbransen et al.¹³, where they showed that a sample with a higher hydrogen content needs a higher pressure to maintain a given hydrogen content.

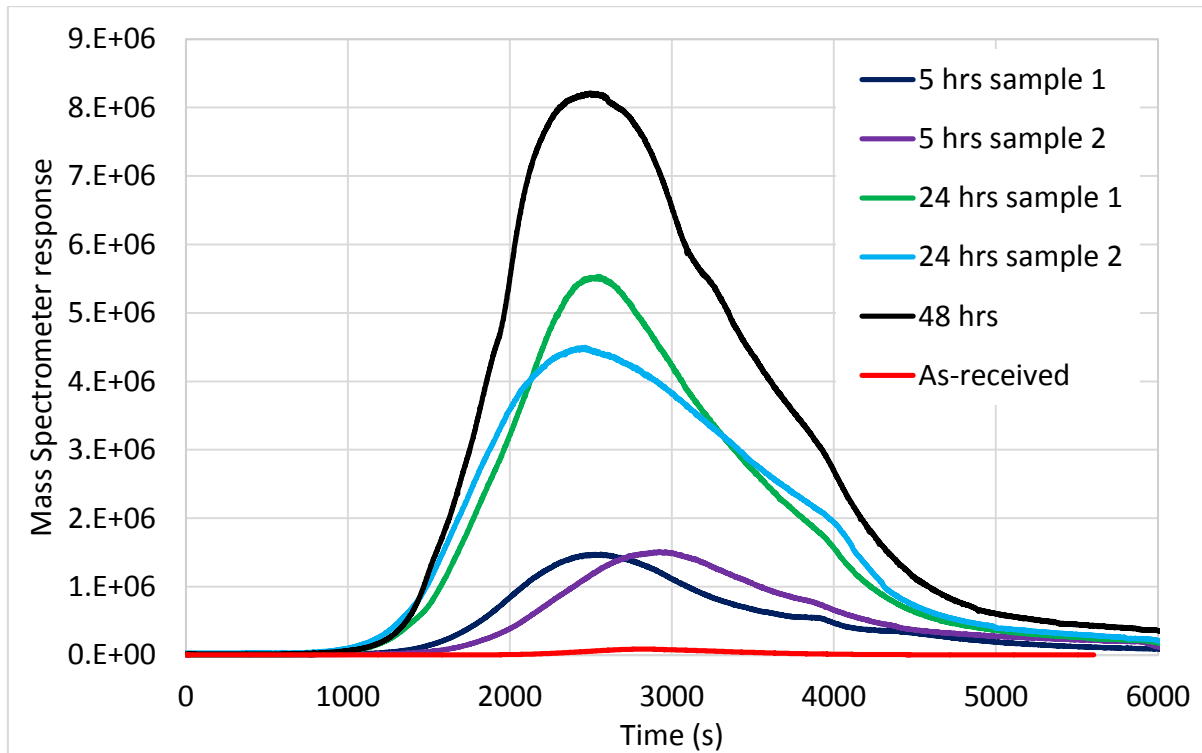


Figure 5.15 – Desorption spectra for hydrogen charged samples, ramp rate = 10 °C/min, emission current = 1 μ A. The as-received spectrum is the same as in Figure 5.1.

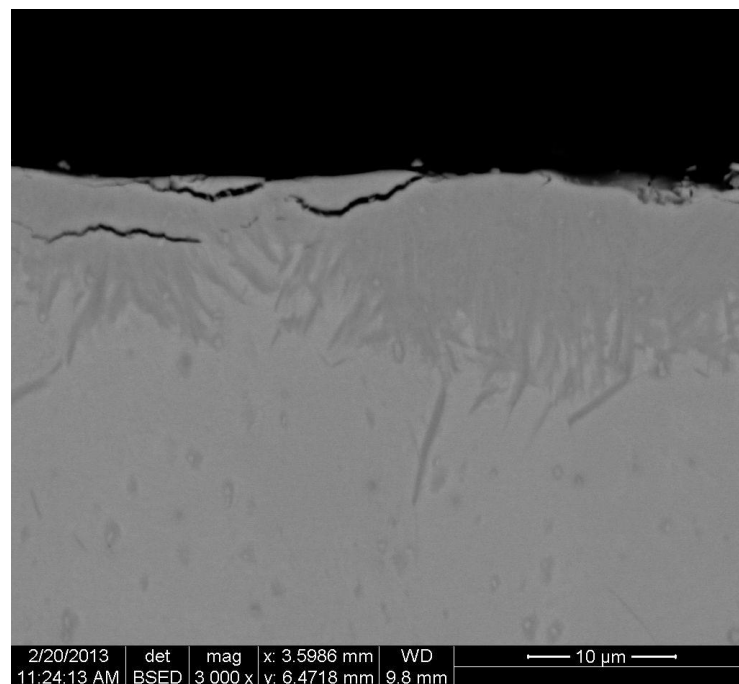


Figure 5.16 – Hydride rim formed on a sample electrolytically charged for 6 hours. (Image courtesy of Helen Hulme of AFW)

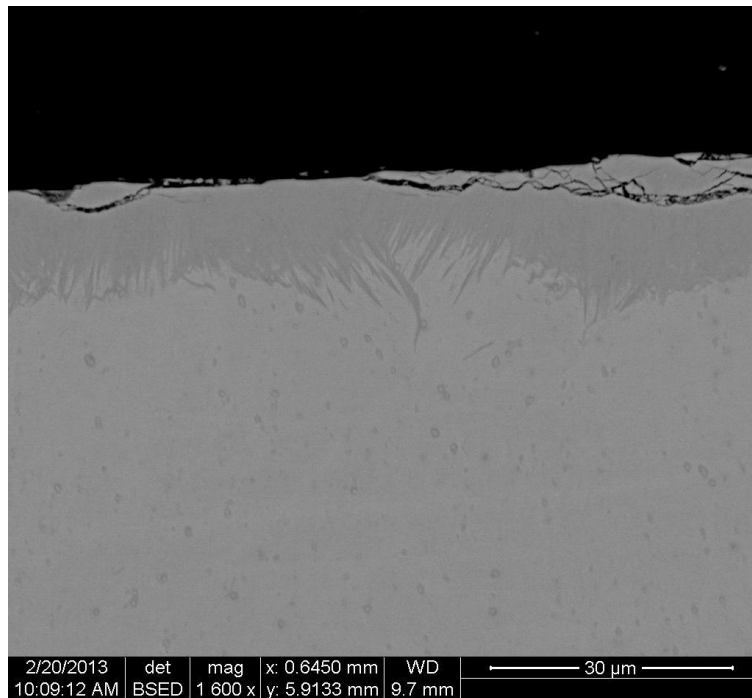


Figure 5.17 – Hydride rim on a sample charged for 24 hours. (Image courtesy of Helen Hulme of AFW)

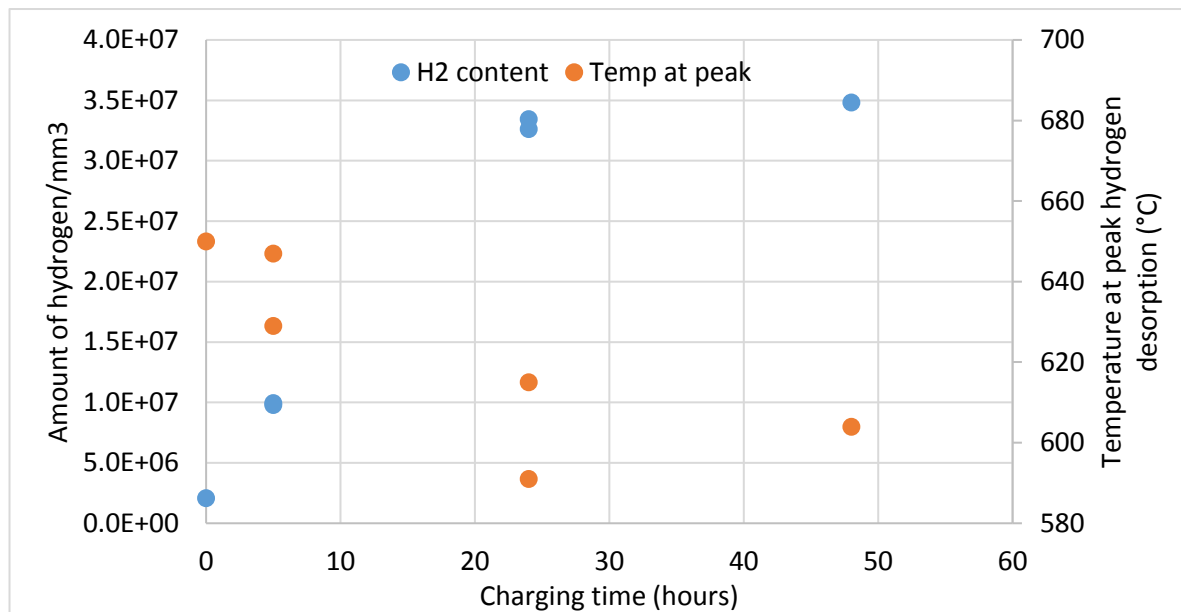


Figure 5.18 – Hydrogen content vs charging time, and temperature at peak hydrogen desorption.

5.2.5 – Impact of Oxide on Hydrogen Desorption

Figure 5.19 shows the desorption graphs for samples oxidized for 45 days at $\text{pH}_{350}=8.32$ (oxide thickness = $1.36\mu\text{m}$), as removed from the autoclave, and with the oxide ground off prior to heating in the TDS. The heating curve of the sample with oxide (dark blue line) shows a slight overshoot before the surface settles to $\sim 830^\circ\text{C}$. This overshoot is due to the exothermic dissolution of the oxide into the metal, as supported by the shiny metallic surfaces of the samples on removal from the TDS.

Since few oxygen-containing species (i.e. no O, O₂, NO, CO, CO₂) are detected at this temperature, most of the oxygen appears to dissolve into the metal matrix.

In the absence of the surface oxide (red line), the hydrogen desorption peaks are at the temperatures seen in the previous plots (~650°C and 330°C), indicating that no new trapping sites are produced in the metal by oxidation. In the presence of the oxide (light blue line), the peaks are shifted to higher temperatures. The main effect of the oxide is to act as a diffusion barrier for the hydrogen desorbing from the metal. A burst of hydrogen is produced just as the oxide starts dissolving. From these graphs I calculated that there is slightly less hydrogen in the sample with the oxide present 1.58×10^7 & 1.74×10^7 for with and without oxide respectively, which is close to the sample-to-sample variation shown in the as-received samples. The result could also indicate most of the hydrogen present is in the metal rather than the oxide, in accordance with the lower solubility of H in the oxide¹⁹⁻²¹.

The elevated pH environment contained 50% deuterated water, Figure 5.20 shows that D-H and D₂ desorption follows the same pattern as H₂ desorption, although the concentrations of these species are far lower than that of H₂.

The desorption of masses 17 (O-H), 18 (H₂O or O-D) and 19 (HDO) is shown in Figure 5.21. There are higher levels of all three species in the sample from which the oxide was left intact. The signals at low temperatures may relate to water adsorbed on the surface of the samples and the vacuum chamber as well as water deeper within the oxide. Hydrogen does, however, bond with oxygen in the oxide²²⁻²⁴. There is also a release around the same time that there is a burst of hydrogen from the sample, indicating that a small fraction of the oxygen in the oxide is desorbed with hydrogen rather than dissolved in the metal. It can also be seen that early on there is a release of HDO from the oxide, which is not present in the sample with the oxide removed. Comparison between the scales of Figure 5.19 and Figure 5.21 shows that the hydrogen desorbing in association with oxygen is more than an order of magnitude less than the hydrogen desorbing without oxygen. With the addition of the H₂O/OD content to the H₂ content of the 45 day with oxide sample the total is 1.68×10^7 , which confirms that most of the hydrogen is being desorbed from the metal.

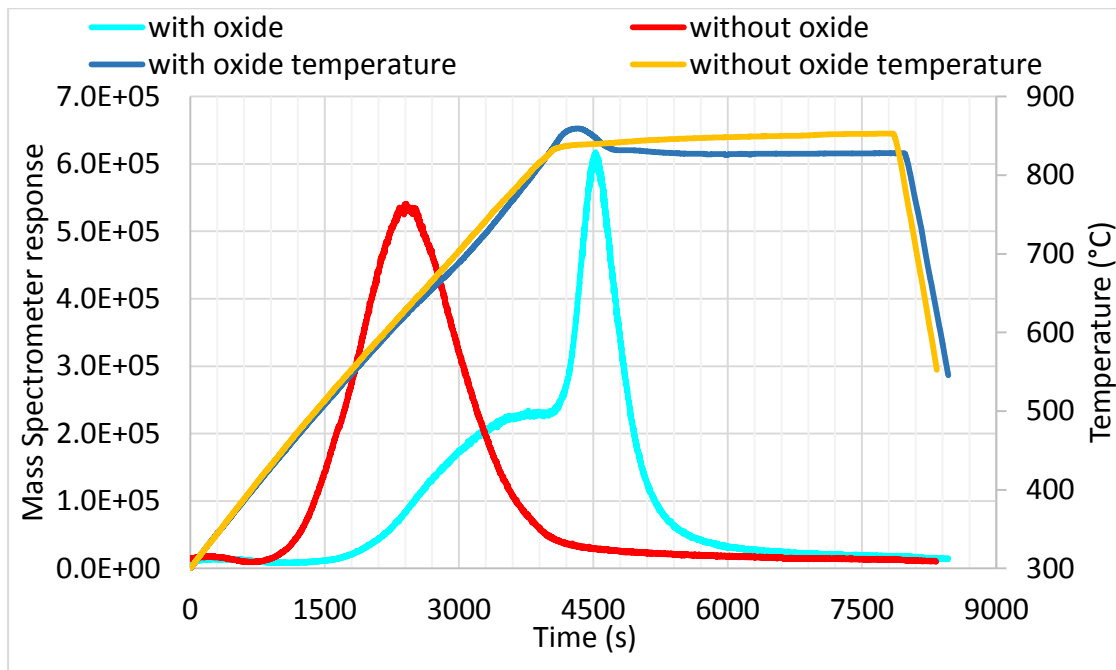


Figure 5.19 – Hydrogen desorption from samples exposed to $\text{pH}_{350}=8.82$ for 45 days, with and without the oxide present.

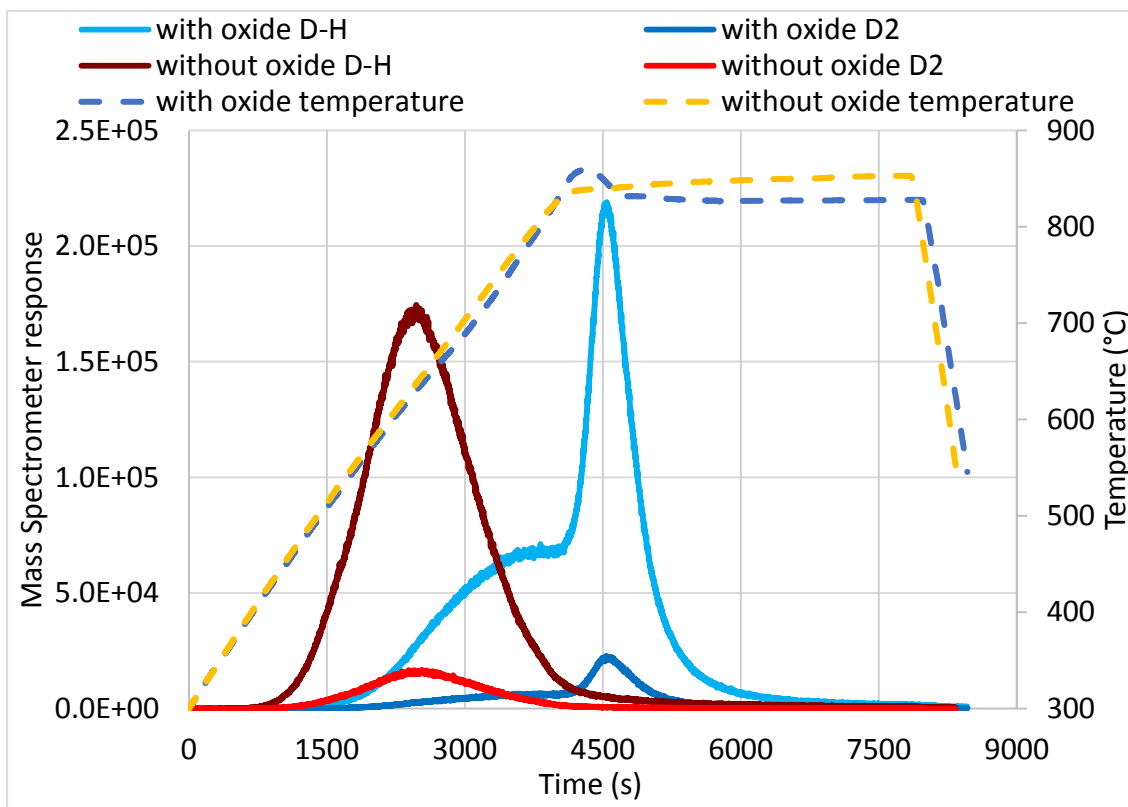


Figure 5.20 – D-H and D₂ desorption for the same samples shown in Figure 5.12.

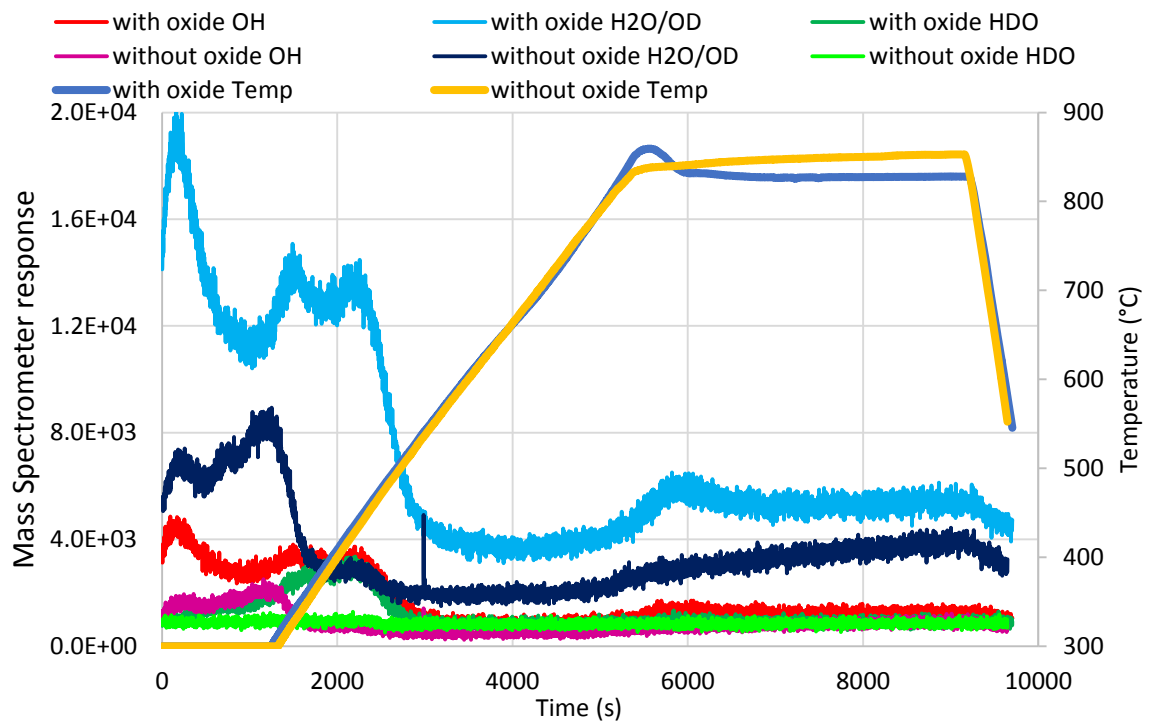


Figure 5.21 – Desorption of oxygen-hydrogen species from samples exposed for 45 days.

5.2.6 – Effect of pH on Hydrogen Content

Figure 5.22 compares the hydrogen (H_2) content from samples oxidized in pure water and the total $H_2 + DH + D_2$ content for samples at high pH. This shows that before transition (approximated to be $2.2\ \mu m$ for both environments in Chapter 4) the pH has little effect on the hydrogen pick-up, which shows that the hydrogen transport properties for both oxides is similar before transition (as discussed in Chapter 4.3). Around transition this effect changes and it can be seen that at transition the sample from pure water has more than twice the amount of hydrogen compared to the high pH sample. This ratio continuously increases after transition and when the oxide reaches $4.5\ \mu m$ thick there is more than three times the amount of hydrogen than in the high pH sample. It seems that a combination of the pH and the period of oxidation are important in hydrogen pick-up.

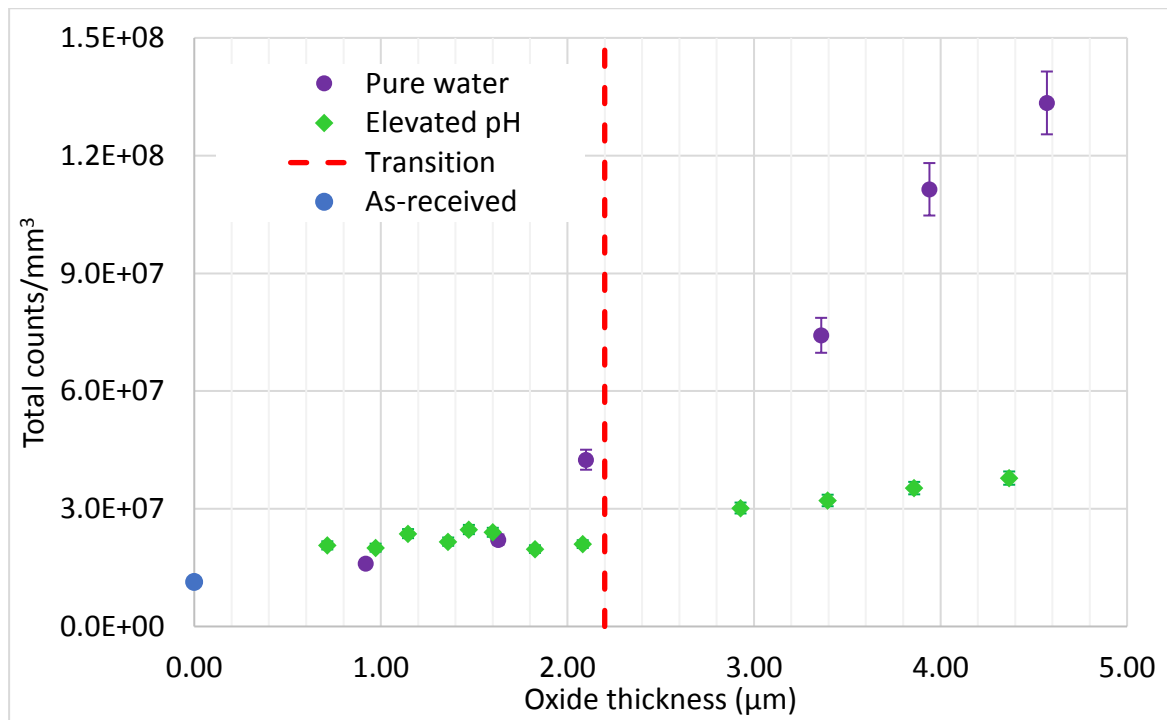


Figure 5.22 – Comparison of hydrogen content (H_2) for samples oxidised in pure water and the combined H_2 + DH + D_2 for samples oxidised in a high pH (50% deuterated), against oxide thickness. The amount found in an as-received material is shown in blue at 0 μm oxide thickness.

5.2.7 – Hydrogen Content of Samples Oxidised at High pH

Figure 5.23 shows the hydrogen content for all the high pH samples, with and without the oxide present. Figure 5.24 shows a closer look at the D_2 plot. There are 4 distinct regions for each species:

1. From 0 – 5 days.
2. Early pre-transition between 5 and 75 days.
3. Late pre-transition after 75 days up to around transition.
4. Post transition.

In region 1 there is a large hydrogen/deuterium pick-up in the first 5 days of oxidation, where the H_2 content is 1.5 times higher on average after 5 days compared to the as-received. This can be explained by the fact that the first 300 nm of oxide is extremely permeable to hydrogen/deuterium, as found by Tupin et al.¹².

For region 2 it can be seen that, for all the species, the hydrogen/deuterium content either increases slightly (for D-H and D_2) or stays roughly constant, regardless of the presence of the oxide layer. A reason that the H_2 count is consistently lower for the samples with the oxide present is that it loses more hydrogen as hydrogen-oxygen molecules (OH, H_2O/OD , HDO).

For region 3 it is observed that the oxide layer has an influence. For all species the separation between the counts for samples with and without the oxide increases.

For region 4 there is a large increase in all species from samples with the oxide present, and it can be seen that for H₂ the count becomes comparable (within error) to the H₂ count for samples with the oxide removed. For the oxide removed graph we see a plateau for H₂ and D₂ in region 3 before another sharp increase after 210 days (which could indicate that another transition is occurring). This correlates to the findings in chapter 4 where I stated that the 243 day sample was passing through transition in parts of the sample.

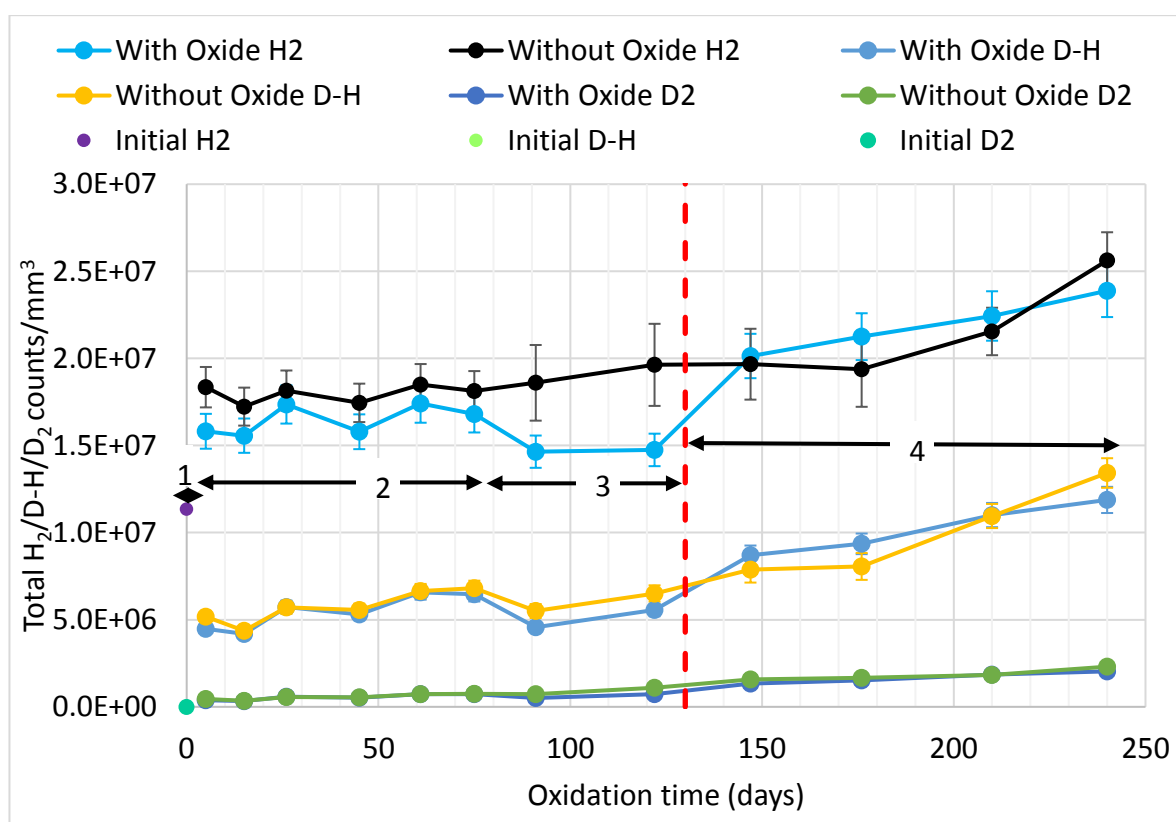


Figure 5.23 – Hydrogen content for samples oxidised in high pH, with and without the oxide layer present. The red dashed line shows the transition point at 130 days. 4 regions can be identified.

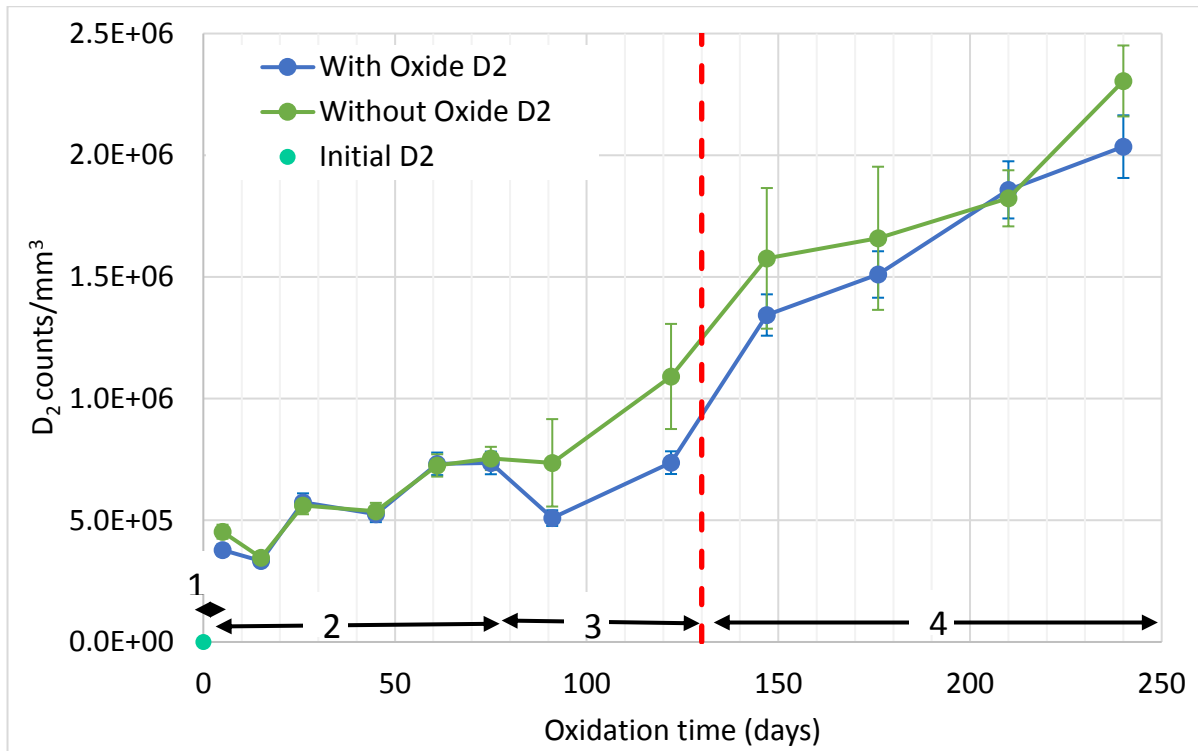


Figure 5.24 – Expanded view of the D₂ content from Figure 5.23. The red dashed line shows the transition at 130 days.

To get a better understanding of how the hydrogen content varies across our samples looking at the ratio of D₂ in the sample compared to H₂ is a useful method. The as-received samples contained around 9 ppm (as quoted by Westinghouse) and virtually no deuterium as the natural abundance is $\sim 10^{-4}$. The samples were exposed to 50% heavy water so that any deuterium detected above that ratio would be due to the oxidation process.

As there is D-H detected this needed to be taken into account. I used the following equation to compute the ratio:

$$\frac{D_2}{H_2} = \frac{\left([D_2]_d + \frac{[D-H]_d}{2}\right)}{\left([H_2]_d + \frac{[D-H]_d}{2}\right)} \quad (1)$$

Where $[x]_d$ denotes the total counts for species x for oxidation time d. Figure 5.23 shows the plot of this ratio for all samples. Since the autoclave exposure was 50% deuterated water while the natural abundance of D is around 0.01% this ratio shows us the hydrogen/deuterium pick-up during oxidation, as a function of the as-received hydrogen content. During the first five days of oxidation, the hydrogen pick-up rate is rapid, with the ratio showing (H₂+D₂) picked up exceeding a third of that originally

present. From 5 days to transition, the amount picked up increases slowly, approaching two-fifths that originally present by transition. After transition the hydrogen pick-up increases steadily.

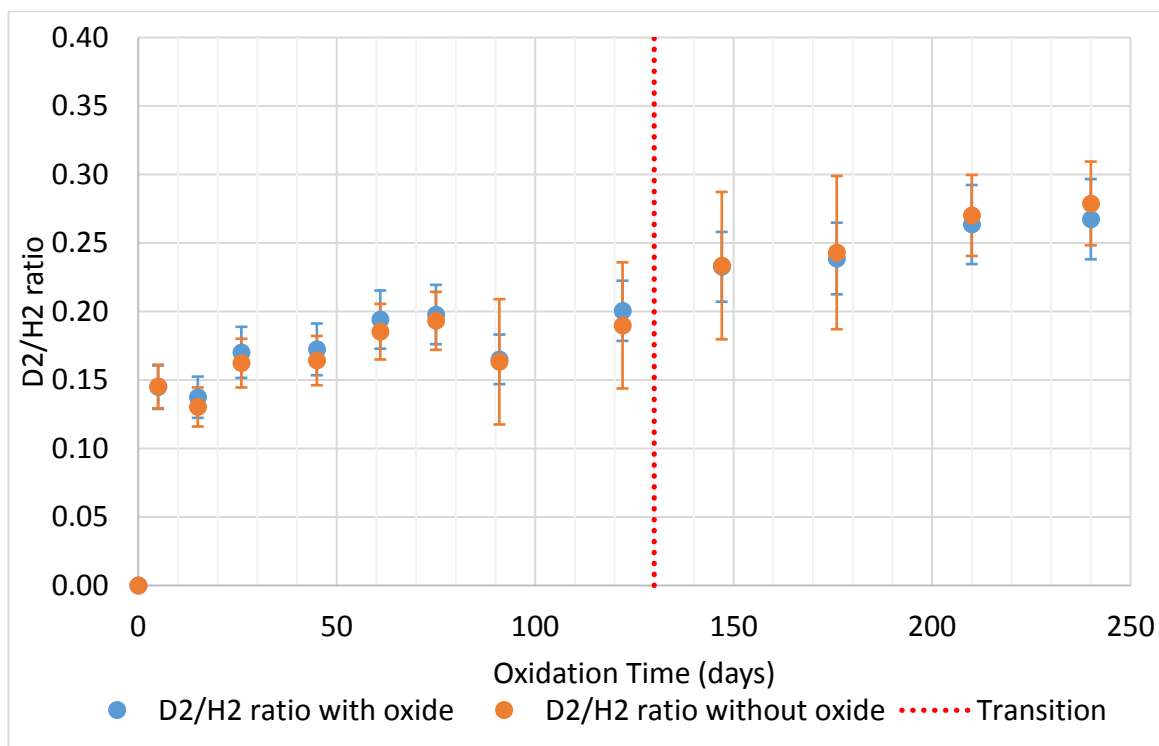


Figure 5.25 – D₂ to H₂ ratio vs oxidation time.

5.3 – Hydrogen Content Measurements by Westinghouse and PSI

Figure 5.26 shows the hydrogen content from the samples exposed to pure water, as measured by TDS (at 5 μ A) and by HHGE carried out by Westinghouse, with the oxide intact for all samples shown. This shows that the points from both techniques match up well. To get a calibration factor we can take the ratio of the TDS result to the Westinghouse results. This is shown in Figure 5.27, where the average for the six data points is 1.15×10^6 with a standard deviation of 6.98×10^4 , giving a standard error of 0.06.

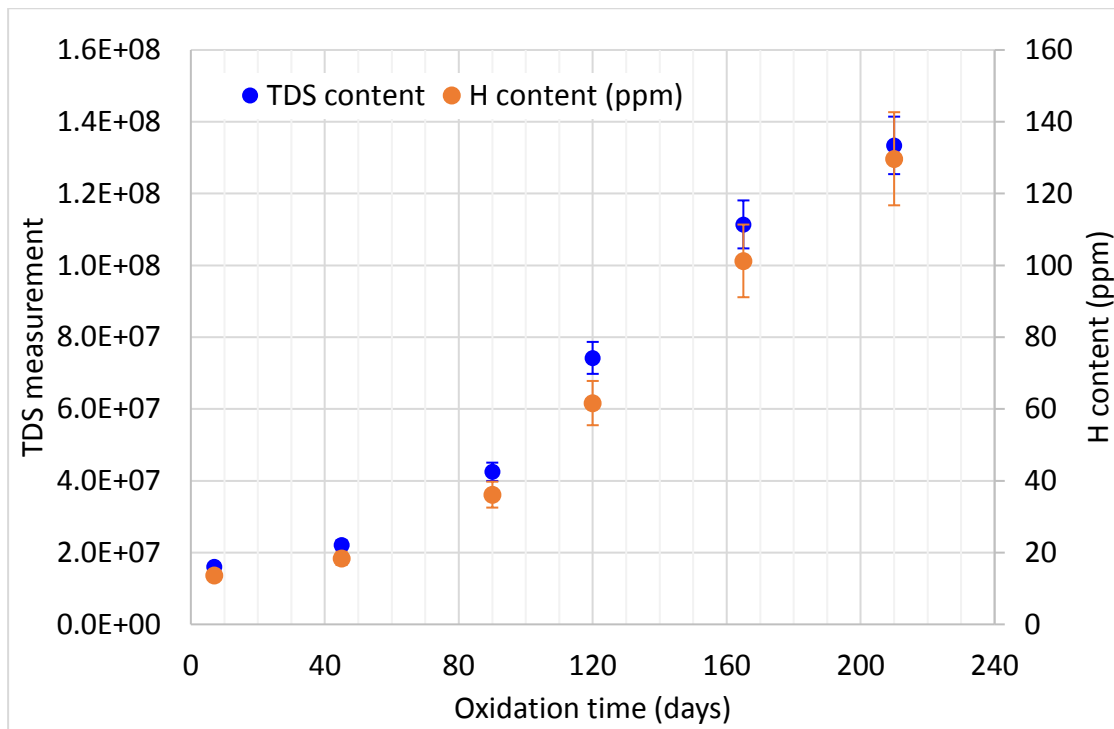


Figure 5.26 – Hydrogen content of pure water samples, from TDS (left y-axis) and from HHGE (right y-axis), as measured by Westinghouse.

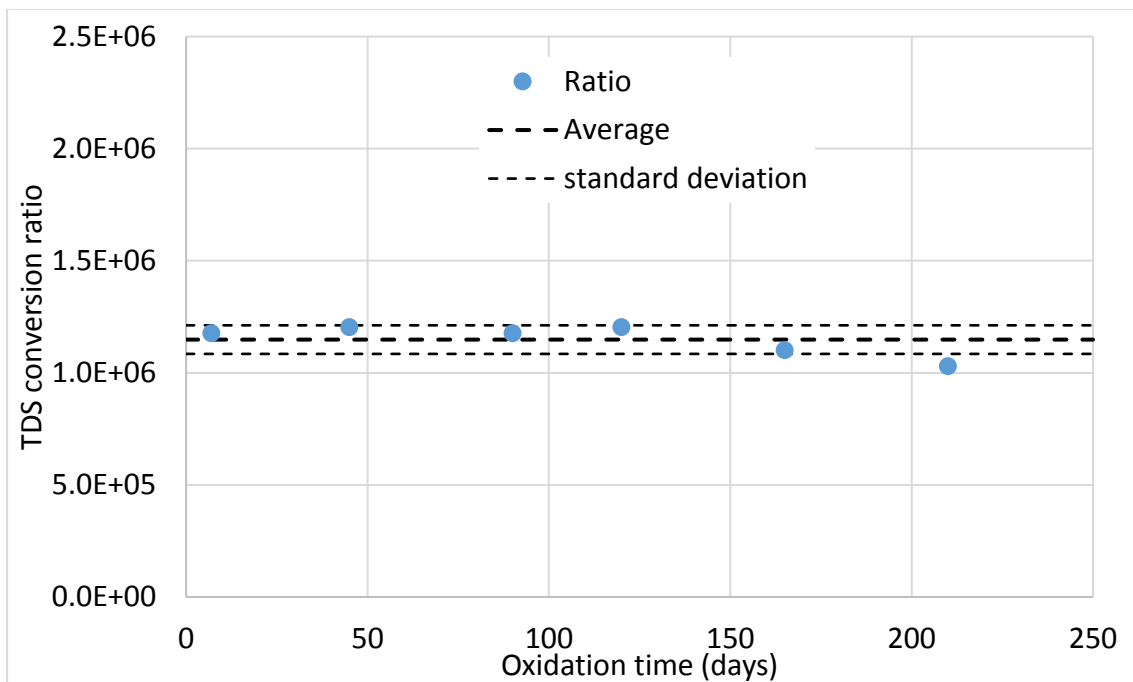


Figure 5.27 – TDS conversion ratio for Westinghouse tested samples. These results have a low dispersion.

Figure 5.28 shows the hydrogen data from samples exposed to high pH, as measured by TDS and HHGE at PSI. The samples tested with the oxide removed show a strong correlation between the different techniques, as well as the as-received and 15 day samples with the oxide intact. However the 123 day with oxide sample shows a different result. The hydrogen content in the 123 day sample with the oxide present was measured as being higher than the sample with the oxide removed by PSI,

which is the opposite found by TDS. It was also found to have increased by a factor of 2 compared to the sample oxidised for 15 days with the oxide.

Figure 5.29 shows the TDS to HHGE ratio. We can see that there is a far greater spread on these results compared to the Westinghouse tested samples. While the average is fairly similar (1.11×10^6), the standard deviation is much higher (6.01×10^5), which gives a standard error of 0.54, a factor of 9 greater than the Westinghouse value. The reasons for this discrepancy are unknown, but could be due to various factors. There were only a small amount of samples run and only two different oxidation times run at PSI. The standards that were used might also not have been accurate.

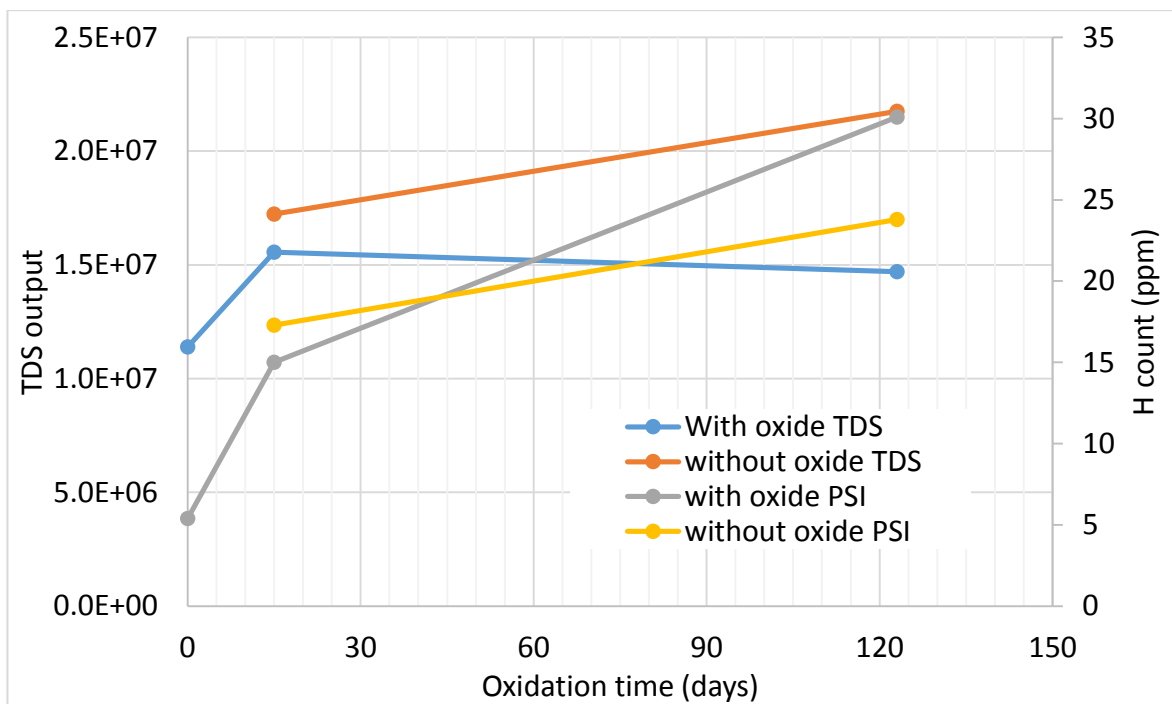


Figure 5.28 – Hydrogen content of high pH samples, from TDS and HHGE, as tested by PSI.

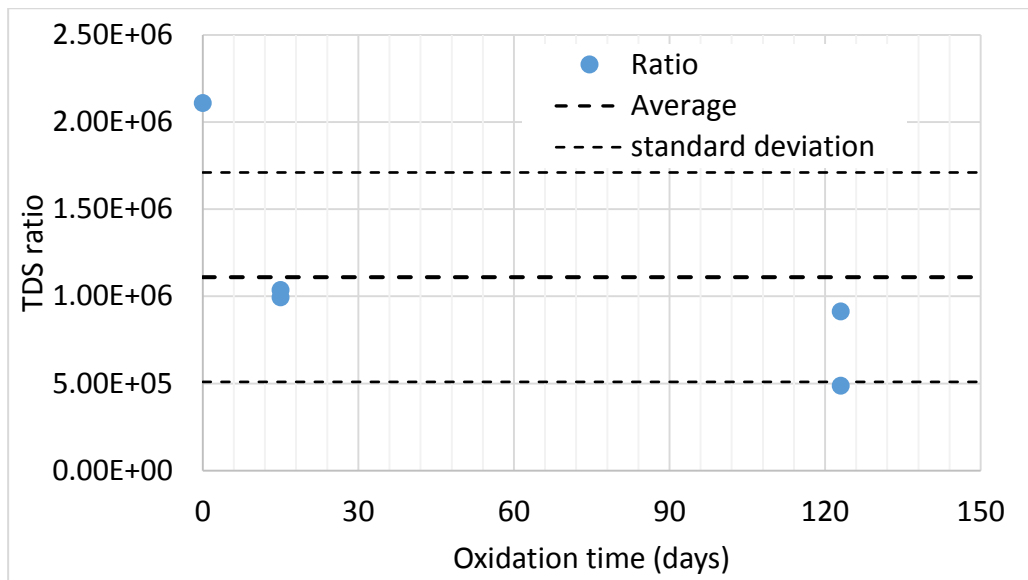


Figure 5.29 – TDS conversion ratio for PSI tested samples. These results have a higher dispersion compared to the Westinghouse tested samples.

Figure 5.30 shows a similar plot to 5.22, but this time I have used the average ratio from the Westinghouse HHGE data to show the comparison between the hydrogen content for samples oxidised in pure water and a high pH in ppm. The average hydrogen content for as-received samples via TDS (at 5 μ A) was 1.14×10^7 , and by using the ratio of 1.15×10^6 , this gives a hydrogen content of 9.91 ppm, which is extremely close to the value (9 ppm) quoted by Westinghouse from their own measurements.

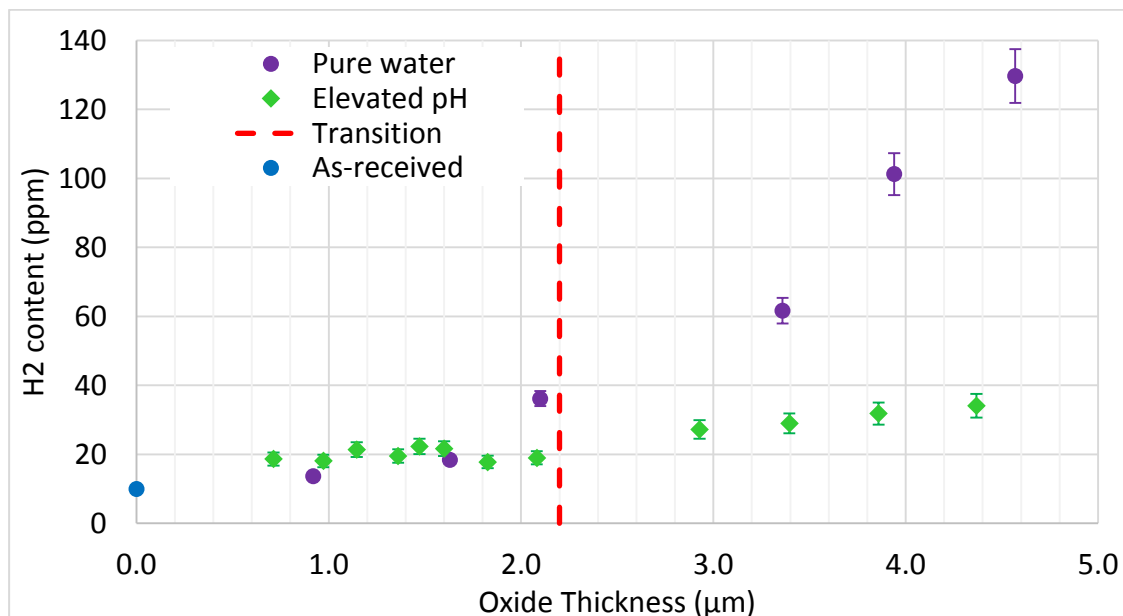


Figure 5.30 – Comparison of hydrogen content (H_2) for samples oxidised in pure water and the combined H_2 + DH + D_2 for samples oxidised in a high pH (50% deuterated), against oxide thickness.

5.4 – NanoSIMS Results

When hydrogen is absorbed by zirconium from the water it must diffuse through the grown oxide. During TDS, the hydrogen released from the metal must diffuse through the metal and the oxide. The location and relative concentration of deuterium/hydrogen in the oxide can be characterized with NanoSIMS, which I am now going to discuss. These experiments were carried out by Dr Kexue Li. First I will show the diffusion coefficient results, followed by the 3D maps generated by Dr Li.

The following samples were examined: 30 days pure water + 31 days pure D₂O (61 day oxide, 1.8 μm thick), 75 days pure water + 31 days pure D₂O (106 day oxide, 2.54 μm thick), and 62 (1.47 μm oxide) and 148 (2.93 μm oxide) day in a high pH (50% deuterated water).

5.4.1 – Diffusion Profiles

Figures 5.31 – 5.35 show a depth profile obtained from each sample that was examined in the NanoSIMS. The green dotted line on all of the graphs shows the approximate OM interface based on the weight gain, and the spikes in the depth profile data (for example, there are two just before and after 0.5 μm in Figure 5.31) are due to areas of high concentration of deuterium, which is covered in more detail in the following section. The depth profiles show a distribution which follows Fick's law, i.e. driven by a concentration gradient, and as such can be fitted to an error function.

The first 3 profiles have been split into two regions, the external and internal oxide as described by Tupin et al.¹². The fourth (of the 148 day high pH oxide) has an intermediate layer of constant hydrogen/deuterium in between the external and internal oxides. One of the depth profiles obtained for the 106 day pure water sample (shown in Figure 5.35) shows the formation of the layer of constant hydrogen/deuterium.

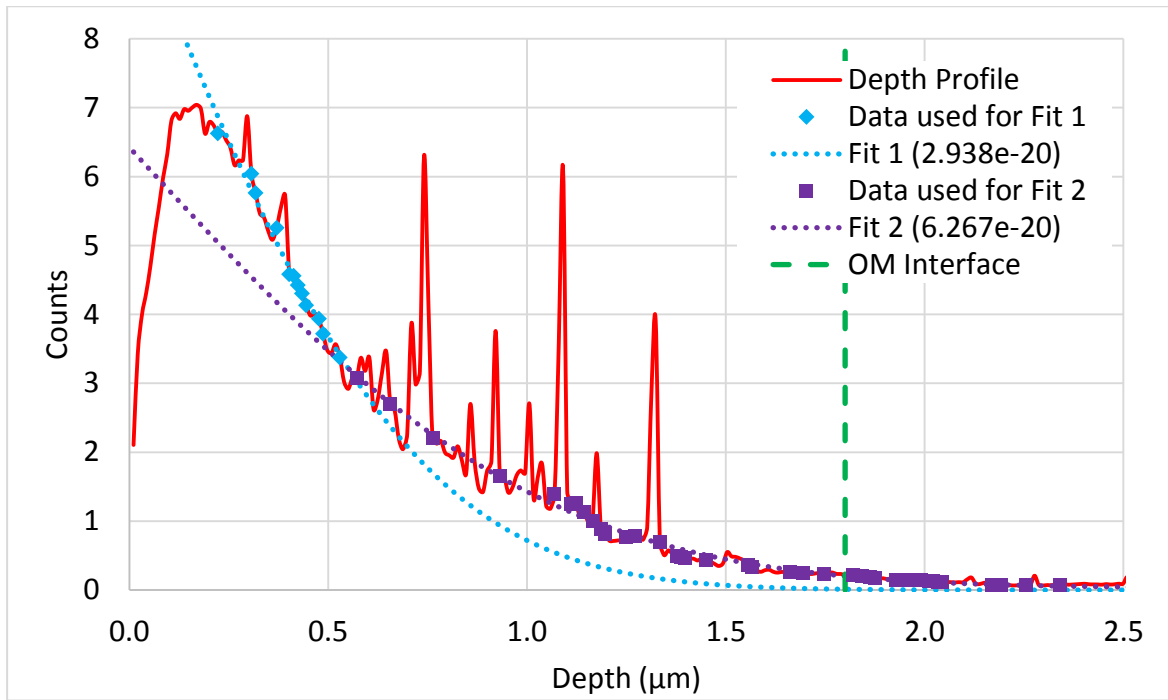


Figure 5.31 – Depth profile from the 61 day oxide (pure water/pure D₂O), with fits for the external (blue line) and internal oxide (purple line). D_0 for the external and internal layers are shown in the legend, with units m²/s.

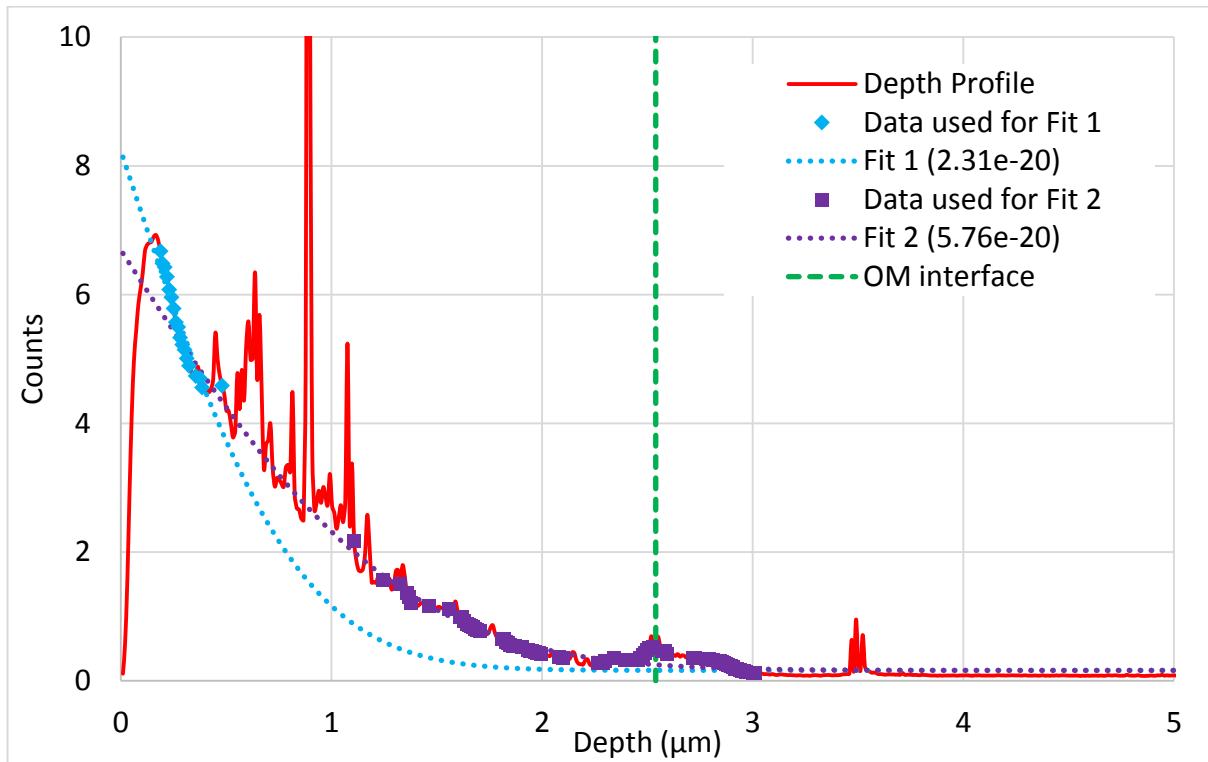


Figure 5.32 – Depth profile from the 106 day pure water oxide, with fits for the external (blue line) and internal oxide (purple line). D_0 for the external and internal layers are shown in the legend, with units m²/s. The large peak at 3.5 μm is probably from a hydride in the metal.

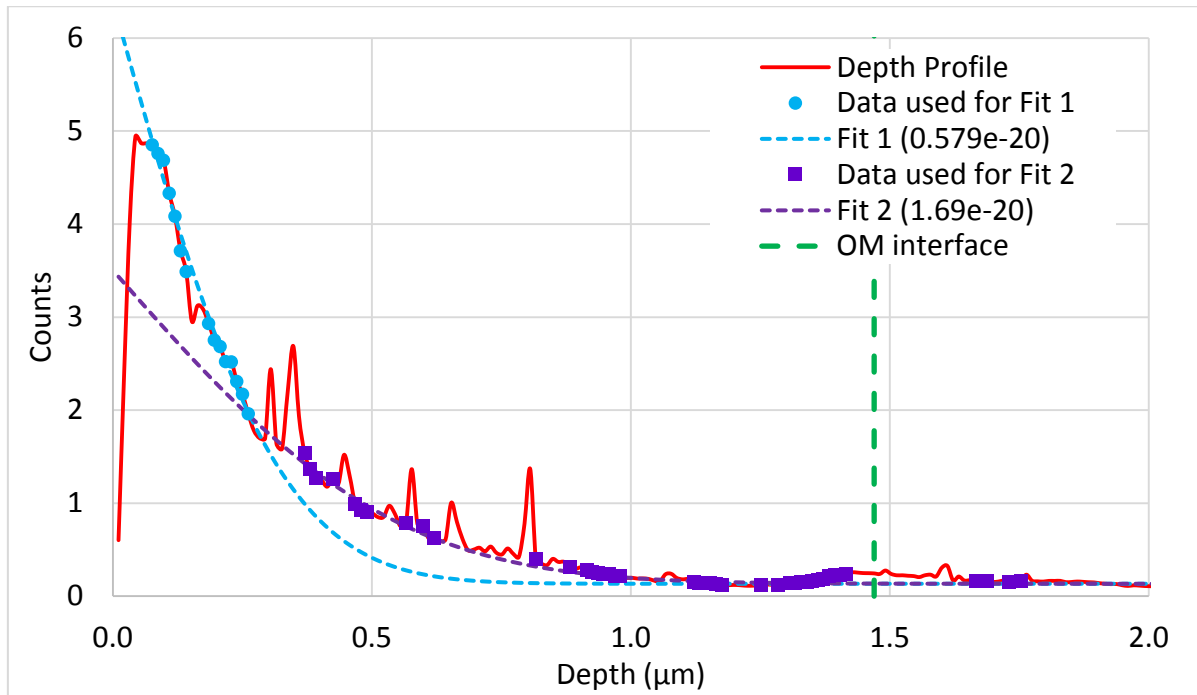


Figure 5.33 – Depth profile for the 62 day high pH sample, with fits for the external (blue line) and internal oxide (purple line). D_0 for the external and internal layers are shown in the legend, with units m^2/s .

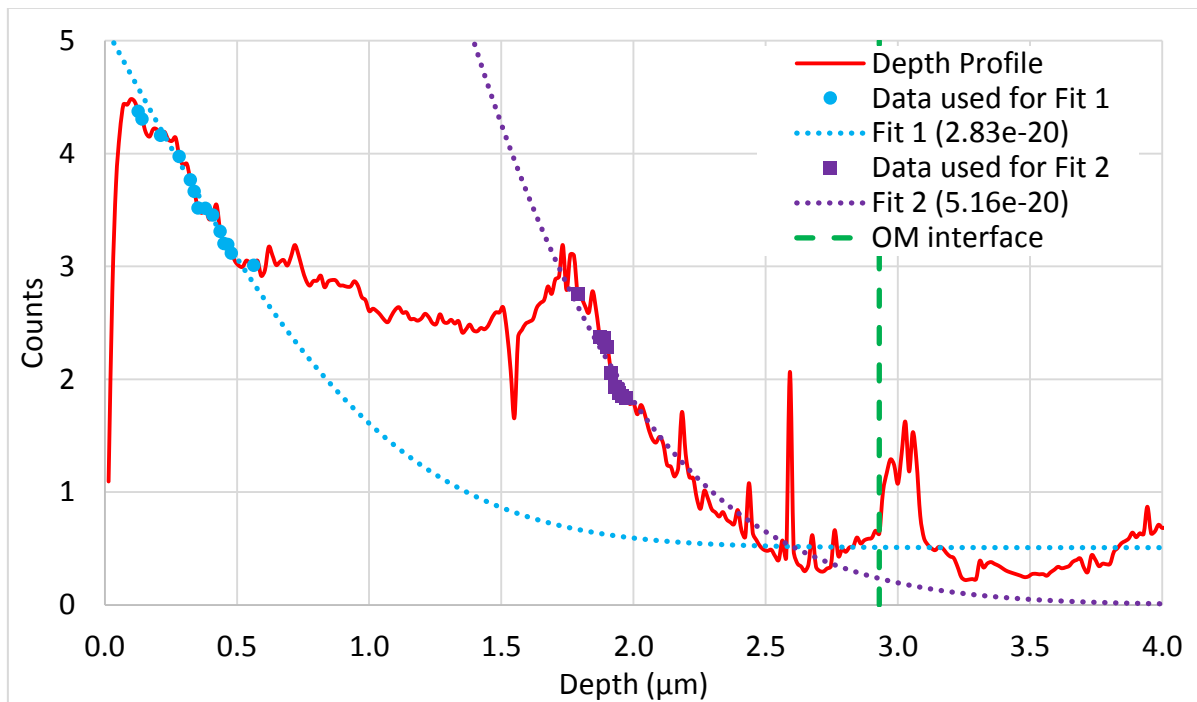


Figure 5.34 – Depth profile for the 148 day high pH sample, with fits for the external (blue line) and internal oxide (purple line). D_0 for the external and internal layers are shown in the legend, with units m^2/s . The spike just after the OM interface is probably from a hydride.

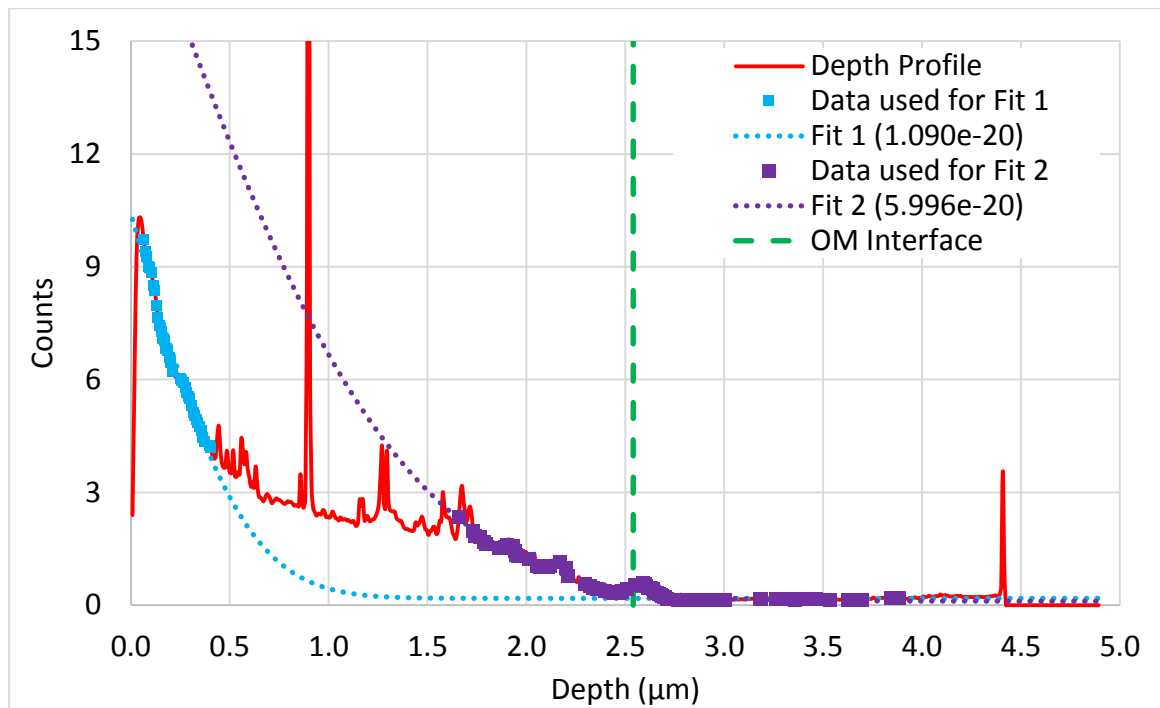


Figure 5.35 – Depth Profile of 106 day pure water oxide, showing the formation of the intermediate oxide between 0.5 – 1.5 μm. Fits for the external (blue line) and internal oxide (purple line) are shown. D_0 for the external and internal layers are shown in the legend, with units m^2/s .

After acquiring the diffusion coefficient (D_0) for both the external and internal oxides on the different samples, I plotted D_0 against oxide thickness, shown in Figure 5.36. This shows that there is not much variation in D_0 in the external oxide, although there is a slightly positive trend for D_0 against oxide thickness. For the internal oxide, D_0 for the 62 day high pH sample is much lower than for the other samples examined, which are roughly the same. An interpretation is that for low oxide thickness, the internal and external oxides have similar diffusion coefficients, and when cracks start to form (in the internal oxide) as the oxide gets closer to transition there is a combination of water ingress through the cracks plus solid state diffusion.

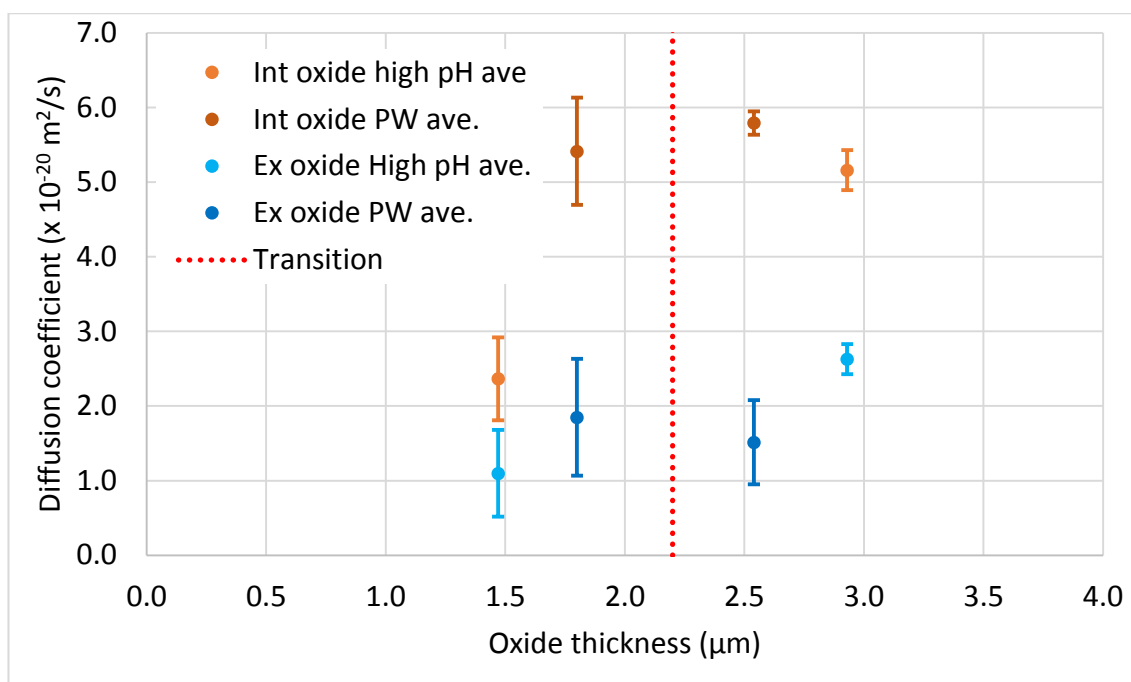


Figure 5.36 – Diffusion coefficients for the external and internal oxides of the samples studied, plotted against oxide thickness. The error bars were calculated from the standard deviation of the data.

5.4.2 – 3D Profiles

It is possible to generate 3D maps of the depth profiles, which are shown below in Figures 4.37 – 4.40 (generated by Dr Kexue Li), are of the same region as the depth profiles shown in Figures 4.31 – 4.34. The Secondary Electron (SE) image is the grey rectangular structure, and the undulating region of the SE image is the OM interface, and the top of the oxide is at the top of the profile. Hydrogen counts are displayed in green, the left-hand image in all the figures (labelled a) shows the pixels where the counts per pixel > 4 . The right-hand images (labelled b) shows the pixels where the counts per pixel ≤ 4 . The images only provide one angle of the depth profile, but Dr Li has published videos moving around the profiles on YouTube, which I would recommend the reader to watch. I have summarised the links in Table 5.2.

Sample	High count	Low counts
61 day pure water	https://youtu.be/iXfqEjO1uHY	https://youtu.be/TeBijMazZ8
106 day pure water	https://youtu.be/jCFuuZkC7Gk	https://youtu.be/XldR7p7DkMc
62 day high pH	https://youtu.be/1_WlogkH_q4	https://youtu.be/ahq3YJdQPHY
147 day high pH	https://youtu.be/Z7GnH-xZmg	https://youtu.be/0jnehdhxjWM

Table 5.2 – Links to 3D profile videos for Figures 4.37 – 4.40.

Figure 5.37 shows the 3D profile for the 61 day pure water oxide. Figure 5.37a shows several large regions in the oxide where H/D has accumulated, which is most likely the free surfaces in cracks, which are the causes of the large spikes seen in the line profile in Figure 5.31. It also shows that there is a large region of high counts near the top of the oxide, which corresponds to the external oxide discussed previously. The low counts image shows that the H/D is uniformly spread out through the internal oxide.

Figure 5.38a shows that for the 106 day pure water sample there are more cracks with H/D present, which correlates to the large spikes in the depth profile in Figure 5.32. There is also a large region near the top of the oxide correlating to the external oxide layer. Figure 5.38b shows a small amount of connection from the oxide to the metal, with an accumulation at the OM interface, again correlating to the depth profile. It also shows that the amount of H/D in the oxide is uniformly spread in the internal oxide.

Figure 5.39a shows that there is relatively little accumulation of H/D in the cracks, except for the region at the top of the oxide, the external oxide. There is much less connectivity throughout the oxide to the OM interface, which may play a part in the lower hydrogen counts in the metal. The small number of possible cracks shown correspond with the cracks seen by STEM in Figure 4.17.

The 148 day high pH oxide (Figure 5.40) shows the highest amount of H/D in the metal, and there is far more H/D at the OM interface in this sample as well. There are several cracks in the oxide, but they are not as large as in the 106 day pure water sample. They are also not as extensive as the ones seen by STEM in Figures 4.27 and 4.28.

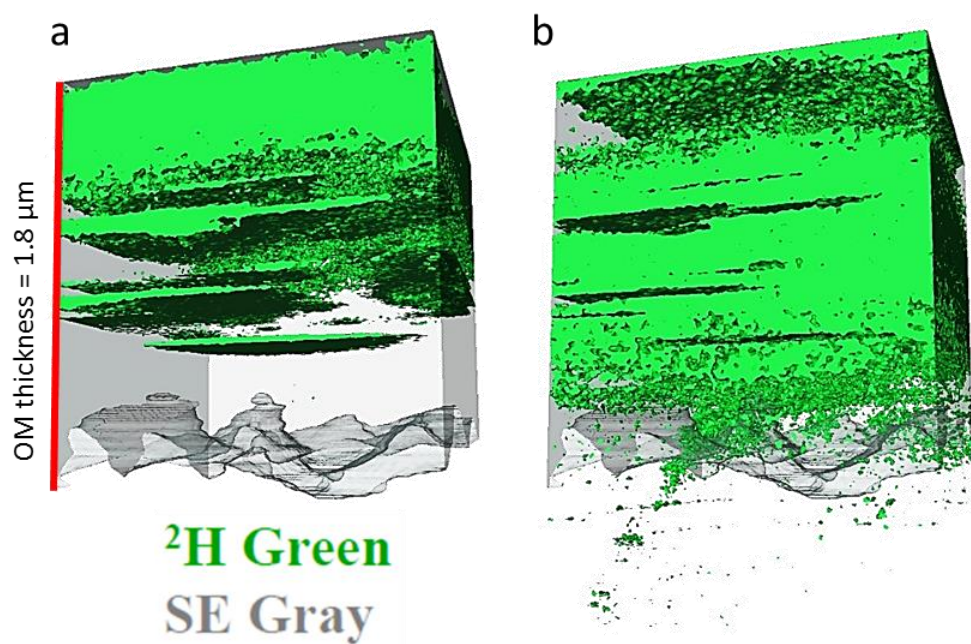


Figure 5.37 – 3D depth profile for 61 day pure water oxide, a) shows the high counts/pixel, and b) shows the low counts/pixel.

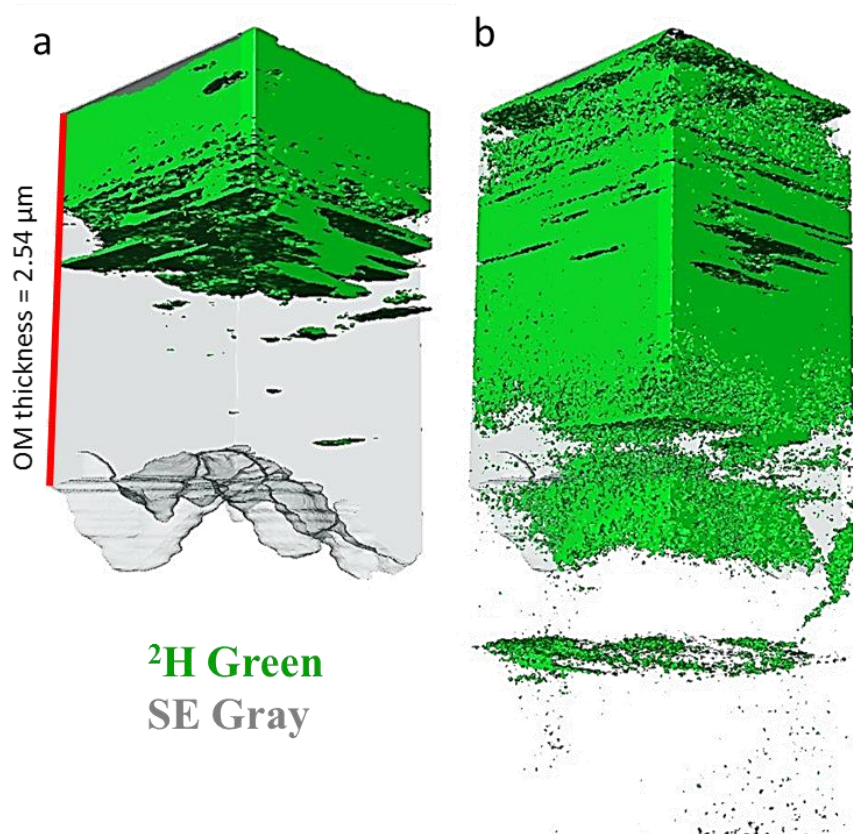


Figure 5.38 – 3D depth profile for 106 day pure water oxide, a) shows the high counts/pixel, and b) shows the low counts/pixel. The large regions below the OM interface in Figure b) show where hydrides are in the metal.

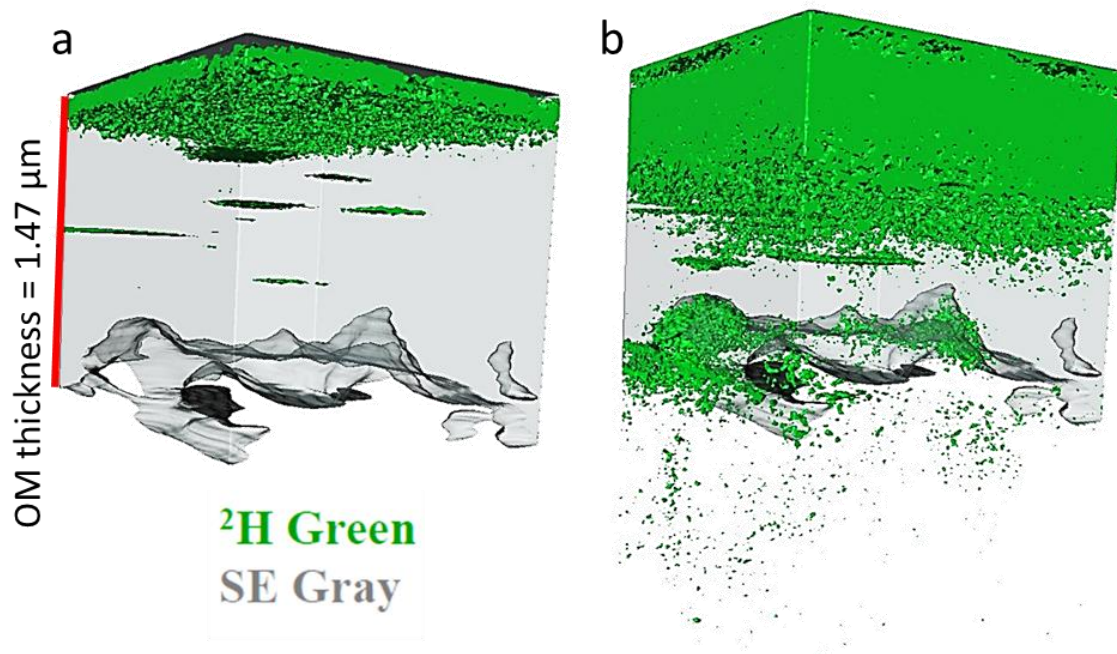


Figure 5.39 – 3D depth profile for 62 day high pH oxide, a) shows the high counts/pixel, and b) shows the low counts/pixel.

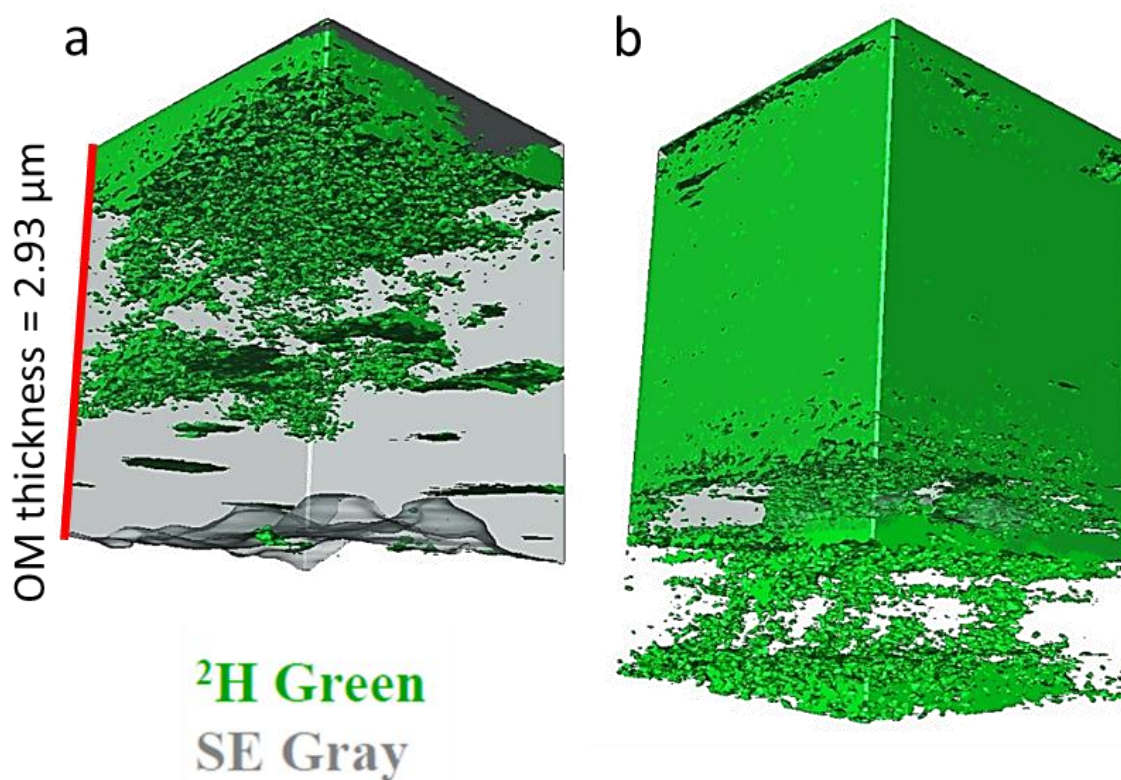


Figure 5.40 – 3D depth profile for 148 day high pH oxide, a) shows the high counts/pixel, and b) shows the low counts/pixel. The high number of counts just below the oxide in Figure b) show the location of hydrides in the metal.

5.5 – Discussion

In section 5.2.1 I showed the desorption of hydrogen from an as-received sample, and mentioned how I adjusted the measured temperature to take into account the emissivity. As I did not know exactly

what the emissivity of any of my samples were I do not know exactly what temperature the desorption starts and when it reaches the peak value. I estimated that the peak of the hydrogen desorption is between 798 – 843°C, and starts at around 598 – 632°C. This is slightly below the value Gulbransen et al.¹³ found, which was approximately 675°C. However, their experiments were carried out in a lower vacuum than in the TDS experiments, which means that hydrogen would be expected to desorb into the vacuum at a lower temperature.

Knowing more about the emissivity of my materials would also be useful for the annealing I carried out on the oxidised samples with the oxide intact, as I could find out the temperature at which the oxide starts dissolving into the metal, and I could also find the temperature the sample settles to after the oxide dissolves.

Figures 5.23 & 5.24 showed that more hydrogen was desorbed from samples with the oxide removed than with the oxide intact. The samples which were cold rolled showed an increase in the amount of hydrogen desorption, and the induced stress on the sample during the oxide removal could have had a similar effect and caused the extra hydrogen desorption. There was also a drop in the amount of all species (H_2 , D-H, D_2) in samples with the oxide intact for the 90 day sample compared to the 75 day sample. The amounts the species decrease are 19%, 33%, and 32% for H_2 , D-H, and D_2 respectively, which are far more than just sample to sample variation. The H_2 is roughly the same in the 123 day sample and these are both less than was found in the 15 day sample. This is contradicted by the HHGE data from PSI, which shows that it increases from 15 to 123 days. The lack of samples tested with HHGE and the oxide intact makes it hard to interpret this data, so it would be beneficial for more of the samples to be tested with this method. It would also be beneficial to run more 90 day samples with the oxide intact.

Figure 5.30 shows that after transition there is about 4 times more hydrogen in the samples exposed to pure water than the elevated pH samples. In chapter 4.1 I showed that the time exponent for the oxide growth at high pH was slightly higher than in pure water, which led to me predicting that f_H would be lower at the end of the second cycle. Using the equation for f_H given by Couet et al.²⁵ I found that after 211 days f_H was ~20% for the pure water sample (as expected from the results shown by Romero et al.²⁶) and ~5% for the high pH sample, which is much lower than any of the MUZIC-2

samples examined. An explanation for this observation is shown by Kido et al.²⁷, where the addition of 950 ppm of boric acid led to the average hydrogen pick-up being 40% of that measured by samples with 0 ppm boric acid (shown previously in Figure 2.14). A similar result was found by the addition of Li. My samples were exposed to both Li and boric acid (as well as KOH) so this is the likely cause in the total hydrogen being higher in the pure water samples. Comparing these results with samples exposed to primary water conditions (which contains Li and boric acid, but not KOH) would allow me to confirm this hypothesis.

From Figure 5.30 I expect that the hydrogen content in the metal is higher for the 106 day pure water sample compared to the 148 day high pH sample, which should mean that the diffusion coefficient would be higher for the 106 day pure water oxide. Figure 5.35 shows that D_0 for the external oxide is slightly higher for the 148 day high pH sample compared to the 106 day oxide, and that D_0 for the internal oxide is similar for both (as well as for the 61 day pure water sample). There is a correlation between oxidation time and D_0 for the internal and external oxide, but D_0 does not appear to be affected by pH.

H/D has penetrated deeper in the 148 day sample than for the rest of the samples tested (one of the depth profiles not shown showed H/D up to 4 μ m from the OM interface). This can be explained by the fact that the pure water samples were only exposed to D₂O for 31 days, after an initial oxidation in pure water, which means the deuterium has had much less time to diffuse through the oxide. For the 148 day sample, the oxide is cracked, especially in the outer, equiaxed region. Some of the cracks will be connected to the surface, so there will be a combination of solid state diffusion from the surface and water ingress. The longer and more numerous the crack network, the larger the fraction of percolation to solid state diffusion. This can be seen in the 3D profiles, where both high pH samples show a higher concentration of H/D in the metal and a much clearer path of the H/D migration. Much more work is needed in this area to obtain a clearer picture of what is happening during and after transition.

5.6 – Summary

In this chapter I have shown that hydrogen which is desorbed is not due to a phase change of the material, but due to ΔF becoming positive at around 600°C, as shown by Gulbransen & Andrew¹³.

The oxide formed acts as a barrier to hydrogen desorption, until the temperature reaches the point at which it is dissolved into the metal, which allows the hydrogen to desorb.

The relationship between hydrogen content and the amount detected by TDS has been calculated from the Westinghouse HHGE data, which shows that there are 1.15×10^6 counts/ppm H_2 in a sample, for a 5 μA emission current. This will allow future users to determine the quantity of hydrogen in a sample without the need to use other equipment.

For the first 1.5 μm of oxide growth, hydrogen pick-up is not affected by the pH, which means that prior to transition hydrogen pick-up is not affected by the availability of protons or H_2 in the environment.

After 1.5 μm of oxide growth the samples exposed to pure water showed a significantly higher hydrogen pick-up than those exposed to a high pH, as shown by Kido et al.²⁷ The NanoSIMS data shows that this could be related to the diffusion coefficient of the H/D in the internal oxide, although it was similar for all the samples tested.

5.7 – References

1. Okamoto H. H-Zr (Hydrogen-Zirconium). *J Phase Equilibria Diffus.* 2006;27(5):548-549. doi:10.1361/154770306X136638.
2. Okamoto H. Sn-Zr (Tin-Zirconium). *J Phase Equilibria Diffus.* 2010;31(4):411-412. doi:10.1007/s11669-010-9734-4.
3. Abriata J, Garcés J, Versaci R. The O-Zr (Oxygen- Zirconium) system. *Bull Alloy Phase Diagrams.* 1986;7(2):116-124.
4. Okamoto H. Fe-Zr (Iron-Zirconium). *J Phase Equilibria Diffus.* 2006;27(5):543-544. doi:10.1361/154770306X136601.
5. Okamoto H. Cr-zr (chromium-zirconium). *J Phase Equilibria.* 1993;14(6):768-768. doi:10.1007/BF02667894.
6. Khatamian D, Root JH. Comparison of TSSD results obtained by differential scanning calorimetry and neutron diffraction. *J Nucl Mater.* 2008;372(1):106-113. doi:10.1016/j.jnucmat.2007.02.010.
7. Kim J-S, Kim Y-S. Effect of thermal history on the terminal solid solubility of hydrogen in Zircaloy-4. *Int J Hydrogen Energy.* 2014;39(29):16442-16449. doi:10.1016/j.ijhydene.2014.08.018.

8. Vizcaino P, Rios R, Banchik A. Hydrogen determinations in a zirconium based alloy with a DSC. *Thermochim Acta*. 2005;429:7-11. doi:10.1016/j.tca.2004.11.019.
9. Giroldi JP, Vizcaíno P, Flores AV, Banchik AD. Hydrogen terminal solid solubility determinations in Zr–2.5Nb pressure tube microstructure in an extended concentration range. *J Alloys Compd*. 2009;474(1-2):140-146. doi:10.1016/j.jallcom.2008.06.104.
10. Setoyama D, Matsunaga J, Ito M, et al. Influence of additive elements on the terminal solid solubility of hydrogen for Zirconium alloy. *J Nucl Mater*. 2005;344(1-3):291-294. doi:10.1016/j.jnucmat.2005.04.057.
11. McMinn A, Darby EC, Schofield JS. The terminal solid solubility of hydrogen in zirconium alloys. In: Sabol GP, Moan G, eds. *Zirconium in the Nuclear Industry: Twelfth International Symposium ASTM STP 1354*. ASTM International; 2000:173-195.
12. Tupin M, Martin F, Bisor C, et al. Hydrogen diffusion process in the oxides formed on zirconium alloys during corrosion in pressurized water reactor conditions. *Corros Sci*. 2017;116:1-13. doi:10.1016/j.corsci.2016.10.027.
13. Gulbransen E, Andrew K. Solubility and decomposition pressures of hydrogen in alpha-zirconium. *JOM*. 1955;7:136-144.
14. Bechmann R, Carpenter LG, Mair WN, et al. The optical emissivity of titanium and zirconium. *Proc Phys Soc Sect B*. 1950;63(8):573-577.
15. Lustman B, Kerze Jr F. *Metallurgy of Zirconium*.; 1955.
16. Murphy E V, Havelock F. Emissivity of zirconium alloys in air in the temperature range 100-400°C. *J Nucl Mater*. 1976;60:167-176.
17. Fong RWL, Paine M, Nitheanandan T. Total hemispherical emissivity of pre-oxidized and un-oxidized Zr-2.5Nb pressure-tube materials at 600°C to 1000°C under vacuum. *CNL Nucl Rev*. 2016;5(1):85-93. doi:http://dx.doi.org/10.12943/CNR.2016.00006.
18. Dupim IS, Moreira JML, Huot J, Santos SF. Effect of cold rolling on the hydrogen absorption and desorption kinetics of Zircaloy-4. *Mater Chem Phys*. 2015;155:241-245. doi:10.1016/j.matchemphys.2015.02.036.
19. Yamanaka S, Nishizaki T, Uno M, Katsura M. Hydrogen dissolution into zirconium oxide. *J Alloys Compd*. 1999;293-295:38-41.
20. Yamanaka S, Fujita Y, Uno M, Katsura M. Influence of interstitial oxygen on hydrogen solubility in metals. *J Alloys Compd*. 1999;293-295:42-51.
21. Miyake M, Uno M, Yamanaka S. On the zirconium–oxygen–hydrogen ternary system. *J Nucl Mater*. 1999;270(1-2):233-241. doi:10.1016/S0022-3115(98)00779-X.
22. Chen W, Wang L, Lu S. Influence of oxide layer on hydrogen desorption from zirconium

- hydride. *J Alloys Compd.* 2009;469(1-2):142-145. doi:10.1016/j.jallcom.2008.01.157.
23. Li YS, Wong PC, Mitchell K a. R. XPS investigations of the interactions of hydrogen with thin films of zirconium oxide II. Effects of heating a 26 Å thick film after treatment with a hydrogen plasma. *Appl Surf Sci.* 1995;89(3):263-269. doi:10.1016/0169-4332(95)00032-1.
 24. Peterson WJ, Gilbert RE, Hoflund GB. The interaction of hydrogen with polycrystalline zirconium Part II. The effect of preadsorbed oxygen. *Appl Surf Sci.* 1985;24:121-124.
 25. Couet A, Motta AT, Comstock RJ. Hydrogen pickup measurements in zirconium alloys: Relation to oxidation kinetics. *J Nucl Mater.* 2014;451(1-3):1-13. doi:10.1016/j.jnucmat.2014.03.001.
 26. Romero J, Partezana J, Comstock RJ, Hallstadius L, Motta AT, Couet A. Evolution of hydrogen pickup fraction with oxidation rate on zirconium alloys. In: *Top Fuel 2015 - Reactor Fuel Performance*. European Nuclear Society; 2015:476-482. Available at: <https://www.euronuclear.org/events/topfuel/topfuel2015/transactions/topfuel2015-transactions-oral-1.pdf>.
 27. Kido T, Wada S, Takahashi T, Uchida H, Komine I, Inoue Y. Behavior of lithium and boron in irradiated and unirradiated oxides formed on Zircaloy-4 claddings. In: Sabol GP, Moan G, eds. *Zirconium in the Nuclear Industry: 12th International Symposium, ASTM STP 1354*. ASTM International; 2000:773-792. doi:10.1520/STP14327S.

6 – Simulation of Thermal Desorption Experiments

Contents

6.1 – Introduction to TMAP	170
6.2 – Input File For TMAP	171
6.3 – Interaction of Hydrogen With Metals.....	173
6.4 – TMAP Tests	174
6.4.1 – Binding Energy.....	176
6.4.2 – Diffusion Coefficient/Energy	177
6.4.3 – Solubility	179
6.4.4 – Fraction of Traps Filled.....	179
6.4.5 – Trap Concentration.....	180
6.4.6 – Two Trap Test	181
6.5 – Discussion	182
6.6 – Summary	185
6.7 – References	185

This chapter will cover my attempts to model the hydrogen desorption peaks shown in Chapter 5 with the Tritium Migration and Analysis Program (TMAP). I will first discuss the way that TMAP works and what parameters we can control. Then I will cover the steps taken to try to model the desorption peaks and my conclusions.

6.1 – Introduction to TMAP

TMAP developed in the 1980s at the Idaho National Engineering and Environmental Laboratory as a method of examining the safety of systems involving tritium. It has since gone through several upgrades and is now at TMAP7, and a manual¹ and validation^{2,3} have been published for further reading.

To briefly summarise TMAP-7, the material being modelled is considered as a one dimensional structure, which is divided into a number of computational slices (also called nodes) determined by the user. The TMAP code then computes a solution to the time dependent one dimensional diffusion equation for concentrations of gaseous and dissolved gaseous species and flows in a connected system of enclosures (the chamber of the TDS) and solid structures (the Zr material). The conditions required for the computation are the time dependent thermal history and the physical properties of the enclosures and structures, along with the initial state and sources/sinks of hydrogen in the system.

TMAP7 has been used to study hydrogen and deuterium diffusion in tungsten^{4,5} and thermal release of deuterium in beryllium⁶⁻⁸, but there does not appear to have been any studies on zirconium with TMAP.

6.2 – Input File For TMAP

An example of the input file used for TMAP is shown in Appendix A.1. There are seven input sections in the file, which I will now summarise.

The first part is the Main Input, which is used to define the diffusion species name (dspcnme, line 6). The model can accommodate different segments in the material, and the number of nodes in each segment of the problem is defined by segnds (line 8). The code uses the term enclosure to describe the atmosphere, and naming a gas in the enclosure is carried out with espnme (line 7), and the number of enclosures is given by nbrencl (line 9). The last part of the Main Input is the segment linking (linksegs, line 10).

The next part is the enclosure input, which defines the type of enclosure used and the parameters associated with it. I have used a boundary enclosure (bdry, line 14), which is the simplest enclosure as it is not affected by convective flows or diffusion effects. Two parameters are defined, the temperature in the enclosure (etemp, line 15), and the partial pressure of the gaseous species in the enclosure (esppres, line 16). These are defined by two equations in the Equations Input section, for the temperature (equation 1, lines 81 & 82) I have used the same heating profile used in the TDS, heating from room temperature at 10°C/min (0.1666 K/s). The partial pressure of the gas is defined in equation 6 (lines 93 & 94) as the pressure typically seen in the vacuum chamber of the TDS, 6.67×10^{-7} Pa.

The Thermal Input section is used to define the heat transfer conditions of each segment in the problem. The thickness of the nodes is defined by delx (line 22), and the thickness of the end nodes must be zero. The initial temperature of each node is defined by tempd (line 23), the thermal conductivity is defined with tcon (line 24). The thermal capacity (rho cp, line 25) is defined as the density multiplied by the heat capacity of the material, and the local heat generation rate (hsr, line 26) can also be defined. The boundary conditions of the segment are described by htrbcl (left, line

27) and htrbcr (right, line 28). The left boundary has been specified to be the same as the enclosure temperature and the right boundary is linked to the second segment. This is followed by the thermal conductance of the gap between the segments (hgap, line 29). The second segment defines the same parameters, and finishes with on line 38 with the statement 'htrbcr=adiab,end'. This adds an insulated boundary to the end of the segment which has no heat transfer through it.

The next section is the Diffusion Input, which starts with the diffusion segment lattice density (nbrden, line 44), concd (line 45) gives the initial concentration values of the mobile diffusion species at each of the nodes in that particular segment. The diffusion coefficient for the segment is given by dcoef (line 46), and is displayed in equation 2 (line 85). Lines 47–53 are used to define different traps types (ttyp), the trap concentration, or traps per atom. (tconc, line 47). For each trapped species (tspc, line 48) there is the trap release rate (alphr in the code, line 48), the fraction of those traps that are filled (ctrapp on line 49), and the trapping rate coefficient (alpht, line 49). The trapping rate and trap release rate are defined by equations 7 (line 96) and 8 (line 98).

The next two lines define terms which are not needed in my modelling, the first (qstrdr, line 54) is a term for if a mixture of mobile species is present. The second (srcsd, line 55) defines a source rate from a radioactive source.

The lines after this define the boundary conditions of the segment, difbcl (left, line 56) and difbcr (right). For the left boundary 'lawdep' defines an equilibrium boundary, into enclosure 1, where single deuterium atoms combine into D_2 . Line 57 gives the pressure exponent from Sieverts Law (0.5), and solcon is the solubility, which is given in equation 3 (line 87). Line 58 shows that the right hand side of the segment is linked to the other segment. The surface area of the segment is defined by surfa. Line 76 shows the right hand side of the second segment has no diffusion across it.

The next section is Control Input, which controls the basic parameters for the program. For example the time for which the simulation will run is controlled by timend on line 109, and the maximum size of a time step is defined by tstep on line 108. When the software is carrying out the computation it prints a list of computational results, and nprint is defines the number of seconds elapsed in the simulation for every line which is printed. TMAP uses an iterative convergence to find solutions, and the number of iterations is given by itemx (line 111).

The last part of the input file is the Plot Input, which controls the data being printed to the output file, known as PLTDATA. This file, along with the 'codeout' and '_codeout' file can be used to plot the data obtained. The frequency at which data is saved to PLTDATA is given by nplot (line 119), the segments to be included in the file listing are specified by plotseg (line 120), the enclosures to be included in the file listing are given by plotencl (line 121), dname (line 122) states which diffusion species will be included in the file listing, and ename (line 123) determines the gaseous species (those which exist in the enclosure) will be included in file listing. The following line, 'dplot=moblinv,sflux,end', determines the relevant diffusion species data to be recorded. The mobile inventory values for each diffusion species is specified by 'moblinv', and the values for the diffusion flux at both surfaces of each segment is specified by 'sflux'.

6.3 – Interaction of Hydrogen With Metals

Figure 6.1 shows the different potential energies which are involved in the process of hydrogen interacting with a metal, and the following description is derived from the same source as Figure 6.1⁹. In the gas phase hydrogen exists as a molecule and must receive a dissociation energy (E_{Di}) to be split into two hydrogen atoms. The chemisorption energy, E_{Ch} is the chemical binding energy between atomic hydrogen and metal atoms at the surface. E_{Ad} is the adsorption energy, and this must be overcome for hydrogen to access a chemisorption site (this is dependent on the surface condition). The solubility energy, E_s , is the energy difference between a dissolved atom and a free one. Depending on the sign of this value the material is defined as exothermic ($E_s < 0$) or endothermic ($E_s > 0$), and Figure 6.1 is an example of an endothermic material. Zirconium is an endothermic material as hydrogen comes out of solution when it is cooled, which is the reason hydrides form in nuclear cladding and there is hydrogen embrittlement. E_D is the diffusion energy, which is the energy required to pass from one solution site to another. The trapping energy, E_T , is the energy of the potential well formed by a trapping site, such as dislocations, grain boundaries or precipitates. The binding energy, E_B is the difference between the trapping energy and the diffusion energy, i.e. $E_B = E_T - E_D$.

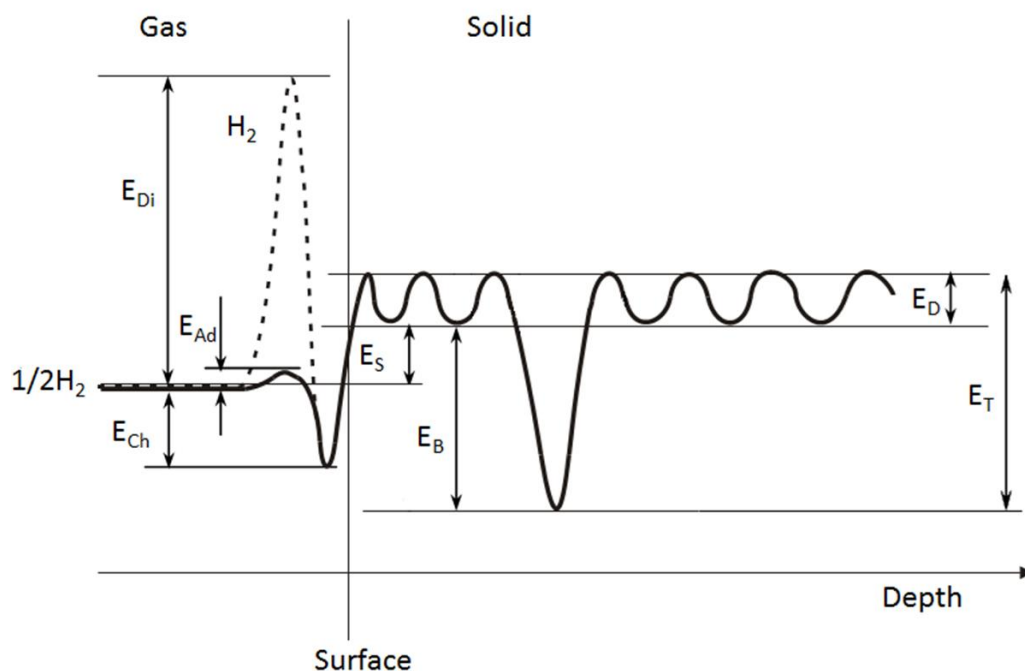


Figure 6.1 – Distribution of potential energies for hydrogen in a metal. © 2012 Peñalva I, Alberro G, Legarda F, Esteban GA, Riccardi B. Published in Reference⁹ under CC BY 3.0 license. Available from: <http://dx.doi.org/10.5772/34469>

6.4 – TMAP Tests

I will first discuss the properties I can determine from the literature, before showing the results when testing different parameters defined previously.

The diffusion equation is governed by an exponential relationship of the form:

$$D_H = D_0 * \exp\left(-\frac{E_D}{RT}\right) \quad (1)$$

Where D_0 is the maximum diffusion coefficient at infinite temperature, E_D is the diffusion energy (also known as activation energy) mentioned in the previous section, R is the molar gas constant and T the temperature in Kelvin. From the literature $D_0 = 7.73 \times 10^{-7} \text{ m}^2/\text{s}$ and $E_D = 45.27 \text{ kJ/mol}^{10,11}$. After dividing E_D by R the value is 5445 K, and to express this in eV, multiply 5445 K by k_B (in eV K^{-1}), which gives 0.47 eV.

The solubility of hydrogen gas in zirconium follows Sieverts law and is of the form:

$$S_H = \sqrt{K * p_H} \quad (2)$$

In equation (2), S_H is the concentration of the dissolved H atoms/ m^3 in Zr, K is the equilibrium constant of the reaction for the reaction H_2 (molecular gas) \rightleftharpoons 2 H (dissolved atoms), and p_H is the

partial pressure of the gas at the interface with Zr. Gulbransen and Andrew¹² showed the relationship between the pressure of hydrogen and concentration, which is:

$$p_H = \left(\frac{N_{H(\alpha)}}{N_s - N_{H(\alpha)}}\right)^2 * \exp\left(\frac{2F_\alpha - F_{H_2(gas)}}{RT}\right) \quad (3)$$

Where the pre-exponential term can be replaced with S_H . Rearranging (3) gives:

$$S_H = \sqrt{p_H} * \exp\left(-\frac{\Delta F}{RT}\right) \quad (4)$$

Where I have replaced the term in the exponential with the term $\Delta F = F_\alpha - 0.5F_{H_2(gas)}$. Gulbransen and Andrew calculated ΔF from 0 – 700°C, which I have plotted in Figure 6.2. The trend line shows that ΔF (J/mol/K) = 62.929*T – 59714. The pressure in the vacuum chamber is 6.667×10^{-7} Pa, and putting these values into equation (4) gives:

$$S_H = 8.165 * 10^{-4} * \exp\left(-\frac{62.929T - 59714}{RT}\right) \quad (4)$$

Note I have initially set K from equation (2) to 1. The following sub-chapters will cover the testing of the different parameters mentioned previously, starting with the binding energy. The sample thickness = 0.25 mm.

The initial conditions I used were:

- Binding Energy = 0.3 eV
- Diffusion Coefficient = 7.73×10^{-7} m²/s
- Diffusion Energy = 0.47 eV
- Solubility pre-exponential = 8.165×10^{-4} m⁻³
- Ctrap = 1.0
- Tconc = 1.00e-4 traps per atom (1 trap per 10 000 atoms)

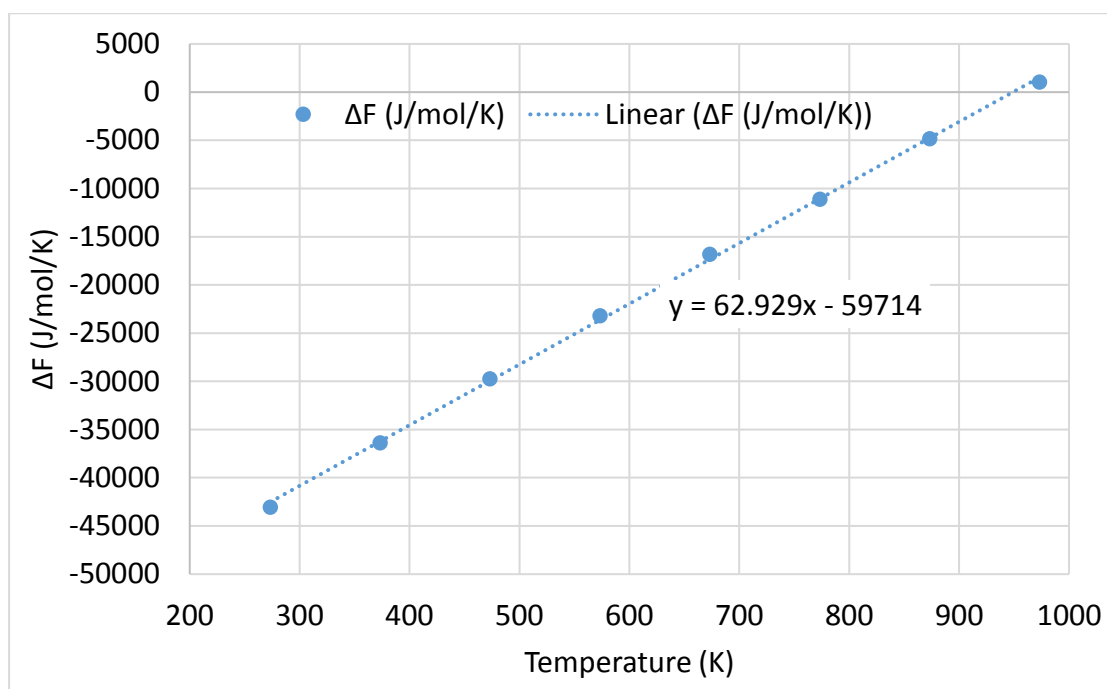


Figure 6.2 – ΔF vs temperature as found by Gulbransen and Andrew¹², showing that ΔF becomes positive around 675°C.

6.4.1 – Binding Energy

Figure 5.6 showed that there are two peaks, a small one around 350°C and a much larger one around 650°C. The first test was to see if I could reproduce at least one of these peaks, and if successful, move to reproducing both peaks. For the first test I varied the trap energy (inside exponential term on line 98 in Appendix A.1) from $E_T = 0.7 - 1.5$ eV ($E_B = 0.23 - 1.03$). The results are shown in Figure 6.3, showing that for $E_B = 0.2 - 0.3$ eV there is a desorption peak ~350°C, which corresponds to the first small peak seen by TDS. For $E_B = 0.93 - 1.03$ eV the high temperature peak is reproduced.

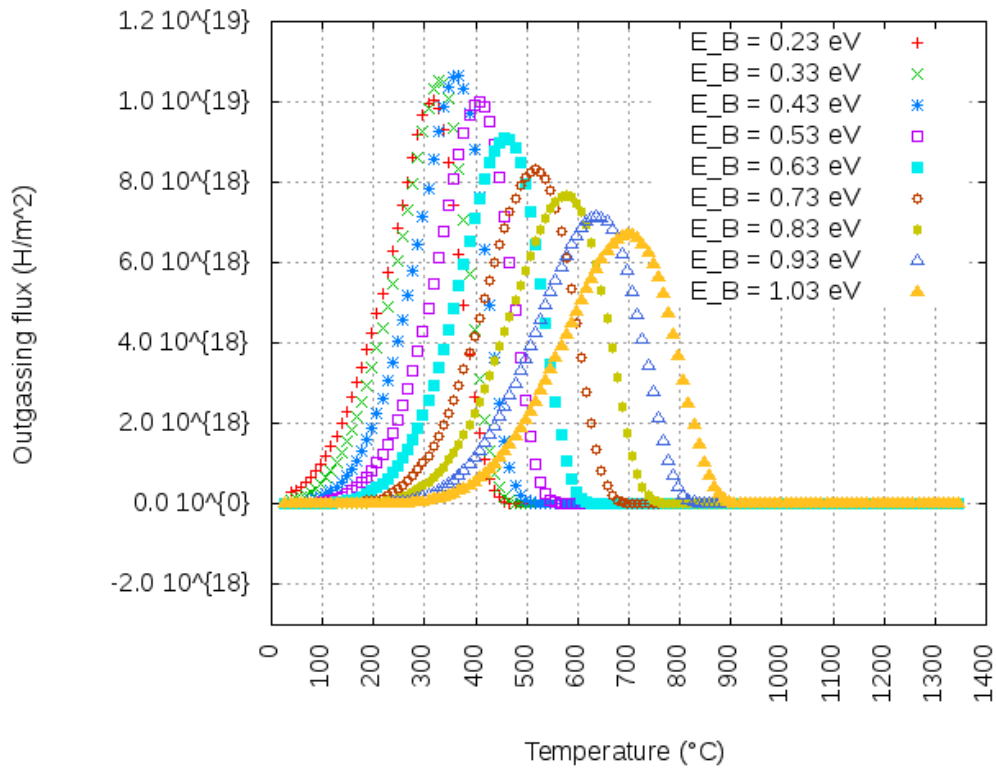


Figure 6.3 – Effect of binding energy on hydrogen desorption vs temperature.

6.4.2 – Diffusion Coefficient/Energy

The pre-exponential of the diffusion coefficient (D_0) was tested first and is shown in Figure 6.4. Making D_0 larger means that the hydrogen is more mobile and will desorb at a lower temperature. As D_0 decreases the peak gets broader.

The effect of changing E_D (from 0.27 – 0.87 eV) is shown in Figure 6.5, whilst keeping E_B constant. As E_D increased the peak shifted to a higher temperature and became broader. Figure 6.5 shows that the desorption can be modelled with $E_B = 0.3$ eV and $E_D = 0.47$ & 0.77 eV for the low and high temperature traps respectively.

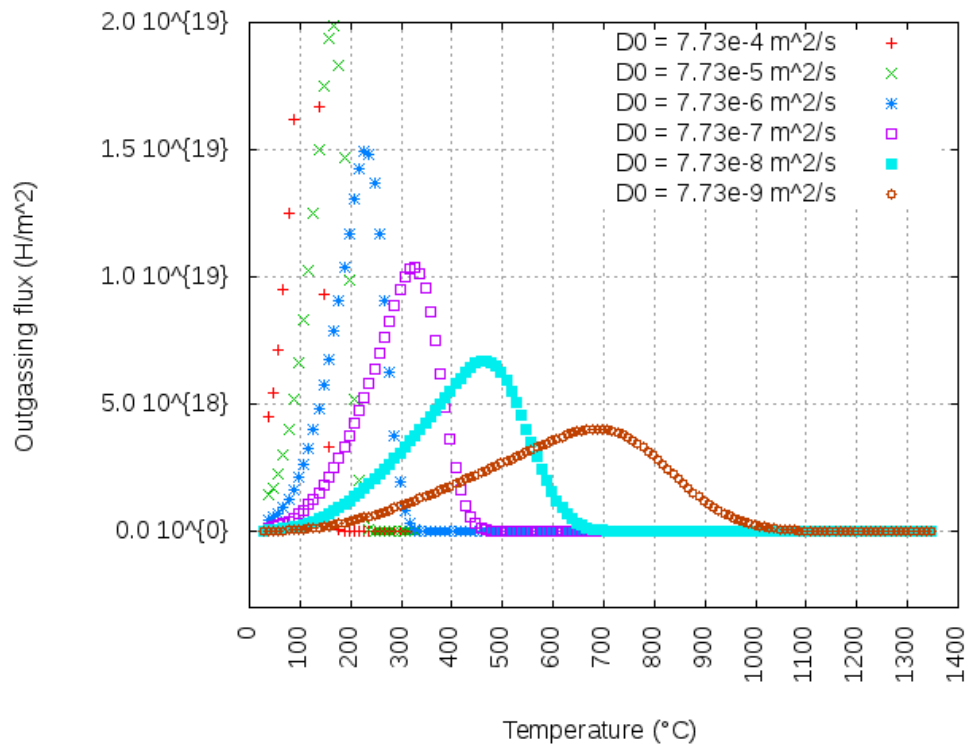


Figure 6.4 – Testing hydrogen desorption vs D_0 .

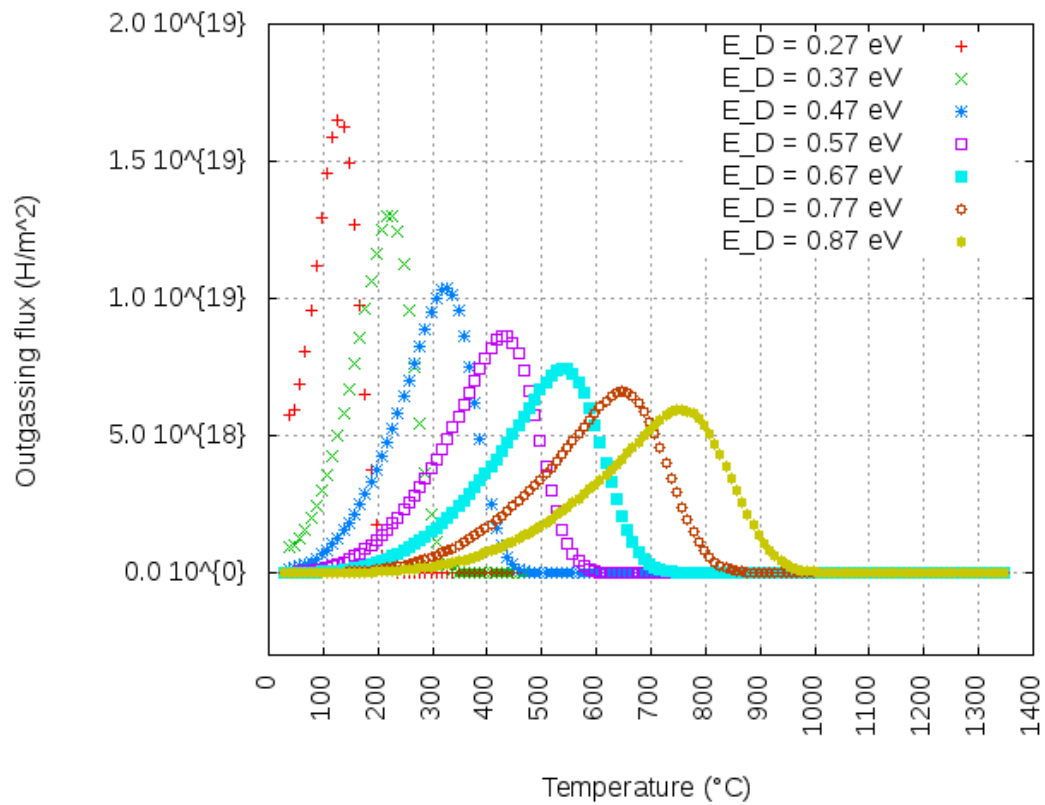


Figure 6.5 – Hydrogen desorption whilst varying D_E across 0.6 eV shifts the peak to a higher temperature whilst broadening the peak.

6.4.3 – Solubility

The effect of changing the solubility by orders of magnitude is shown in Figure 6.6, showing that the pre-exponential term has no effect on the desorption.

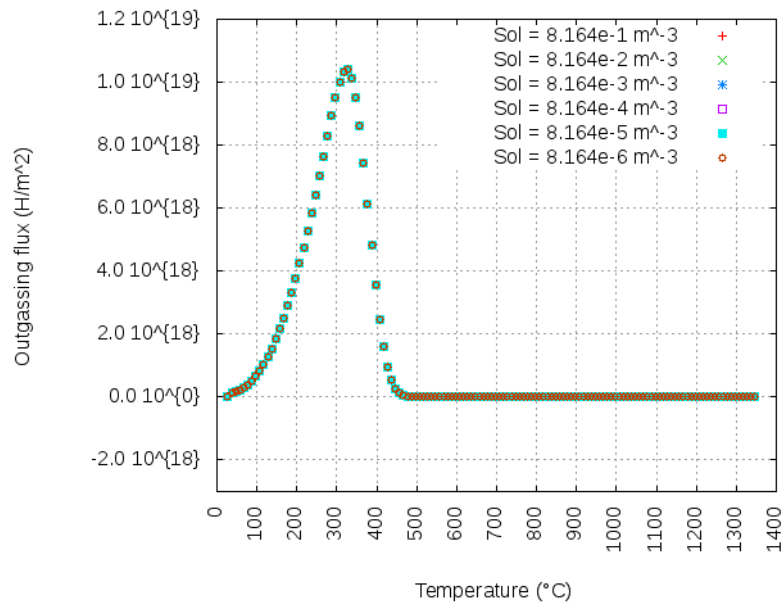


Figure 6.6 – Effect of solubility pre-exponential term on hydrogen flux.

6.4.4 – Fraction of Traps Filled

Figure 6.7 shows that increasing the percentage of traps which are filled leads to more hydrogen being desorbed with the same peak temperature.

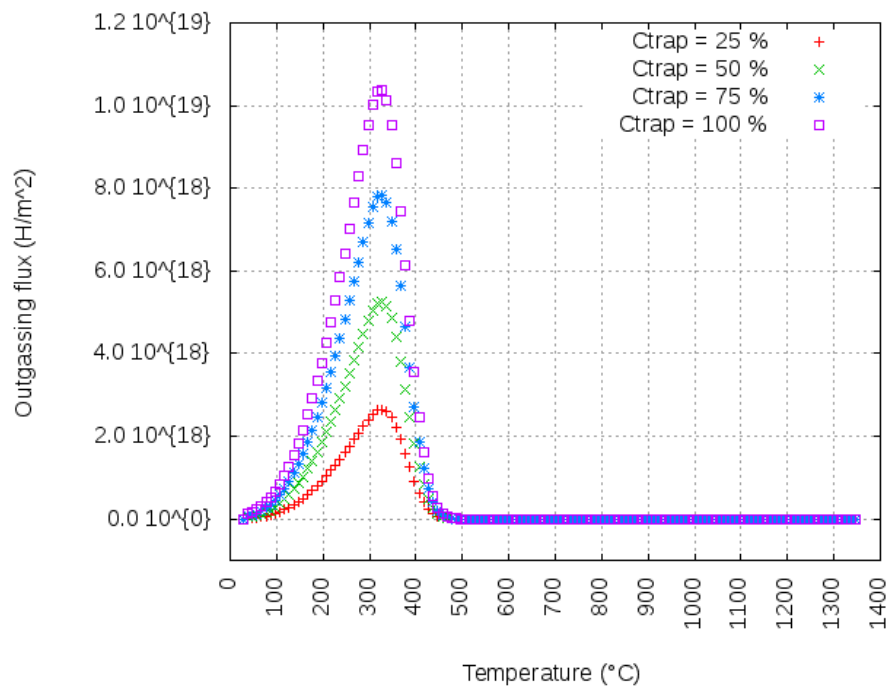


Figure 6.7 – Hydrogen desorption when changing percentage of traps filled.

6.4.5 – Trap Concentration

The amount of traps per atom (Tconc) can be adjusted. Figure 6.11 shows the effect of altering Tconc by orders of magnitude (from around 1 trap per 10 atoms to 1 in 100 000 atoms). As expected the amount of hydrogen released decreases as the number of traps per atom is decreased. Looking at a log scale on the y-axis (Figure 6.12) shows that changing the number of traps per atom by an order of magnitude leads to an order of magnitude more of hydrogen being desorbed, and a slight shift in the peak to a higher temperature for a higher trap concentration.

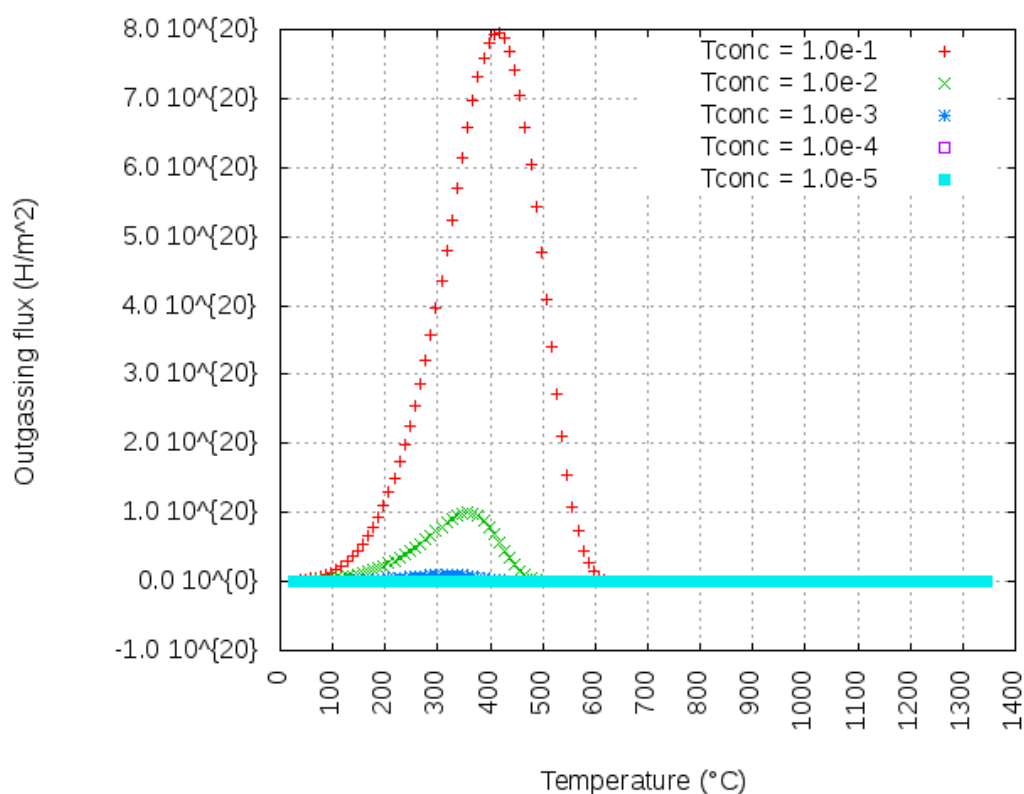


Figure 6.11 – Variation of hydrogen desorption with a variation of traps per atom.

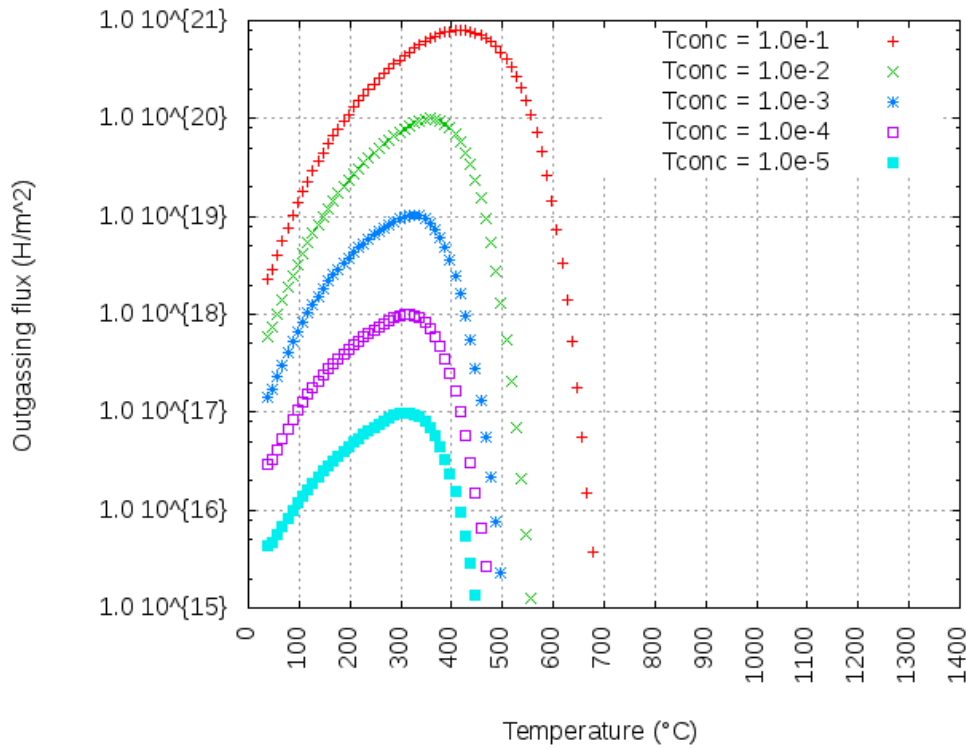


Figure 6.12 – Log graph of Figure 6.11.

6.4.6 – Two Trap Test

Figure 6.13 shows the results of my attempts at reproducing the TDS results, with a peak at 350°C and one at 750°C.

The input file for this plot is shown in Appendix A.2, which shows that I split the zirconium into two segments, one with $E_D = 0.77$ eV (74.30 kJ/mol) and $E_B = 0.3$ eV, and the other with $E_D = 0.87$ eV (83.95 kJ/mol) and $E_B = 0.3$ eV. I made the first segment thicker than previously, with each node 0.1 μm thick. This made the segment thickness = 1.8 μm , which was 0.7% of the total thickness. The second segment had the same distribution of nodes as in the previous computations. The first segment had 5 traps per 1000 Zr atoms, and the second segment had 1 traps per 1000 Zr atoms.

It is possible that the first segment could be modelling the native oxide layer formed on Zr, although in this example it is much thicker than in reality.

The binding energy of each trap is within the range found in the literature, but E_D is much higher than that found in the literature for both segments. I will discuss this result in the next section.

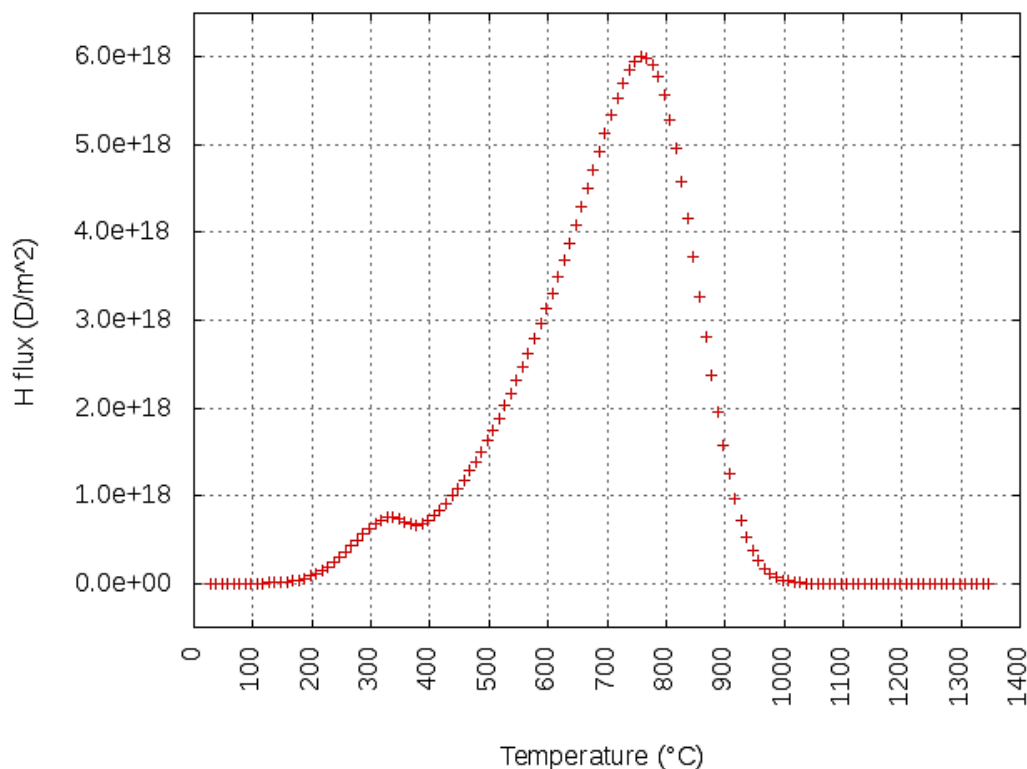


Figure 6.13 – Results from testing for two traps, showing a peak ~300°C and one at 750°C.

6.5 – Discussion

It has been possible to reproduce the peaks of hydrogen seen by TDS using TMAP, although so far it is not 100% correct. Whilst trying to model the two different parts simultaneously I came across several different issues which I had to work around. The first problem is that E_D is much higher in this solution than has been found in the literature, by 0.3eV (28.95 kJ/mol) and 0.4 eV (38.59 kJ/mol) for the low and high energy trap respectively. This is probably partly due to the issue with the number of nodes and their thickness, as described below.

The other problem is that throughout the simulations the peaks have been much wider than those seen by TDS. For the as-received sample (shown in Figure 5.6) the FWHM of the peak was approximately 150°C, but the results shown in Figure 6.13 show the FWHM to be ~250°C. The only part of the input file that can control the width of the peak is the number of nodes and the thickness of the nodes. Figures 6.14 & 6.15 show an example of this. In Figure 6.14 there were 100 nodes of thickness 1µm (total thickness = 0.1 mm), which gave a desorption peak at ~280°C, the peak flux of hydrogen was ~5 x 10¹⁹, and the FWHM = ~100°C. In Figure 6.15 there were 100 nodes of thickness 10µm (total thickness = 1 mm) which shows a peak at ~510°C, the peak flux of hydrogen was ~1.7 x 10²⁰, and the FWHM = 300°C. This shows that to simulate the material used (which was 0.5 mm) in the TDS would

require either 500 nodes 1 μm thick or 50 nodes 10 μm thick. The former would be more accurate, but the computing time increases dramatically when the number of nodes increases. For 50 nodes the simulation does not take long but the peak would be much wider than in reality. This area needs more investigation to find the ideal node size and number of nodes, but it is worth noting that as there is a limit of 1000 nodes which can be used. I have also not included an oxide layer in these simulations, which will be necessary in the future as a thin oxide layer is readily formed on zirconium.

There are a few general limitations I have not mentioned yet with using TMAP to simulate hydrogen desorption, which is covered by Baldwin et al.⁸ and summarised here. One is that the model only allows single occupancy per trap, and it has been found that a single Zr vacancy can trap up to 9 H atoms⁶. Another is that the trap energies are discrete values, which is not going to be constant throughout a material. The distribution and concentration of traps are constant and immobile throughout the simulation, although these could change as the sample is heated. There is also no clear method for describing the chemistry of hydrides in the metal, which is important due to the ease with which hydrides form in zirconium. The simulation also does not tell the user what type of trap is present in the material, just that there are traps present.

During these tests I took the Sieverts constant (K in equation 2) to be 1. It has been found that this constant also follows an Arrhenius equation^{9,13,14}, so in the future it would be useful to insert this into the solubility equation.

This has been a successful sensitivity study in that it has been possible to simulate the desorption of hydrogen with the known values from the literature. It would be beneficial to study the effect of the node thickness in more depth, and being able to get access to a computer cluster to speed up the computations is a must.

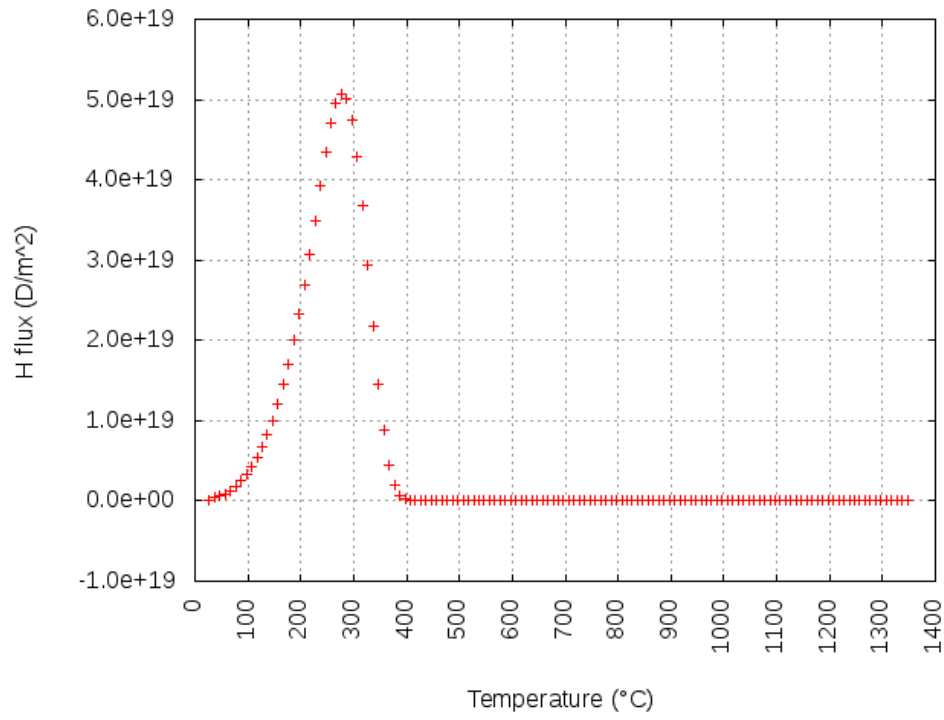


Figure 6.14 – Hydrogen desorption with 100 nodes, each of which were 1 μm thick. $E_D = 0.47$ eV, $E_B = 0.3$ eV.

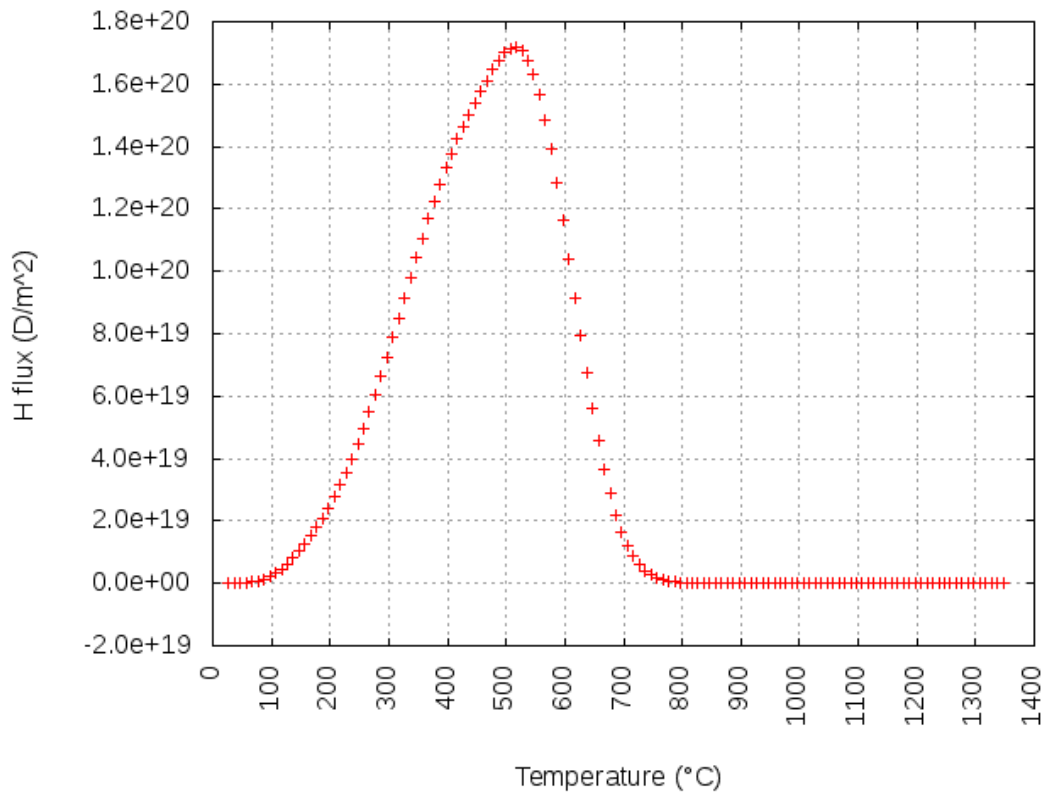


Figure 6.15 – Hydrogen desorption with 100 nodes, each of which were 10 μm thick. $E_D = 0.47$ eV, $E_B = 0.3$ eV.

6.6 – Summary

In this chapter I have introduced TMAP and shown the capability it has on reproducing the hydrogen desorption seen by TDS. Using the literature values as a starting point, I found that they were all in the correct order of magnitude.

The lower temperature peak was reproduced with $E_B = 0.2 - 0.3$ eV and $E_D = 0.47$ eV. The higher temperature peak was shown with $E_B = 0.93$ and $E_D = 0.47$ eV.

By keeping $E_B = 0.3$ eV and varying E_D at the same time as E_T it was possible to reproduce the high temperature peaks shown during the TDS analysis. This is at the upper end of E_B from the literature for H in Zr vacancies, which indicates that this is where the hydrogen observed from TDS is released from.

It was possible to reproduce the lower temperature peak along with the higher temperature peak simultaneously, however E_D was higher than found in the literature for both peaks. More work is needed in this area to obtain a better solution.

6.7 – References

1. Longhurst GR. *TMAP7 User Manual*.; 2004. doi:dx.doi.org/10.2172/910958.
2. Ambrosek J, Longhurst GR. *Verification and Validation of TMAP7*.; 2008. doi:https://doi.org/10.2172/952009.
3. Merrill BJ, Humrickhouse PW, Shimada M. Recent development and application of a new safety analysis code for fusion reactors. *Fusion Eng Des*. 2016;109-111:970-974. doi:10.1016/j.fusengdes.2016.01.041.
4. Gasparyan YM, Golubeva A V, Mayer M, Pisarev AA, Roth J. Ion-driven deuterium permeation through tungsten at high temperatures. *J Nucl Mater*. 2009;390-391:606-609. doi:10.1016/j.jnucmat.2009.01.172.
5. Moshkunov KA, Schmid K, Mayer M, Kurnaev VA, Gasparyan YM. Air exposure and sample storage time influence on hydrogen release from tungsten. *J Nucl Mater*. 2010;404(3):174-177. doi:10.1016/j.jnucmat.2010.07.011.
6. Baldwin MJ, Schwarz-selinger T, Yu JH, Doerner RP. TMAP-7 simulation of D2 thermal release data from Be co-deposited layers. *J Nucl Mater*. 2013;438:967-970. doi:10.1016/j.jnucmat.2013.01.210.
7. Baldwin MJ, Doerner RP. Effect of layer thickness on the thermal release from Be–D co-deposited layers. *Nucl Fusion*. 2014;54:6. doi:10.1088/0029-5515/54/8/083032.

8. Baldwin MJ, Schwarz-Selinger T, Doerner RP. Experimental study and modelling of deuterium thermal release from Be–D co-deposited layers. *Nucl Fusion*. 2014;54:10. doi:10.1088/0029-5515/54/7/073005.
9. Peñalva I, Alberro G, Legarda F, Esteban G, Riccardi B. Interaction of Copper Alloys with Hydrogen. In: Collini DL, ed. *Copper Alloys - Early Applications and Current Performance - Enhancing Processes*. InTech; 2012:186. doi:10.5772/34469.
10. Chandra K, Kulkarni AS, Ramanjaneyulu PS, et al. Determination of diffusion coefficients of hydrogen and deuterium in Zr–2.5% Nb pressure tube material using hot vacuum extraction-quadrupole mass spectrometry. *J Nucl Mater*. 2015;461:151-156. doi:10.1016/j.jnucmat.2015.03.021.
11. Kearns JJ. Diffusion coefficient of hydrogen in alpha zirconium, Zircaloy-2 and Zircaloy-4. *J Nucl Mater*. 1972;43:330-338.
12. Gulbransen E, Andrew K. Solubility and decomposition pressures of hydrogen in alpha-zirconium. *JOM*. 1955;7:136-144.
13. Yamanaka S, Tanaka T, Miyake M. Effect of Oxygen on Hydrogen solubility in Zirconium. *J Nucl Mater*. 1989;167(C):231-237. doi:10.1016/0022-3115(89)90446-7.
14. Miyake M, Uno M, Yamanaka S. On the zirconium–oxygen–hydrogen ternary system. *J Nucl Mater*. 1999;270(1-2):233-241. doi:10.1016/S0022-3115(98)00779-X.

7 – Summary and Future Work

Contents

7.1 – Oxide Growth.....	187
7.2 – SPP Oxidation	188
7.3 – Hydrogen Pick-up Results.....	189
7.4 – Modelling	190
7.5 – Future Work	191

7.1 – Oxide Growth

The oxidation of Zircaloy-4 was not affected significantly by the pH range tested ($\text{pH}_{360} = 6.15$, $\text{pH}_{350} = 8.82$) of the oxidising water. By comparing the oxidation rates in the different environments I found that there was an effect of both temperature and pH on the oxidation. The growth of the suboxide layer was similar in both environments, which leads me to believe the effect of pH is small on the oxide growth and the difference observed is mainly due to the temperature. This means that oxidation is not limited by the availability of protons in the oxidising water. The available protons are used for charge balance with the electrons liberated during corrosion, either by the electrons flowing through the oxide to form hydrogen gas, or by the inward migration of hydrogen to form hydrides. Therefore, if changing the number of available protons does not change the oxidation rate, the rate of electron transport must be much higher than the proton transport through the oxide. This would also indicate that the amount of hydrogen pick-up in the pre-transition regime would be similar as both materials have similar hydrogen transport rates, which was confirmed in section 5.2.6 as the pre-transition hydrogen pick-up was similar for both environments.

I examined the OM interface and the growth of the OSZ and ZrO layers as oxidation occurs. The OSZ and ZrO layers show a cyclical nature, in that they both gradually get thicker as the oxidation time increases, before being consumed at transition, and then re-growing in the second stage of oxidation. There did not appear to be any difference in the growth rate or morphology in the different environments tested.

The TEM foils I examined from the 243 day sample had oxides much thinner than calculated from the weight gain. In some places the oxide was passing through transition, as evidenced from the shape of the plasmon peaks in those regions.

7.2 – SPP Oxidation

The SPPs generally show the same oxidation behaviour. Cracks form above and below the SPPs as they are embedded in the oxide. Zr in the SPP was oxidised first, with oxidation at the surface of the SPP as the SPP encounters the oxide, even while part of the SPP was in contact with the metal. The solubility of metals in oxides is very low, so the metallic Cr and Fe migrated out of the oxidised regions of the SPP. As the OM interface moved further into the metal, leaving the SPP within the oxide, Zr oxidation progresses further into the SPP, the metallic Cr and Fe migrated into the cracks surrounding the SPP. As the OM interface moves further away from the SPP and the oxygen potential increases, Cr began to oxidise, and metallic Fe migrated away from the oxidised Cr.

In the cracks the Cr started oxidising in regions of low Fe first (after around 10 days). In regions with Cr and Fe together, the Cr did not oxidise in Fe until the SPP has been in the oxide for over 130 days (2.1 μm oxide thickness). Fe was not oxidised in the crack at 2.1 μm but was at 2.45 μm , which means it oxidises in between these regions.

I used 3 different parameters to determine if the Cr and Fe were oxidised in the SPPs and whether their oxidation state had changed, which has proved useful as a single parameter was somewhat inconsistent. The energy difference between the O-K edge and the Cr/Fe L_3 , $\Delta E(\text{Cr/Fe})$ did not show any oxidation of Cr based on the literature values. The $\Delta E(\text{Fe})$ values were slightly more consistent. The FWHM data was sensitive to the sample thickness so is only really useful if all samples are of the same thickness. The L_3/L_2 ratio was the most consistent of the 3 parameters, in that there was a noticeable increase as the SPPs were in the oxide for longer but was still not easy to interpret on its own.

I measured the Fe/Cr ratio on the SPPs I examined, and the Fe/Cr ratio in the centre of the SPP shows the same trend shown previously, and is virtually zero after 0.8 μm into the oxide. The Fe/Cr ratio in the cracks initially increases as Fe migrates faster from the SPP than Cr, except for in one SPP (SPP1

in Figure 4.79) which had a uniform Fe/Cr ratio in the SPP and crack. After this, the Cr content increases in the cracks.

There was an increase in the O content in the crack after the SPP distance from the OM interface passes 2.2 μm (the oxide thickness at transition). This SPP was the first one which showed that both Fe and Cr were oxidised.

7.3 – Hydrogen Pick-up Results

I have shown that hydrogen which is desorbed is not due to a phase change of the material, but due to the difference in free energy between hydrogen in the metal and the gas phase becoming positive at around 600°C.

The oxide formed acts as a barrier to hydrogen desorption, until the temperature reaches the point at which the oxide is dissolved into the metal, which allows the hydrogen to desorb.

The relationship between hydrogen content and the amount detected by TDS has been calculated from the Westinghouse HHGE data, which shows that there are 1.15×10^6 counts/ppm H_2 in a sample, for a 5 μA emission current. This will allow for a quick quantification of hydrogen content for samples subsequently tested with TDS.

There is a drop in the amount of all species (H_2 , D-H, D_2) in samples with the oxide intact for the 91 day sample compared to the 75 day sample. The amounts the species decrease are 19%, 33%, and 32% for H_2 , D-H, and D_2 respectively, which are far more than just sample to sample variation. The samples which were cold rolled showed an increase in the amount of hydrogen desorption, and the induced stress on the sample during the oxide removal could have had a similar effect and caused the extra hydrogen desorption. The H_2 is roughly the same in the 123 day sample and these are both less than was found in the 15 day sample. This is contradicted by the HHGE data from PSI, which shows that it increases monotonically from 15 to 123 days.

For the first 1.5 μm of oxide growth, hydrogen pick-up is not affected by the pH range tested, which means that prior to transition hydrogen pick-up is not affected by the availability of protons or H_2 in the environment. After 1.5 μm of oxide growth the samples to high pH showed a much lower hydrogen pick-up than those exposed to pure water, and also lower than any other material tested in

the MUZIC-2 collaboration. This likely due to the addition of Li and boric acid to the oxidising environment, which has previously been shown to reduce f_H .

The NanoSIMS results show that D_0 for the external oxide is slightly higher for the 148 day high pH sample compared to the 106 day oxide, and that D_0 for the internal oxide is similar for both (as well as for the 61 day pure water sample). There is a correlation between oxidation time and D_0 for the internal and external oxide, but D_0 does not appear to be affected by pH.

H/D has penetrated deeper in the 148 day sample than for the rest of the samples tested (one of the depth profiles not shown showed H/D up to $4\mu\text{m}$ from the OM interface). This can be explained by the fact that the pure water samples were only exposed to D_2O for 31 days, after an initial oxidation in pure water, which means the deuterium has had much less time to diffuse through the oxide. For the 148 day sample, the oxide is cracked, especially in the outer, equiaxed region. Some of the cracks will be connected to the surface, so there will be a combination of solid state diffusion from the surface and water ingress. The longer and more numerous the crack network, the larger the fraction of percolation to solid state diffusion. This can be seen in the 3D profiles, where both high pH samples show a higher concentration of H/D in the metal and a much clearer path of the H/D migration. Much more work is needed in this area to obtain a clearer picture of what is happening during and after transition.

7.4 – Modelling

A successful sensitivity study using TMAP been carried out. TMAP has the ability to reproduce the hydrogen desorption seen by TDS. Using the literature values as a starting point, I found that they were all in the correct order of magnitude.

The lower temperature peak was reproduced with $E_B = 0.2 - 0.3 \text{ eV}$ and $E_D = 0.47 \text{ eV}$. The higher temperature peak was shown with $E_B = 0.93$ and $E_D = 0.47 \text{ eV}$.

By keeping $E_B = 0.3 \text{ eV}$ and varying E_D at the same time as E_T it was possible to reproduce the high temperature peaks shown during the TDS analysis. This is at the upper end of E_B from the literature for H in Zr vacancies, which indicates that this is where the hydrogen observed from TDS is released from.

It was possible to reproduce the lower temperature peak (from hydrogen near the surface of Zr), along with the higher temperature peak, however E_D was higher than found in the literature for both peaks.

7.5 – Future Work

To help with characterising SPPs it would be useful to carry out measurements of the three parameters mentioned on pure samples of Cr, Cr^{3+} , Fe and Fe^{2+} to obtain a standard to compare results with.

Carrying out emissivity tests of my materials would be beneficial as it would be possible to determine more accurately what temperature the hydrogen is desorbed. It would also help determine the exact temperature at which the oxide starts dissolving into the metal in oxidised samples, and the temperature the sample settles to after the oxide dissolves could also be determined.

Testing samples exposed to primary water conditions with TDS would help determine if the addition of Li and boric acid is the cause of the reduced f_H for samples exposed to high pH in this thesis.

There was a discrepancy between the amount of hydrogen detected by HHGE at PSI and my tests with TDS. The lack of samples tested with HHGE and the oxide intact makes it hard to interpret the data, so it would be beneficial for more samples to be tested with this method. It would also be beneficial to run more 91 and 123 day high pH samples with the oxide intact in the TDS.

More work needs to be carried out with TMAP to model both desorption peaks simultaneously. There needs to be a more thorough study on the node thickness and how it affects the peak widths. By carrying out the simulations on a computer cluster it would be possible to carry out the simulations with a larger number of nodes and in a smaller time-scale.

Appendix A- TMAP input file

Contents

A.1 – Example Input File.....	192
A.2 – Example Input File For 2 Traps	194

A.1 – Example Input File

```
1. title input
2. TDS of Zr sample without a thin oxide film
3. end of title input
4. $
5. Main Input
6. dspcnme=d,end
7. espcnme=d2,end
8. segnds=20,117,end
9. nbrencl=1,end
10. linksegs=1,2,end
11. end of main input
12. $
13. Enclosure Input
14. start bdry,1,end
15. etemp=equ,1,end
16. espres=d2,equ,6,end
17. end of enclosure input
18. $
19. thermal input
20. $ Segment 1 - Zr film
21. start thermseg,end
22. delx=1*0.0,18*1.0e-9,1*0.0,end
23. tempd=20*300.0,end
24. tcon=const,22.6,end
25. rhocp=const,1.81e6,end
26. hsrc=const,0.0,srcpf,20*0.0,end
27. htrbcl=stemp,equ,1,end
28. htrbcr=link,end
29. hgap=const,1.0e6,end
30. $ Segment 2 - Zr metal - half thick
31. start themseg,end
32. delx=1*0.0,1*1.0e-9,1*1.e-8,51*1.e-7,51*1.e-6,1*1.e-5,10*1.888e-5,1*0.0,end
33. tempd=117*300.0,end
34. tcon=const,22.6,end
35. rhocp=const,1.81e6,end
36. hsrc=const,0.0,srcpf,117*0.0,end
37. htrbcl=link,end
38. htrbcr=adiab,end
39. end of thermal input
40. $
41. diffusion input
42. $ Segment 1 - Zr film
43. start diffseg,end
```

```

44. nbrden=4.3e28,end
45. concd=d,20*3.6e10,end
46. dcoef=d,equ,2,end
47. trapping=ttyp,1,tconc,const,1.00e-3
48. tspc,d,alphr,equ,8 $2.6e-2
49. alpht,equ,7,ctrp,const,1.0 $2.5e-6
50. ttyp,2,tconc,const,0.0,tspc,d,alphr,equ,5 $0.5e-2
51. alpht,equ,7,ctrp,norm,1.0,0.0,2.500000e-06,1e-6 $2.5e-6
52. ttyp,3,tconc,const,0.0,tspc,d,alphr,equ,6 $1.0e-2
53. alpht,equ,7,ctrp,norm,1.0,0.0,3.000000e-07,0.0,end $2.5e-6
54. qstrdr=d,const,0.0,end
55. srcsd=d,const,0.0,srcpf,20*0.0,end
56. difbcl=lawdep,encl,1,dspc,d,d2
57. pexp,0.5,solcon,equ,3,end
58. difbcr=link,d,solcon,equ,3,end
59. surfa=1.04e-4,end
60. $
61. $ Segment 2 - Zr foil - foil thickness
62. start diffseg,end
63. nbrden=4.3e28,end
64. concd=d,117*3.6e10,end
65. dcoef=d,equ,4,end
66. trapping=ttyp,1,tconc,norm,1.00e-3,0.0,10.000000e-04,0.0
67. tspc,d,alphr,equ,8 $2.6e-2
68. alpht,equ,7,ctrp,const,1.0 $2.5e-6
69. ttyp,2,tconc,const,0.0,tspc,d,alphr,equ,5 $0.5e-2
70. alpht,equ,7,ctrp,norm,1.0,0.0,2.500000e-06,1e-6 $2.5e-6
71. ttyp,3,tconc,const,0.0,tspc,d,alphr,equ,6 $1.0e-2
72. alpht,equ,7,ctrp,norm,1.0,0.0,3.000000e-07,0.0,end $2.5e-6
73. qstrdr=d,const,0.0,end
74. srcsd=d,const,0.0,srcpf,117*0.0,end
75. difbcl=link,d,solcon,equ,5,end
76. difbcr=nonflow,end
77. surfa=1.04e-4
78. end of diffusion input
79. $
80. equation input
81. $ (1) Temperature History Equation
82. $y= (300.0+0.16666*time)*(1-int(time/4638))+ 1073.0 *(int(time/4638)),end
83. y= (300.0+0.16666*time),end
84. $ (2) - (5) Diffusion and Solubility Equations
85. $ (2) Diffusion (m2/s) of H in Zr
86. y= 7.73e-7*exp(-5445/temp),end
87. $ (3) S (Hydrogen/m^3)
88. y=8.167e-4*exp(-((62.929*temp)-59714)/8.31446/temp),end
89. $ (4) Diffusion (m2/s) of H in Zr
90. y= 7.73e-7*exp(-5445/temp),end
91. $ (5) S (Hydrogen/m^3)
92. y=8.167e-4*exp(-((62.929*temp)-59714)/8.31446/temp),end
93. $ (6) Pressure History
94. y=6.67e-7,end
95. $ (7) Alpht for h in tungsten (1/s)
96. y=5.16e12*exp(-5445.0/temp),end
97. $ (8) Alphr for trap 1 in tungsten (1/s)
98. y=8.252e12*exp(-0.7/8.617e-5/temp),end

```

```

99.  end of equation input
100. $
101. $
102. table input
103. end of table input
104. $
105. $
106. control input
107. time=0.0,end
108. tstep=6.0,end
109. timend=8000.0,end
110. nprint=10,end
111. itemx=90,end
112. delcmx=1.0e-8,end
113. bump=1.e-2,end
114. bound=2.0,end
115. omega=1.3,end
116. end of control input
117. $
118. plot input
119. nplot=10,end
120. plotseg=1,2,end
121. plotencl=end
122. dname=d,end
123. ename=end
124. dplot=moblinv,sflux,end
125. eplot=end
126. end of plot input
127. $
128. end of data

```

A.2 – Example Input File For 2 Traps

```

1.  title input
2.  TDS of Zr sample without a thin oxide film
3.  end of title input
4.  $
5.  main input
6.  dspcnme=d,end
7.  espcnme=d2,end
8.  segnds=20,117,end
9.  nbrencl=1,end
10. linksegs=1,2,end
11. end of main input
12. $
13. enclosure input
14. start bdry,1,end
15. etemp=equ,1,end
16. esppres=d2,equ,6,end
17. end of enclosure input
18. $
19. thermal input
20. $ Segment 1 - Zr film
21. start thermseg,end
22. delx=1*0.0,18*1e-7,1*0.0,end
23. tempd=20*300.0,end

```

```

24.  tcon=const,22.6,end
25.  rhocp=const,1.81e6,end
26.  hsrc=const,0.0,srcpf,20*0.0,end
27.  htrbcl=stemp,equ,1,end
28.  htrbcr=link,end
29.  hgap=const,1.0e6,end
30.  $ Segment 2 - Zr metal - half thick
31.  start themseg,end
32.  delx=1*0.0,1*1.0e-9,1*1.e-8,51*1.e-7,51*1.e-6,1*1.e-5,10*1.888e-5,1*0.0,end
33.  tempd=117*300.0,end
34.  tcon=const,22.6,end
35.  rhocp=const,1.81e6,end
36.  hsrc=const,0.0,srcpf,117*0.0,end
37.  htrbcl=link,end
38.  htrbcr=adiab,end
39.  end of thermal input
40.  $
41.  diffusion input
42.  $ Segment 1 - Zr film
43.  start diffseg,end
44.  nbrden=4.3e28,end
45.  concd=d,20*3.6e10,end
46.  dcoef=d,equ,2,end
47.  trapping=ttyp,1,tconc,norm, 5.0e-3,0.0,10.000000e-04,0.0
48.    tspc,d,alphr,equ,9 $2.6e-2
49.    alpht,equ,7,ctrp, const,1.0      $2.5e-6
50.    ttyp,2,tconc, const,0.0,tspc,d,alphr,equ,9      $0.5e-2
51.    alpht,equ,7,ctrp, const,1.0      $2.5e-6
52.    ttyp,3,tconc, const,0.0,tspc,d,alphr,equ,6      $1.0e-2
53.    alpht,equ,7,ctrp, norm,1.0,0.0,3.000000e-07,0.0,end      $2.5e-6
54.  qstrdr=d, const,0.0,end
55.  srcsd=d, const,0.0,srcpf,20*0.0,end
56.  difbcl=lawdep,encl,1,dspc,d,d2
57.  pexp,0.5,solcon,equ,3,end
58.  difbcr=link,d,solcon,equ,3,end
59.  surfa=1.04e-4,end
60.  $
61.  $ Segment 2 - Zr bulk
62.  start diffseg,end
63.  nbrden=4.3e28,end
64.  concd=d,117*3.6e10,end
65.  dcoef=d,equ,4,end
66.  trapping=ttyp,1,tconc,norm,1.00e-3,0.0,10.000000e-04,0.0
67.    tspc,d,alphr,equ,10 $2.6e-2
68.    alpht,equ,8,ctrp, const,1.0      $2.5e-6
69.    ttyp,2,tconc, norm,0.0,0.0,10.000000e-04,0.0,tspc,d,alphr,equ,9      $0.5e-2
70.    alpht,equ,7,ctrp, const,1.0      $2.5e-6
71.    ttyp,3,tconc, const,0.0,tspc,d,alphr,equ,6      $1.0e-2
72.    alpht,equ,7,ctrp, norm,1.0,0.0,3.000000e-07,0.0,end      $2.5e-6
73.  qstrdr=d, const,0.0,end
74.  srcsd=d, const,0.0,srcpf,117*0.0,end
75.  difbcl=link,d,solcon,equ,5,end
76.  difbcr=nonflow,end
77.  surfa=1.04e-4
78.  end of diffusion input

```

```

79.  $
80.  equation input
81.  $ (1) Temperature History Equation
82.  $y= (300.0+0.16666*time)*(1-int(time/4638))+ 1073.0 *(int(time/4638)),end
83.  y= (300.0+0.16666*time),end
84.  $ (2) - (5) Diffusion and Solubility Equations
85.  $ (2) Diffusion (m2/s) of H in Zr film
86.  y= 7.73e-7*exp(-0.77/8.617e-5/temp),end
87.  $ (3) S (Hydrogen/m^3)
88.  y=8.167e-4*exp(-((62.929*temp)-57910)/8.31446/temp),end
89.  $ (4) Diffusion (m2/s) of H in Zr bulk
90.  y= 7.73e-7*exp(-0.87/8.617e-5/temp),end
91.  $ (5) S (Hydrogen/m^3)
92.  y=8.167e-4*exp(-((62.929*temp)-57910)/8.31446/temp),end
93.  $ (6) Pressure History
94.  y=6.67e-7,end
95.  $ (7) Alpht for h trap 1 in film (1/s)
96.  y=5.16e12*exp(-0.77/8.617e-5/temp),end
97.  $ (8) Alpht for h trap 2 in bulk (1/s)
98.  y=5.16e12*exp(-0.87/8.617e-5/temp),end
99.  $ (9) Alphr for trap 1 in film (1/s)
100. y=8.252e12*exp(-1.27/8.617e-5/temp),end
101. $ (10) Alphr for trap 2 in bulk (1/s)
102. y=8.252e12*exp(-1.27/8.617e-5/temp),end
103. end of equation input
104. $
105. $
106. table input
107. end of table input
108. $
109. $
110. control input
111. time=0.0,end
112. tstep=6.0,end
113. timend=8000.0,end
114. nprint=10,end
115. itermx=90,end
116. delcmx=1.0e-8,end
117. bump=1.e-2,end
118. bound=2.0,end
119. omega=1.3,end
120. end of control input
121. $
122. plot input
123. nplot=10,end
124. plotseg=1,2,end
125. plotencl=end
126. dname=d,end
127. ename=end
128. dplot=moblinv,sflux,end
129. eplot=end
130. end of plot input
131. $
132. end of data

```